University College London

Department of Chemistry

Diamond Light Source

In-situ synchrotron based investigations of the structure of iron substituted microporous catalysts under operating conditions

A thesis submitted to the University College London

For the degree of doctor of philosophy

By

Gregory Pavlos Gregori

2017

Supervisors: G. Sankar, C.R.A. Catlow, E. Shotton, A. Kroner

"Science is a way of trying not to fool yourself. The first principle is that you must not fool yourself, and you are the easiest person to fool"

Richard Feynmann; adapted from a 1974 Caltech commencement address - published in Surely You're Joking, Mr. Feynman! p.343

Declaration

I, Gregory Gregori, confirm that the work presented in this thesis is my own. Where information has been derived from other sources, I confirm that this has been indicated in the thesis.

Copyright

Abstract

Microporous aluminosilicates and aluminophosphates have been studied for a variety of applications. Incorporation of a transition metal ion into their framework structure allows them to be modified into functional redox catalysts for a wide range of industrially important processes. In particular, FeZSM-5 has shown remarkable catalytic activity under mild conditions for the oxidation of benzene to phenol (OBP) using N_2O as oxidant. Recent work has shown that the aluminophosphate FeAlPO-5 is also equally active as a catalyst for this reaction. Therefore, the aim of this work is to investigate the changes occurring during the calcination (activation) and catalytic reaction conditions of various Fe-substituted nanoporous catalysts using synchrotron based X-ray diffraction and spectroscopic methods.

High-resolution powder diffraction (HRPD) measurements were carried out on FeAlPO-5 and FeZSM-5 to investigate changes to the crystal structure occurring during calcination. Pawley refinement, indicates strong negative thermal expansion upon loss of template for FeAlPO-5. The local structure and oxidation state changes of Fe located in FeAlPO-5 and FeSAPO-34 were studied using XAS during calcination in air. In addition to the above, ruthenium containing system is also investigated to examine the possible synergistic effects between Ru and Fe by supporting over Fe containing nanoporous materials. FeMFI, FeSAPO-5, RuFeMFI and RuFeSAPO-5 were then studied using *in situ* Fe and Ru K-edge EXAFS during calcination in air, activation in He, and pulsed experiments with N_2O/benzene. The results show reduction of Fe and Ru upon the introduction of benzene to the system, indicating that the catalytic mechanism for the (OBP) reaction may require this step for the generation of the active Fe species. In summary, the project allowed us to examine the host crystalline material and catalytically active sites using synchrotron based X-ray techniques, and complementary characterisation methods.

Acknowledgements

I would like to thank my supervisor first of all Professor Gopinathan Sankar for his support, wisdom and encouragement throughout the last few years. I would also like to thank him for the opportunity to do this PhD thesis and his confident attitude that helped give me hope when it all seemed like it was getting too much. Also a thanks to Professor Richard Catlow for his support. I would also like to thank my industrial supervisors Dr. E. Shotton and Dr. A. Kroner, from Diamond Light Source for their help and advice and aid at beam time. I have obtained assistance and guidance from many people in UCL and Diamond, and especially to the staff at the I11 and B18 beamlines of Diamond Light Source, and would like to express my gratitude.

I would also like to say a big thank you to my friends and colleagues, Tom Daley, Husn Islam, Andy Smith, Anastasia Mantalini, and Martin Martis for useful discussions, and brightening up the day during the time of my research project. Tom in particular has saved my hide on more than one occasion. In addition, I am extremely grateful to my brother Chris, my mother Chloe and my father Pavlos, and my grandmother Elpida for spiritual, financial and emotional support during the tough times! Very special thanks goes to all who I had a chance to work during beamtime for help, keeping awake, entertaining conversation, and all for many inspirational nights in the pub or student union. Also big thanks to all my friends for support without whom none of this would have been possible. There were too many friends, colleagues, travellers, teachers, strangers and lovers encountered on the way, which have my gratitude.

List of Figures and Tables

Figure 3.2*. a) Waterfall plot of XRD patterns collected in-situ; b) Selected XRD patterns collected for FeZSM-5 (temperatures in degrees Celsius). The gap occurring in the patterns at around 2θ = 20° is due to subsequent removal of a reflection peak caused by the quartz capillary tube used to mount the sample.*

Figure 5.2. *Temperature profile of the high temperature activation of the catalysts in He to 550°C, followed by the pulsed benzene/N_2O experiment at 350°C.*

Figure 5.3. *Variation of the position of the rising edge absorption energy E_0 and maximum pre-edge intensity values for the normalised Fe K-edge XANES data collected for FeMFI during activation in He at 30°C (blue), 350°C (red) and 850°C (green). The reference compounds $FePO_4$-quartz (brown - T_d geometry) and $FePO_4.2H_2O$ (purple - O_h geometry) are also plotted for comparison. As the temperature is increased the E_0 moves to lower values as the Fe ions in the catalyst are reduced. The pre-edge feature also drops as the temperature is raised, indicating a reduction of symmetry from a near totally octahedral state to one with the majority of ions in a tetrahedral coordination state.*

Figure 5.4. *Variation of rising edge absorption energy E_0,(a) and maximum pre-edge intensity (b) values for the normalised Fe K-edge XANES data collected for FeMFI during activation in He up to 800°C. Errors of the white line positions are ± 0.1 eV, and for pre-edge intensity ± 5%.*

Table 5.1. *White line energy E_0, pre-edge intensity and pre-edge energy position of selected samples and references. Errors in the white line positions are ± 0.1 eV, and for pre-edge intensity ± 5%.*

Figure 5.6. *Fits tot the Fe-Kedge EXAFS data analysed in k-space.(k^3-weighted) with associated Fourier transforms for FeMFI in helium at 30°C.*

Figure 5.7. *Fits tot the Fe-Kedge EXAFS data analysed in k-space.(k^3-weighted) with associated Fourier transforms for FeMFI in helium at 850°C.*

Figure 5.8. *Variation of parameters from Fe K-edge EXAFS fits during activation in He up to 880°C for FeMFI; (a) Fe-O bond length, (b) Debye-Waller factor, (c) coordination number. Errors for bond lengths are ± 0.01 Å. Errors in coordination number N, and $2\sigma^2$ are ~10%.*

Figure 5.9. *Comparison of the variation of position of the rising edge absorption energy E_0 and maximum pre-edge intensity, for the normalised Fe K-edge XANES data collected for FeMFI and RuFeMFI during activation in He. From the movement of the rising edge to lower energy values and the drop in pre-edge peak intensity it is clear that the sample is both being reduced, and undergoing a change to lower symmetry from an original tetrahedral-like geometry. The Fe in both samples starts in a very similar state, but the evolution of Fe reduction and uncoordination during the pre-tereatment seems to be affected to a large extent by the presence of Ru in the samples. The Fe in RuFeMFI does not reach as high a level of reduction as the FeMFI at 850°C.*

Figure 5.10. *Comparison of E_0 value for FeMFI and RuFeMFI between 30-850°C in helium. Errors of the white line positions are ± 0.1 eV.*

Figure 5.11. *Variation of the Fe K-edge absorption energy E_0 (a), and maximum pre-edge intensity (b) values for the normalised XANES data collected for Ru/FeMFI during activation in He up to 850°C. The general trend is observable showing a general increase in pre-edge feature form an average value of 0.151 at 30°C intensity as the temperature is increased, to 1.62 at 800°C. Errors of the white line positions are ± 0.1 eV, and for pre-edge intensity ± 5%.*

Figure 5.12. *Variation of parameters from EXAFS fits during activation in He up to 880°C for Ru/FeMFI; (a) Fe-O bond length, (b) Debye-Waller factor, (c) coordination number. Errors for bond lengths are ± 0.01 Å. Errors in coordination number N, and $2\sigma^2$ are ~10%.*

Figure 5.13. *Ru K-edge EXAFS spectra measured during activation in He up to 450°C for Ru/FeMFI.*

Figure 5.14. *Variation of rising edge absorption energy E_0 for the normalised Ru K-edge XANES data collected for RuFeMFI during activation in He up to 570°C. Errors of the white line positions are ± 0.1 eV.*

Figure 5.15. *Variation of parameters from Ru K-edge EXAFS fits during activation in He up to 450°C for Ru/FeMFI; (a) Ru-O bond length, (b) Debye-Waller factor, (c) coordination number. Errors for bond lengths are ± 0.01 Å. Errors in coordination number N, and $2\sigma^2$ are ~10%.*

Figure 5.16. *Variation of rising edge absorption energy E_0,(a) and maximum pre-edge intensity (b) values for the normalised Fe K-edge XANES data collected for FeSAPO-5 during activation in He up to 570°C. Errors of the white line positions are ± 0.1 eV, and for pre-edge intensity ± 5%.*

Figure 5.17. *Variation of parameters from Fe K-edge EXAFS fits during activation in He up to 600 °C for FeSAPO-5; (a) Fe-O bond length, (b) Debye-Waller factor, (c) coordination number. Errors for bond lengths are ± 0.01 Å. Errors in coordination number N, and $2\sigma^2$ are ~10%.*

Figure 5.18. *Fits to the Fe-Kedge EXAFS data analysed in k-space (k^3-weighted) with associated Fourier transforms for RuFeSAPO-5 in helium at 30 °C.*

Figure 5.19. *Variation of rising edge absorption energy E_0,(a) and maximum pre-edge intensity (b) values for the normalised Fe K-edge XANES data collected for Ru/FeSAPO-5 during activation in He up to 530 °C. Errors of the white line positions are ± 0.1 eV, and for pre-edge intensity ± 5%.*

Figure 5.20. *Variation of parameters from Fe K-edge EXAFS fits during activation in He up to 530 °C for RuFeSAPO-5; (a) Fe-O bond length, (b) Debye-Waller factor, (c) coordination number. Errors for bond lengths are ± 0.01 Å. Errors in coordination number N, and* $2\sigma^2$ *are ~10%.*

Figure 5.21. *Variation of rising edge absorption energy* E_0 *values for the normalised Fe K-edge XANES data (from each individual measurement – not merged like EXAFS data) collected for Ru/FeSAPO-5 during the pulsed experiment. (a) During activation ramp to 550°C. (b) Pulsed gas experiment. Red marks indicate the introduction of benzene and blue marks a switch to* N_2O*. Green at the end denotes a return to He atmosphere to purge the system of reactant gas. Errors of the white line positions are ± 0.1 eV. Each scan took around 6 minuites.*

Table 5.22. *Variation of calculated parameters* E_0*,* $R_{Fe\text{-}O}$*,* $2\sigma^2$*, and coordination number N, for the normalised Fe K-edge XANES data collected for Ru/FeSAPO-5 during pulsed experiment. Each value is calculated from the merged XAS spectra of the last three scans taken after 15 minutes under each respective gas flow.*

Figure 5.23 *Variation of rising edge absorption energy* E_0*,(a) and Ru/*RuO_2 *mass fraction (b), values for the normalised Ru K-edge XAS data collected for Ru/FeSAPO-5 during activation in He up to 530 °C. Errors of the white line positions are ± 0.1 eV, and for mass fraction ± 10%.*

Figure 5.24. *EXAFS and resulting fourier transform plot for Ru K edge data of RuFeSAPO-5 at 23°C*

Figure 5.25 *a) Change in rising-edge position and intensity of Ru K-edge XANES spectrum for RuFeSAPO-5 in He and benzene. b) FT EXAFS plot showing clear differences in environment around Ru under different atmospheres.*

Fig 5.26. *Comparison of evolution of* RuO_2*-like fraction (blue triangles) and metallic* Ru^0 *fraction (red squares) over the course of the experiment at 350°C. Benzene vapour was introduced at the point indicated by the dotted line in helium at 350°C. Time between scans is 3 minutes. Errors in the calculated mass fraction are approximately ±10%.*

Fig 5.27. *UV-Vis Diffuse Reflectance spectra of selected catalysts.*

Fig 5.28. *SEM image of FeMFI.*

Fig 5.29. *SEM image of RuFeMFI.*

Fig 5.30. *SEM of FeSAPO-5*

Fig 5.31. *SEM of RuFeSAPO-5*

Contents

Chapter 2: Theory and Experimental Techniques

Chapter 3: Characterization of thermal expansion behaviour in FeZSM-5 and FeAlPO-5; an in situ XRD study.

Chapter 4: Characterization of iron active sites in FeAlPO-5 and FeSAPO-34; an in situ XAS study.

Chapter 5: In situ XAS investigation of Fe and Fe/Ru substituted microporous catalysts under operating conditions

Chapter 1

Iron substituted Nanoporous Catalysts

1.1 Introduction

Zeolites and aluminophosphates are crystalline solids containing pores and channels of molecular dimensions (Figure 1). They occur naturally, but synthetic varieties are mostly used in industry. These microporous materials are used widely in a variety of applications with a global market of several million tonnes per annum. Major uses include petrochemical cracking, ion-exchange, the separation and removal of gases and solvents, agriculture and construction[1,2]. In the pure silicate or aluminophosphate form these solids possess a neutral framework, but by introducing lower valent metal ions into the framework cation sites, for example trivalent transition metal ions and other main group elements into the Si^{4+} sites in the structure, either during or after synthesis, they can be modified into functional catalysts for a wide range of industrially important processes.

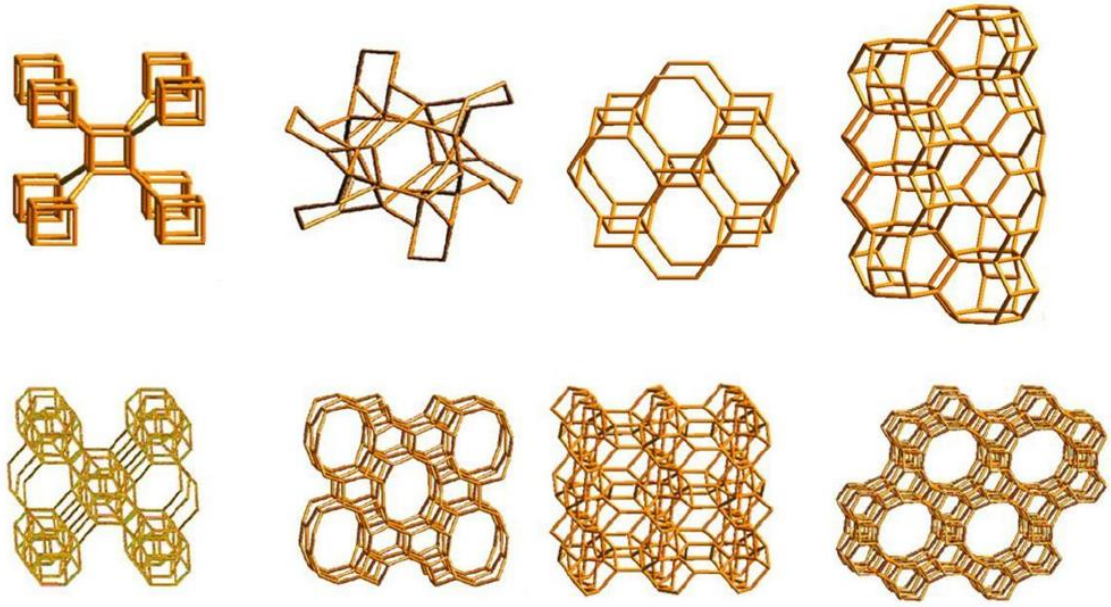

Figure 1. *Molecular sieves – the nanoporous framework structures of some zeolites are shown.*[4]

1.2 The Structure and Composition of Nanoporous Solids

1.2.1 Aluminosilicates

Aluminosilicates consist of $[AlO_4]^{5-}$ and $[SiO_4]^{4-}$ tetrahedra linked together by corner sharing oxygen atoms to form chains and rings that leads to an extended three-dimensional open framework structure with molecular sized cavities (Figure 1.1).[13] The extra negative charge from the $[AlO_4]^{5-}$ units is balanced by the presence of various cations such as H^+, Na^+ or K^+ which are distributed throughout the structure in extra-framework sites. When H^+ is the cation, these act as Brønsted acid sites in the inner surface of the zeolite framework.

Aluminosilicates can be synthesised with varying Si/Al ratios. The framework charge discrepancy, arising from the more negatively charged $[AlO_4]^{5-}$ subunits, leads to an increase in the surface acidity with decreasing Si/Al ratio. Water molecules are also often found in the micropores, and can be coordinated to cations and charged framework sites. Organic templates used as structure directing agents during synthesis may also be present in the as-synthesised zeolite and are often removed by calcination in air during pre-treatment for catalytic use.[3] The presence of loosely bound hydrated cations in microporous solids gives rise to their important ion exchange and absorption functionality and can affect the overall structure and physicochemical properties of the zeolite. It is the shape and size selectivity resulting from the dimensions of the zeolite pores that is the key to the "molecular sieving" effect – allowing only molecules of certain shapes and sizes to pass in and out.

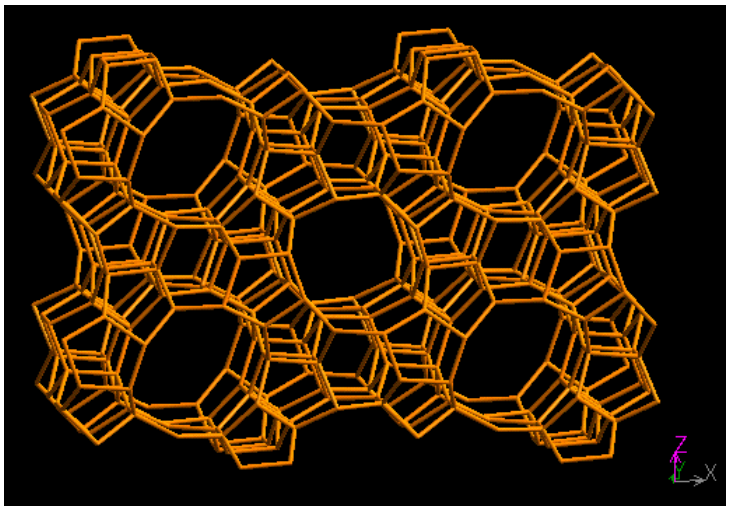

Figure 2. *The microporous structure of ZSM-5.*[4]

Microporous solids can be modified by introducing transition metal ions such as iron, titanium, copper and manganese[5,6,7,8] into the framework during synthesis (isomorphous substitution) or introducing them post synthesis through various methods such as aqueous ion exchange or CVD.[9] The introduction of metal ions often leads to modification of the surface structure and properties, often allowing the creation of novel catalysts for a variety of functions. The activity of these catalytic materials is highly dependent on not only the particular zeolite or metal but also on the method used for the introduction of the metal and particularly its coordination environment as well as electronic properties.

Zeolites form a diverse and exciting group of advanced inorganic materials, where their crystal structures contain regular arrays of channels and voids of similar dimensions to small molecules (ranging from 0.3 nm to over 1 nm) thereby allowing the diffusion of guest molecules into the interior of their structure. Their framework is generally built of $[SiO_4]^{4-}$ and $[AlO_4]^{5-}$ tetrahedra which corner share oxygen atoms to form 3-dimensional nanoporous structures with varying ring size, shape, and dimensionality. Aluminosilicate zeolites have a negatively charged framework due to the charge deficiency from a fraction of framework Al^{3+} in contrast to Si^{4+} found in pure silica zeolites. Therefore charge compensating cations (i.e. H^+) are required, which leads to the formation of a Brønsted acid site on a neighbouring oxygen atom (Figure 3). The shape and size of the zeolite cavities, plus this Brønsted acidity, has lead to them being called "shape-selective catalysts".

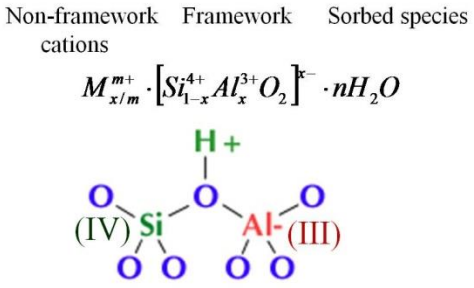

Figure 3. *Zeolite framework with alternating AlO_4 and SiO_4 tetrahedra, where charge deficiency from the Al^{3+} leads to the formation of a Brønsted acid site on a neighbouring Oxygen, also shown is the general composition.*

In addition to their environmentally friendly character, and synthesis from cheap starting materials, zeolites have been found to be stable under vacuum and in air up to high temperatures and therefore have potential industrial usage.

Although their stability is of upmost importance for their use as practical catalysts it is often the case that in order to generate active sites in particular zeolites, a pre-treatment method often needs to be employed which actually results in the partial destruction of the zeolite structure by causing the removal of some of the tetrahedral units. Most often the less thermodynamically stable substituted transition metal ions such as Fe and even Al, are removed from the framework, whereas the bulk $[SiO_4]^{4-}$ tetrahedra remain largely unchanged in comparison. This work will investigate some of the transformations occurring during such pre-treatment methods using advanced in-situ X-ray synchrotron techniques.

1.2.2 Aluminophosphates

Aluminophosphates are microporous solids related to zeolites that are composed of strictly alternating $[AlO_4]^{5-}$ and $[PO_4]^{3-}$ tetrahedral units linked in a similar fashion to zeolites. The strict alternation of Al^{3+} and P^{5+} tetrahedra avoids the formation of Al-O-Al groups and is known as Lowenstein's rule.[10] In aluminosilicate zeolites, this is only an issue in when the Al-Si ratio is 1, forcing strict alternation of Si and Al, otherwise the aluminium is distributed homogenously as to maximise the Al-Al distance. In AlPOs the resulting charge balancing of their composition forms an electrically neutral open-framework (Figure 4), which unlike aluminosilicate zeolites, requires no extra-framework cations. Another characteristic where AlPOs differ from zeolites (which can be made using only inorganic reactants) is that AlPOs *must* be synthesized with an organic amine or quaternary ammonium ion, more frequently the former, which acts as a 'structure directing' agent (template). AlPOs are usually stable upon removal of the organic template and have been found to exhibit thermal stability up to 1000 ^{o}C[11].

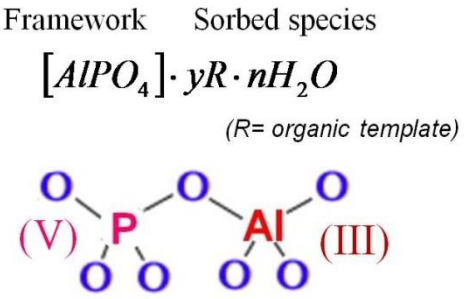

Figure 4. *Aluminophosphate framework with alternating AlO_4 and PO_4 tetrahedra forming a neutral framework, also shown is the general composition.*

The microporous structure of aluminophosphates means they too have shape and size selectivity. FeAlPO-5 has been shown to act as a selective catalyst for the oxidation of benzene to phenol, without any additional high temperature treatment, which is usually required for FeZSM-5 catalysts.

In the early 1990s the incorporation of transition-metal ions and other elements into the AlPO framework was also reported with monovalent (Li), divalent (Be), trivalent (Cr), tetravalent (Ti), and pentavalent (As) elements. The bonding concepts in these materials were studied by Martens,[12] who classified the different types of elements (e.g. monovalent) with a specific substitution mechanism. The monovalent, divalent and trivalent elements (E) were all found to substitute into a hypothetical aluminium site resulting in an E-O-P bond; whereas the tetravalent and pentavalent elements were found to substitute into a hypothetical phosphorus site resulting in an E-O-Al bond. They were also able to confirm that silicon is the only element which can substitute as pairs into adjacent aluminium and phosphorus sites with a "heterogeneous" mechanism, forming what's known as silicon islands; if the substitution of Si^{4+}into the $Al^{3+}$and P^{5+} sites is equivalent then the framework remains neutral. It was also noted that these bonding concepts have remained valid for all stable, calcined structures describable as tetrahedral nets[13] Although transition metal substituted aluminophosphate catalysts have long been studied, little literature exists on Fe-AlPO catalysts used for selective oxidations; however a few recent studies have shown them to be promising catalysts for the oxidation of benzene to phenol reaction using N_2O as an oxidant.[5,14,18]

This incorporation of heteroatom into the AlPO framework can render them negative, for example if a divalent metal ion such as Co^{2+} substitutes for Al^{3+} the framework is rendered anionic, hence a Brønsted acid site is created in which a proton charge balances. These

Brønsted acid sites are only formed after removal of the positively charged organic template which resides in the pores of the AlPO framework. This is achieved by calcination in air. These processes also result in materials that also exhibit Lewis acidity due to anionic vacancies deriving from missing lattice oxygen atoms.

1.2.3 Framework classification

The structures of AlPOs and other molecular sieve materials can be understood on the basis of their construction from fundamental building units. AlPOs and zeolites comprise of TO_4 tetrahedra (framework T atoms refers to Al, P or Si atoms) which are referred to as primary building units (PBUs) as they are the basic structural building units. Each T atom can be described as 4-connected vertices (as each T atom is connected to 4 oxygen atoms), and since each oxygen atom is connected to two T atoms, the structure of AlPOs and zeolites can be described as a (4, 2)- connected net.

Their frameworks can be classified through defining a system of secondary building units (SBUs) which contain up to 16 T-atoms with an assumption that the entire framework is made up of only one type of SBU. These SBUs are always non-chiral, with the oxygen atoms omitted and represented by the presence of a single straight line between two T atoms (represented by a circle). The SBUs for various structure types of nanoporous materials containing tetrahedral PBUs are summarized in Figure *Figure 5.* 5. For example, the AEI framework (i.e. AlPO-18 material) contains four types of SBUs; including 4, 6, 4-2, and 6-6 units, any of which can be used to describe its framework structure.

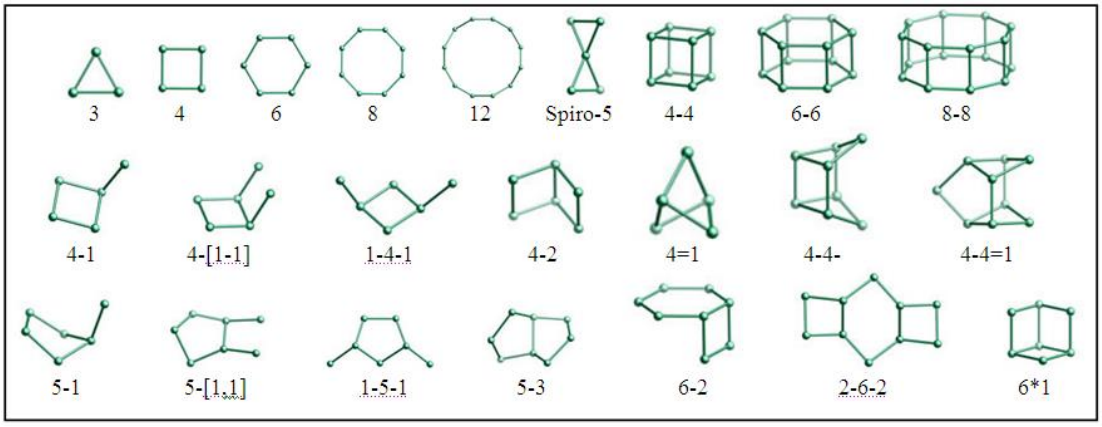

Figure 5. *Secondary building units (SBUs) found in nanoporous materials which contain TO_4 unit*[15]

Some molecular sieve materials contain cage-building units, which can be used to identify relationships between framework types. Cages are generally described in terms of the *n*-rings defining their faces and are different from SBUs since they are not required to be achiral, and cannot necessarily be used to build the entire framework. For example, a truncated octahedron (also known as a β-cage or sodalite cage) has a surface which is defined by six 4-rings and eight 6-rings, is designated a $[4^6 6^8]$ cage and is present in many zeolite frameworks including SOD, FAU, EMT, FAR, FRA, GIU, LTA, LTN, MAR, and TSC, see Figure 6. Other examples of common cages are D4R (designated 4^8) and D6R (designated $4^6 6^2$) which represent double 4-membered rings (4-4) and double 6-membered rings (6-6), respectively. A cage, possessing at least one face which has a ring size large enough for a guest species to enter is referred to as cavity.

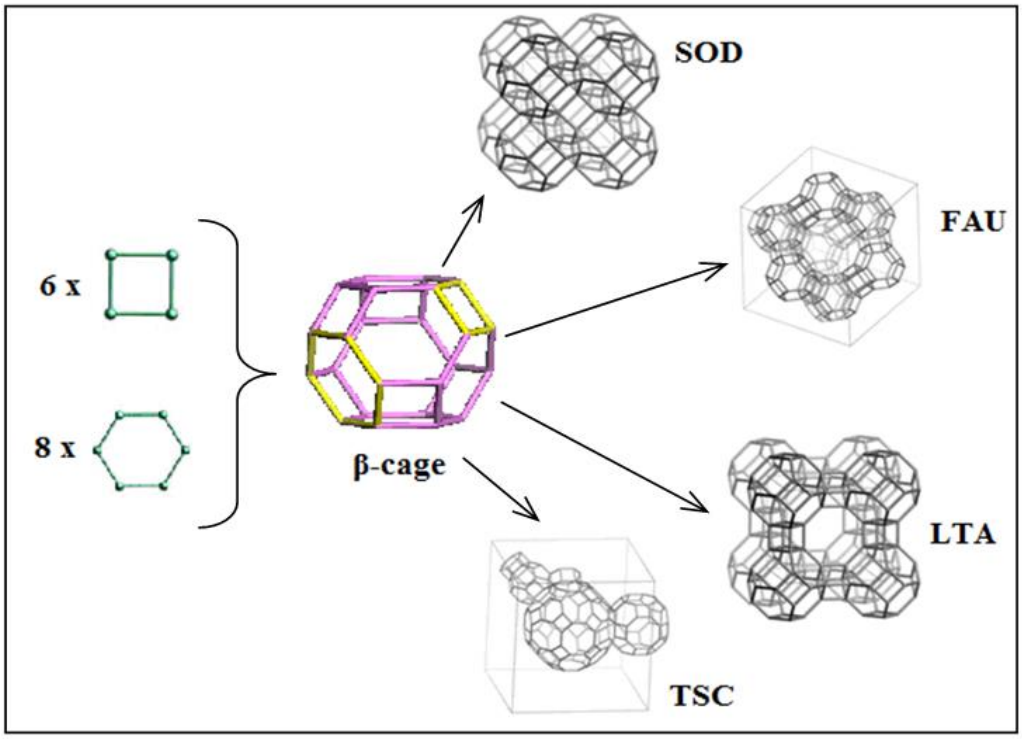

Figure 6. *The β-cage (sodalite cage) which is constructed from six 4-membered rings, and eight 6-membered rings. Examples of zeolite frameworks which contain this cage-building unit are also shown.*[15]

Nanoporous materials can also contain chain-building units, in which there are five different types pictured in Figure 7. In general, the narsarsukite chain is found more often in AlPO structures[4], whereas the double narsarsukite chain is characteristic of high-silica zeolites. Dimensionality is another characteristic which can be used to classify molecular sieve materials. For example, AlPO-18 (AEI) is 3-dimensional, AlPO-12 (ATT) is 2-dimensional and AlPO-5 (AFI) is only 1-dimensional.

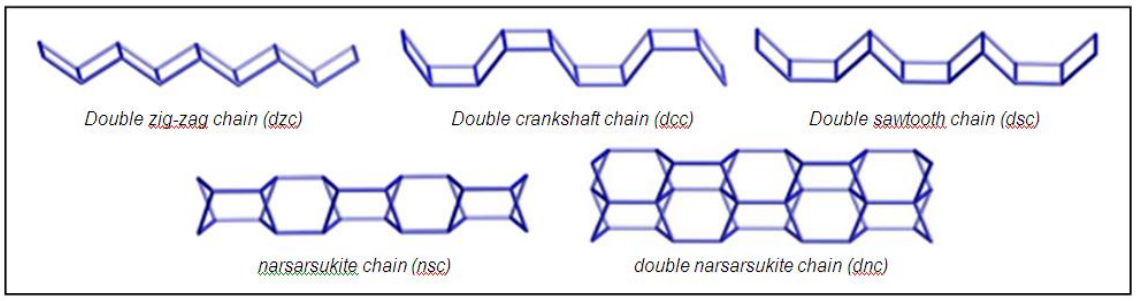

Figure 7. *Chain building units which occur in several molecular sieve materials*[4]

The AlPO-based family of nanoporous materials has over 200 members and in excess of 50 structure types ranging from structures with extra large pores (>12 T-atoms in a ring), such as AlPO-8 (AET), to structures with very small pores (6- T atoms in a ring), such as AlPO-20 (SOD) (Figure 8). As with aluminosilicate zeolites, AlPOs obey Löwenstein's rule[16] in which Al-O-Al bonds are avoided due to Al-Al electrostatic repulsion. As a result of this combined with the instability of P-O-P bonds in these materials, the rings within the structures must be formed by an even number of atoms. This is in contrast with aluminosilicate zeolites where stable Si-O-Si bonds form allowing odd numbered rings to form. However, this is not always the case with AlPOs; the coordination numbers for aluminium can be greater than four due to aluminium coordinating with water groups and/or anionic species adopting five- or six- fold coordination. This behaviour is also possible with substituted metal atoms.

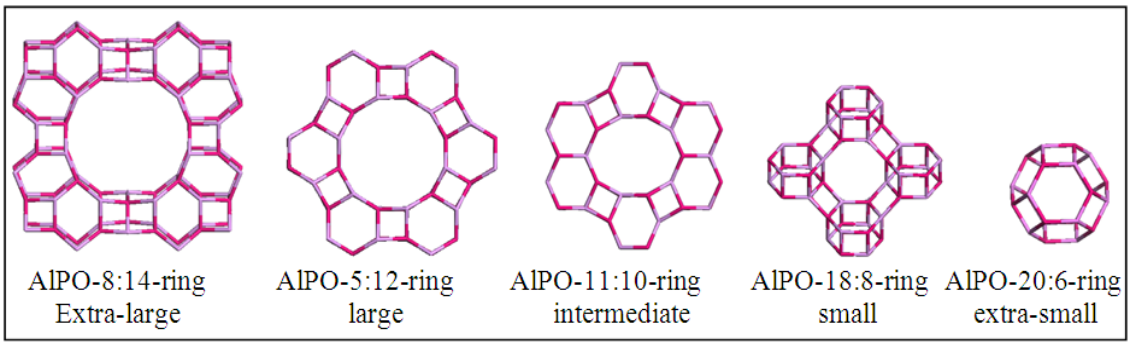

Figure 8. *Several $AlPO_4$-n structures with different ring sizes (pore openings).*[15]

1.2.4 Typical aluminophosphate structures

The nanoporous materials concerned within this thesis are predominantly comprised of the large pore AlPO-5 (AFI) or the small pore SAPO-34 (CHA) frameworks. The AFI framework can be described as a 1-dimensional channel system consisting of a 12-ring pore opening with a diameter of 7.3 Å. The structure contains narsarsukite chains and can be built from the SBUs; 12, 6 or 4. Nanoporous materials with CHA structure are 3-dimensional frameworks with a pore opening of *ca.* 3.8 Å (8-ring). These small pore materials consist of 8, 6 and 4-membered rings, including the CHA cage, and can be built from 6-6, 6, 4-2 or 4 SBUs.

A closely similar structure to the CHA framework is AEI (AlPO-18), this structure is also described as a 3-dimensional network with a similar pore opening (3.8 Å) built from the same SBUs. However, due to a difference in the stacking sequence of the SBUs, the AEI structure does not contain CHA cages and is therefore classified as a unique framework. Another small pore structure described in this thesis is the AEN framework (AlPO-53), this 2-dimensional framework also contains 8, 6 and 4-membered rings with asymmetric pore openings of 4.3 x 3.1 Å and 5.0 x 2.7 Å. Unlike the AEI and CHA structures, the AEN framework can only be built from the SBUs 6 or 4. All of these structures discussed are shown in Figure 9.

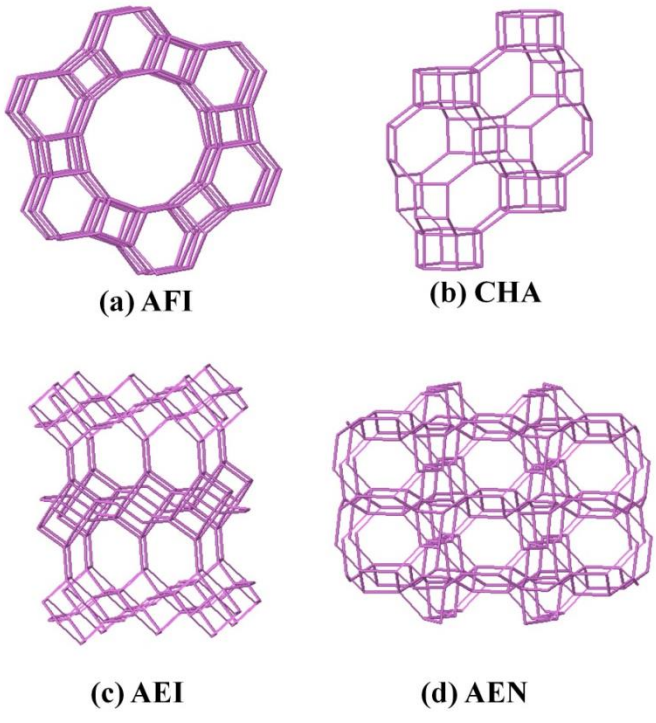

Figure 9. *Examples of various aluminophosphate framework structures.*[15]

1.2.5 Framework substitution: aluminophosphate derivatives

The incorporation of heteroatoms into AlPO materials can be achieved through incipient wetness impregnation, ion exchange or isomorphous substitution. Isomorphous substitution is of particular interest as the heteroatoms, such as transition metal ions, are substituted into framework sites through the direct addition of the metal source to the synthesis mixture.

AlPOs are isoelectronic with SiO_2, therefore, in theory, a neutral AlPO framework can be derived from a neutral pure silica zeolite by replacement of two Si^{4+} cations with one Al^{3+} and one P^{5+} cation. This concept led the researchers at Union Carbide Corporation to synthesise a variety of AlPOs by isomorphic substitution of Al^{3+} and/or P^{5+} with Si^{4+} to form silicoaluminophosphates (SAPO) or with divalent metal cations which are able to adopt tetrahedral coordination (e.g. Co^{2+} Zn^{2+}, Fe^{2+}, Mn^{2+} and Mg^{2+}) to form metalaluminophosphates (MAPOs). or with a combination of both to form metalsilicoaluminophosphates (MSAPOS).

This incorporation of heteroatoms into the AlPO framework can render them negative, for example if a divalent metal ion such as Co^{2+} substitutes for Al^{3+} the framework is rendered

anionic, hence a Brønsted acid site is created in which a proton charge balances, see Figure 10. These Brønsted acid sites are only formed after removal (through calcination) of the positively charged organic template which resides in the pores of the AlPO framework. These materials also exhibit Lewis acidity (anionic vacancies deriving from missing lattice oxygen atoms).

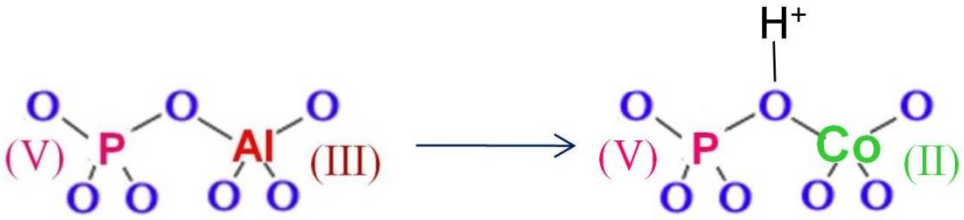

Figure 10. *AlPO and MeAlPO frameworks; the cobalt substituted MeAlPO framework has a Brønsted acid site due to charge compensation.*

Metal substituted aluminophosphates have a wide range of applications in different acid catalysed reactions. The introduction of metal ions into the framework of AlPOs is a significant advancement of their use in industrial processes; however the incorporation of heteroatoms lowers the thermal and hydrothermal stability of the crystal compared to the pure AlPO analogues.[17]

The discovery of open-framework metal substituted AlPOs and SAPOs has brought about a number of conceptual breakthroughs in the area of nanoporous materials. The compositional and structural diversity of these materials and their derivatives has also improved the current application areas of nanoporous materials in many fields.

1.2.6 Heterogeneous Catalysis

Catalysis has always been at the backbone of the chemical and materials industry. It provides a means of enhancing the rates at which chemical reactions occur, and controlling the yield and selectivity of chemical processes in order to increase the amounts of desirable products and reduce the amounts of undesirable ones. The application of zeolites in catalysis has been widely employed and research of new systems continues with much interest in creating

important new catalysts for the petrochemical and fine chemicals industry. Due to their unique porous properties and capacity for functionalisation, ion-exchange, selectivity and tunability, zeolites are ideal candidates for the development of selective catalyst materials.[17]

A catalyst is a material or substance that when introduced into a chemical system, increases the rate of a particular reaction without itself being consumed by the end of the process. Enzymes are an example of naturally occurring catalysts responsible for many essential biochemical reactions. Generally speaking, a reaction between the catalyst and a reactant occurs, forming an intermediate that is then able to react more readily with another reactant in order to form the desired end product. A key point is that during the reaction between the chemical intermediates and the reactants, the catalyst is regenerated. Catalysis by solid materials has been observed quantitatively at temperatures as low as 78 K and as high as 1500 K, at pressures between 10^{-9} and 10^{3} bar. Its yields can be as low as $10^{-5}s^{-1}$ (one turnover per day) and as high as $10^{9}s^{-1}$.

Environmental catalysis is required for cleaner air, soil and water. Catalysts are applied in environmental technologies to convert environmentally hazardous materials into harmless compounds, suitable for rerelease into the environment. Examples are the selective catalytic reduction (SCR) of NO_x, removal of volatile organic compounds (VOC), the decomposition N_2O, and oxidation of CO and hydrocarbons from exhaust gas emissions. A variety of catalysts, such as noble metals, rare earth oxides, transition metal compounds and clusters, and zeolites and aluminophosphates, can be employed for these types of reactions and much more. It is not an understatement that catalysis is an fundamental principal component of essentially all current industrial chemical manufacturing and emissions control processes.

1.3 Catalytic Oxidation of Hydrocarbons

1.3.1 The Importance of Selective Oxidation

A great number of organic reactions that employ molecular sieves involve a selective oxidation step. Although a basic redox process is generally defined as one that involves an element achieving a net gain (reduction), or loss (oxidation) of electrons. In general, redox reactions involve the transfer of electrons between species.

Selectively oxidized hydrocarbons are some of the most important building blocks for plastics and synthetic fibres. They also play an equally dominant role as intermediates for the manufacture of standard and fine chemicals for a variety of applications. Oxidised hydrocarbon products are prepared from natural gas and volatile fractions of petroleum by partial oxidation. This often involves gas or liquid phase reactions using homogeneous or solid surface catalysts. The current existing oxidation processes for converting benzene into phenol all have their various advantages and disadvantages, and the challenge of developing a one-step hydroxylation process for a molecule as stable as benzene cannot be underestimated.

1.3.2 A Historical Overview of Phenol Production

Phenol also known as carbolic acid, is the common name for hydroxy benzene, an aromatic organic compound with the molecular formula C_6H_5OH. Molecularly it can be described as consisting of a hydroxyl group attached onto a phenyl group ($–C_6H_5$). It was discovered in 1834 by Friedlieb Ferdinand Runge, who extracted it in impure form, from coal tar.[18] It was later isolated in its pure form by the French chemist Auguste Laurent in 1841[19]. The structure is shown below (Figure 11).

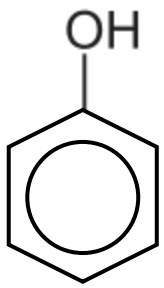

Figure 11. *The molecular structure of phenol.*

Most phenol is primarily produced from benzene (C_6H_6), which is the archetypical example of a molecule exhibiting enhanced stability resulting from aromaticity. The great scientist Michael Faraday, was the first who isolated and identified benzene in 1825 from the oily residue derived from the production of illuminating gas, and giving it the original name *bicarburet of hydrogen*[20]. Following on from these early developments, along with evolution of the discipline that would become organic chemistry, the empirical formula for benzene was established. However, its highly polyunsaturated structure, with just one hydrogen atom for each carbon atom, was challenging to determine and rationalise. Around 1865, the German chemist Friedrich August Kekulé published a paper suggesting that the structure contained a ring of six carbon atoms with alternating single and double bonds[21,22]. Kekulé's symmetrical ring could explain the chemistry of the derivatives of benzene, as well as benzene's 1:1 carbon-hydrogen ratio. Interestingly it was not actually until 1929 that the cyclic structure of the benzene molecule was confirmed unambiguously by Kathleen Lonsdale[23].

In terms of the electronic configuration of the molecule, this model of bonding describes a conjugated system often represented as a series of alternating single and double bonds in the carbon ring. This configuration formally allows for the electrons in the molecule to be delocalized around the ring and increasing the molecule's stability[24]. The molecule cannot be represented by one structure, but rather a resonance hybrid of different structures, such as with the two resonance structures of benzene (Figure 12.b). According to the molecular orbital theory for the bonding modes of a benzene, the particular planar arrangement of carbon and hydrogen atoms and the corresponding combination of each carbons sp^2 hybrid orbitals result in the formation of three delocalized orbitals spanning all six carbon atoms above and below the benzene ring. It is the side-on overlap of carbon *p*-orbitals that produces the delocalised π-orbitals, above and below the plane of the ring (Figure 12.c). This effect often called aromaticity, results in the striking stability of the benzene molecule and the difficulty in activating it for reactions. Over the last century or so a number of processes have been developed to produce phenol, each one with their own benefits and drawbacks.

a)

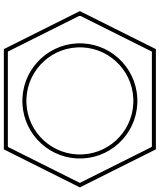

b)

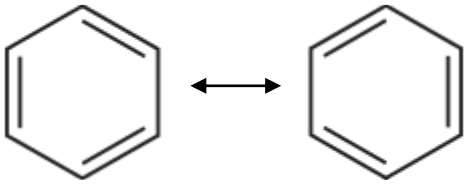

c)

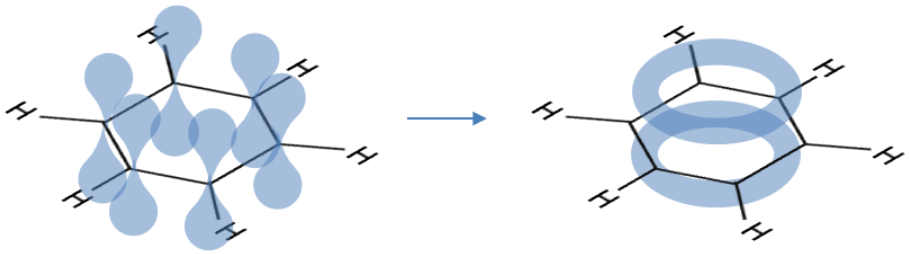

Figure 12. *(a) Benzene as commonly represented with the delocalised bonding. (b) Showing the two resonance forms. (c) Diagram showing molecular orbital arrangement in benzene. The sp^2 hybridised carbon atoms at the hexagons vertices are each bonded to a hydrogen atom and to 2 carbon neighbors by σ-bonds (not shown) and project un-bonded p-orbitals perpendicular to the plane of the ring (left). The extensive overlap of the p-orbitals forms a system whereby the electrons of those orbitals are shared around all 6 carbon atoms in the ring, forming delocalised π-orbitals above and below the ring. The resulting stability makes the molecule extremely stable.*

1.3.2.1 Sulphonation Process

Synthetic phenol was first produced in 1899 by BASF via the sulphonation of benzene, followed by the subsequent hydrolysis of the resulting benzene sulphonic acid with alkali.[25]

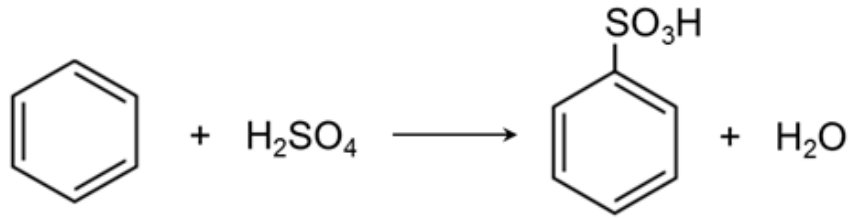

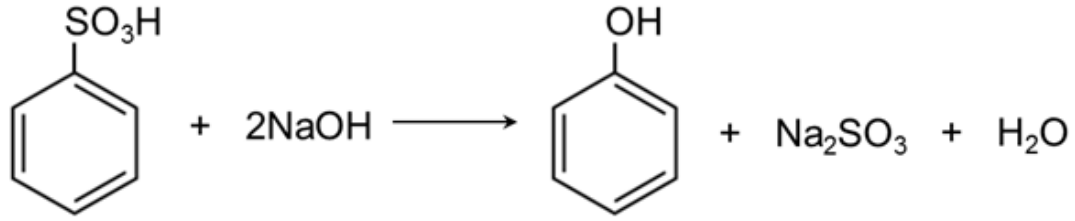

Despite the use of large volumes of such potentially dangerous reagents as sulphuric acid, this method was used to make more than 99% of synthetic phenol worldwide throughout the 1890s.

1.3.2.2 Chlorination Process

A novel chlorination process was developed in 1924. In this process benzene is converted to chlorobenzene, which is then reacted in the presence of sodium hydroxide to form phenol. This process is no longer used because of the safety risks of using chlorine gas, and adverse economics of chlorine and alkali production.[26]

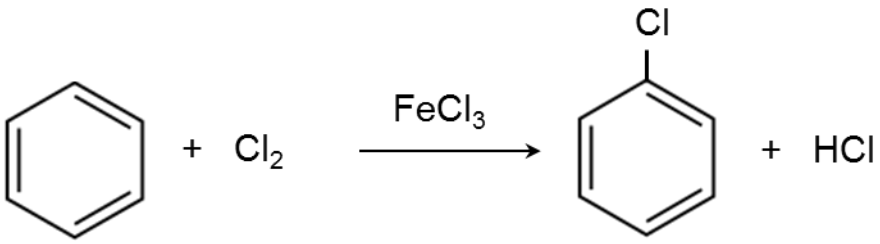

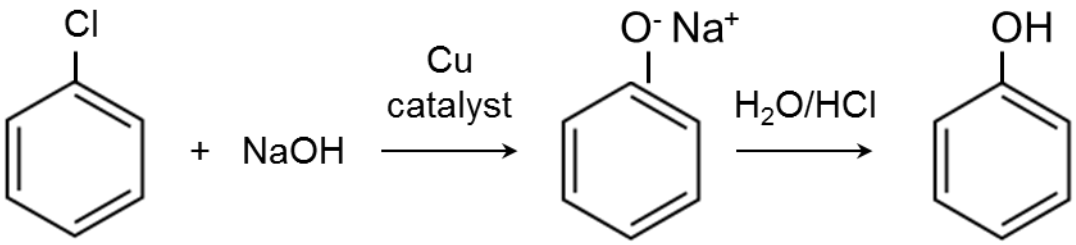

1.3.2.3 Cumene Process

The cumene process converts two relatively cheap starting materials, benzene and propylene, into more valuable phenol and acetone using molecular oxygen and a catalytic Lewis acid. The methodology was first developed independently by R. Udris[27] and P. Sergeyev in the former Soviet Union in 1942 and H. Hock[28] in 1944. It is by far the most important method of phenol production in the world, now accounting for 95% of all synthetic phenol. It is also an important source of acetone, a useful and valuable side product. The process is named after the intermediate cumene, the common name for isopropyl benzene.

The first step of the process is a gas-phase Friedel–Crafts alkylation of benzene with propene using a Lewis acid catalyst such as aluminium trichloride or most often, phosphoric acid to produce cumene. The cumene is then oxidised in air at 80-120°C, forming the cumene radical via abstraction of the tertiary benzylic hydrogen. This radical species initiator can then abstract hydrogen from more cumene forming benzyl hydroperoxide and another cumene radical, which can go on and propagate the chain reaction forming more hydroperoxide. The hydroperoxide is then hydrolysed in acid via a Hock rearrangement to give phenol and acetone. The overall reaction for the process is outlined below.

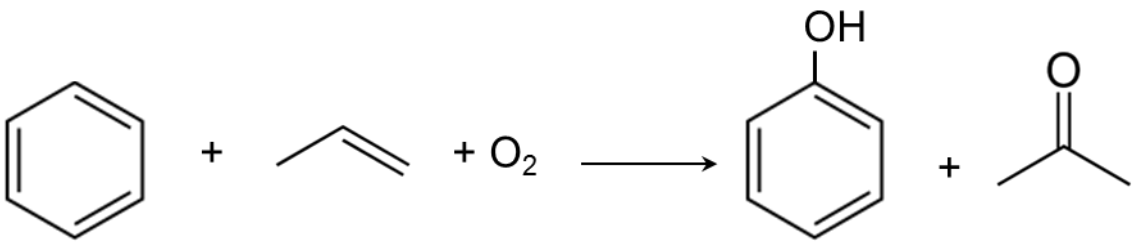

Most of the worldwide production of phenol and acetone is now based on this method. In 2003, nearly 7 million tonnes of phenol was produced by the cumene process[29]. In order for this process to be economical, there must also be demand for the acetone by-product as well as the phenol.

1.3.3 Direct One-step Hydroxylation

Despite its popularity, the cumene process has significant disadvantages, including the fact that market growth for phenol and acetone is quite different and a method that decouples their productions would be more preferable. Aggressive reagents such as phosphoric acid or aluminium trichloride, as well as contaminated waste water produced by the method further highlights the many advantages that a new economical and environmentally friendly method could deliver. A simple one-step process for direct hydroxylation would have clear cost, energy, and environmental advantage compared to the current industrial processes. Due to the aromatic nature of benzene, the production of a reactive or radical oxygen species is necessary to achieve direct hydroxylation.[13] The source of this reactive oxygen would most likely come from the catalytic activation of molecular oxygen (O_2), nitrous oxide (N_2O), nitrogen dioxide (NO_2) or hydrogen peroxide (H_2O_2). Each of these oxidants has its own specific advantages and disadvantages in terms of chemistry, economy and environmental effect.

1.4 New heterogeneous catalysts for the production of Phenol

The iron substituted silicate forms of the aluminosilicate ZSM-5 (FeZSM-5) and iron substituted aluminophosphate (FeAlPO-5) have shown great potential in the selective oxidations of benzene.[14,9,30,31,33] Benzene is thermally stable and rather difficult to activate due to its aromatic bonding configuration. The selective oxidation and functionalization of the compound into valuable feedstock compounds for the pharmaceutical, petrochemical and fine chemical industry have long represented challenges, as outlined in the harsh reagents required in historical processes. The search for more sustainable and ecologically sound

methods for the industrial production of such common chemical precursors is also a matter of great interest.

The recent advent of the FeZSM-5 catalyst seems to be one of the most promising candidates for such processes that may overcome several issues outlined above.[32] FeZSM-5 shows remarkable redox properties and catalytic activities under mild conditions. Specifically, it can convert benzene to phenol in a single step, with high yield and selectivity (not less than 90%).[33] Furthermore N_2O, a common industrial waste product and greenhouse gas is used as the oxidant for the direct benzene hydroxylation reaction over Fe-ZSM-5 zeolite, turning a problematic effluent into a valuable feedstock. The use of such heterogeneous catalysts also aids in moving away from often toxic and corrosive liquid catalysts, which are also often very difficult to remove from the reaction mixture.

1.5 The nature of FeZSM-5

The first ZSM-5 catalyst was synthesized by Argauer and Landolt in 1969. The aluminosilicate ZSM-5 is a zeolite of the pentasil family, with framework type MFI. It is a medium pore zeolite with channels defined by ten-membered rings , with the estimated pore size of the main channels being 5.4–5.6 Å. Its formal chemical formula is reported as $Na_nAl_nSi_{96}–nO_{192}•16H_2O$ $(0<n<27)$.[3] The crystallographic unit cell of ZSM-5 has 96 T sites (Si or Al), 192 O sites, and a number of compensating cations depending on the Si/Al ratio, which ranges from 12 to infinity. This thesis is concerned primarily with the iron substituted form of the zeolite, where Fe has been incorporated into the framework structure via isomorphous substitution.

The catalytic activity of zeolites is often modified or enhanced by substituting some of the T atoms in the synthesis with a redox active metal atom such as Fe.[34] Iron may also be supported on ZSM-5 by other post-synthesis methods such as aqueous impregnation[35] or CVD[36]. FeZSM-5 has been employed to catalyse a number of reactions, including the isomerization of alkanes, selective catalytic reduction of nitric oxide by ammonia,[37] the conversion of syngas to light olefins,[38] methane to aromatic hydrocarbons,[39] and the selective oxidation of methane to methanol[40]. By far the most extensively studied reaction involving FeZSM-5 in the last few decades is the one-step hydroxylation of benzene to phenol using

N_2O as oxidant[32,33]. The reasons behind the versatile catalytic properties as well as the nature of active sites in FeZSM-5, which are not typical for oxidation reactions (for example deactivation by O_2, enhancement in the presence of NO) have been widely debated[14,15,33.] It is these unique properties that have indicated the importance of identifying the iron species present in the cavities of FeZSM-5.

As mentioned, the introduction of iron into extra-framework position of zeolites can be achieved by impregnation, ion exchange, including solid state ion exchange or sublimation of a suitable iron precursor. By contrast, the isomorphous substitution of iron during the hydrothermal synthesis of FeZSM-5 introduces Fe into the structure at framework T atom positions. Once removed from the autoclave and calcined, these materials often need further activation in order to remove part of Fe from framework T atom positions to new extra-framework positions. These extra-framework Fe species can be nanometric bulk oxides or smaller Fe oxide clusters, dimers or single ions.

Isomorphous substitution seems to generate more active catalysts in the case of FeZSM-5 than any of the other methods – particularly after activation by autoreduction or steaming.[2] This leads to the initial assumption that highly dispersed forms of Fe predominate, but that further reduction of the initial Fe^{3+} to Fe^{2+} and possibly the formation of dimers and clusters leads to enhancements in the catalytic activity in the best candidates.

The iron ions in FeZSM-5 can generally occupy four different environments in the zeolytic aluminosilicate matrix:

(i) isolated ions substituting framework T positions
(ii) isolated ions grafted onto the framework
(iii) as cationic or neutral iron oxo-complexes in the microporous voids
(iv) as clusters or finely dispersed iron oxide nanoparticles on the external surface of the zeolite crystals.

Many attempts have been made to elucidate the active site structures and mechanistic details about the OBP reaction, but despite progress, no definite conclusions have been drawn yet.

In FeZSM-5 it has been supposed that dehydroxylation of two isolated $Fe(OH)^+$ in close enough proximity can result in $[Fe\text{-}O\text{-}Fe]^{2+}$ and that this complex is a possible oxygen carrier. The amount of Fe in the material as well as the presence of Al seems to have a large effect on the dispersion of Fe. This particular formation of $[Fe\text{-}O\text{-}Fe]^{2+}$ clusters has been well established for Fe/Y for a Si/Al ratio of 2.5 allowing a close proximity of the negatively charged Al occupying tetrahedra.

Panov *et al.* assumed that an iron complex stabilized in ZSM-5 zeolites produces a new form of surface oxygen (denoted as α-oxygen) upon the decomposition of N_2O[31,32]. The α-sites are often proposed to be a binuclear iron complex stabilized in the zeolite micropore system. The complexes are formed presumably by Fe atoms leaving the framework during thermal treatment of the FeZSM-5.

1.6 Synthesis of Microporous Solids

The hydrothermal synthesis of zeolites has been most extensively carried out using the methodology set out by Barrer *et al.*[41] The basic method involves the hydrothermal crystallisation of a reactive gel of appropriate composition at temperatures between 100-200°C. The final structure of the crystallisation product is very sensitive to the reaction conditions and a number of factors must be considered very carefully, including the gel composition (silica, alumina, cations, metals, organic templates), pH, temperature and crystallisation time.[42]

The starting gel can be prepared from either a silica or phosphorus source (for zeolites or aluminophosphates respectively), a source of alumina, water, organic template cations, and often other cations or a source of fluoride. The exact composition of the reaction gel is vital for the successful crystallisation of the desired product. Once the gel has been made and stirred until homogenous it is placed in a stainless steel autoclave and subjected to high pressures and temperatures for a set time, and then washed and filtered giving the desired product in powder form.

1.7 The Oxidation of Benzene to Phenol using Fe-based Microporous Materials

The active site complexes for the oxidation of benzene to phenol are presumably formed by Fe atoms leaving the framework during thermal treatment of the FeZSM-5. There is no commonly accepted mechanism for the reaction, but based on all the literature outlined in this thesis a simplified summary of the elementary steps may be given. In the reaction mechanism the deposition of oxygen from nitrous oxide to form the active α-[O] species is the first step.

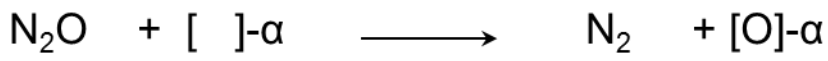

The α-sites are inert to oxidation by molecular oxygen and their peculiarity is the ability to decompose nitrous oxide at relatively low temperature and produce a new reactive form of surface oxygen. It is this oxygen species that is thought to go on to oxidise the benzene

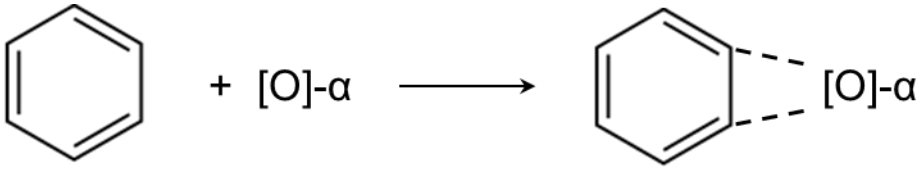

The formation of phenol then proceeds by abstraction of hydrogen from –OH on the zeolite lattice, and the desorption of the product molecule from the active site, regenerating it.

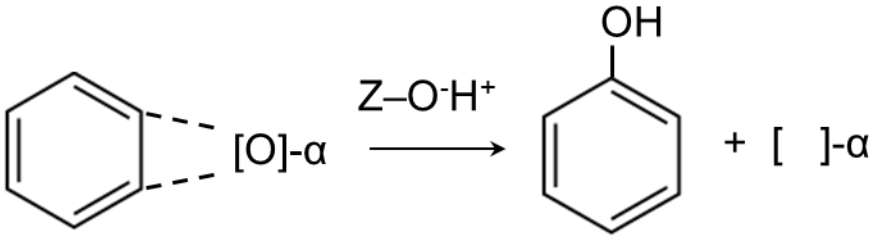

The α-sites are inert to oxidation by molecular oxygen and their peculiarity is the ability to decompose nitrous oxide at relatively low temperature and produce a new reactive form of surface oxygen. The state of Fe in these α-sites is of considerable interest and it is reported to be Fe^{2+} although it is Fe^{3+} that present in the as synthesised material. The high temperature autoreduction and steam treatments for the activation of FeZSM-5are believed to bring about

the presence of coordinatively unsaturated Fe^{2+} active sites that can form the basis for an active site that can then decompose N_2O.

1.8 Activation Procedures and the Active Site

In FeZSM-5 prepared using hydrothermal methods where the iron has been introduced during synthesis, iron can be found as a variety of species, including monomeric FeO_x species, framework incorporated FeO_4 tetrahedra, Fe^{2+} grafted onto the framework, Fe_xO_y type clusters and nanoparticles, and large Fe_2O_3 particles (Figure 13).

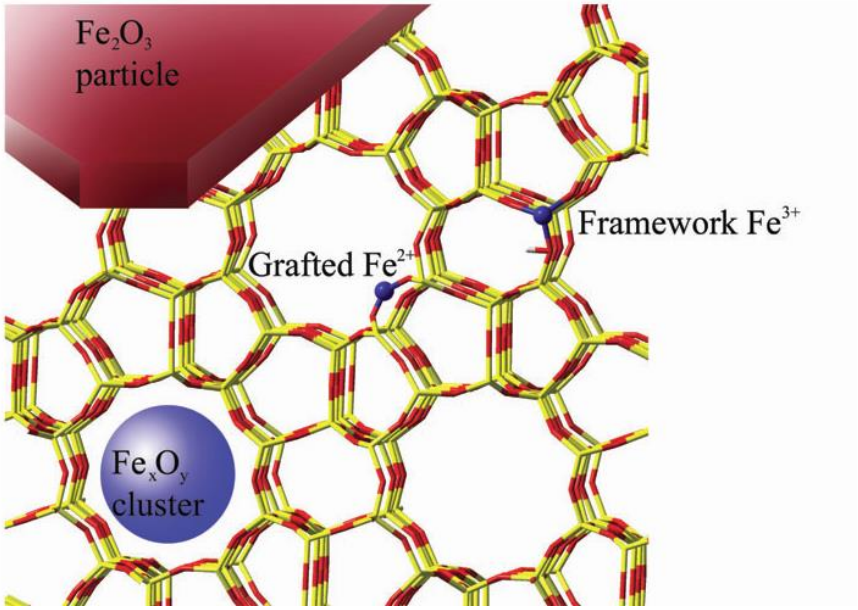

Figure 13. *– The microporous structure of Fe-ZSM-5 and the distribution of possible Fe species*[43]

As previously mentioned it was observed that pre-treatment of FeZSM-5 either by high temperature treatment in inert gas[44] or steaming at lower temperatures[45] increases the activity of the catalyst. This is thought to be due to the formation of highly dispersed extra-framework iron species trapped in the zeolite pores, which are considered likely candidates for the α-sites. In FeZSM-5 samples where iron is incorporated during synthesis, the iron mainly occupies a T-atom position (tetrahedral building unit/ Si site) in the zeolite framework. Upon calcination (usually performed to remove the organic template used during

synthesis) and especially during harsher pre-treatments, some of the iron atoms can become dislodged as O-Fe bonds begin to be broken. Here the Fe coordination changes from regular tetrahedron, to an irregular geometry with higher coordination number.

Two main processes can occur during the pre-treatment:

1. Extraction of Fe from a framework position to an extra framework position
2. The autoreduction of Fe^{3+} to Fe^{2+}

It is thought that these two processes lead to the formation of the active α-sites. Fe-ZSM-5 samples with low concentrations of iron lead to better dispersed Fe cations and better catalysis. Catalysts with high iron contents tent to form large iron oxide clusters, upon pre-treatment, which are inert to the OBP reaction[10]. Panov and his group have proposed that α-sites are binuclear iron clusters, as evidenced by Mossbauer spectroscopy results[46] , which is an attractive hypothesis due to the similarity with the binuclear active site of the enzyme MMO which is also a selectively oxidising catalyst[10]. However the interpretation of these spectra has been questioned by other groups[47]. A number of oxygen bridged bimetallic species of the type Fe-O-Fe and Fe-O-Al as well as peroxide species (Fe-O-O-Fe) with various oxidation states have also been proposed as possible active sites[48]. The fact that samples with higher aluminium content seem to be more active, has led to the proposal that a special arrangement of the extra framework iron cations in the close vicinity of aluminium is required for the creation of active sites[49]. Even the most purely silicaceous samples would often still have small aluminium impurities unless special precautions were taken. It is likely that mononuclear, binuclear and oligonuclear Fe can all be present at different concentrations in active catalyst samples, depending on synthesis procedure, composition and activation history and all types may be active sites for the reaction, albeit at different rates.[50]

Ultimately, despite the abundance of research on the topic, the exact identity of the active α-site in FeZSM-5 and the mechanism by which the benzene is activated and oxidised is still unclear. However, very interesting results have been collected that can help us understand the factors that govern the activity of samples, which can then lead to revelations about what types of active sites are plausible. In summary, there are a number of important points that differentiate the active sites from other catalysts and can be used to help understand the possible identity of these sites:

- Though both are active for the reaction FeZSM-5 is always more active than Fe-silicalite containing the same amount of Fe.

- The active sites are formed during activation in inert atmosphere. There is a widespread agreement that after this treatment a large fraction of iron is in the divalent state.

- Activity augments with increasing activation temperature in inert gas; the same happens with the number of active sites.[33]

- The catalyst activity (calculated per Fe centre) increases with dilution[51]. From this, it can be safely concluded that the active sites contain a very small number of Fe atoms or, more likely, a single atom. From this it is also inferred that the concentration of clustered species becomes relevant at the highest Fe contents and that their catalytic activity in N_2O decomposition is lower than that of isolated species. The debate concerning the nuclearity of the catalytic sites (mono- or dinuclear) is still alive. The number of α-sites grows with the concentration, this growth being smaller than that of clustered species.[52]

- An interesting point is the positive effect of NO, which is enhances the decomposition rate of N_2O.[53]

Further studies, especially those harnessing synchrotron radiation for X-ray diffraction and X-ray absorption spectroscopy, will help to characterise the active sites, particularly when performed as time-resolved *in situ*, studies, observing changes in the catalyst material during the reaction.

In 2002 the gas-phase selective oxidation of benzene to phenol with N_2O, catalysed by $FePO_4$, both alone and bonded to various oxide support materials such as silica, alumina, zirconia, and titania was studied by Ren *et al*[54]. Only the quartz-phase crystalline $FePO_4$ and silica-supported $FePO_4$ seemed to exhibit substantial catalytic activity for the reaction under the conditions investigated. The maximum selectivity they managed to achieve was quite

high at ~85% (less than Fe-ZSM-5) but the actual conversion efficiency was relatively low (<7%). The quartz phase of $FePO_4$ is well known to contain Fe^{3+} in a stable tetrahedral coordination.

Around the same time Sankar *et al.* at UCL established that the iron-substituted aluminophosphate FeAlPO-5 also contains Fe^{3+} in the as synthesised state, although in an octahedral coordination,[55] unlike the tetrahedral Fe^{3+} found in $FePO_4$. The group carried out *in-situ*, time resolved combined EXAFS/XRD measurements, allowing them to observe the changes occurring during the calcination of the iron-substituted aluminophosphates FeAlPO-5 (medium pore size - 7.3 Å) and FeAlPO-18 (small pore size - 3.8 Å). They showed that in the case of FeAlPO-5 the octahedral Fe^{3+} centres desorb two water molecules at around 120^{o}C, to yield tetrahedrally coordinated Fe^{3+} in the catalyst – a species much more alike to the iron found in quartz-phase $FePO_4$. In the case of FeAlPO-18 the iron exists in its uncalcined as-synthesised state as a mixture of tetrahedral Fe^{2+} ions and octahedral Fe^{3+}. Both of species of iron also fully convert to purely tetrahedrally coordinated Fe^{3+} after prolonged high temperature treatment in air. Bringing together their own results and those from Fe-ZSM-5 studies, and the Ren group[54], Sankar *et al.*[56] then went on to examine FeAlPO-5 as a catalyst for the selective oxidation of benzene to phenol using nitrous oxide as an oxidant since Fe(III) ions were present in both the aluminophosphates and the quartz phase $FePO_4$ catalyst, and its nanoporous structure could confer other beneficial catalytic properties and a higher surface area.

Iron containing AlPO-5 materials were prepared using a well-established hydrothermal synthesis procedure, with 0.1, 1.0 and 4.0 wt% Fe, using tetraethylammonium hydroxide as an organic structure directing template. They were then tested for catalytic activity at atmospheric pressure, over a range of temperatures. The gas phase was composed of benzene, N_2O and He as diluent. All of the catalysts studied showed some activity with a selectivity for phenol, up to over 95%, but the catalyst with 1% Fe loading was the most active, reaching a maximum of 13.4% conversion of benzene at a temperature of about 653 K (Figure 14).[4]

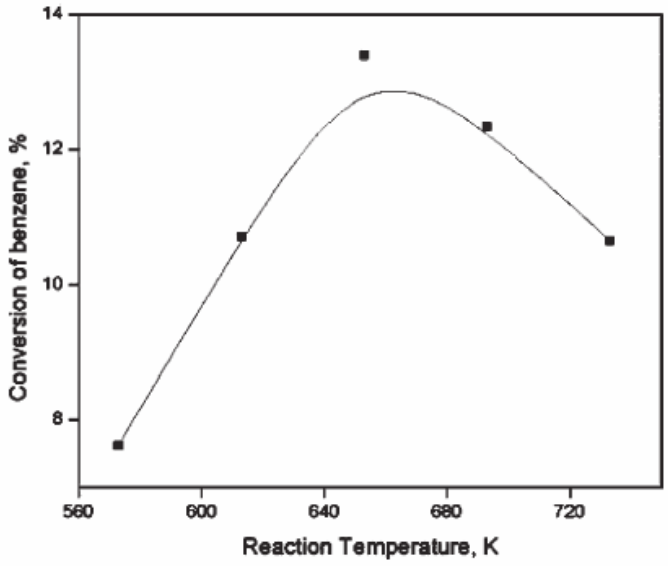

Figure 14. *Catalytic activity of 1 wt% FeAlPO-5 as a function of temperature for the oxidation of benzene to phenol.*

Despite all these efforts still the nature of iron containing microporous material is debated. Therefore, this work will focus on the study of the structure of iron-substituted catalysts used specifically for the selective oxidation of benzene to phenol, under in situ conditions. In addition to FeZSM-5, iron substituted aluminophosphates, in particular,FeAlPO-5 (as it is large pore and can be produced relatively easily) microporous materials will also be studied in detail to evaluate the structural details of the overall structure and also the local structure around iron during the activation and catalytic process. To do so, we have used the appropriate X-ray techniques, in particular X-ray diffraction and X-ray absorption at the Fe K-edge. In addition to the above two materials, the work also explored the presence of another active metal, ruthenium, supported on the iron containing microporous materials to investigate the influence of Ru on the catalytic properties.

References

1 R.M. Barrer, *Hydrothermal Chemistry of Zeolites*. 1982: Academic Press.

2 R. Szostack, *Molecular Sieves: principles of synthesis and identification*. 2 ed. 1998, London: Blackie Academic & Professional.

3 F. Delprato, L. Delmotte, J. L. Guth, L. Huve, *Zeolites*, 10(6) 546-552 (1990)

4 C. H. Baerlocher and L.B. McCusker, Database of Zeolite Structures: http://www.iza-structure.org/databases

5 H. Yahiro, M. Iwamoto, *Appl. Catal. A-Gen.*, 222, 163-181 (2001)

6 I. Melia´n-Cabrera, F. Kapteijn, J.A. Moulijn, *Catalysis Today* 110, 255–263 (2005)

7 L. Zhou, J. Xu, C. Chen, F. Wang and X. Li, *Journal of Porous Materials*, 15, 7-12, (2006)

8 C. R. A. Catlow, S. A. French, A. A. Sokol, J. M. Thomas, *Catalytic ChemBiochem.* A363, 913 (2005).

9 A. Zecchina, M. Rivallan, G Berlier, C Lamberti, G Ricchiardi, *Physical Chemistry Chemical Physics*, 9, 3483–3499, (2007)

10 D.C Konningsberger, B. L. Mojet, G. E. V. Dorssen, D. E. Ramker, *Topics in Catalysis*, 10, 143-155 (2000)

11 Yu, J. H.; Xu, R. R., *Chemical Society Reviews*, (2006) 35, 593.

12 Martens, J. A.; Jacobs, P. A., *Advanced Zeolite Science and Applications*, Elsevier Science Publ B V: Amsterdam, (1994); Vol. 85, pp 653.

13 Yu, Jihong, R Xu. *"Insight into the construction of open-framework aluminophosphates." Chemical Society Reviews*, 35.7 (2006): 593-604.

14 G. Sankar, R. Raja and J.M. Thomas, *Catalysis Letters*, 1998, 55, 15

15 Baerlocher, C.; McCusker, L. B., *Database of Zeolite Structures.* http://www.iza-structure.org/databases/

16 Lowenstein, W., *American Mineralogist*, (1954) 39, 92.

17 J. Cejka, A. Vinu, *Catalysis by Mesoporous Materials, "Ordered Porous Solids: Recent Advances and Prospects"* Editors: Valtchev, Mintova and Tsapatsis, Elsevier, Netherlands (2009)

18 F. F. Runge (1834*) "Ueber einige Produkte der Steinkohlendestillation" (On some products of coal distillation), Annalen der Physik und Chemie,* 31 : 65-78, 308-328.

19 Auguste Laurent (1841) *"Mémoire sur le phényle et ses dérivés" (Memoir on benzene and its derivatives),* Annales de Chimie et de Physique, series 3, 3 : 195-228.

20 Faraday, M. (1825). *"On new compounds of carbon and hydrogen, and on certain other products obtained during the decomposition of oil by heat".* Philosophical Transactions of the Royal Society 115: 440–466.

21 Kekulé, F. A. (1865). *"Sur la constitution des substances aromatiques"*. Bulletin de la Societe Chimique de Paris 3: 98–110.

22 Kekulé, F. A. (1866). "*Untersuchungen über aromatische Verbindungen Ueber die Constitution der aromatischen Verbindungen. I. Ueber die Constitution der aromatischen Verbindungen"*. Liebigs Ann. Chem. 137: 129–196.

23 Lonsdale, K. (1929). *"The Structure of the Benzene Ring in Hexamethylbenzene"*. Proceedings of the Royal Society 123A: 494. ++,B39= Lonsdale, K. (1931). "An X-Ray Analysis of the Structure of Hexachlorobenzene, Using the Fourier Method". Proceedings of the Royal Society 133A (822): 536–553.

24 Rocke, A. J. (2015*). "It Began with a Daydream: The 150th Anniversary of the Kekulé Benzene Structure"*. Angew. Chem. Int. Ed. 54: 46–50.

25 http://www.greener-industry.org.uk/pages/phenol/4PhenolProdMethSum.htm accessed 01/05/15

26 Boyd, Robert W.; Morrison, Robert (1992). *Organic chemistry*. Englewood Cliffs, N.J: Prentice Hall.

27 http://izgudrojumi.lza.lv/izg_en.php?id=54 accessed 13/02/15

28 Hock, H. and Lang, S. (1944), *Autoxydation von Kohlenwasserstoffen, IX*. Mitteil.: Über Peroxyde von Benzol-Derivaten. Berichte der deutschen chemischen Gesellschaft (A and B Series), 77: 257–264

29 Manfred Weber, Markus Weber, Michael Kleine-Boymann *"Phenol"* in *Ullmann's Encyclopedia of Industrial Chemistry* (2004), Wiley-VCH

30 F. M. F de Groot, W. M. Heijboer, D.C. Konningsberger, B.M. Weckhuysen, Catalysis Today, 110, 228-238 (2005)

31 N. R. Shiju, S. Fiddy, O. Sonntag, M. Stockenhuber, G. Sankar, *Chemical Communications*, 4955-4957 (2006)

32 G. I. Panov, A. S. Kharitonov, V. I. Sobolev, *Applied Catalysis A - General, (*1993) 98, 1-20.

33 V. Valtchev, S. Mintova, M. Tsapatsis, *Ordered Porous Solids – recent advances and prospects*, 2009: Elsevier

34 Chu, Cynthia TW, and Clarence D. Chang. *The Journal of Physical Chemistry*, 89.9 (1985): 1569-1571.

35 Phu, Nguyen Huu, *Applied Catalysis B: Environmental*, 34.4 (2001): 267-275.

36 M. Pasqualino, L. Drozdova, G. D. Piringruber, A. Kogelbauer, R. Prins,*Physical Chemistry Chemical Physics* 3.24 (2001): 5585-5595

37 R. Q. Long, R. T. Yang., *Journal of the American Chemical Society* 121.23 (1999): 5595-5596.

38 Inui, Tomoyuki, H. Matsuda, O. Yamase, A. Miyamoto,Journal of Catalysis 98.2 (1986): 491-501.

39 C. D. Chang, W. H. Lang, A. J. Silvestri. *Journal of Catalysis* 56.2 (1979): 268-273.

40 P.Pantu, , S. Pabchanda, and J. Limtrakul. " *Chemical Physics Physical Chemistry* 5.12 (2004): 1901-1906.

41 A. Simmen, L. B. McCusker, C. Baerlocher, W. M. Meier, *Zeolites*, 11, 654-661, (1991)

42 C. S. Cundy, P. A. Cox, *Microporous and Mesoporous Materials*, 82, 1-78 (2005)

43 A. Zecchina, M. Rivallan , G. Berlier , C. Lamberti, G. Ricchiardi, *Physical Chemistry Chemical Physics.* (2007); 9 273483-99.

44 K.A. Ovanesyan, Y. L. Sobolev, K. A. Dubkov, G. I. Panov and A. A. Shteinman, *Journalof Catalysis*, 207, 341 (2002)

45 J. B. Taboada, A. R. Overweg, P. J. Koyman, I. W. C. E. Arends, G. Mul, *J. Catal.* 231, 56, (2005)

46 G. I. Panov, A. K. Uriarte, M. A. Rodkin, V. I. Sobolev, *Catalysis Today*, 41, 365-385 (1998)

47 J. B. Taboada, A. R. Overweg, A. R. Craje, M. W. J. Arends, G. I. Mul, A. V. van der Kraan, *Microporous Mesoporous Materials* 75, 237-246 (2004)

48 G. Yang, J. Guan, L. Zhou, X. Han, X. Bao, *Catalysis Survey Asia 14*, 85–94 (2010)

49 E. J. Hensen, Q. Zhu, R. A. van Santen, *Journl of Catalysis*, 220, 260-264 (2002)

50 S.Keqiang, *Journal of Catalysis* 254.2 (2008): 383-396

51 I. Yuranov, D. A. Bulushev, A. Renken, L. Kiwi-Minsker, *Journal of Catalysis*, 227, 138 (2004)

52 N. Hansen, B. Peters, A. T. Bell, F. J. Keil, *J. Phys Chem. B.* 109, 1857, (2005)

53 G. Mul, J. Perez-Ramirez, F. Kaptejin, J. A. Mouljin, *Catalysis Letters*, 77, 7, (2001)

54 T. Ren, L. Yan, X. Zhang and J. Suo, *Appllied Catalysis A*, 244, 11 (2003)

55 C. Zenonos, G. Sankar, F. Cora, D. W. Lewis, Q. A. Pankhurst, C. R. A. Catlow, J. M. Thomas, *Physical Chemistry Chemical Physics.* 4, 5421-5429, (2002)

56 G. Sankar, N. R. Shiju, I. D. Watts, S. Nikitenko and W. Bras, *Research on Chemical Intermediates*., 34, 5-7, 649-658, (2008)

Chapter 2 - Theory and Experimental Techniques

2.1 Introduction

The complex structure, low active site concentration and the seemingly random distribution of metal ions, as well as the presence of the incorporated metal in a number of coordination environments and oxidation states, has greatly complicated the successful characterisation of microporous catalyst systems. In particular the exact identity of the active iron species in FeZSM-5 is still hotly debated. Conventional spectroscopic techniques are often not powerful enough to provide detailed information on the local structure of such sites. However techniques harnessing the intense, coherent light from synchrotron sources are well suited for these types of studies.

An extensive range of lab and synchrotron techniques can be used to determine the structure and properties of microporous materials. In particular X-ray and neutron diffraction, infrared spectroscopy (IR), UV-visible spectroscopy, scanning electron microscopy (SEM), transmission electron microscopy (TEM), X-ray absorption spectroscopy (XAS), thermo-gravimetric analysis (TGA) and computational modelling. By utilizing any single technique on its own, one is usually limited to information about only one particular structural characteristic of a material. Hence, a combination of characterization techniques is essential to provide a comprehensive model of the structure of a complex microporous system.

X-ray scattering and absorption measurements are one of the most commonly used techniques for investigating the structure of microporous materials. They can be used to study the structure in ambient and working conditions, as the short wavelength of the X-rays allows them to pass through air and most liquids, and so does not require the sample to be held in near vacuum conditions. Incidentally these properties make X-ray diffraction and spectroscopy techniques particularly useful for carrying out *in situ* measurements. If the data can be suitably measured at a fast enough sample rate, detailed time-resolved information on chemical and physical changes can be mapped in complex dynamic systems.

2.2 X-rays

In the laboratory, X-rays are most commonly produced using X-ray tubes. The tube is under high vacuum, wherein there is a cathode (a heated filament made of tungsten or other material) which emits electrons, which are accelerated onto an anodic stationary or rotating target. The electrons accelerated using high voltage power source (~50kV) connected across the cathode and anode. X-ray photons are emitted as a continuous spectrum caused by the rapid deceleration of the electrons as they impact the metal nuclei of the target anode. This type of radiation is called Bremsstrahlung radiation (from German meaning 'breaking-radiation'), and is emitted as a continuous spectrum. The energy of the emitted photon created by this process can take any value up to a maximum corresponding to the total kinetic energy of the incident electron.

The other process by which x-rays are produced in an x-ray tube is not caused by the simple deceleration of electrons, but rather by the ejection of core shell electrons from the inner *1s* (K-shell) orbital of the metal target atoms via ionisation by an electron with sufficient energy. Once the core-shell electron is ejected, outer orbital electrons (usually *2p* or *3p*) will readily transition to fill the core-hole vacancy left behind. An X-ray photon corresponding to the orbital energy difference of the transition in the metal target is thus emitted (Figure 2.1). This leads to so called characteristic emission lines. The spectrum in Figure 2.2 shows both the Bremsstrahlung and characteristic radiation peaks for tungsten at various accelerating voltages.

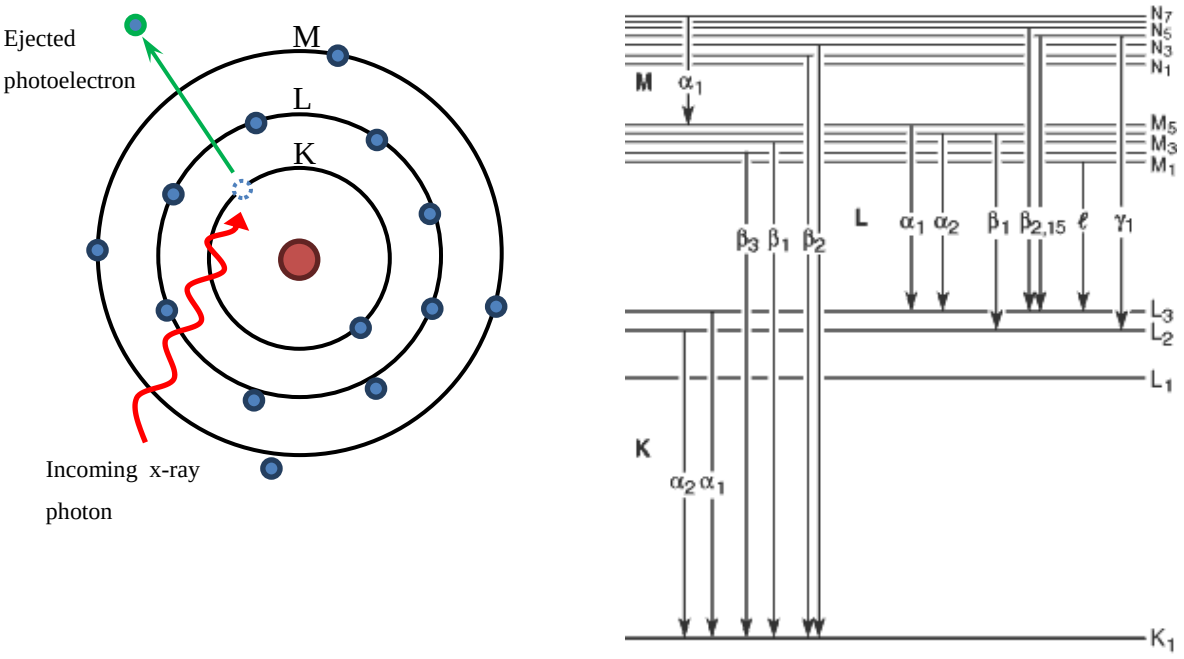

Figure 2.1 *The generation of a photoelectron by the absorption of an X-ray photon.*[1]

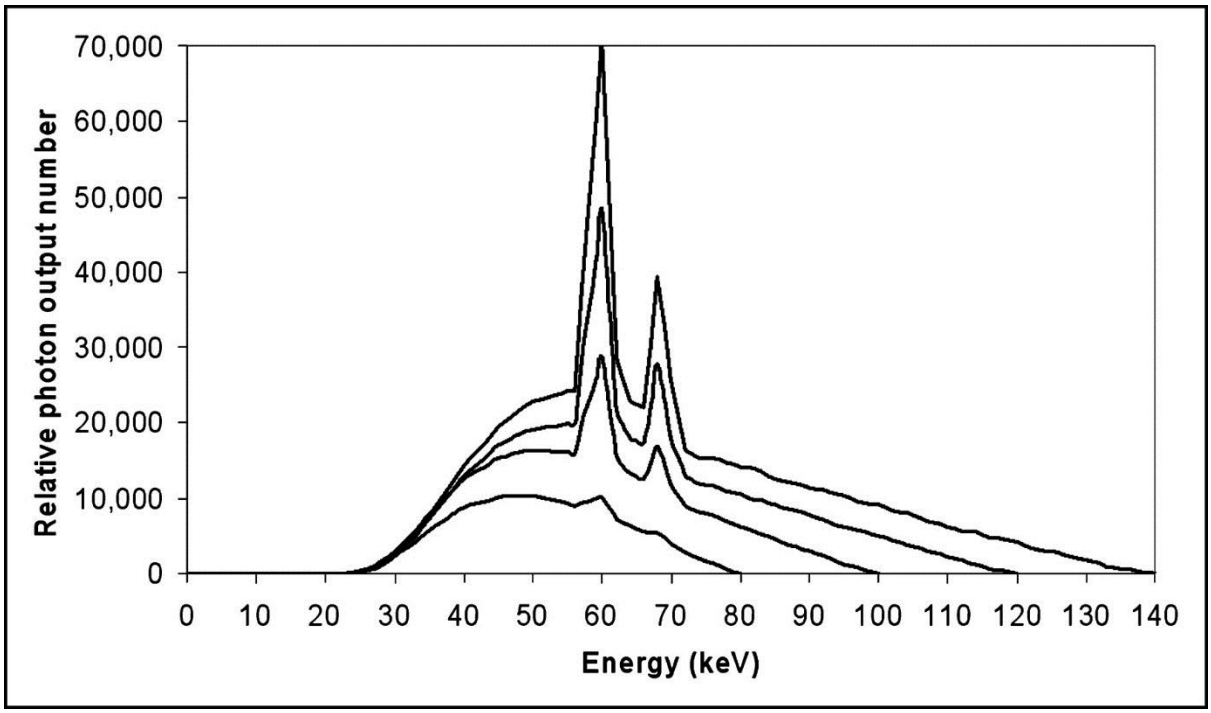

Figure 2.2 *X-ray emission from a lab based machine (tungsten source).* [1]

Whilst all the above mentioned X-ray techniques were developed using laboratory based X-ray sources, the intensity, tenability could not be achieved as efficiently as one would require performing experiments, in particular X-ray absorption spectroscopy. Therefore, a more powerful tunable X-ray source is required to perform measurements to yield more precise structural information. Synchrotron Radiation offers such characteristics that could be exploited for a range of techniques.

2.2.1 Synchrotron Radiation

Synchrotrons[2] are a particular type of cyclic particle accelerator where both the magnetic field and electric field are carefully synchronised with the travelling particle beam (usually electrons), in order to accelerate and bend the path of those particles. The intense electromagnetic radiation produced by the acceleration of electrons at relativistic speeds, is termed synchrotron radiation. The synchrotron techniques mentioned in this study were carried out at the Diamond Light Source in Oxfordshire (Figure 2.3) which generates and utilises a 3 GeV electron beam.

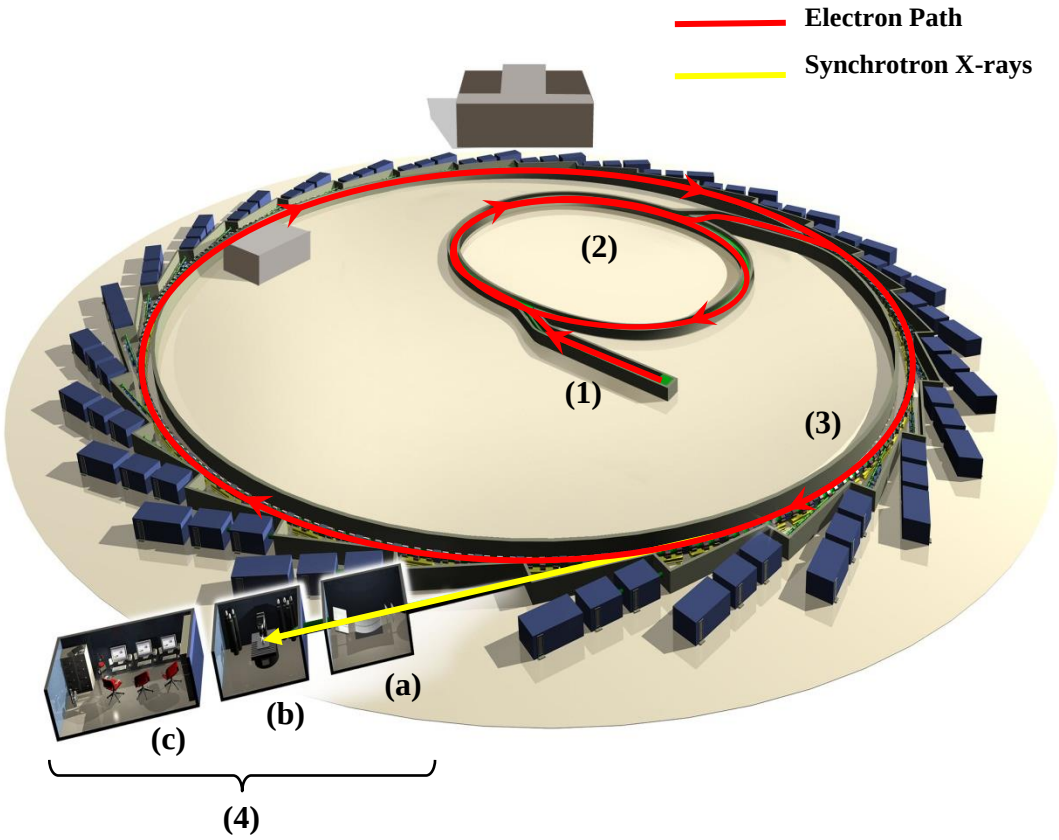

Figure 2.3 *The Diamond Light Source, the UKs National Synchrotron Facility. (1) Electron gun and linear accelerator, (2) booster synchrotron ring, (3) electron storage ring, (4) beamline, with detail of, (a) the optics hutch, (b) the experiment chamber, and (c) the beamline control room.*

The process of the generation of synchrotron radiation begins at the electron gun (Fig 2.3) where electrons are emitted via thermionic emission from an electron gun. They are then accelerated through a 100 MeV linear accelerator (LINAC). The linear accelerator leads to a 158 m circumference booster ring, where the electrons achieve their final energy of 3 GeV. Once the electron bunches have acquired the required energy, they are injected into the storage ring where a continuous electron beam may circulate for many hours. The storage ring at Diamond consists of 24 linear sections, connected together by dipole magnets at the vertices, forming a loop 562 m in circumference. Electrons complete this circuit in approximately two millionths of a second, equivalent to travelling around the earth 7.5 times in a single second.

To minimise energy lost by the electrons scattering by air, the beam is kept under a constant ultrahigh vacuum. Energy losses are however inevitable, and can be caused by collisions, scattering, and the radiative events that produce the X-ray photons themselves. The energy lost is replaced by three RF (Radio Frequency) cavities. The radio frequency system at the synchrotron varies the electromagnetic field in the RF cavities so that there always exists a positive electric field in front of the electron bunch and a negative one behind as it passes the full length of the cavity, thus providing a boost to the energy of the electrons. In this way the electrons can be circulated in the storage ring for hours ($\lambda > 10$ h) at a constant energy.[2]

The acceleration of the electrons around a curved path is what generates the useful high-energy electromagnetic radiation used at the beamlines in experiments. This function is executed by bending magnets, which mark the corners of the storage ring; or by insertion devices which are located in the straight sections of the ring.

A bending magnet is essentially a strong dipole magnet at one of the ring vertices. Here the high energy electrons are forced to travel in a curved path by a strong electromagnetic field. The acceleration of the electrons emits an intense, brilliant white beam of electromagnetic radiation at a tangent to the curve. The synchrotron radiation produced (mainly in the X-ray energy range) is then sent down various beamlines situated around the storage ring.

The beamlines typically include X-ray optical devices which control the bandwidth, photon flux, beam dimensions, focus, and collimation of the rays. The specialisation and equipment at the beamlines allows a range of advanced spectroscopic and crystallographic measurements to be carried out.

The optical devices include slits, attenuators, crystal monochromators, and mirrors. At the end of the beamline is the experimental end station, where samples are placed in the line of the radiation, and detectors are positioned to measure the resulting diffraction, scattering or secondary radiation. The high intensity monochromatic X-rays produced allow for very powerful characterisation of many types of materials.

2.3 X-ray Diffraction

X-ray Diffraction (XRD) experiments can often be carried out in a laboratory for most materials using X-ray tubes. In these cases the X-rays are produced by accelerating a beam of electrons onto a metal target, resulting in the ionisation of the atom via the ejection of the *1s* (K-shell) electrons. Outer orbital electrons (*2p* or *3p*) then consequently drop in energy level in order to fill the hole in the *1s* orbital. This causes the emission of an X-ray photon during the transition, corresponding to a particular wavelength. This wavelength is given by Planck's law $\lambda=hc/E$, where the energy E, is equal to the difference in energy of the initial and final orbital for the transition. Common metal targets used in X-ray tubes include Cu and Mo.

The combination of certain X-ray wavelengths and certain elements present in a sample can lead to strong fluorescence which increases the background in the diffraction pattern. A notorious example is the presence of iron in a sample when using copper radiation. Another limitation is that the intensity of traditional generators is relatively low, requiring lengthy exposure times and precluding any time dependent measurement. The advent of synchrotron radiation sources drastically changed this picture and caused

powder diffraction methods to enter a whole new phase of development. Not only is there a much wider choice of wavelengths available, but the brilliance of the synchrotron radiation makes it possible to collect data at an extremely fast rate, and thus observe changes in the diffraction pattern during chemical reactions, temperature ramps and changes in pressure.

X-rays interact with the electrons in atoms. In an XRD measurement, a beam of X-rays with known wavelength is targeted onto either a single crystal or a powdered sample of the material being investigated. X-ray crystallography harnesses information obtained from the *elastic scattering* events, whereby outgoing X-rays have the same energy, and hence the same wavelength, as the incoming X-rays, only with altered direction. By contrast, *inelastic scattering* occurs when energy is transferred from the incoming X-ray to the impinging matter, by exciting an inner-shell electron to a higher energy level. Such inelastic scattering reduces the energy (increases the wavelength) of the outgoing beam. Inelastic scattering techniques can be useful for probing excitations and energy levels, but not for determining the distribution of within the sample, which is the main objective of X-ray diffraction[3].

2.3.1 Bragg's Law

The diffraction pattern produced from the elastic scattering events created by the interactions of the X-ray photons with the electron clouds of the atoms in the sample can be used to identify the sample and derive information about the unit cell and crystal structure. Crystals can diffract X-rays because the spacing between atoms in a crystal is similar to the wavelength of the X-rays (~1 Å). The diffraction from the electron cloud surrounding the atomic nuclei is actually random; however it is because these atoms are arranged in a well defined repeating periodic array (i.e. as a crystal lattice) that allows the refracted waves to interfere both destructively and constructively, thereby forming a diffraction pattern which contains useful information about the sample. William Lawrence Bragg and William Henry Bragg proposed a model in 1913 in order to explain their discovery that crystalline solids produced surprising patterns of reflected X-rays[4]. They found that these crystals, at certain specific wavelengths and incident angles, produced intense peaks of reflected radiation. W. L. Bragg suggested that the

diffraction pattern can be explained in terms of reflections from imaginary planes in the crystal lattice (Figure 2.4).

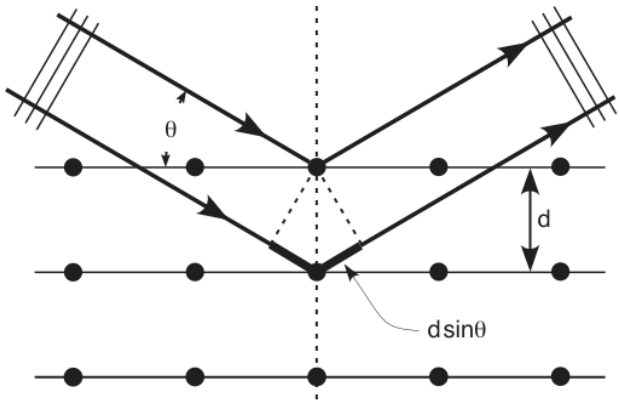

Figure 2.4. *Bragg reflection from crystal planes, with lattice plane spacing d and angle of reflection θ.*

From this he formulated what is now known as Bragg's law,

$$n\lambda = 2d_{hkl}sin\,\theta$$

where n is an integer, λ is the wavelength of the incident X-ray photon, θ is the angle of diffraction, and d_{hkl} is the distance between the planes formed by the atoms in the crystal. The subscript *hkl* denotes the three Miller indices, integers which denote a plane orthogonal to a direction in the basis of the reciprocal lattice vectors.

XRD patterns can be collected from either single crystals or powders. Whether a lab-based X-ray tube or a synchrotron is used as the source of radiation, the basic methodology is usually very similar. With the zeolite samples studied in this project, powder diffraction is used almost exclusively. In a typical experiment, the powdered sample (consisting of many crystallites in random orientations) is mounted into a capillary or flat plate. The sample is then placed into the path of a monochromatic X-ray beam, attached to a goniometer, which allows the sample to be accurately rotated to a particular angle. The X-rays are diffracted at particular Bragg angles θ, and the

intensities of these reflections can then be recorded. The data can then be plotted as intensity vs 2θ to give the powder diffraction pattern. This pattern may then be indexed to give the unit cell dimensions, and the space group can then be determined. It may then be possible to solve the structure by direct methods[5], Patterson method[6] or maximum entropy techniques [7] and refined using the Rietveld or Pawley method.[8]

2.3.2 HRPD Measurements and Analysis

XRD patterns can be collected from either single crystals or powders. Whether a lab-based X-ray tube or a synchrotron is used as the source of radiation, the basic methodology is usually very similar. With the zeolite samples studied in this project, powder diffraction is used almost exclusively. In a typical experiment, the powdered sample (consisting of many crystallites in random orientations) is mounted into a capillary or flat plate. The sample is then placed into the path of a monochromatic X-ray beam, attached to a goniometer, which allows the sample to be accurately rotated to a particular angle. The X-rays are diffracted at particular Bragg angles θ, and the intensities of these reflections can then be recorded. The data can then be plotted as intensity vs 2θ to give the powder diffraction pattern. This pattern may then be indexed to give the unit cell dimensions, and the space group can then be determined. It may then be possible to solve the structure by various methods.

High Resolution Powder Diffraction (HRPD) is the most widely used X-ray diffraction technique for characterising materials when a single crystal is not available. The nature of a powder means that the crystalline domains are randomly oriented in a given sample. Therefore, the 2-D diffraction pattern is a series of concentric rings. These correspond to the scattering peaks corresponding to different *d*-spacing in the crystal lattice. The positions and the intensities of the peaks can then be used for identifying the underlying structure of the material.

The collapsing of the three-dimensional reciprocal space of the individual crystallites on the one-dimensional *2θ* axis can result in the following consequences:

- systematic overlap of diffraction peaks due to symmetry conditions

- accidental overlap caused by the limited experimental resolution
- difficult definition of the background
- non-random distribution of the crystallites in the specimen

The advantage of the powder diffraction to other methods is a relatively fast, non-destructive examination of multi- component materials, with relatively simple sample preparation[2]. These can be quickly analyzed, and identified by comparison to known standards or databases (such as International Centre for Diffraction Data, and Cambridge Structural Database). The powder diffraction also allows one to determine the levels of crystallinity, phase transitions, lattice parameters, and size and strain broadening.[11]

The analyses of powder diffraction pattern require the following steps[16]:

1) Collection of highly resolved powder diffraction patterns
2) Indexing the powder pattern
3) Determining the space group
4) Obtaining the integrated intensities
5) Refining of the structure by the Pawley method.

The determination of the crystal structure from powder diffraction can be done, but it is extremely difficult due to overlap of the reflections in the experiment.
The atomic position within the cell is independent of the position of a diffraction peak, and is entirely determined by the size and shape of the unit cell. Each peak represents a certain lattice plane, and is characterized by a Miller index. The integrated intensities from a powder diffraction pattern can be obtained by many methods such as the traditional Rietveld[9], and the Pawley method[10] used in this work.

2.3.3 Pawley Refinement

The Pawley method[10] is based on a non-linear least squares refinement, where the integrated intensities are refined variables in addition to the profile parameters. The peak overlap can cause instability in the least squares, and sometimes provide negative integrated intensity values which must be discarded, and for this reason the method needs positivity constraints. This method has a particular advantage for direct space methods on structure determination from powder diffraction data. The covariance matrix of the Pawley fit describes the degree of correlation between the individual intensities of neighbouring reflections and can actively be used in the calculation of the level of agreement between the measured intensities and those of the trial structures in a global optimization process. In order to solve a structure from powder data it is necessary to extract as many *hkl* and intensity values as possible from the data set. Until the 1980s, this wasn't feasible due to the overlapping nature of the peaks in a powder diffraction profile. However, with the development of high-speed modern computers with large memories and high-resolution diffractometers pattern decomposition became a viable and important part of the analysis of powder data. The high resolution, high intensity measurement at a synchrotron X-ray beamline is perfectly suited for obtaining the kind of high quality data needed for a rigorous analysis using these methods. All the method uses pattern decomposition rather than deconvolution because the exact peak-width function is not known *a priori*, but in effect the end result is similar.

Pawley suggested that angle-dispersive powder diffraction profiles could be fitted with only the following parameters:

- $I(hkl)$ - intensity of each reflection
- $A, B, C, D, E, F, \ldots$ - unit-cell metric tensor parameters
- $2\theta_{zero}$ - instrumental zero error
- U, V, W - peak width parameters
- η, etc. - peak shape parameters

In the Pawley method, every reflection is assumed to have:

(i) a peak intensity $I(hkl)$

(ii) a peak position determined by A, B, C, D, E, F,… and the $2\theta_{zero}$ instrumental error

(iii) a peak width determined by the resolution function parameters U, V, and W

This can be contrasted to the more complete structure solution offered by the Rietveld method, in which the intensity of the peaks is calculated from the structure factures, $F(hkl)$, which are themselves calculated from the parameters of the atoms in the model structure. In terms of the least-squares minimization procedure used in TOPAS, this requires the typical computation of a $(10+N) \times (10+N)$ square matrix where N is the number of symmetry-independent reflections generated for the 2θ range covered by the data. This is computationally expensive but can be achieved in an automated fashion once initial input files have been set up reasonable time using the software TOPAS Academic. Using this software suite, the user can change fitting windows, remove peaks, and vary the method and number of fitting parameters until a good agreement with low R-values is obtained. Given a correct unit cell and a plausible peak shape model, the Pawley fit corresponds well with the measured pattern. Additionally, this fitting procedure has been found to be particularly useful in the validation of a potential indexing or unit cell. A poor choice of space group or incorrect indexing will result in a poor fit.

Once an appropriate input file has been created for adequate interpretation of the data, TOPAS can be used via a command line interface, and a script (.bat file) can be written to automatically process the large number of XRD scans collected during the experiment. The Pawley method is also the best suited for the purposes of extracting lattice parameters from a known starting symmetry as in this investigation.

2.4 X-ray Absorption Spectroscopy

X-ray absorption spectroscopy (XAS) is a widely used technique for determining the local geometric and electronic structure of matter. XAS data is obtained using synchrotron radiation by tuning the photon energy using a crystalline monochromator to a range where the core electrons of the targeted atoms can be excited (~0.1 - 100 keV).

When electromagnetic radiation passes through matter, it loses intensity due to absorption. For a path length dx for the radiation passing through a material the decrease in the intensity is given by

$$dI = -\mu(E) I_t dx$$

Where $\mu(E)$ is the linear absorption coefficient at a given energy E and is dependent on the absorption characteristics of the material. Integrating this over the total thickness x yields an expression giving the measured intensity I_t of radiation transmitted, which is proportional to the incident intensity and the thickness of the material. This is known as the Beer-Lambert law;

$$I_t = I_o e^{-\mu(E)x}$$

where I_t and I_o are the transmitted and incident intensities of the beam respectively. When the energy of the photons matches the binding energy of a core electron they are absorbed and the electron is ejected into the continuum state (*i.e.* as a photoelectron) and a sharp rise in the absorption of that particular wavelength of radiation is observed. This results in an absorption edge. A plot of the absorption coefficient (natural log of I_t/I_o) versus photon energy gives the absorption spectrum (Figure 2.6).

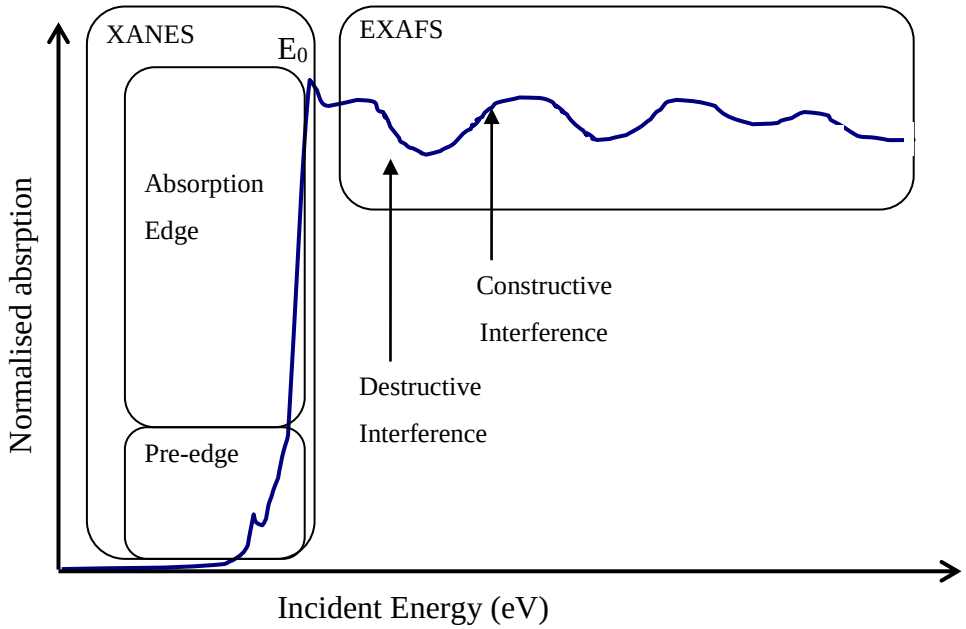

Figure 2.5. *A typical XAS spectrum, with pre-edge, XANES, and EXAFS regions highlighted*

In the schematic X-ray absorption spectrum shown in Figure 2.6, the large jump at E_0 known as the rising or absorption edge, corresponds to the threshold energy, where the photons at that energy are absorbed and a core electron has been excited to a higher state. This region of the spectrum is known as the X-ray absorption near edge (XANES), and the higher energy region beyond that is known as the extended X-ray absorption fine structure (EXAFS). XANES provides information mainly on the oxidation state and coordination geometry of the absorbing atom, whereas the EXAFS region can be used to extract information about the local structure surrounding the absorbing atom. In X-ray absorption spectra, the X-ray absorption coefficient is usually normalised to unit step height. This is done by fitting a regression line to the region before and after the absorption edge, subtracting the pre-edge line from the entire data set and dividing by the absorption step height, which is determined by the difference between the pre-edge and post-edge lines at the absorption edge (E_0).

2.4.1 XANES

The XANES region of the XAS spectrum contains information on the coordination geometry and oxidation state of the absorbing atom. In the XANES region, transitions

of core electrons to non-bound levels with close energy occur. Because of the high probability of such transition, a sudden rise in absorption is observed, manifesting as the absorption edge. In principle the edge position can be related to the effective atomic number of the metal centre, and thus be correlated with oxidation state; however, changes in the coordination number, symmetry and the metal-ligand bonding can have a significant effect on the apparent edge position which makes it an unreliable indicator of oxidation state. [11]

The small peak found just before the absorption edge is known as the pre-edge. Unlike the edge jump, analysis of the pre-edge region for transition metal K-edge spectra can be very informative. The intensity of the pre-edge transition feature in the XAS spectrum depends on the geometry around the absorbing metal and can be correlated to structural symmetry.[12]

The energy position of the centroid peak of pre-edge absorption feature contains information about the ligand fields and oxidation state around the absorbing atom and oxidation state. Higher oxidation of the metal leads to greater stabilization of the 1s orbital with respect to the metal d orbitals, resulting in higher energy of the pre-edge. Bonding interactions with neighbouring atoms also cause changes in the metal's effective nuclear charge (Z_{eff}) which in turn also cause to changes in the energy of the pre-edge feature. To understand this phenomenon one must consider the Laporte selection rules[13]. These are the spectroscopic selection rules based on quantum mechanics, that apply to centrosymmetric molecules (those with an inversion centre) and atoms. It states that electronic transitions that conserve parity, either symmetry or antisymmetry with respect to an inversion centre are canonically forbidden. The allowed transitions in such molecules or atoms in crystals, must involve a change in parity, either $g \rightarrow u$ or $u \rightarrow g$. As a consequence, if a molecule is centrosymmetric, transitions within a given set of *p* or *d* orbitals (i.e. those that only involve a redistribution of electrons within a given orbital subshell) are forbidden.[14] Absorption occurs once core shell electrons are excited to higher unfilled or half-filled orbitals as dictated quantum mechanically by the orbital momentum selection rule $\Delta l = \pm 1$.[15] Thus the majority of transitions contribute to the intense rising edge feature of the spectrum, and they will be from $s \rightarrow p$ orbitals (known as K edge if core electron is *1s*, L_1 edge if *2s*) and $p \rightarrow d$ (known as the L_2 and L_3 edges from $2p_{1/2}$ and $2p_{3/2}$ states respectively).

The pre-edge feature is caused by the formally forbidden the *1s→3d* transition. It is canonically forbidden as this would involve *Δl=2*, which is against quantum mechanical selection rules. However, in a perfect tetrahedral geometry there is enough *p-d* orbital mixing to allow the transition a large enough probability to effectively occur.[12] Octahedral geometries however have a much smaller pre-edge as this transition is formally forbidden; however a small pre-edge is often observed due to an electronic quadrupole coupling mechanism.[16]

Thus the height of the pre-edge peak can be used to distinguish between tetrahedrally and octahedrally coordinated transition metal atoms, whereby the pre-edge peak has the highest intensity when the central atom is in tetrahedral coordination geometry[17]. The position of the pre-edge peak is sensitive to the oxidation state of the absorbing metal atom. A study of Fe K-edge XANES spectra measured for more than 35 Fe(II) and Fe(III) bearing minerals was conducted by Farges and co-workers[18]. It was found that the separation between the average pre-edge centroid positions for Fe(II) and Fe(III) is 1.4 ± 0.1 eV. Examination of calculated pre-edge features of mechanical mixtures of phases containing different proportions of Fe(II) and Fe(III) revealed that different trends of pre-edge position *vs.* pre-edge intensity can be observed, depending on the coordination environment, in what is an approximately linear relationship (Figure 2.6).

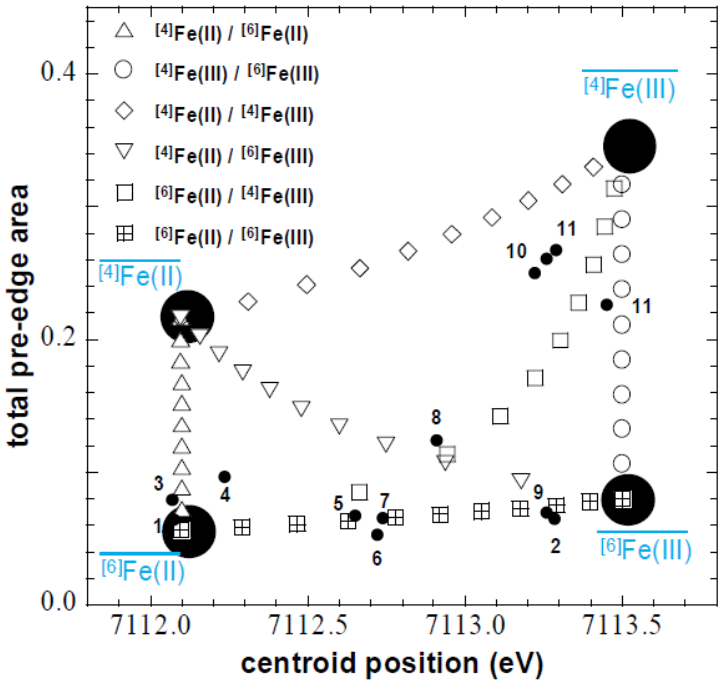

Figure 2.6. *Summary of pre-edge characteristics for the binary mixtures between* $^{[4]}$*Fe(II) (tetrahedral),* $^{[6]}$*Fe(II) (octahedral),* $^{[4]}$*Fe(III), and* $^{[6]}$*Fe(III). Pre-edge information for Fe in example minerals is also plotted (Black circles) Tetrahedral complexes have higher pre-edges than octahedral ones, and the centroid position is well separated for the different Fe oxidation states.*[48]

2.4.2 EXAFS

The EXAFS region of the spectrum contains the oscillations that begin at just after the absorption edge, and extend to around ~1000 eV beyond that. EXAFS appears above the absorption edges whenever the absorbing atom is closely surrounded by other atoms *i.e.* in solid state, in liquids or in molecular gases. In case of free atoms, as for example in noble gases or monatomic vapours, there is no EXAFS component in the absorption spectrum.

EXAFS arises from the core photoelectron that is ejected during photon absorption at the edge jump region. When an X-ray photon is absorbed an inner shell electron is ejected as a photoelectron with kinetic energy E_K equal to the difference between the photon energy $h\nu$, and the work function, φ;

$$E_K = h\nu - \varphi$$

For absorption that occurs precisely the absorption edge, the kinetic energy of the ejected photoelectron (E_K) is taken and defined to be the the zero-point energy or "inner potential" of the system, denoted E_0. Quantum mechanically, this photoelectron can be considered as propagating away from the absorbing atom as an outgoing spherical wave with wavelength λ.

$$\lambda = 2\pi/k$$

where k is the wave vector in reciprocal space;

$$k = \sqrt{\left(\frac{8\pi^2 m_e}{h^2}\right)(h\nu + E_0 - E_{edge})}$$

where E_{edge} is the absorption edge energy, h is Planck's constant and m_e is the electron mass.

Using the dipole approximation, the probability of transition for this photoelectric event is proportional to the cross section of the event which is equivalent to the linear absorption coefficient $\mu(E)$. Thus transition probability can be expressed as a function of the initial-state and final-state wavefunctions;

$$\mu(E) = C\left|\left\langle \psi_f \left| \hat{W} \right| \psi_i \right\rangle\right|^2 \rho\left(E_f - E_i - h\nu\right)$$

The coefficient $C = 4\pi a^2 \hbar \nu$ where a is the fine structure constant; a = 7.297 x 10^{-3}. Here, ψ_f and ψ_i are the final and initial state wavefunctions respectively, and the same notation is used for the energy E. The operator $\hat{W}$ of the dipole transition induced by the incident electromagnetic radiation is the dot product of contributions from the electric field vector $\boldsymbol{\varepsilon}$ and the atomic dipole moment $e\mathbf{r}$, represented as $\hat{W} = e\mathbf{r}\cdot\boldsymbol{\varepsilon}$.

The electron orbitals of the atoms surrounding the targeted excited atom then backscatter the photoelectron waves which then interfere with the forward-propagating waves of the initial photoelectron.

The resulting constructive and destructive interference of these waves shows up as a modulation of the measured absorption coefficient, affected by the electromagnetic effect of these waves. This causes the sinusoidal variation of the absorption coefficient EXAFS spectra, which depends on the nature of the local environment (i.e. the type, position and distance of surrounding atoms as well as the mode of bonding).

The fundamental equation describing the total background subtracted EXAFS contribution is given in the equation below[19] ;

$$\chi(k) = \sum_j \left(N_j \Big/ R_j^2 k \right) \exp(-2\sigma_j^2 k^2) F(k) \sin\left[2R_j k + \varphi(k)\right]$$

where N_j is the coordination number of the j^{th} shell of radius R_j, σ_j, is the Debye-Waller factor, k is the photoelectron wave vector, $F(k)$ is the backscattering amplitude and $\varphi(k)$ is the phase shift.

Structural determinations by EXAFS depend on resolving the data into individual waves corresponding to the neighbours of the central atom. This is done by Fourier transforming the data and then refining by fitting a model system to the experimental data.

2.4.3 XAS Data Analysis

The XAS and EXAFS data processing for this project was carried out using a number of programs. Artemis and Athena are part of the IFEFFIT suite of interactive programs for XAFS analysis, combining high-quality and well-tested XAFS analysis algorithms, tools for general data manipulation, and graphical display of data. An older program EXCURVE was also used throughout the data analysis of this project. A brief overview of the various programs is given below.

- ATHENA: Interactive graphical utility for processing EXAFS data. It handles most of the common data handling chores of interest, including deglitching, aligning, merging, background removal, Fourier transforms, and much more. The background removal and a portion of the data processing and model fitting is carried out using the IFEFFIT suite of software based on the FEFF code.

- ARTEMIS: An interactive graphical utility for fitting EXAFS data using theoretical standards from FEFF and sophisticated data modelling along with flexible data visualization and statistical analysis. ARTEMIS includes interfaces to FEFF.

- EXCURVE: An integrated environment for the analysis of EXAFS spectra using the fast spherical wave method, published by Gurman, Binsted and Ross.[20] The spherical-wave method employed does not require the input of crystallographic data in order to create a sitting model, unlike the newer ARTEMIS program. Thus it its better for fitting data belonging to a sample with high heterogeneity, multiple absorption environments, or amorphous structure. This makes it an especially useful program for investigating materials such as isomorphically substituted zeolites that have a small concentration of metal ions, which might be found in differing coordination environments.

As stated, the data processing prior to analysis in this study were completed the program Athena. A generalised outline of the procedure is as follows. Following the data

collection the data files are processed and the measured intensities are converted to energy versus absorption coefficient $\mu(E)$. Measurement errors are then corrected manually (such as obvious glitches or artefacts) and the data is re-binned to remove noise. This noise/background in the initial data is caused by a number of effects including self-absorption, detector glitches, detector dead time and electromagnetic background noise.

The threshold energy E_0, of the absorption event is then identified, usually by taking the maximum of the first derivative of $\mu(E)$. In practice the first derivative $(d\mu/dE)$ may have more than one local maximum near the edge jump and so the selection of this value is actually somewhat arbitrary. The best value and the method of its choosing remains the choice of the person doing the analysis, and consistency in methodology is the key to avoiding pitfalls that can brought about by this. The key is to use what is most reproducible for the particular set of data files and then keep the method of choice for computing E_0 consistent throughout the set.

A smooth pre-edge function (a simple polynomial) is fitted to the spectrum just below the edge and the edge jump $\Delta\mu$, is approximated. This is edge jump is then subtracted from $\mu(E)$ in order to remove any instrumental background effects and absorption from other unwanted edges. The normalisation performed allows edge jumps to be compared and is essential for XANES analysis (Figure 2.7).

A post-edge smooth spline function is then fitted along the post-edge (EXAFS) part of the spectrum. This spline acts as an approximation for the absorption of a single isolated atom $\mu_0(E)$. By subtracting this we can then extract the EXAFS spectrum.

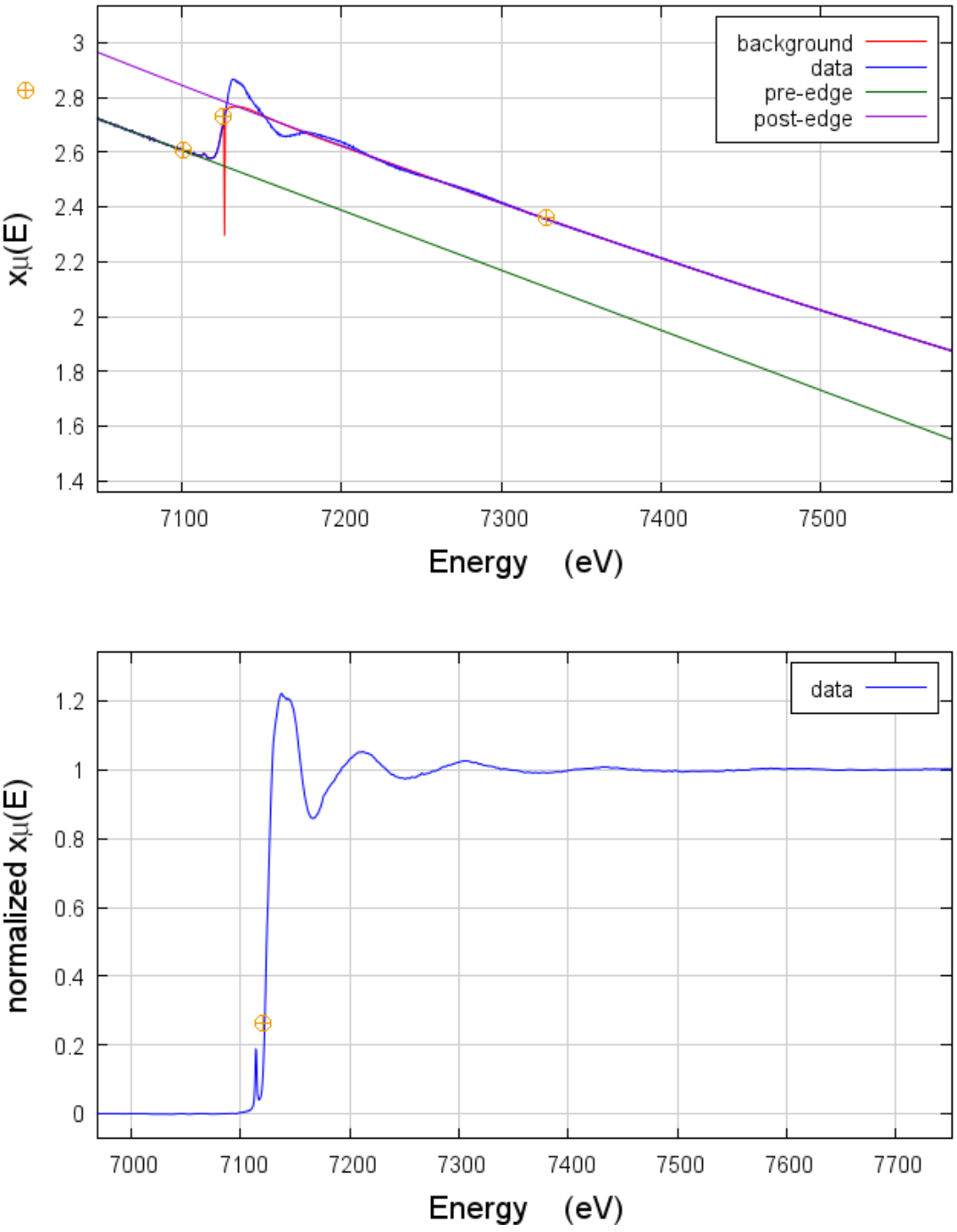

Figure 2.7 *- Normalisation of the XAS spectrum - The un-normalised spectrum shown above with pre- and post-edge lines along with background function. Below is the resulting normalised spectrum.*

The EXAFS data *χ(k),* is the summation of all the perturbations to the absorption coefficients of the atomic orbitals caused by the interference patterns of the photoelectron wave scattered off all the atoms and is obtained according to the EXAFS

equation. Once extracted $\chi(k)$ is then multiplied by a power of n ($n = 3$ usually) to give $k^n(\chi(E))$ where k is the wave vector. This is done in order to compensate for the attenuation of the EXAFS at higher values and to prevent the larger oscillations at low k values from dominating the spectrum.

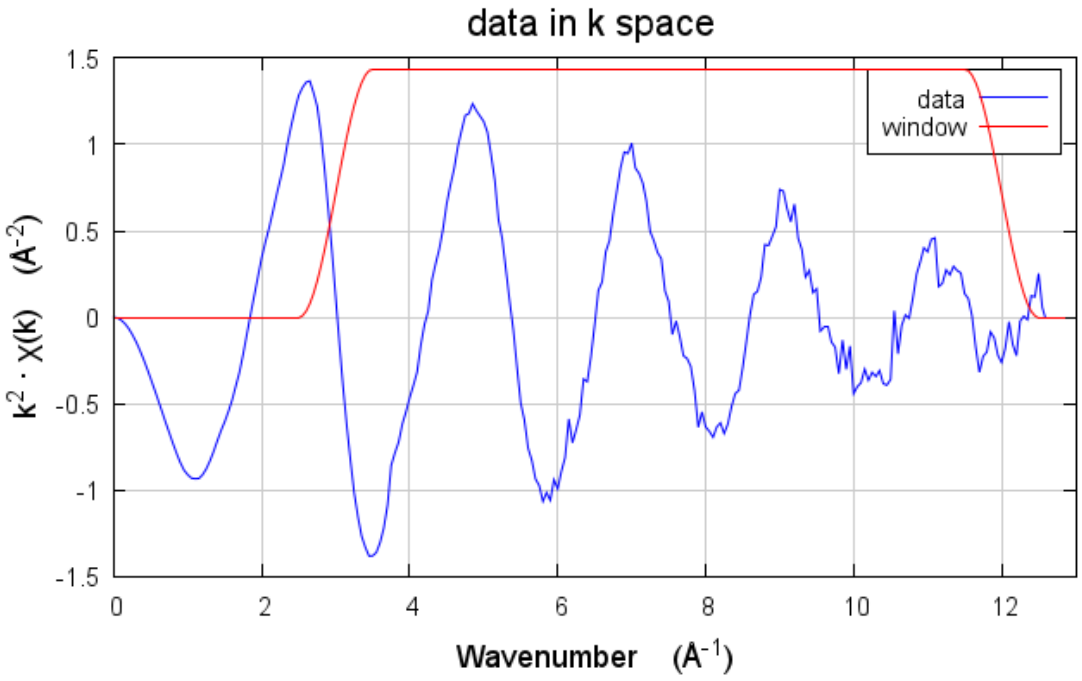

Figure 2.8. *Extraction of $k^2(\chi(E))$ from the EXAFS spectrum, and fitting window.*

In complex systems such as the ones investigated here, EXAFS data have signal to noise ratios greater than unity up to k^n ~ 12-14 Å^{-1}, and the region below k^n ~1.5 Å^{-1} is excluded because of possible complications from multiple scattering etc. Multiple scattering is not a concern for first shell analysis, however.

Including high k-regions of the spectrum where the signal is swamped by noise mainly adds spurious structure to the transforms and makes them difficult to interpret and fit to models. Merging several independent scans is very helpful in this regard and three scans were merged together in each calculation that was performed.

An extended form of the EXAFS equation is essentially what is eventually used as the basis for interpretation once the data has been normalised. The extracted $\chi(k)$ data

consist of sum of damped sine waves corresponding to the signal contributions from the different atomic shells surrounding the central absorbing atom. To deconvolute the signals and reduce the number of fitting parameters, the signals from the contributions different shells can be separated using Fourier filtering methods. These also permit a decomposition of the oscillations into amplitude and phase functions.

The Fourier transform of an integrable function is given by

$$\tilde{\chi}_{\alpha}(r) = \int e^{-ikr} W_{\alpha}(k)\chi(k)dk$$

where $W_{\alpha}(k)$ includes the k^n weighting, and the subscript α indicates a dependence on certain parameters (such as the width) characterizing the k-space window. This resulting Fourier–transform is a complex function with both imaginary and real components related to the phase-shifts generated by the atomic backscattering events. When plotted, the modulus of $\tilde{\chi}_{\alpha}(r)$ results in peaks that correspond to the various coordination shells, converting the k-space data into complementary real-space information. Great care must be exercised when interpreting the resulting Fourier-transforms and a comparison between this and what is already known about the system must be considered and analysed in detail to insure the correct background removal and normalisation has been carried out. The resulting plot of the modulus is often erroneously referred to as a "radial distribution function". This however is definitely not the case, as although the peaks represent, and are a consequence of, the numbers, types and positions of the atoms, the peak interpretation is by no means trivial, due to it being an artefact of complex-wave interference and associated phase shifts.

In reality the position of the peak corresponds to the average frequency of the corresponding shell's EXAFS signal, which is related to the average distance of the shell from the central absorbing atom.

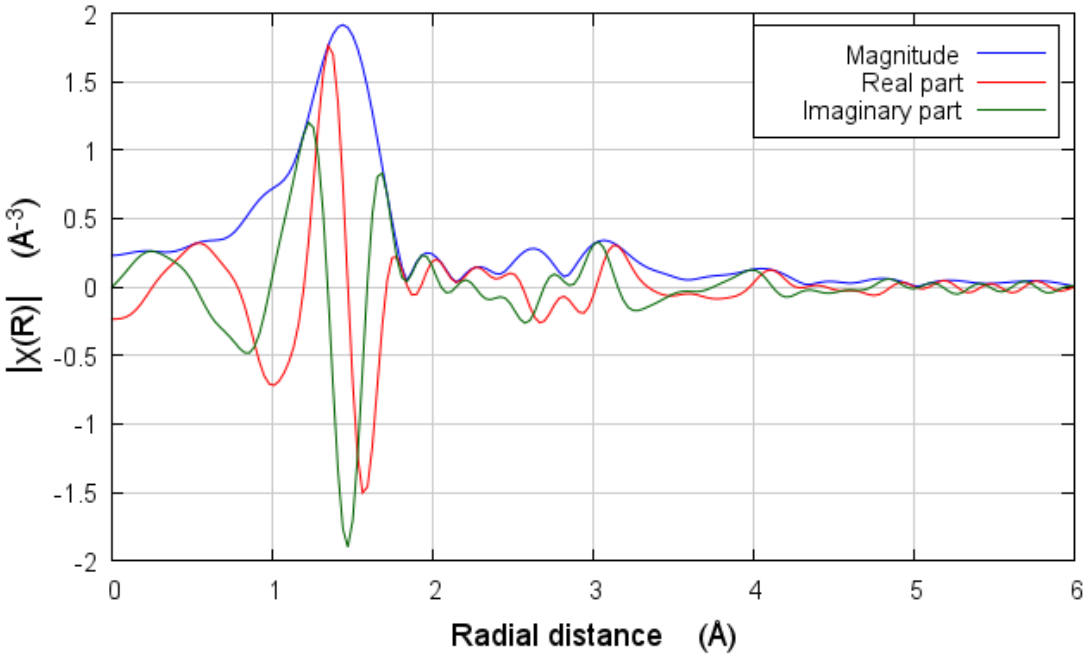

Figure 2.9 *Plot of the resulting Fourier-transform of the EXAFS data.*

The peak height in the Fourier transform plot is related to the average amplitude of the (k^n-weighted) EXAFS over the k-space data range, and is therefore related to the number of atoms in the shell, the disorder parameter σ^2, the atomic number of the atoms in the shell *N*, and the k-space window chosen. The transform peak position is only a crude measure of the average distance as in actuality it represents the derivative of the average phase of the backscattered photoelectron wave and cannot generally be used for accurate distance determination. Disorder in the system whether static or dynamic in origin, can also cause significant peak shifts as well as overall dampening of the EXAFS. Similarly the peak maxima cannot be used for the determination of coordination numbers except in a very approximate manner, because atomic number, disorder, and other effects are also important. The Fourier-transform is simply an intermediate step in the Fourier-filtering and fitting process although a final one in the initial data processing using Athena. A detailed analysis and fitting the data to an appropriate model is then carried out using either the Excurve or Artemis data processing software.

The curved-wave theory based EXCURVE 98 software package was used primarily for the Fe K-edge EXAFS analysis. It supports both single scattering and full multiple-scattering analysis of EXAFS data. Within the single scattering mode, as used in this study, the package reports the radius of shells of atoms surrounding the emitter, the Debye-Waller factors, and the occupation numbers of the shells. The program allows for full calculation, fitting and visualization of the EXAFS spectra using a simple command line user interface and GUI output. Although much older than Artemis and the FEFF code, it is a very robust and reliable software package which has undergone many updates over the years and can fit models using curved-wave theory without the use of crystallographic input files, unlike Artemis.

Once the measured EXAFS spectra have been normalised and background-corrected using Athena it can then be imported into EXCURVE or ARTEMIS for proper analysis and fitting. When using EXCURVE to proceed with the fitting procedure of the EXAFS spectra, the potentials and corresponding phase shifts must be calculated for each constituent atom of the material being examined. The code allows at most two atom types per cluster during potential and phase shifts calculations, and the user has a choice as to how these calculations are carried out. It is often best to choose the nearest neighbours and that of lowest atomic number *Z*. Atomic potential calculations are then carried out with the use of the $Z = Z+1$ approximation. The most important part of the program package is the ability to then iteratively refine the theoretical EXAFS spectra in order to obtain the best fit with the experimental data and thus to solve the structure. The refinement procedure is based on least squares minimization in *k* space under restrained conditions based on defined known elements of the structure. The parameters which are then refined are the Debye-Waller factors σ^2, the Fermi energy E_f, the number of atoms in each shell *N*, together with the associated average shell radius *R* of a particular surrounding atom from the central atom. Each of these parameters can be refined either individually or together by applying constraints on related or correlated physical quantities.

Using ARTEMIS to analyse and fit the EXAFS data relies on paths generated by the FEFF algorithm. The FEFF program calculates the backscattering amplitudes $(F_j(k))$ and phase shifts $(\varphi_{ij}(k))$ of the atoms based on the user inputted structure file (usually a *.cif* input file) and provides single and multiple scattering paths, which are then used in

the modelling of the Fourier transformed experimental EXAFS spectrum. The path parameters for each atomic shell being computed are then set to user generated math expressions from a fitting model. These expressions can be setup to be refined or fixed in value at different points of the analysis. The ARTEMIS program is used to adjust the structural parameters in the EXAFS equation until a least-squares fit is obtained between the theoretical (modelled) and experimental EXAFS spectra. The model is iteratively adjusted as needed (e.g., with different scattering paths and starting parameters) until the best possible fit is obtained between theoretical and experimental spectra. ARTEMIS runs through all the input data sets, FEFF generated paths, -and user input parameters. It also runs a number of sanity checks to avoid certain obvious situations which will result in an unsuccessful fit. Statistics, including errors and correlations also are calculated, as well as R-factor and an arbitrary but consistent and comparable "goodness of fit" value that can be compared between different attempted iterations and models. The iterative procedure can be controlled by tuning of the input parameters, number of iterations and the step size. Once the fit has been completed, the refined parameters are outputted along with statistical measures such as correlations between parameters, R-factor and Fit Index between the theoretical and experimental EXAFS spectra.

2.5 Error Analysis

After the best parameters of the included paths are found by using numerical methods based on the maths expressions, restraints, and starting values, they are summed and this theoretical spectrum is compared with experiment.

Information theory is used to correlate the amount of information in the original EXAFS spectrum to the information in Fourier transform spectrum as determined from the Nyquist criterion;

$$N_{ind} = \frac{2}{\pi}\Delta k \Delta R + 1$$

where N_{inp} is the number of independent points, Δk is the Fourier transformed data range (k-range) and ΔR is the window used in R-space for the EXAFS data analysis. In general a robust fitting model must use much fewer variables (N_{var}) than the defined N_{inp},

$$N_{var} \ll N_{ind}$$

Keeping the number of refined variables less than N_{inp} is recommended because the information contained within the EXAFS signal is not ideally packed. Throughout the analysis in this thesis this was consistently checked and ensured.

During the data fitting procedure performed by the program, the variable EXAFS parameters and mathematical variables are adjusted to arrive at a least-squares fit between the experimental and theoretical spectra. The fit results include the user defined variables, their best-fit values, and the calculated uncertainties and correlations of the variables. Along with this is also important information about the statistics of the model, including the number of independent points, N_{idp}, the number of variables N_{var}, the χ^2 (chi-square) and χ_v^2 (reduced-chi-square) values, and an *R*-factor[21]. The accuracy of the structural parameters in EXAFS has been discussed at length by Marius Vaarkamp[22].

The primary measure of the statistical goodness of a particular fit to the data is through the calculated value of chi-square;

$$\chi^2 = \sum_{i=min}^{max} \frac{1}{\sigma_i^2}[d_i - t(x_i)]^2$$

The primary measure of a goodness of a particular fit to the data is through the calculated value of chi-square; Where d_i is the experimental data, $t(x_i)$ is the data from the fit, σ_i is the estimated variance of the data, for each data point i. From this it can be seen that χ^2 depends on the square of the difference between the experimental data and the fit spectrum, at each point i in R-space. Artemis estimates the variance of the data (σ_i) based on the white-noise in the data. This estimate works well for very noisy data, but tends to underestimate the uncertainty in particularly good quality data, as it completely misses any non-stochastic components to the uncertainty. It should be noted that the isolated EXAFS signal is denoted as $\chi(k)$ and should not be confused with the goodness-of-fit chi-square parameter χ^2. A problem of this statistical measure is that for a good fit it should be approximately equal to 1, but the practice shows that for real samples it is usually between 10-100, due to unavoidable systematic errors introduced by the experimental setup and inherent errors in the measurement apparatus. Changes in the reduced chi-square parameter, χ_ν^2, are used to compare different EXAFS models. To compare models with different numbers of variables the χ_ν^2 values must be used, which are calculated by dividing χ^2 by the degrees of freedom in the fit, ν.

$$\chi_\nu^2 = \frac{\chi^2}{\nu}$$

$$\nu = N_{ind} - N_{var}$$

The R-factor is another value that should be considered as a measure of the closeness of the fit to the experimental data, and is defined as:

$$R = \frac{\sum_i [d_i - t(x_i)]}{\sum_i d_i}$$

A calculated value of $R \leq 0.05$ is generally considered a close fit.

During the fit procedure, the physical meaning of the parameters (as interpreted by the user), the size of their error bars and their correlations (as provided in the programs output) should all be considered. In terms of the reliability of the analysis methodology, the normalisation and background removal of the data is especially important and a lot of time is often devoted to ensuring this has been performed well. The fitting procedure must also be systematic; this includes the background removal, method of choosing E0, the order of varying parameters, k-window and weighting, and the fixing of various parameters whilst floating the others in the calculation. These factors must be carefully considered and kept consistent, both in the fitting methodology used, and between data sets that will be compared. The best result fits obtained in the exploration of various models based on the relevant reference spectra data was used to define the initial starting parameters for the fits.

Overall, the definitive accuracy of the structural parameters derived from the analysis of an EXAFS spectrum is still under debate due to the large number of sources for both systematic and statistical errors[22]. A general approach to the problems and errors that should be dealt with during measurements can be found in the book "X-ray Absorption" edited by Koningsberger and Prins[23] and were followed closely in the analysis of the data in this thesis. Many effects are also qualitatively unambiguous, such as large oxidation state changes (from change in E0 value and edge-jump height) and appearance/disappearance of absorption peaks which clearly correspond to expected neighbouring atomic shells. This information must also be considered and incorporated to the interpretation of the results. The final justification for a good EXAFS fit, beyond taking all these aforementioned factors and respecting the statistical information analysis, is ultimately reliant on the scientific intuition and knowledge of the system of the person performing the analysis.

2.6 *In situ* combined XAS/XRD studies

As stated, the low concentration and random distribution of the iron sites as well as the presence of multiple Fe species in the samples has made the characterisation of the active sites in both Fe-ZSM-5 and AlPO-5 very difficult. FeAlPOs can also catalyse the OBP reaction, although less research has been done on these systems. Therefore, Fe-ZSM-5 and Fe-AlPOs need to be compared, in terms of the structural development under the same reaction conditions using high resolution powder diffraction combined with X-ray absorption spectroscopy.

Using the *in-situ* XAS/XRD techniques applied to Fe samples almost simultaneously will provide a full structural characterisation of Fe catalytic materials, in particular the local structure of Fe located in the frame work and extra-framework and oxidation state by analysis of the pre-edge features and the EXAFS spectrum. The structural stability of the microporous material will be determined by XRD. Information from *in situ* catalytic studies and gas switching experiments will allow derivation of detailed information on the mechanistic aspects of the OBP reaction, and help to determine the full role played by the individual reactants.

2.7 Transmission Electron Microscopy (TEM)

TEM experiments were carried out to determine the size, shape and location of the dispersed particles. The samples were examined at the Catalysis Researh Centre at Harwell with an F20 Transmission Electron Microscope using a 200 kV Voltage and a C2 aperture at 30 and 50μm. Powder samples were suspended in ethanol, and placed on holey carbon coated Cu metal grids. Transmission electron microscopy is a commonly used technique that uses electrons transmitted through a sample to derive image data on microscopic level much greater than that of optical microscopes. The instrument utilises a tungsten filament as a source of electrons. Generally it consists of four main components; an electron optical column, a vacuum system, the necessary electronics (lens supplies for focusing and deflecting the beam and the high voltage generator for

the electron source), and control software. A modern TEM typically comprises an operating console surmounted by a vertical column and containing the vacuum system, and control panels conveniently placed for the operator. The microscope may be fully enclosed to reduce interference from environmental sources. The electron beam emerges from the electron gun, and passes through a thin specimen, transmitting electrons which are collected, focused, and projected onto the viewing device at the bottom of the column. The entire electron path from gun to camera must be under vacuum. The electrons can penetrate into the sample and reveal information such as crystal planes and morphology.

2.8 Scanning Electron Microscopy (SEM)

Scanning Electron Microscopy (SEM) images of the samples studied in this thesis were collected on a JEOL JSM-6301F (JEOL Ltd., Tokyo, Japan) with an INCA-sight detector (Oxford Instruments) at the Institute of Archaeology UCL. In a typical experiment, SEM images were collected from finely grounded powder samples which were sprinkled on circular aluminium stubs with double-sided sticky tape and then coated with a gold film. SEMs are primarily designed for surface imaging with extremely high spatial resolution by use of a scanning beam and displaying the signal from an electron detector. Bombardment of the sample surface with high energy electrons results in the formation of secondary electron emission from the sample and backscattered electrons. The scattering intensity is increased with atomic number due to regions of higher electron density. Regions with higher electron density across a sample appear brighter in backscattered electron images. In an SEM, many components such as the electron gun and lenses are similar to those of a transmission electron microscope. There are however a few important differences between a transmission electron microscope and a scanning electron microscope. Rather than the broad static beam used in TEM, the SEM uses an electron beam that is focused to a fine point and scans linearly over the sample surface in a rectangular raster pattern, resulting in a 3D image of the sample surface. The accelerating voltages are much lower than in TEM because it is no longer necessary to penetrate the specimen; in a SEM they range from 50 to 30 keV. In SEM the specimen need not be thin like TEM, greatly simplifying specimen preparation.

2.9 Visible Near-infrared Diffuse Reflectance Spectroscopy

The principles behind the technique of Visible Near-infrared Diffuse Reflectance Spectroscopy (VisNIR DRS) is based the measurement of diffusely reflected spectra from the sample after it has been exposed to visible and near-infrared radiation (350-2500nm). The spectrometer is comprised of an energy source, a dispersive element, which enables the intensity at different wavelengths to be recorded and a detector. With diffuse reflectance spectroscopy (DRS) the resulting spectrum does not produce a directly proportional relationship between wavelength intensity and analyte concentration. Corrections and statistical analysis therefore must be used to interpret the resulting data, which is beyond the scope of this thesis and this technique was used as a supplementary technique to confirm or deny the presence of framework and extra-framework iron as well as larger iron oxide nanoparticles. DRS is ideal for application to samples of rough light-diffusing surfaces. Particle size can influence VisNIR DRS's final spectra, and thus grinding and sieving of samples was performed in the experimental procedure.

References

1 J. Nucl. Med. Technol. *September 1,* 2004 *vol. 32 no. 3 139-147*

2 http://www.diamond.ac.uk/Home/Technology.html

3 P. P. Ewlald, *Fifty years of X-ray diffraction*. Utrecht: International Union of Crystallography (1962)

4 W. H. Bragg and W. L. Bragg, Proceedings of the Royal Society of London. Series A, Containing Papers of a Mathematical and Physical Character, Vol. 88, No. 605, 1913, 428-438

5 M. M. Woolfson, *Rep. Prog. Phys.* 1971, *34*, 369

6 M. G. Rossmann and E. Arnold. *International Tables for Crystallography,* 2006, Vol. B, ch. 2.3, 235-263

7 S. Xiang, C.W. Carter Jr., G. Bricogne, and C. J. Gilmore, *Acta Cryst.* 1993, D49, 193-212

8 A. Albinati and B. T. M. Willis. *International Tables for Crystallography,* 2006, Vol. C, ch. 8.6, 710-71

9 H. M. Reitveld, Acta Cryst. (1967). 22, 151-152

10 G. S. Pawley, J. Appl. Cryst. (1981). 14, 357-361

11 L. A. Grunes, *Phys. Rev. B, 27,* 2111 (1983)

12 Westre, T. E.; Kennepohl, P.; DeWitt, J. G.; Hedman, B.; Hodgson, K. O.; Solomon, E. I. J. Am. Chem. Soc. 1997, 119, 6297-6314

13 Laporte, O.; Meggers, W.F. (1925). "Some rules of spectral structure" (abstract). Journal of the Optical Society of America 11 (5)

14 Atkins, Peter; Paula, Julio de (2010) [1st. Pub. 1978]. "Chapter 13". Physical Chemistry. Oxford University Press. p. 494.

15 H. Ebert, V. Popescu, D. Ahlers, *Phys. Rev.* 1999, B 60, 7156

16 T. E. Westre, J. G. DeWitt, B. Hedman, K. O. Hodgson, E. I. Solomon, *J. Am. Chem. Soc.*, 119(27), 6297-6314, (1997)

17 Kau, L. S.; Spira-Solomon, D. J.; Penner-Hahn, J. E.; Hodgson, K. O.; Solomon, E. I. J. Am. Chem. Soc. 1987, 109, 6433-6442.]

18 M. Wilke, F. Farges, P. E. Petit, V. A. Sole, *J. Synchrotron Rad*. 8, 952-954 (2001)

19 B. K. Teo, EXAFS: *Baisic Principles and Data Analysis*, Berlin: Springer Publishing House (1986)

20 J Gurman, N Binsted and I Ross 1986, *J. Phys. C: Solid State Phys.* 19 1845.

21 Bevington PR, Robinson DK. Testing the fit. Data Reduction and Error Analysis for the Physical Sciences. 1992:194-8.

22 Vaarkamp, Marius. "Obtaining reliable structural parameters from EXAFS." Catalysis today 39.4 (1998): 271-279.

23 X-ray absorption. Edited by D. C. Koningsberger and R. Prins. Published by John Wiley and Sons, New York, 1988

Chapter 3

Characterization of thermal expansion behaviour in FeZSM-5 and FeAlPO-5; an *in-situ* XRD study.

3.1 Introduction

The zeolite samples prepared for study are formed as micron sized powders as opposed to large crystals. This makes high resolution powder diffraction the key characterisation method to be used for the elucidation of global crystallographic structure. Although good X-ray diffraction data of FeZSM-5 and FeAlPO-5 can be obtained using modern standard laboratory instruments; significant improvements in resolution, accuracy, signal-to-noise ratio and speed of data collection can be achieved by using synchrotron radiation sources.

The synchrotron beam line is equipped with detectors able to achieve a very high sampling rate and this combined with the high brilliance and coherence of the electromagnetic radiation, also allows one to follow phase changes, thermal expansion, sintering and other physic-chemical events as close to real time as possible, down to microsecond resolution, if the experiment is designed in such a way.

In order to create microporous materials, it is often necessary to use an organic templating agent. This is a molecule used to direct the structure formation during hydrothermal synthesis. This leads to the template molecule being are incorporated in the pores of the final hydrothermally crystallised product. The organic template can then be removed from the as-synthesized inorganic material. This is conventionally carried out by heating the material in air to temperatures around 550°C, a process commonly referred to as calcination. Other methods such as microwave irradiation[1] and decomposition using ozone[2] have also been developed as methods that remove the template but do not expose the framework to high temperatures for long periods that may destabilise it.

Although the majority of these systems are known to be stable after removing the organic template, some systems are found to lose their structural integrity upon calcination.[3] The choice of template has also been shown to influence the hydrothermal stability of the calcined product, as in the case for SAPO-34[4]. In order to produce viable and commercially useful catalysts, it is necessary to develop an understanding of the structural integrity of the material and examine what changes occur during the calcination process.

In this particular study, we chose to investigate the effects of increasing temperature on the microporous structures of the pre-calcined iron-substituted aluminosilicate FeZSM-5 and the aluminophosphate FeAlPO-5 in air. This was done in order to investigate structural changes occurring during the calcination/activation of the catalytic materials, as well as following any thermal expansion/contraction or phase transformations that may occur.

A property that has been previously observed to in many types of nanoporous materials is that they exhibit *negative thermal expansion* (NTE) during heating.[3,5-8] Most materials expand with temperature due to the effective increase in average inter-atomic distances within the material due to increased thermal vibrations upon heating. However, recently many materials have been found to contract with temperature, and are said to exhibit a *negative thermal expansion* coefficient. Many zeolites have been found to have this property and variable-temperature studies using neutron and X-ray powder diffraction, and microcrystal X-ray diffraction have shown that zeolites with the framework structures MWW, ITE, STT[5], MFI[22], AFI, DOH, MTN, DDR[6], ISV, STF,[7] IFR[8], and CHA[9], among others, all show NTE at various temperature ranges. As we shall see, we have shown that both FeZSM-5 and FeAlPO-5 also exhibit aspects of negative thermal expansion, albeit in very different ways.

The most popular hypothesis for the mechanism for NTE is based on the transverse thermal motion of oxygen in T-O-T linkages. If the M-O bonds are sufficiently strong, they will show negligible thermal expansion. The primary vibration of oxygen in such a strongly bonded unit will be perpendicular to a line joining the two metal atoms. As the temperature increases, the average displacement of oxygen atoms will increase. If the

average M-O-M angle is about 180°, this increased vibration will pull the T atoms together which can then shrink the entire lattice in appropriate structures.

One question that has been raised is how these motions are correlated over the entire lattice. This correlation can be readily treated by considering the TO_4, polyhedra as rigid bodies, as in the "Rigid Unit Mode" theory of NTE. In this model, linked polyhedra tilt back and forth to give the transverse thermal motion of oxygen and provides a good explanation of the observed NTE.[7,10]

In zeolites, a range of thermal expansion behaviour is present, depending on the framework structure and elemental composition of the material in question, with both positive and negative thermal expansion having being observed at various temperatures. From data currently available on seventeen microporous materials, it is clear that NTE should be considered the norm rather than the exception.

Evidence has pointed to positive thermal expansion being encouraged when the structure has a relatively high framework density and a one-dimensional channel system.[11] Substitution of framework T atoms with transition metals has also been reported to cause significant changes to the unit cell dimensions of many nanoporous materials.[12,13]

In this work, the primary aim is to determine the lattice expansion properties of FeZSM5. This experimental study intended to provide information on:

a) The flexibility and deformation of the microporous frameworks of FeMFI and FeAlPO-5 (contraction and expansion of unit cell).
b) The thermal stability of the framework structure at high temperatures
   Does the framework exhibit enough flexibility in the to accommodate large carbonaceous material formation during catalysis.

Information derived from the *in situ* XRD study can then be related to findings from XAS analysis of the same compounds and deduce weather changes occurring to the local Fe environment have an effect on changes in the bulk crystalline microporous

structure of the material. This is important in understanding the thermal activation of such catalysts.

3.2 Sample Preparation

FeZSM-5 with Si/Fe ratio of 1:33 was prepared via an isomorphous substitution method via hydrothermal synthesis. FeAlPO-5 was synthesised with an Fe content of 4wt%.

In the typical synthesis of FeZSM-5, water was first acidified with H_2SO_4 until reaching a pH below 1. To this solution the appropriate amount of $Fe(SO_4)_3.7H_2O$ was then added and stirred until fully dissolved, leaving a deep red solution. Alongside this, sodium silicate as $NaSiO_3.9H_2O$ was dissolved in water. The sodium silicate solution was then very slowly added drop wise, to the acidified iron solution with vigorous stirring. The organic structure directing template TPAOH (tetrapropylammonium hydroxide) was then added and the solution was stirred until homogenous (~ 2 hours), the composition of the final gel being $3SiO_2:0.015Fe_2O_3:25TPAOH:230H_2O$ The resulting gel was then placed in a Teflon lined autoclave and heated to 165°C for 4 hours. Following this the crystallised product was then filtered, washed with distilled water and dried overnight, resulting in a fine tan coloured powder.

FeAlPO-5 was synthesised with a nominal Fe content of 4 wt%. Aluminium hydroxide hydrate ($Al(OH)_3.xH_2O$) was first dissolved in a solution of phosphoric acid (H_3PO_4, 85%) with deionised water in a polypropylene beaker. An aqueous solution of iron acetate ($Fe(CH_3COO)_2.4H_2O$) was then dissolved in a minimum amount of water and added drop wise to the solution mixture under stirring. After stirring of the gel for two hours, tetraethyl ammonium hydroxide ($(C_2H_5)_4NOH$) was then added slowly to the solution and stirred for a further 4 hours. The final gel composition was $0.94.Al_2O_3:0.8P_2O_5:0.04Fe_2O_3:0.75TEAOH:30.8;H_2O$. A Teflon liner was then filled with the gel to 50% of the total volume and was placed in a stainless steel autoclave and heated under autogenous pressure at 165°C, for 4.5 hours. After cooling, the product was recovered by filtration and washed several times with deionized water until a neutral pH was obtained from the washing solution. This was then dried at 120°C for 12 hours, followed by subsequent calcination in air for 5 hours at 550 °C resulting in a fine white powder product. To confirm the successful synthesis, the product was

initially examined by X-ray diffraction (XRD) measurements which were performed on a Bruker-D4 diffractometer, using Cu K-α radiation at room temperature. The diffraction patterns were measured using a position sensitive detector in a 2θ range of 5 - 55° and steps of 0.02°. The powders were densely packed onto a flat-plate sample holder. The characteristic MFI (FeZSM-5) and AFI/CHA structures (FeAlPO-5/FeSAPO-34 respectively) were clearly evident in the collected diffraction pattern, and the products were found to be phase pure.

3.3 In situ *High Resolution Powder Diffraction (HRPD)*

The high resolution powder diffraction data were collected at synchrotron X-Ray powder diffraction beamline (I11) at the Diamond Light Source. The advanced design, novel detector system and ease of wavelength scanning available on Beamline I11 make it the instrument of choice for such studies (Figure 3.1). The collection of high quality powder patterns at fast rates (microsecond – millisecond per pattern) is not usually possible using conventional detector systems. However, with the combined effect of the fast position sensitive detector (PSD) and the inherent high flux of synchrotron radiation, *in situ* studies of zeolites are possible, yielding temporally-dependent structural information with high resolution.

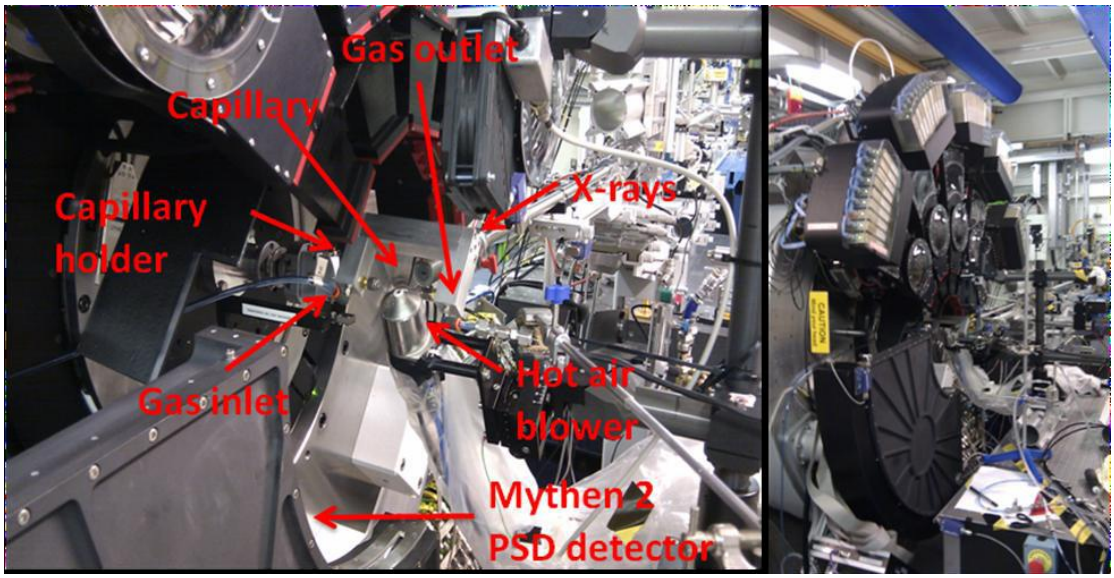

Figure 3.1. *HRPD set-up used at beamline I11 during the in situ calcination of the catalysts FeZSM-5 and FeAlPO-5 from 30-700 °C under flow of air.*

The wavelength was determined to be 0.826018 Å (a wavelength of choice, as this is well above the Fe K-edge absorption as well as that provides the highest flux) by measuring and refining a NIST silicon standard. The sample was loaded into a 0.5mm sapphire capillary and mounted onto the reactor. Once the beam was aligned and preliminary scans had been obtained to ensure correct calibration, diffraction patterns were collected using the

PSD every 12 s, as the temperature was increased using a hot air blower placed directly below the sample.

The temperature was ramped up to 550°C in air (ramp rate = 0.16 °C s^{-1}) to calcine the sample. It was held here for one hour in order to check thermal stability of the structure at this temperature (data were collected throughout this time). The sample was then ramped to 700°C using the same ramp rate, and heated for one hour at that temperature under a H_2O/He mixture (5 ml min-1 flow rate with the bubbler at room temperature, resulting in an estimated partial pressure of water of around 2.34 kPa[14]). This was achieved by bubbling helium gas through water, and passing that on to the reactor, and is a common method of activation, particularly for the FeZSM-5 type catalysts[15].

Pulsed experiments were then carried out in order to assess any changes in structure due to introduction of reactants (alternation of benzene and N_2O, with He as carrier gas). The original experimental plan was to also assess the catalytic mechanism *via* the determination of products produced during the reaction using a mass spectrometer, but after trying two different mass spectrometers, both seemed to be faulty and gave clearly anomalous results). While the mass spectroscopy component of the experiment cannot be used, the XRD data collected during the catalysis was analysed to understand the structural changes occurring.

All the XRD data analysis was performed using TOPAS 4 XRD analysis software which is capable of analysing multiple-data sets. TOPAS can be used with a graphical user interface for single data files analysis, or can be run via a command line interface. Scripts (.bat files) were written to automatically process the large number of XRD scans collected during the experiment. The Pawley fitting method[16] was used to determine the change in lattice parameters and unit cell volumes. The Pawley method is also the best suited for the purposes of extracting lattice parameters from a known starting symmetry as in this investigation.

3.4 Results and Discussion

3.4.1 FeZSM-5

Figure 3.2 below shows the XRD patterns collected at various temperatures for the examined sample of FeZSM-5. The sample seems phase pure and displays the typical diffraction pattern of the MFI framework. No indications for the formation of any large particle or bulk iron oxide phase were observable. XRD shows an increase in intensity for the low angle peaks between 2θ = 6–10° – this can likely be related to the occupancy change as the template molecules are removed from the microporous voids of the zeolite framework.

The purely silicaceous FeZSM-5 has MFI framework structure with an orthorhombic unit cell.[17] The synthesised material was phase pure, with high crystallinity, and could be indexed to the space group *Pnma*. Although no other phases could be determined from the XRD, there is the possibility that a highly dispersed nanoclusters of FeOx may be present in small amounts. Figure 3.3 shows the calculated lattice parameters *a* (a) and *b* (b) and *c* (c) and the calculated unit cell volume (d) for the temperature range of 30-700°C, calculated using the Pawley fitting method[18]. Some selected parameters are shown in Table 3.1.

The XRD fitting results were obtained with calculated errors of less than 0.01 Å for the individual unit cell dimensions. The reliability of the data fits is indicated by the calculated values of the R-weighted pattern factor (R_{wp}), given by:

$$R_{wp} = \sqrt{\frac{\sum w_m \left(Y_{o,m} - Y_{c,m}\right)^2}{\sum w_m Y_{o,m}^2}}$$

where $Y_{o,m}$ and $Y_{c,m}$ are the observed and calculated data respectively at point *m*, and w_m, the weighting given to data point m which for counting statistics is given by,

$w_m = 1/\sigma(Y_{o,m})^2$ where $\sigma(Y_{o,m})$ is the error in $Y_{o,m}$.

a)

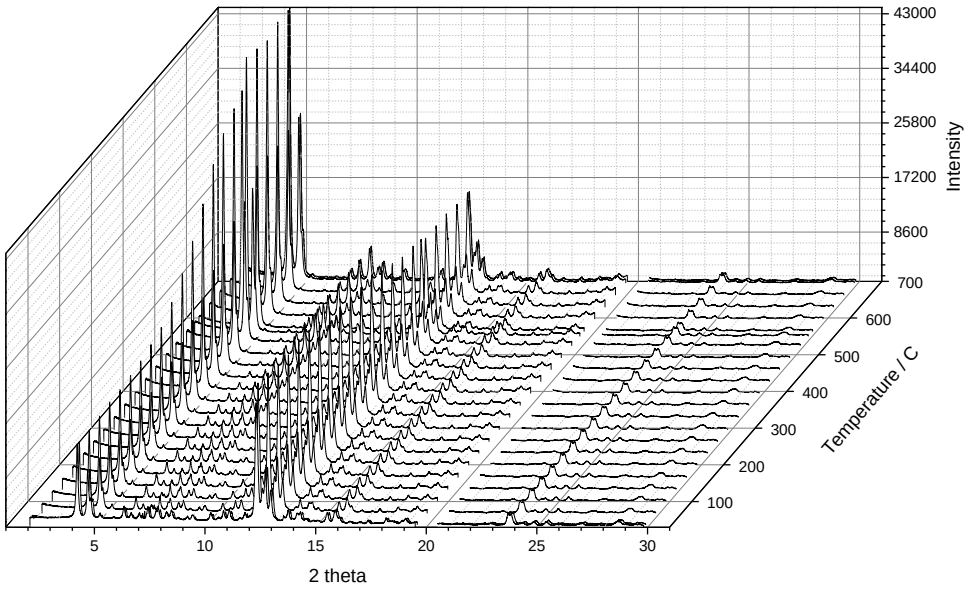

b)

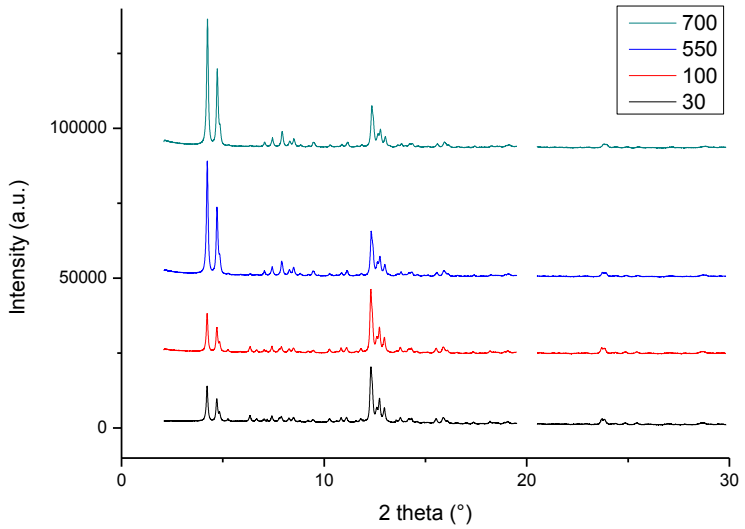

Figure 3.2*. a) Waterfall plot of XRD patterns collected in-situ; b) Selected XRD patterns collected for FeZSM-5 (temperatures in degrees Celsius). The gap occurring in the patterns at around 2θ = 20° is due to subsequent removal of a reflection caused by the quartz capillary tube used to mount the sample.*

The goodness of fit (*GOF*) was also used as an indicator of reliability, and is given by

$$GOF = \frac{R_{wp}}{R_{\exp}} = \sqrt{\frac{\sum w_m \left(Y_{o,m} - Y_{c,m}\right)^2}{\sum M - P}}$$

where M is the number of data points, and P the number of parameters used in the calculation. For the data obtained in these experiments R_{wp} ~ 2.8-4.3 and *GOF* ~1.5-2 indicating very good fits obtained between the calculated and observed diffraction patterns for both samples. The results of the Pawley fit for each scan were calculated with calculated errors of less than ±0.01 Å for cell volume and ±0.006 Å for the individual cell parameters *a, b,* and *c*.

Table 3.1. *Parameters from XRD analysis of FeZSM-5*

T / °C	R_{wp} overall	GOF	Cell Vol/ Å^3	a/ Å	b/ Å	c/ Å
30	2.894	1.383	5395.11	20.084	19.999	13.432
100	3.350	1.462	5397.05	20.089	19.997	13.435
300	3.293	1.447	5403.79	20.097	20.003	13.442
550	4.146	1.951	5369.80	20.055	19.956	13.417
700	4.216	1.995	5350.82	20.026	19.934	13.404

a)

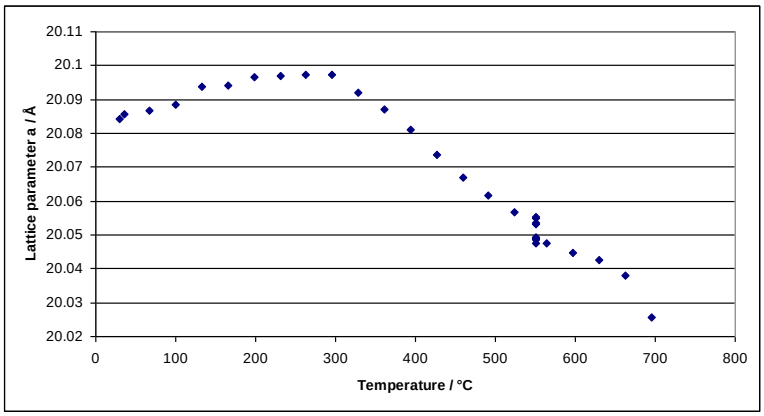

b)

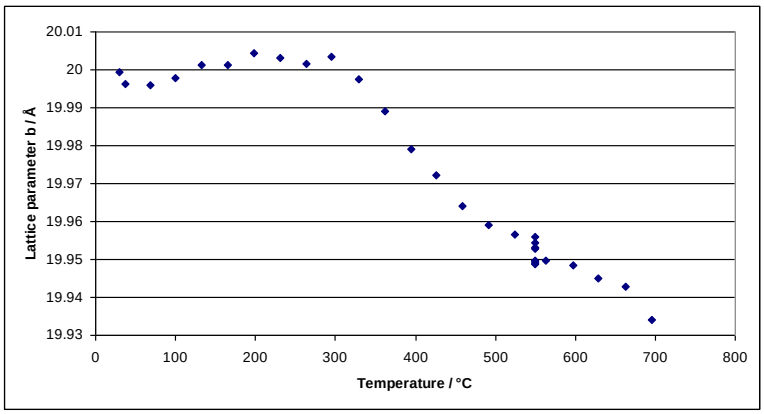

c)

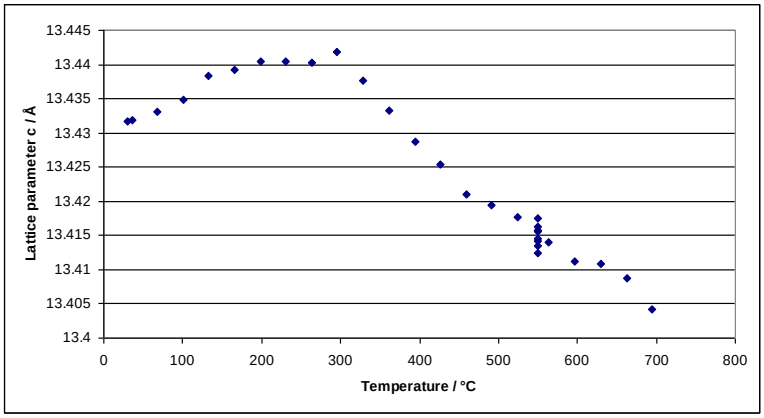

d)

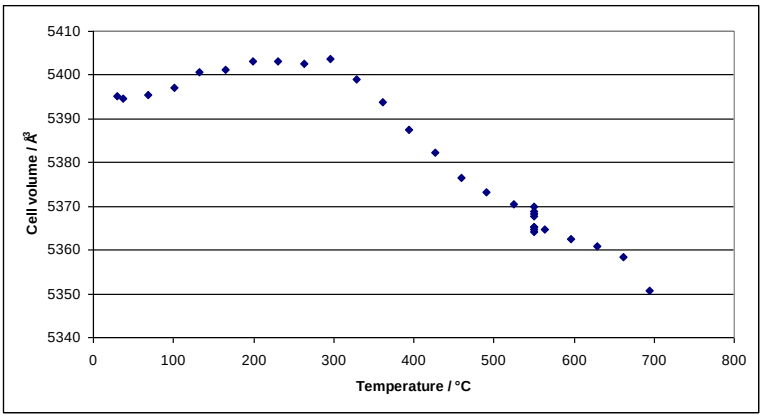

Figure 3.3 *Plots of lattice parameters a (a), b (b), and c (c) and cell volume (d) versus*

temperature for FeZSM-5 during calcination in air. The results of the Pawley fit for each scan were calculated with calculated errors of less than ±0.01 Å for cell volumes and ±0.006 Å for the individual cell parameters a, b, and c.

As seen from values in Table 3.1 and Figure 3.3, the calculated expansion and contraction of the unit cell FeZSM-5 is similar for all axes. The change ion unit cell parameter behaviour can be groups into two broad temperature range windows. The first is characterised by an initial small positive thermal expansion from 30-300°C. At 300°C this expansion is followed by a sudden change in the behaviour of the system with an inflexion point in the plot is seen at this temperature whereby the positive thermal expansion changes to strong linear negative thermal expansion - apparent for all crystallographic axes up to at least the maximum temperature investigated of 700°C. The calculated unit cell volume for the sample agrees with the changes in individual crystallographic axes. The negative thermal expansion from 300-700°C is much greater for parameters *a* and *b* (~ 0.07 Å) compared with the contraction of *c* (~ 0.04 Å). This inflexion point may correlate with the combustion of the organic template molecule used during synthesis, occurring at around 300-350°C.[19] The presence of occluded organic template molecules can prevent the framework structure from relaxing and contracting. Upon their calcination and combustion of the organic template, the microporous channels become void, and thus the framework is able to relax and in many cases contract. A possible method to help confirm this would be to perform a thermogravimetric analysis (TGA) of the samples. The thermal behaviour of as-synthesised MFI framework structures during calcination was extensively studied in the past.[20,21,22] These studies confirm our findings whereby the structure contracts at temperatures above 300°C. The temperature interval where the contraction occurs in these studies also coincides with the template removal and furthermore, the unit cell of the calcined framework is smaller than the as-synthesized one. Gulatieri et al.[23] calculated cell parameters of TPA-silicalite-1 studied during calcination. They determined that the template decomposition is accompanied by a large contraction of the unit cell and that the rate of change of unit cell dimensions during template removal are not affected significantly by the heating rate. Consequently, the rate of contraction is approximately proportional to the heating rate, which corroborates with the nearly linear rate of NTE observed from 300-700°C for all axes.

A similar study on the thermal expansion of siliceous FeMFI was carried out by Bhange et al.[24] with different samples containing varying amounts of isomorphously substituted Fe (Si/Fe = 50, 75, 100 and ∞). All the (pre-calcined) samples they studied were shown to exhibit NTE behaviour in the temperature range 100 – 500°C. They also found that the magnitude of the thermal expansion coefficient depends strongly on the amount of Fe in the sample, and the presence of more Fe ions, leads to a greater change in unit cell dimensions upon heating It was concluded that by changing the composition of the framework of MFI, enhanced negative thermal expansion could be obtained – this would be an interesting topic for further research, particularly using synchrotron techniques. Although we do see NTE behaviour in the as-synthesised FeMFI sample studied in this work, its onset does not occur until around 300°C compared to 100°C seen by Bhange *et al*[12]. This is likely to be because of the organic template molecules which are still occluded in the sample are preventing the contraction in the framework from occurring at lower temperatures. The template molecules sterically hinder the lattice contraction, and may also retard certain vibrational modes that would have been established had the pores been void. In turn this explains the discrepancy between the negative thermal expansion onset in our results and those reported in analogous studies on AFI and MFI pre-calcined samples.[9,22-24] Qualitatively their results generally agree very well with ours over the temperature range studied, although the positive expansion at temperatures below 300°C is not apparent in their results except a slight increase in the *c* axis. This agrees with our hypothesis that the presence of templating molecule in the framework may prevent the system from expanding/contracting in a particular way, until it is removed. This data also emphasises the importance of guest molecule interactions with the framework structure in the synthesis, activation, and operation of such microporous catalysts, and the information that can be gained from such in-situ XRD investigations. The calculated thermal expansion coefficients for the expansion period between various temperature points is presented in Table 3.2.

Table 3.2 *The calculated thermal expansion coefficients between various temperature points.*

Temperature /°C	α_a **/ Å**	α_b **/ Å**	α_c **/ Å**	α_v **/ Å^{-3}**
30-300	2.40×10^{-6}	7.41×10^{-7}	2.76×10^{-6}	5.96×10^{-6}
300-660	-9.81×10^{-6}	-9.58×10^{-6}	-7.85×10^{-6}	-2.72×10^{-5}

The framework changes induced by thermal effects, and the history, composition and preparation method can all have an effect on the state of MFI type materials, and the behaviour is complex. Other interesting thermal changes that been observed in MFI structures, include that structure has been found exhibit orthorhombic symmetry (space group *Pnma* as identified in this study) up to high temperatures, but a phase transition to the monoclinic space group *P21/n* occurs on cooling below a transition temperature which which occurs between 27-77°C[25]. This transition was also observed by Olson et al.[26] who measured the variation of the cell parameters with temperature, using high resolution XRD and obtained a continuous decrease of the monoclinic angle, approaching 90° at high temperatures, with no well-defined transition point.

The thermal behaviour of Silicalite-1 (MFI) was first studied with XRD by Park et al.[27] who measured the thermal expansion coefficients of the zeolite and obtained a small volume-expansion rate below, and a cell contraction above, the monoclinic–orthorhombic transition temperature, which they located at about 150°C, much lower than the inflexion point observed in this work. Others have performed computational work which has revealed even more disparity in the matter with reports from groups whose calculations deny the phase change is thermodynamically plausible[28]. Overall the symmetry group and thermal transitions of MFI structures are clearly complex and there is still much debate over the particular effects. However no change in symmetry group was indicated by the Pawley fitting results and XRD analysis in this work, and all errors obtained in the fit results were small (less than ±0.01 Å for calculated unit cell volumes and ±0.006 Å for the individual unit cell parameters a, b, and c) and did not dramatically change at any point in the heating ramp. The XRD pattern was not

measured again after cooling to see if a symmetry change did occur on ramping down but can be an avenue for further investigations in the future.

During the experiment the sample was also held at 550°C under steam at for 1 hour, under flow of He/H_2O through use of a bubbler apparatus at the gas inlet. During this time no significant changes were observed for the XRD pattern after this treatment, indicating that the structure is stable under these activation conditions, and any changes activating the catalyst must be localised on the Fe sites throughout the sample, as opposed to any overall change in the Si-O framework structure. It also indicated that even though Fe ions are known to be removed from the framework during these types of harsh activation conditions[29] the disruption to the crystallinity of the system is not enough to be observed, as it remains largely intact. No phase separation or formation of FeO_x particles is observed in the samples studied in this investigation either, corroborating with the likely formation of isolated or very highly dispersed Fe ions in the zeolite framework, and no evidence of large bulk iron oxide being formed. TEM images of the FeZSM-5 sample used in this study were also recorded and are shown in Figure 3.4.

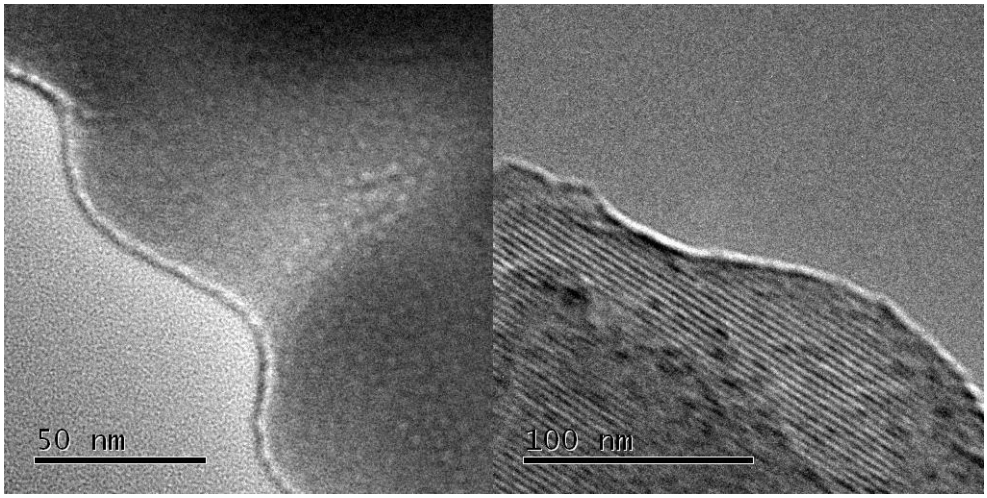

Figure 3.4 *TEM image of the calcined FeZSM-5 sample. Spots on the order of 5Å – similar to large pores of MFI are visible in the left hand side image. Terraces formed by the framework structure along the pore openings, lying perpendicular to the pore*

channels shown on the right. Differing contrast on the crystal surface in the image is related to the thickness of the crystal.

3.4.2 FeAlPO-5

Figure 3.3 shows the XRD patterns collected at various temperatures for FeAlPO-5. The sample seems phase pure and displays the typical diffraction pattern of the AFI framework structure. No indications for the formation of any iron oxide or dense $FePO_4$ or $AlPO_4$ phase were observed throughout the activation study.

The XRD analysis shows increase in intensity for the low angle peaks between $2\theta = 6–10°$ – this can likely be related to the occupancy change as the template molecules are removed from the microporous voids. The data plots in Figure 3.4 show significantly different behaviour for crystallographic axes *a* and *c* over the temperature range studied. Lattice parameter *a* shows a large overall steady expansion over the low temperature range between 30-400°C of around 0.11 Å. Above 400°C, we begin to see a decrease in the expansion, and eventual contraction of parameter *a*, up to 700°C. This contraction is much less dramatic than the earlier expansion at lower temperatures (0.01 Å). Lattice parameter *c* shows startlingly different behaviour to that of the *a* parameter upon heating in air. As shown in Figure 12, there is an initial strong contraction of the unit cell dimensions along the *c* axis from room temperature to around 100°C. This unexpected feature may however be due to the loss of water (possibly from the large 12-ring channels that run parallel with the c axis – see Figure 3.6) from the as synthesised sample, which is almost certainly present in the pores of the material. It is interesting to note that a slight positive thermal expansion is then apparent, followed by a very large increase in the thermal expansion coefficient at temperatures above *ca.* 300°C, where the value of *c* increases dramatically from 8.406Å to a maximum of 8.432Å at 500°C. This change may be due to loss of the template molecule during calcination, freeing the pores and allowing the framework to expand to a more relaxed state, and also allowing different vibrational modes to dominate the system.

a)

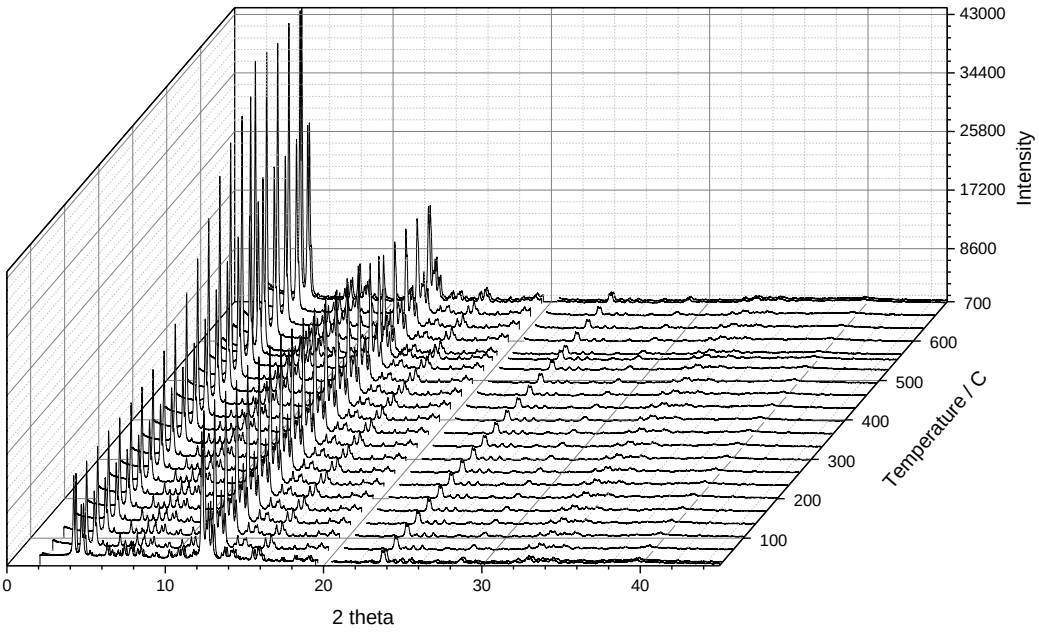

b)

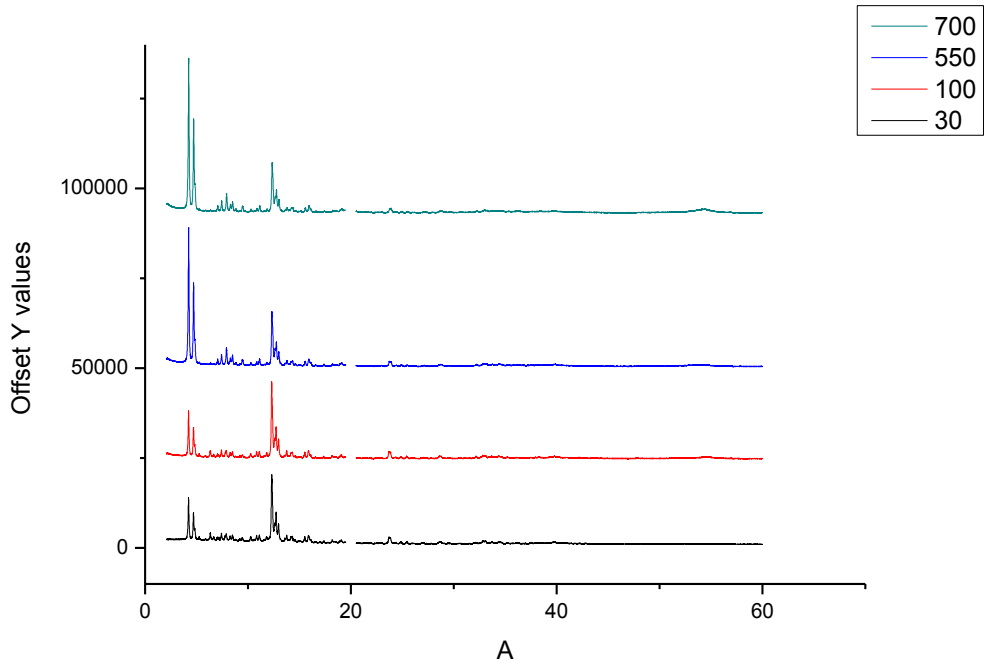

Figure 3.5 *a) Waterfall plot of XRD patterns collected in-situ; b) Selected XRD patterns collected at various temperatures (in degrees Celsius) during the activation of FeAlPO-5. The gap occurring in the patterns at around 2θ = 20° is due to subsequent removal of a reflection caused by the quartz capillary tube used to mount the sample.*

Figure 3.6 shows the calculated cell volume (a), and lattice parameters a (b) and c (c), for the temperature range investigated (30-700°C), calculated via Pawley fitting using

TOPAS 4.2. There was no need to calculate parameter *b* as it is equivalent to parameter *a* as FeAlPO-5, has AFI framework structure with a hexagonal unit cell (see Figure 3.5). The synthesised materials are phase pure, with high crystallinity, and could be indexed to the space group *P6/mcc*. The results were calculated with errors of less than ±0.01 Å for cell volume and ±0.006 Å for the individual cell parameters *a* and *c*.

Table 3.3. *Parameters from XRD analysis of FeAlPO-5*

T/°C	**R_{wp} overall**	**GOF**	**Cell vol. /Å^3**	***a*/Å**	***c*/Å**
50	7.918	3.725	1366.82	13.689	8.423
120	7.846	3.751	1367.59	13.711	8.400
300	7.777	3.806	1385.52	13.790	8.413
550	6.960	3.545	1389.71	13.797	8.430
640	6.504	3.365	1388.45	13.792	8.428

a)

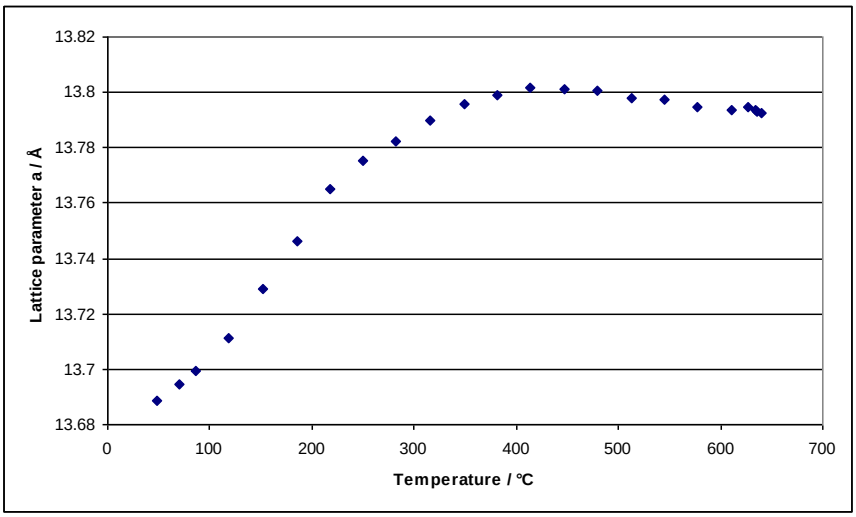

b)

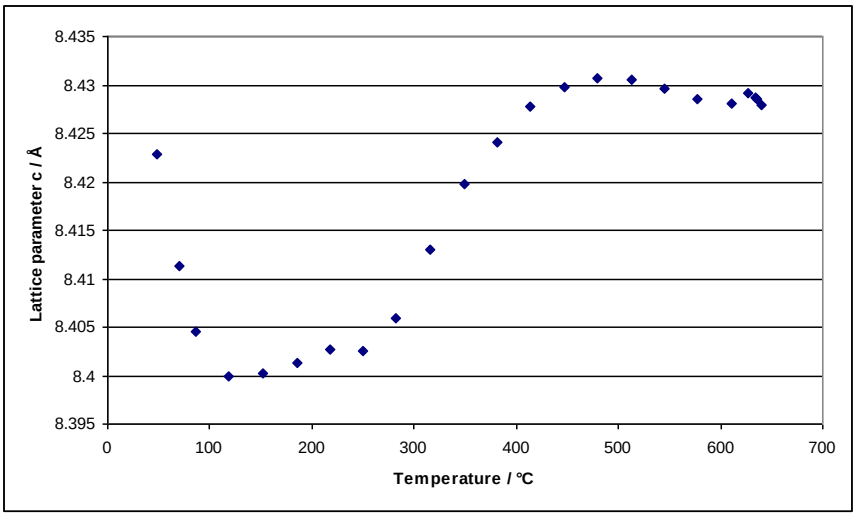

c)

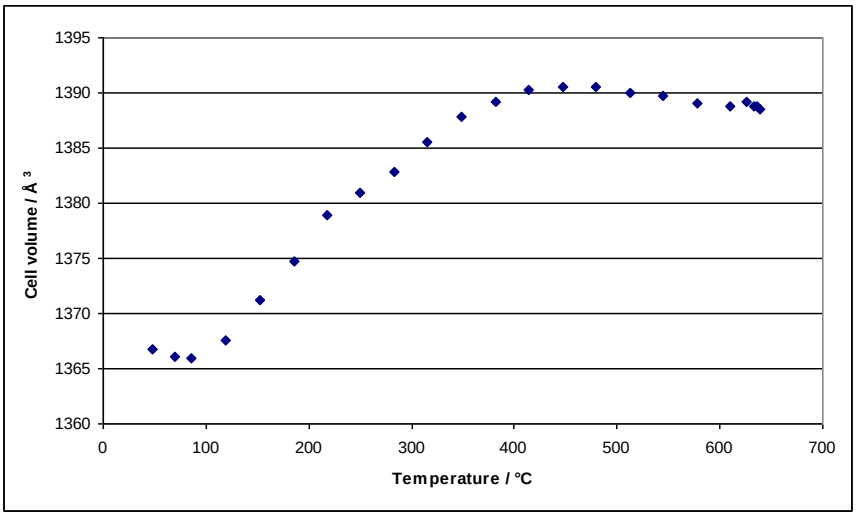

Figure 3.6. *Plots of lattice parameters a(a), c(b), and cell volume (c) versus temperature for FeAlPO-5. The results of the Pawley fit for each scan were calculated with calculated errors of less than ±0.01 Å for cell volumes and ±0.006 Å for the individual cell parameters a and c.*

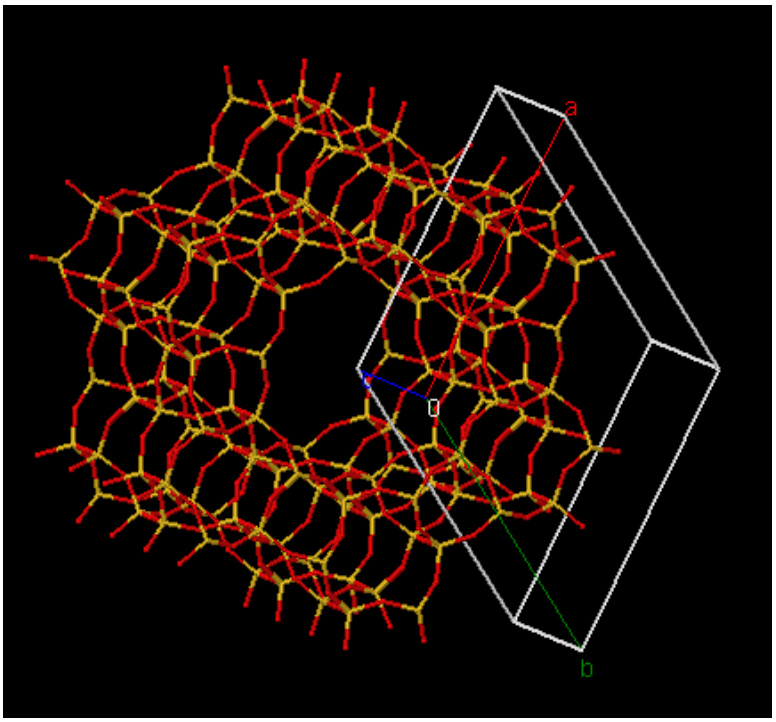

Figure 3.7*. Diagram showing the AFI structure of FeAlPO-5. Al and P are shown in yellow and connecting O atoms in red. The unit cell is also illustrated, along with axes a (red), b (green) and c (blue).*[9]

From 470-700°C we see a change from positive to negative thermal expansion, although this is less dramatic than the steep gradients observed for the earlier negative expansion at temperatures below 100°C. Figure 3.7. is a diagram showing the non-interconnecting one-dimensional channels found in the AFI structure running parallel to the *c*-axis. The calculated unit cell volume corroborates with the changes in unit cell dimensions. The large differences in these four distinct temperature regions indicate that the processes occurring are substantially more complex compared to the results obtained for the FeZSM-5 sample. The calculated thermal expansion coefficients for the expansion period between various temperature points is presented in Table 3.4.

Table 3.4 *The calculated thermal expansion coefficients for the expansion period between various temperature points.*

Temperature /°C	α_a **/ Å**	α_c **/ Å**	α_v **/ Å^3**
30-120	2.40×10^{-6}	2.76×10^{-6}	5.96×10^{-6}
120-550	-9.81×10^{-6}	-7.85×10^{-6}	-2.72×10^{-5}
550-640	-9.81×10^{-6}	-7.85×10^{-6}	-2.72×10^{-5}

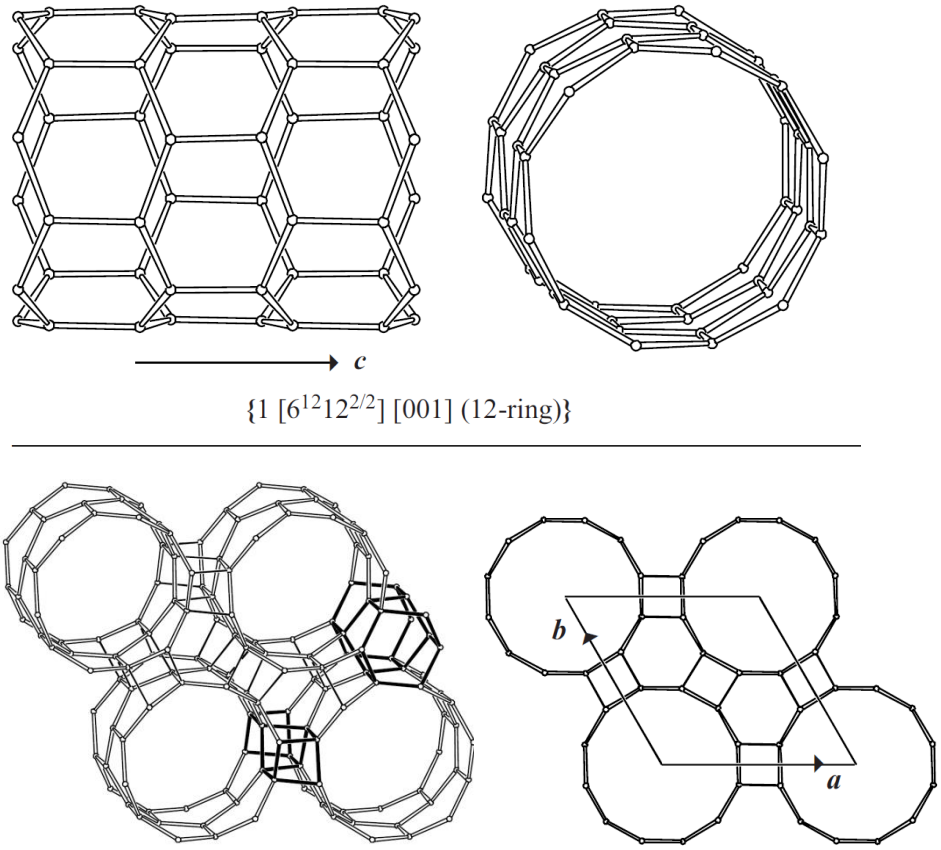

Figure 3.6 *a) Diagram showing the non-interconnecting one-dimensional channels found in the AFI structure running parallel to the c-axis. Channel shown perpendicular to c axis (left) and along c axis (right). b) Connection mode and unit cell content in AFI*

along c in perspective view (left) and in parallel projection (right) along with unit cell axes a and b.[30]

3.5 Conclusions

The above results only cover the calcination and activation stages of the experiment. A full analysis of the diffraction data collected during the pulsed experiments will be performed to understand the effects of catalysis on the structure.

Thermogravimetric analysis (TGA) would be useful to determine degradation temperatures of the template molecule, and the loss of absorbed moisture content of both FeZSM-5 and FeAlPO-5. With these results a better interpretation of the thermal expansion behaviour of these materials should be possible.

With the limited structural information available so far, it cannot be said whether the mechanism driving NTE in FeAlPO-5 has a static or dynamic origin. A likely explanation for these transformations is a theory based on rigid unit modes or RUMS.[7,31,32] This theory describes a model for framework silicates in which the SiO_4 and AlO_4 tetrahedra are treated as perfectly rigid units, but joined via flexible bonds able to rotate, about the shared bridging T-O-T oxygen atoms. From this model it has been possible to identify low-energy vibrational modes and configurations of distortion in the structure - called rigid unit modes. This allows for a rationalisation of the observed NTE behaviour - for example, the model allows the tetrahedra to rotate away from their ideal orientations forming strained T-O-T bond angles without any significant first-order distortions of the fundamental rigid tetrahedral units. This has been proposed as a reason for why some silicates have small or negative thermal expansion, and why the volume (and hence Si-O bond lengths) of some silicates appear to depend on the size of a constituent cation which occupies a large cavity site, as well as the distortion caused by the incorporation of host molecules[24]. The fact that these kinds of transverse atomic vibrational modes are often directed along a certain crystal axis which fits well for the behaviour observed in FeAlO-5 in this study whereby the negative thermal expansion due to water loss occurring below 150°C was almost entirely directed along the c axis which runs parallel with the large 12-ring channels of

the microporous AFI framework. It is also worth noting however that alternatively Tao and Sleight[33] proposed that the presence of RUMs is not necessary to explain the phenomenon of NTE observed in zeolites, but that charge compensating extra-framework cations can add additional stress due to their size, coordination or charge, and thus cause changes to the internal T–O–T angles of the bridging oxygen joints. In this case the changes in the structure are then controlled by a self-regulating mechanism which depends solely on the effects of the topological geometry and inherent symmetry properties of the three-dimensional domains underlying the frameworks. The effect of having Fe isomorphously substituted into the microporous materials studied here is also expected to have a large effect on the structure, particularly its stablility, vibrational modes, and surface acidity

Another useful investigation that may shed light on the energetic viability of such mechanisms and complement the findings of the work in this XRD study would be computational simulations of the materials throughout the temperature range studied experimentally. For example GULP is a program for performing a variety of types of simulations on materials using boundary conditions of 0-D (molecules and clusters), 1-D (polymers), 2-D (surfaces, slabs and grain boundaries), or 3-D (periodic solids).[34] The focus of the code is on analytical solutions, through the use of lattice dynamics and force field potentials. Many groups have recently used simulations in the study of zeolites and aluminophosphates including *ab initio* calculations regarding negative thermal expansion on AlPO-5[35] and DFT studies on the loss of water from the framework in SAPOs[36] showing important relationships between structure and composition with and the interaction of water with structurally different microporous solid frameworks. The data from the in situ XRD experiments in this thesis will assist in corroborating such findings and help further greater understanding these materials. The importance of understanding the behaviour of these materials at high temperatures, and in activation conditions is crucial in developing industrially viable, efficient catalytic processes by rationalising the catalysts intrinsic structure and function relationships.

References

1 He, J., Yang, X., Evans, D.G. Duan, X., (2003) 77(1), pp.270-275.

2 Heng, S., Lau, P.P.S., Yeung, K.L., Djafer, M. Schrotter, J.C.,, (2004), 243(1), pp.69-78.

3 G. Sankar, J. K. Wyles and C. R. A. Catlow, *Topics in Catalysis* (2003), *24*, 173-184

4 Briend, M., Vomscheid, R., Peltre, M.J., Man, P.P. and Barthomeuf, D., *The Journal of Physical Chemistry*, (1995) 99(20), pp.8270-8276.

5 D. A. Woodcock; P. Lightfoot; L. A. Villaescusa.; M. Y. Diaz-Cabanas; M. A. Camblor.. *Journal of Materials Chemistry*. (1999), *9*, 349.

6 S. H. Park.; R. W. G. Kunstleve; H. Graetsch; H. Gies, *Progress in Zeolites and Microporous Materials, Part A-C* (1997), *105*, 1989.

7 P. Lightfoot; D. A. Woodcock.; M. J. Maple; L. A. Villaescusa; P. A. Wright, *Journal of Materials Chemistry*. *(*2001), *11*, 212.

8 D. A. Woodcock; P. Lightfoot; L. A. Villaescusa.; M. Y. Diaz-Cabanas; M. A. Camblor.; D. Engberg, *Chemical Materials* (1999), 11, 2508.

9 M.M. Martı´nez-Inesta,; R. F. Lobo; *Journal of Physical Chemistry B* (2005), *109*, 9389

10 A. K. A. Pryde , K. D. Hammonds, M. T. Dove, V. Heine, J. D. Gale, M. C. Warren, *Phase Transitions*. (1997),61:141.

11 A. W. Sleight, *Current Opinion in Solid State & Materials Science* (1998) 3, 128

12 Jhung, S.H., Chang, J.S., Hwang, Y.K., Grenèche, J.M., Férey, G. and Cheetham, A.K., (2005) *The Journal of Physical Chemistry B*, 109(2), pp.845-850.

13 http://pubs.rsc.org/en/content/articlepdf/2015/fd/c4fd00179f

14 David R. Lide, ed. (2005). *CRC Handbook of Chemistry and Physics.* Boca Raton, Florida: CRC Press. p. 6-8

15 Zhu, Q., Van Teeffelen, R.M., Van Santen, R.A. and Hensen, E.J.M., (2004). *Journal of Catalysis*, 221(2), pp.575-583.

16 G. S. Pawley, *Journal of Applied Crystallography* (1981). 14, 357-361

17 http://izasc.ethz.ch/fmi/xsl/IZA-SC/Atlas_pdf/MFI.pdf - *accessed 15/05/2015*

18 G. S. Pawley, *Journal of Applied Crystallography*, 14, 1981, 357-361

19 F. Bérubé, S. Kaliaguine, J. *Microporous and Mesoporous Materials*, (2008), *115:3*, 469–479

20 E.R. Geus, H. van Bekkum, *Zeolites* 15 (1992)

21 M. Milanesio, G. Artioli, A.F. Gualtieri, L. Palin, C. Lamberti, *Journal Of the American Chemical Society*, 125 (2004) 14549

22 J. Dong, Y.S. Lin, M.Z.-C. Hu, R.A. Peascoe, E.A. Payzant, *Microporous and Mesoporous Materials* 34 (2000) 241.

23 M. L. Gualtieri, A. F. Gualtieri, J. Hedlund, *Microporous and Mesoporous Materials* 89 (2006) 1–8

24 D.S. Bhange, V. Ramaswamy, *Materials Research Bulletin,* (2006), *41*, 1392–1402

25 C. A. Fyfe, G. J. Kennedy, G. T. Kokotailo, J. R. Leyrla and W. W.Flemming, *J. Chem. Soc., Chem. Commun.,* (1985), 740.],

26 D. H. Olson, G. T. Kokotailo, S. L. Lawton, and W. M. Meier, *The Journal of Physical Chemistry (1981)* 85 (15), 2238-2243

27 S. H. Park, R.-W. Große, H. Graetsch and H. Gies, in Progress in Zeolite and Microporous Materials, ed. H. Chon, S.-K. Ihm and Y. S. Uh, *Studies in Surfice Science and Catalysis*, (1997), 105, 1989.]

28 P. Demontis, S. Suffriti, J. Chem. Soc., *Faraday Transactions*., (1991), 87, 1657.

29 Kucherov, A.V., Montreuil, C.N., Kucherova, T.N., Shelef, M., Catalysis letters, (1998). 56(4), pp.173-181.

30 http://www.iza-structure.org/databases/ModelBuilding/AFI.pdf

31 Dove, M., *Mineralogical Magazine*, (1995), 59(397), 629-639

32 V., Welche, P. and Dove, M. *Journal of the American Ceramic Society*(1999), 82(7), 1793-1802.

33 J. Z. Tao and A. W. Sleight, *Journal of Solid State Chem.,* (2003), 173,442–448

34 http://projects.ivec.org/gulp/overview.html - *accessed 12/09/2013*

35 Berlie, A., Kearley, G.J., Liu, Y., Yu, D., Mole, R.A., Ling, C.D. and Withers, R.L., *Physical Chemistry Chemical Physics*, (2015) 17(33), pp.21547-21554.

36 Fischer, M.,. *Physical Chemistry Chemical Physics*, (2016) 18(23), pp.15738-15750.

Chapter 4

Characterization of iron active sites in FeAlPO-5 and FeSAPO-34; an *in situ* XAS study.

Summary

In this study, the aim was to investigate the chemical and geometric structure of the active sites in the iron-substituted aluminophosphate FeAlPO-5 and silico-aluminophosphate FeSAPO-34. To do so we have used X-ray absorption spectroscopy at the Fe K-edge and examined the catalysts under operating conditions.

4.1 Introduction

Since the discovery of the first microporous framework aluminophosphates in 1982[1] much study has been dedicated to AlPOs and their metal substituted analogues, mainly pertaining to their synthesis, characterisation, physical properties and catalytic activity. A large number of novel microporous aluminophosphate framework structures have been synthesised and characterised[2,3] and they have found uses in many important applications[4]. Microporous aluminophosphates all share the same chemical composition of aluminium phosphate ($AlPO_4$) but have framework structures with microporous cavities comparable to their better studied counterparts the aluminosilicate zeolites. They are also analogous to zeolites with respect to being composed of small tetrahedral building blocks with corner sharing O atoms. Owing to their composition aluminophosphate frameworks are made up of alternating AlO_4 and PO_4 tetrahedra. This is not unique to microporous framework structures, the denser cavity-less crystalline $AlPO_4$ mineral berlinite, also shares the same alternating AlO_4 and PO_4 tetrahedra.[5]

The aluminophosphate framework structures vary one from another in the orientation of the constituent AlO_4 and PO_4 tetrahedral units to form different sized cavities, cages and channels and connective configuration. Unlike aluminosilicate zeolites, aluminophosphates (AlPOs) have a charge neutral framework, and thus cannot be ion exchanged and lack any solid acid sites. However charge imbalance and thus acidic sites and ion exchange can be achieved by replacing a portion of the phosphorus atoms with silicon generating silicoaluminophosphates[6]. Substitution of tetrahedral units with other metallic elements is also possible, and a range of AlPOs and SAPOs have been synthesised with varying P, Al, Si and transition metal compositions[1,7].

SAPOs have found many applications as catalysts. In particular, the use of SAPOs in converting alcohols and ethers into olefins, particularly ethylene and propylene has garnered much research attention when small pore systems were used for this reaction[8]. Transition metal substituted SAPOs such as Cu or Fe substituted SAPO-34 have important established commercial uses in automobile after-exhaust emissions treatment for the selective catalytic reduction (SCR) of NOx[9].

Much recent research in these types of catalysts has been in large part focused on the need for greater stability at high temperatures. Initially popular metal oxides have been partially replaced by copper and iron-exchanged zeolites which are stable at higher temperatures (up to 600 °C).[10,] More recently attention has generally shifted from the established large and medium pore zeolites to include zeolites and other molecular sieves with small-pore frameworks.[11,12] Two of the most prominent are CuSSZ-13 and CuSAPO-34 which are known to be largely stable after steaming at 800 °C [13,14,15]. Their superior hydrothermal stability has repeatedly been attributed to the small size of their pores, which prevents detached $Al(OH)_3$ moieties from exiting the framework. Once the catalyst is cooled down again, the aluminium hydroxide moiety settles back into the framework, and dealumination has thus been averted because the framework stays intact.[16,17,18] However, while stability is largely a high temperature issue for most zeolites, there have been some reports of poor stability in silicoaluminophosphates exposed to a relative humidity above 40% even at room temperature.[19,20]

FeSAPO-34 has also been recently synthesised via isomorphous substitution of Fe into the framework and was shown to have improved activity over the Cu based catalysts for the SCR of NOx[21]. The catalysts exhibited a very good performance and good thermal stability up to a temperature of 800 °C. For comparison it is worth noting that the Fe-substituted aluminosilicate zeolite FeZSM-5 was found not to be suitable for this type of application. When studied for their use in SCR and to investigate the effect of high temperature steam treatment on the framework stability FeZSM-5 showed good catalytic activity at certain temperatures but after steam treatment the activity of decreased due to the dealumination of the ZSM-5 framework and the migration of Fe ions forming ferromagnetic iron agglomerates.[22]

Research into Fe-based aluminophosphates for the selective oxidation of benzene to phenol using N_2O was originally inspired by the study of the gas-phase reaction catalysed by unsupported $FePO_4$, and $FePO_4$ nanoparticles supported onto various oxides such as silica, alumina, zirconia, and titania.[23] Only two samples in the study proved functional for this reaction – namely the unsupported quartz-phase crystalline $FePO_4$, and silica-supported $FePO_4$. For the silica-supported $FePO_4$ catalyst with a Fe loading content of 5% by weight, the maximum conversion of benzene and product

selectivity to phenol reached 7 and 90%, respectively. The results of X-ray diffraction characterization confirmed that the supports affected the structure of $FePO_4$ deposited on their surfaces by inducing strain effects, and that quartz-phase $FePO_4$ was also the active phase formed on the silica surface. X-ray amorphous $FePO_4$ was found to be formed on the other oxides' surfaces which proved to be inactive. The active centre of the iron phosphate catalysts in such selective oxidation was proposed to be tetrahedrally-coordinated Fe on the surface of the quartz-phase $FePO_4$ crystallites which could undergo some coordinative unsaturation. Another study found that bulk-$FePO_4$ is selective in the N_2O mediated oxidation of methane and ethane, and involves a selectivity promoting function of the phosphate groups.[24]

Following these findings it had been discovered that the porous Fe-substituted aluminophosphate FeAlPO-5 was an exceptionally good catalyst for the selective oxidation of cyclohexane in air – a particularly important reaction for the industrial production of adipic acid[25]. A short time later, Sankar et al. at UCL established that the iron-substituted aluminophosphate FeAlPO-5 also contains Fe^{3+} in the as synthesised state, although in an octahedral coordination[6], unlike the tetrahedral Fe^{3+} found in $FePO_4$. The group carried out in-situ, time resolved combined EXAFS/XRD measurements using synchrotron X-rays, allowing them to observe the changes occurring during the calcination of the iron-substituted aluminophosphates FeAlPO-5 (medium pore size - 7.3 Å) and FeAlPO-18 (small pore size - 3.8 Å). They showed that in the case of FeAlPO-5 the octahedral Fe^{3+} centres desorb two water molecules at around 120°C, to yield tetrahedrally coordinated Fe^{3+} in the catalyst – a species much more alike to the iron found in quartz-phase $FePO_4$. In the case of FeAlPO-18, in its uncalcined as-synthesised state, it contains a mixture of tetrahedral Fe^{2+} ions and octahedral Fe^{3+}. Both of species of iron also fully convert to purely tetrahedrally coordinated Fe^{3+} after prolonged high temperature treatment in air.

FeAlPO-5 has also more recently been shown to exhibit good low temperature activity in the catalytic reduction of N_2O with methane. The Fe species in the FeAlPO have been found to play a large effect on the N_2O conversion[26]. However sufficient characterisation of the possible active sites for these catalysts was lacking, as only the global structure and particle morphology was measured using XRD and SEM respectively.

Bringing together information from on the structure and catalytic activity of well-established catalysts such as FeZSM-5, FeSAPO-34 and the work of Sankar *et al.*[27] who examined FeAlPO-5 as a catalyst for the selective oxidation of benzene to phenol using nitrous oxide as an oxidant, highlights the importance of Fe^{3+} ions play in both zeolites and more conventional catalysts such as quartz phase $FePO_4$. It is reasonable to assume that the porous structure and composition of nanoporous materials could confer other beneficial catalytic properties. More detailed study is necessary to provide an insight into the catalytic performance of these types of FeAlPO and FeSAPO materials which show such promise for applications as catalysts. In the typical activation of these catalysts, calcination in air is performed in order to remove the occluded organic templating molecules. Although characterisation methods such as XRD provide overall structural information on the framework, it is necessary to use Fe K-edge X-ray absorption spectroscopy (XAS) to determine the local structure of the active sites, as the Fe concentration is very low, inhomogeneous, and does not possess any long range structural order.

4.1.1 The Structure of AlPO-5 and SAPO-34

The nanoporous materials investigated in this *in-situ* XAS study are the large pore FeAlPO-5 (AFI) and the small pore FeSAPO-34 (CHA) aluminophosphates. The AFI framework[28] can be described as a 1-dimensional channel system consisting of a 12-ring pore opening with a diameter of 7.3 Å. The structure contains narsarsukite chains and can be built from the SBUs; 12, 6 or 4. Nanoporous materials with CHA structure are 3-dimensional frameworks with a pore opening of *ca.* 3.8 Å (8-ring). These small pore materials consist of 8, 6 and 4-membered rings, and include a CHA cage, and can be built from 6-6, 6, 4-2 or 4 SBUs.

A closely similar structure to the CHA framework is AEI (AlPO-18), this structure is also described as a 3-dimensional network with a similar pore opening (3.8 Å) built from the same SBUs. However, due to a difference in the stacking sequence of the SBUs, the AEI structure does not contain CHA cages and is therefore classified as a unique framework. This is represented schematically in Figures 4.1 and 4.2.

AFI **Framework Type** **P6/mcc**

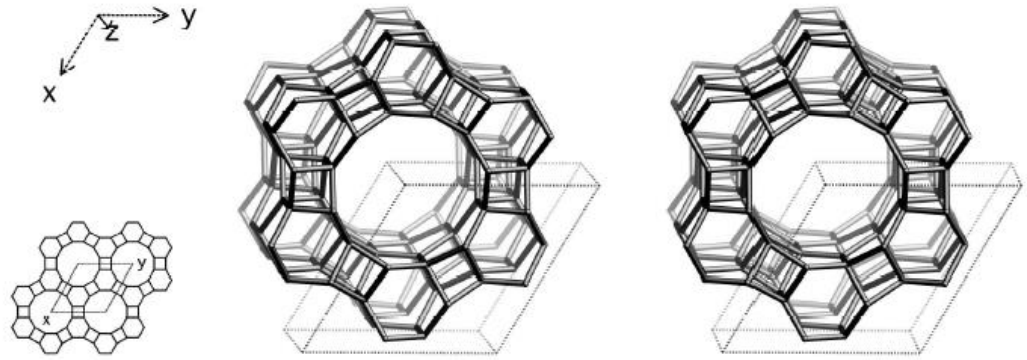

framework viewed along [001] (bottom left: projection down [001])

Idealized cell constants: hexagonal, P6/mcc, a = 13.8Å, c = 8.6Å

CHA **Framework Type** **R$\bar{3}$m**

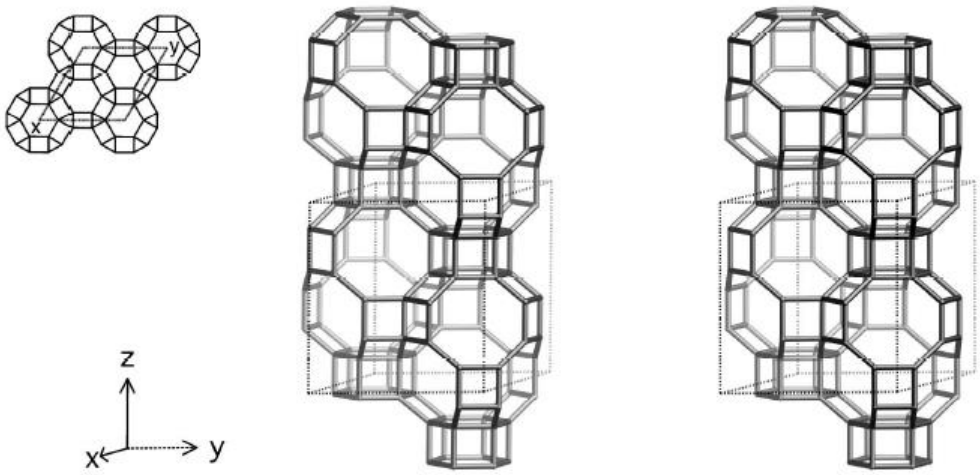

framework viewed normal to [001] (top left: projection down [001])

Idealized cell constants: trigonal, R$\bar{3}$m, a = 13.7Å, c = 14.8Å

Figure 4.1 *Framework structure showing unit cells of AlPO-5 (AFI- top) and AlPO-34 (CHA – bottom) Taken from the IZA Atlas of Zeolite Structures.*[2]

(a) Common structural units:

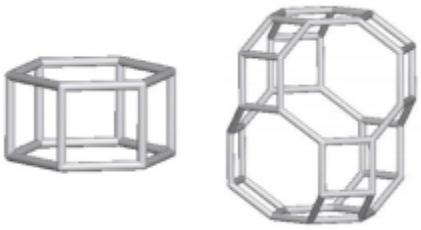

Arrangement in framework structure:

(b) AlPO-18 - AEI Structure *(c) SAPO-34 - CHA Structure*

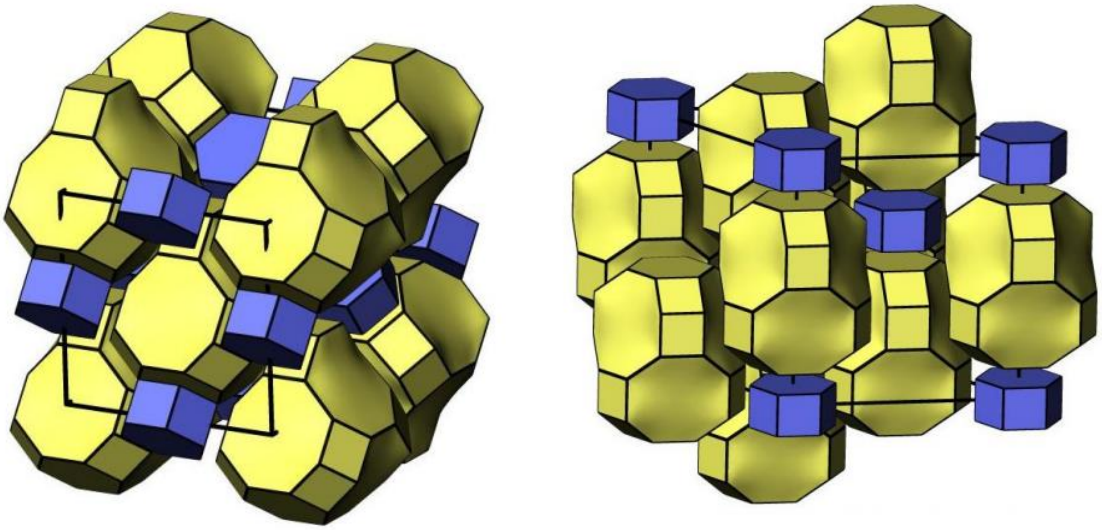

Figure 4.2 *Structural units common to both AEI and CHA frameworks (a). The structures are similar in the types of building units, but their orientation is different in the two framework types as shown for AEI (b) and CHA (c).*[2]

4.2. Sample Preparation

For the FeAlPO-5 and FeSAPO-34 synthesis, aluminium hydroxide hydrate ($Al(OH)_3.xH_2O$) was first dissolved in a solution of phosphoric acid (H_3PO_4, 85%) with deionised water in a polypropylene beaker. An aqueous solution of iron acetate ($(CH_3COO)_2Fe.4H_2O$) was then added and stirred. In the FeSAPO-34 synthesis, an appropriate amount of silica sol (SiO_2) was also added to the solution mixture at this point of the preparation. This mixture was then stirred until homogeneous for 4 hours. After rigorous stirring of the gel for two hours, the organic template TEAOH (tetraethyl ammonium hydroxide) was then added slowly dropwise to the solution. The final gel composition was $0.94.Al_2O_3:0.8P_2O_5:0.04Fe_2O_3:0.75TEAOH:30.8;H_2O$ for FeAlPO-5 and $0.04SiO_2:1.0Al_2O_3:1.0P_2O_5:0.04Fe_2O_3:0.75TEAOH:30.8;H_2O$ for FeSAPO-34. The final viscous orange gels were then stirred vigorously for 20 hours at 300 rpm.

A Teflon liner was filled with the gel to 50% of the total volume and was placed in a stainless steel autoclave and heated at 165°C for a period of 4.5 h and 2 days for FeAlPO-5 and FeSAPO-34 respectively. After cooling, the product was recovered by filtration and washed with deionized water.

4.3 DR-UV-Vis Spectra

Diffuse reflectance spectra were recorded on a Shimadzu UV-2100 spectrophotometer, equipped with an integrating sphere assembly. A special cell, loaded with the solid sample powder and covered by a quartz window, was used in all measurements. All the spectra were recorded at room temperature against barium sulphate and plotted in terms of absorbance. The DR-UV spectra recorded all exhibit a single large broad absorbance band at 260 nm. Absorption features between 200-300 nm are usually assigned to charge transfer interactions of transition metals in the framework. The spectrum of the FeAlPO-5 sample shows a much less intense relative absorbance compared to that of the Si substituted CHA FeSAPO-34. This could indicate more extraframework Fe in the sample or may be due to the increased number vibrational modes induced by the presence of Si in the sample, due to increased compositional inhomogeneity in the sample. The band localised at approximately 260 nm can also be assigned to framework and extra-framework tetrahedral aluminium and iron atoms

arising from M-O charge transfer transitions.[29] Variables such as the aluminium and oxygen charge density, M-O distances, the crystallographic position of the metal atoms in the framework structure and the origin and nature of the surroundings (water molecules, adsorbed gas molecules, organic templates) can greatly influence the wavelength and intensity of the charge transfer band.

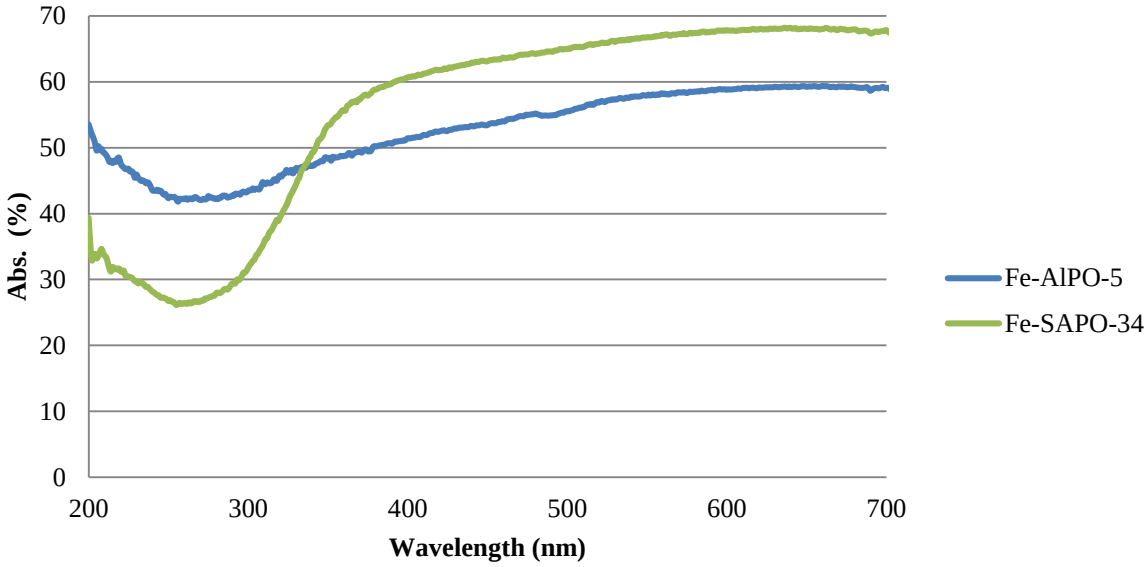

Figure 4.3 *DR-UV-Vis of FeAlPO-5 and FeSAPO-34.*

4.4 DR-NIR Spectra

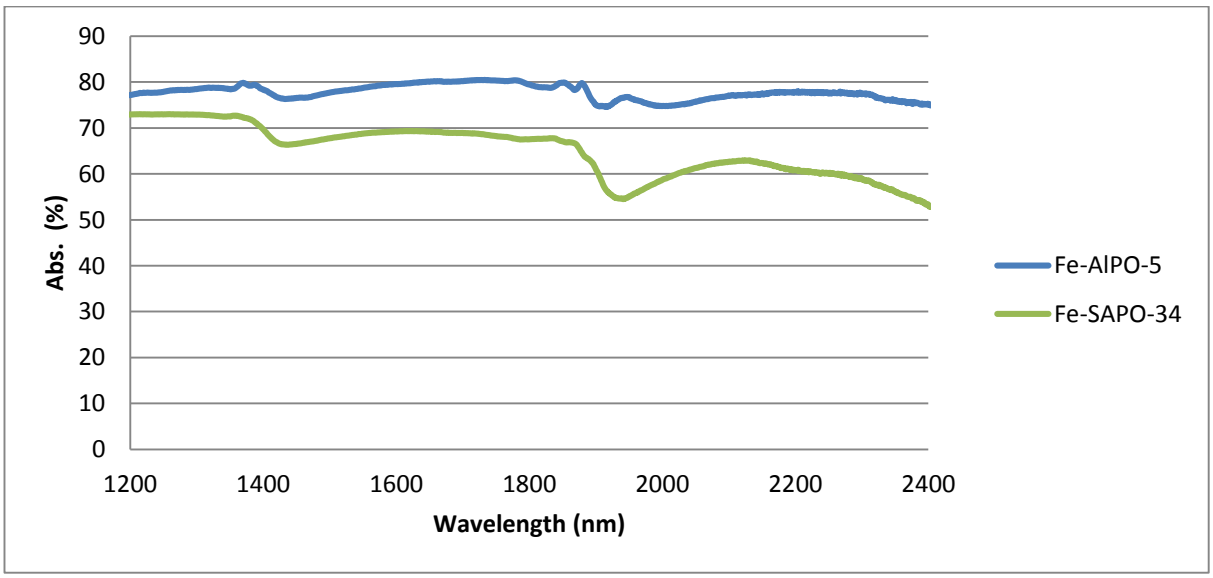

Figure 4.4 *DR-NIR Spectra of FeAlPO-5 and FeSAPO-34.*

The absorbance band observed for all samples at 1920 nm corresponds to the combination vibration band (δ' + ν) of water molecules adsorbed onto the zeolite[30]. The intensity of this absorbance band is highly variable between the three samples. It is weakest for FeAlPO-5 which, seems to exhibit a fine structure, which could not be assigned. The combination water absorbance band is larger for the Si containing FeSAPO-34, corresponding to more adsorbed water. The spectrum for FeSAPO-34 has the broadest and the most intense absorption band, indicating even more hydration for this sample, which is to be expected due to the larger amount of framework charge imbalance and formation of acid sites in the SAPO, from the inclusion of Si for this sample as well as Fe.

A weak absorbance band is also observed at 1400 nm for al samples, which can be assigned to the presence of OH groups bound to Fe or Al species and of bridging OH groups. Their relative intensity is more relatively less variable compared to the combination vibration band for the two samples, indicating bridging OH groups and those bound to metal centres are found in relatively similar concentrations in both the samples.

4.5 *In situ* EXAFS/XRD measurements

In situ combined XAS/XRD experiments were performed at beamline B18 at the Diamond Light Source in order to determine the types of chemical changes occurring to the iron species during the catalyst activation procedures, as well as changes occurring in the overall framework structure. The samples were formed into pellets and inserted into a custom made stainless steel furnace. *In situ* XAS and XRD measurements were then performed in alternation as the temperature was increased from 30°C to 550°C with a ramp rate of 5°C min^{-1} under flow of air.

The XAS data from FeAlPO-5 and FeSAPO-34 were background subtracted and normalised using the Athena software program[31] and the data was then fitted to simulations created using EXCURVE.[32] EXCURVE provided good reasonable results that concurred with expected results and has gives low statistical error (R-values) for the fits. This is because EXCURVE can perform single-scattering calculations from the input parameters (absorbing atom -Fe surrounding atoms – O, Si/Al/P etc., initial values of N, σ^2, $R_{\text{Fe-X}}$) and create a suitable physical model to fit the EXAFS results.

The small concentration and random distribution of the Fe atoms in the materials does not allow this use of a crystal structure in the calculation, as none exist that provide any justifiable model for these iron sites.

The program ATHENA was used to remove the background effects and normalise the data. The energy in eV was converted to k-space over the region from 1-10 $Å^{-1}$ for Fe K edge data, and an amplitude reduction factor S_0 of 0.7414 was used in the fits.

4.5.1 FeAlPO-5 XAS

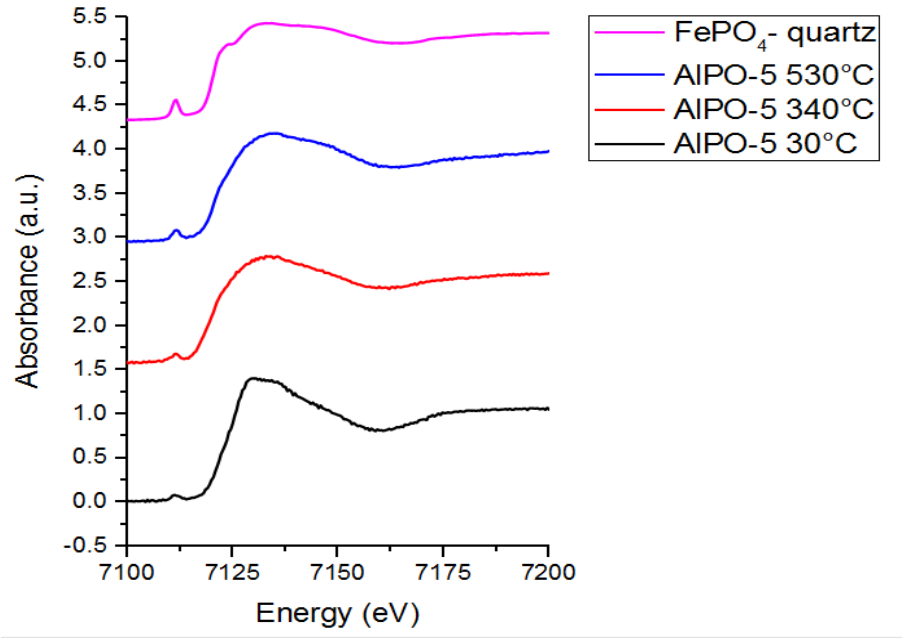

Figure 4.5 *EXAFS spectrum for FeAlPO-5 between 30 and 550°C in air and $FePO_4$ reference spectrum at room temperature.*

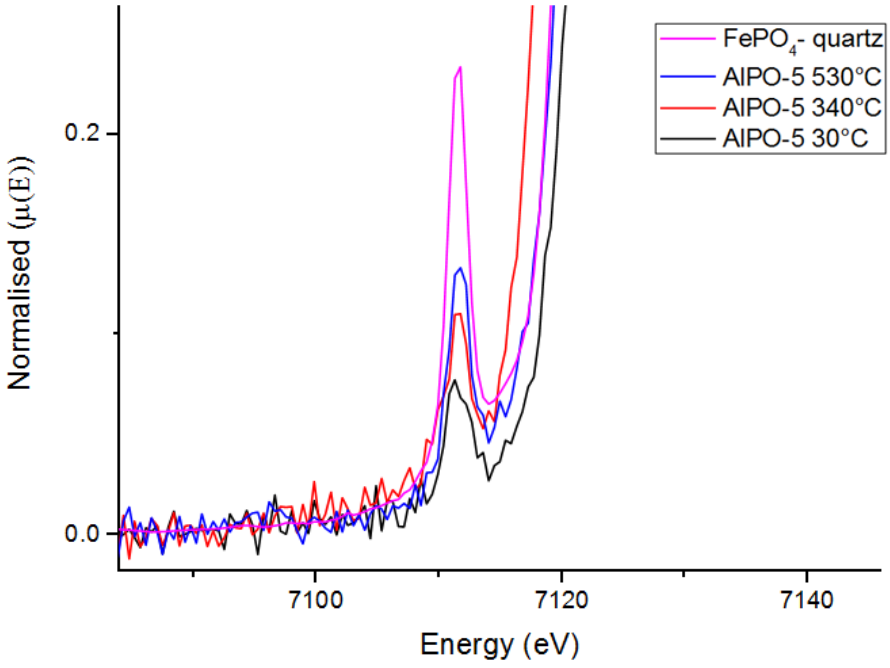

Fig. 4.6 *Pre-edge feature for FeAlPO-5 between 30 and 550°C in air.*

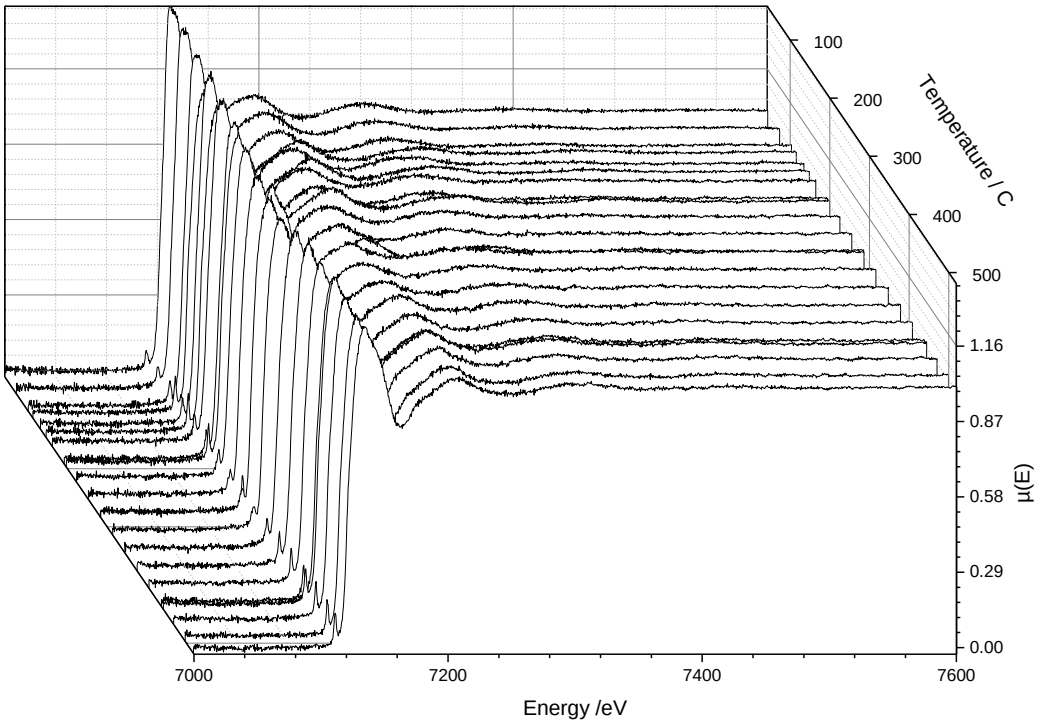

Figure 4.6 *EXAFS spectrum for FeAlPO-5 between 30 and 550°C in air.*

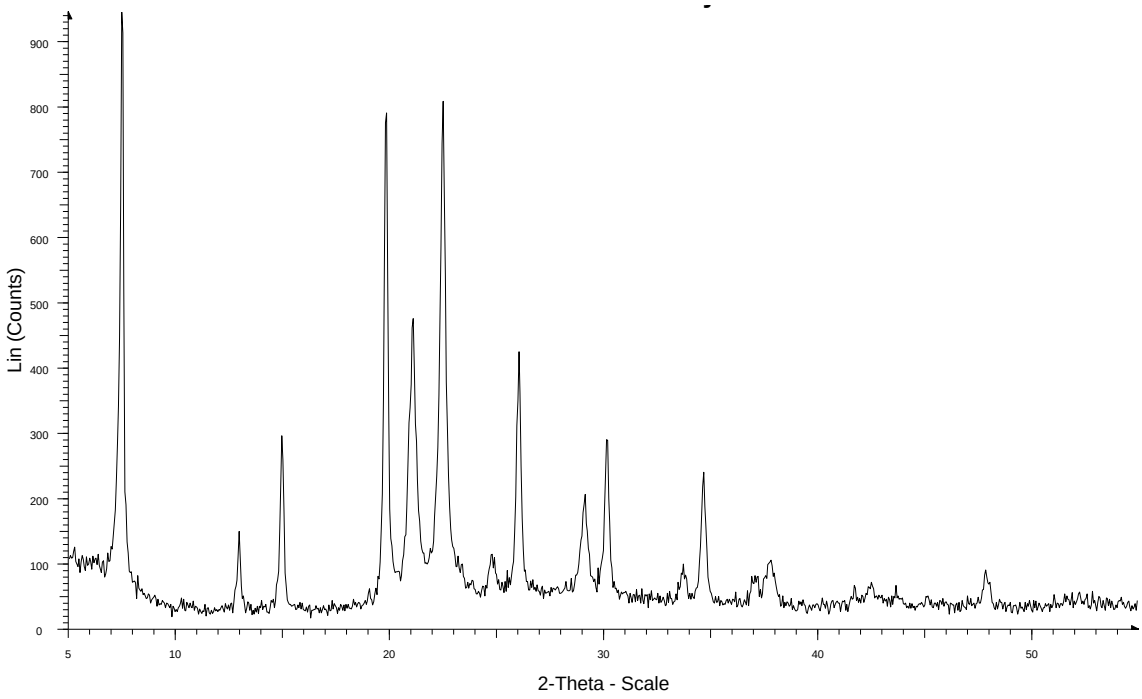

Figure 4.7 *XRD plot for FeAlPO-5 collected on a lab diffractometer.*

Figure 4.6 shows the XAS data collected between 30 and 550 °C. A first shell fit analysis was completed, with oxygen as the nearest neighbouring atom to the absorbing central Fe atom using a k-range of 3.5-10 $Å^{-1}$. Errors for all parameters were < 10%, except for the coordination number which has an error of about 10-15% ; R factors were very good and in the range of R ~ 25-30% for all scans (a measure of reliability of fit, good fits should have an R factor of less than 50%. Figure 4.8 shows background subtracted, normalised EXAFS data analysed in k-space (k^3-weighting) and corresponding Fourier transform plots at 30 °C and 550 °C for FeAlPO-5.

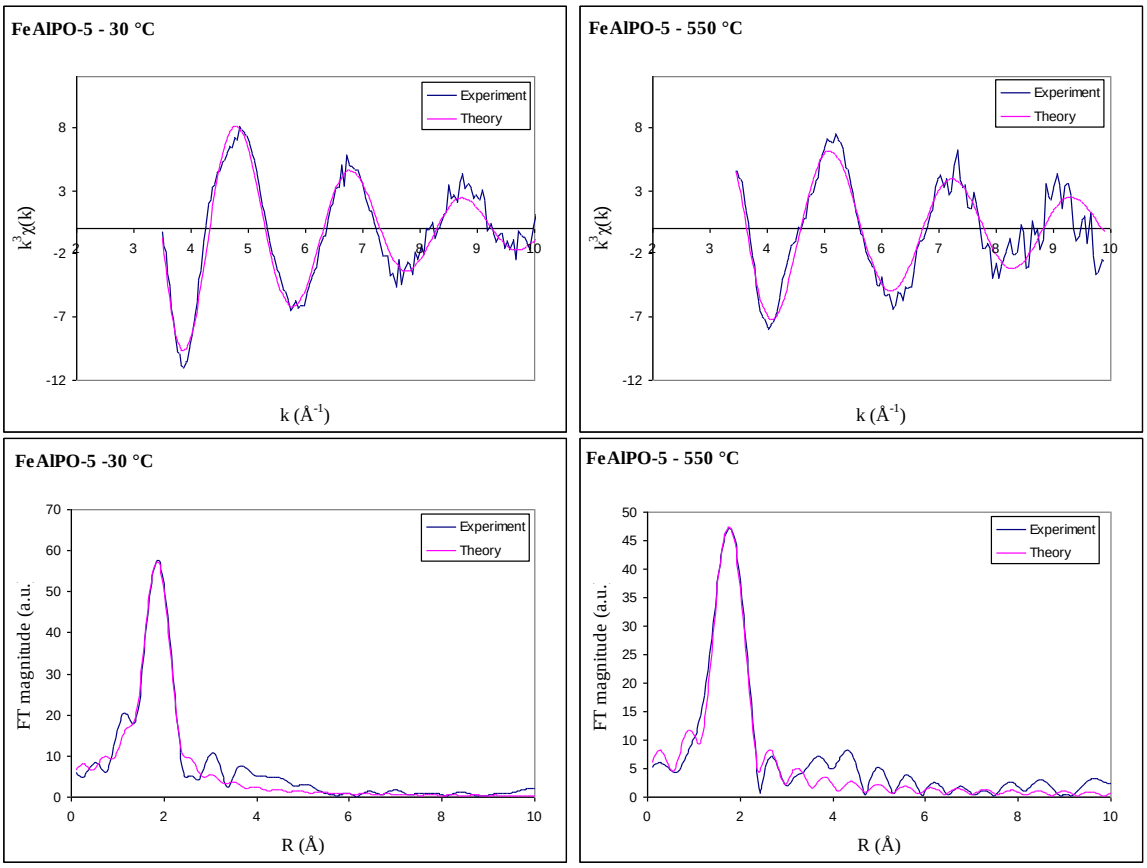

Figure 4.8 *EXAFS and Fourier transform plots from EXCURVE analysis for FeAlPO-5*

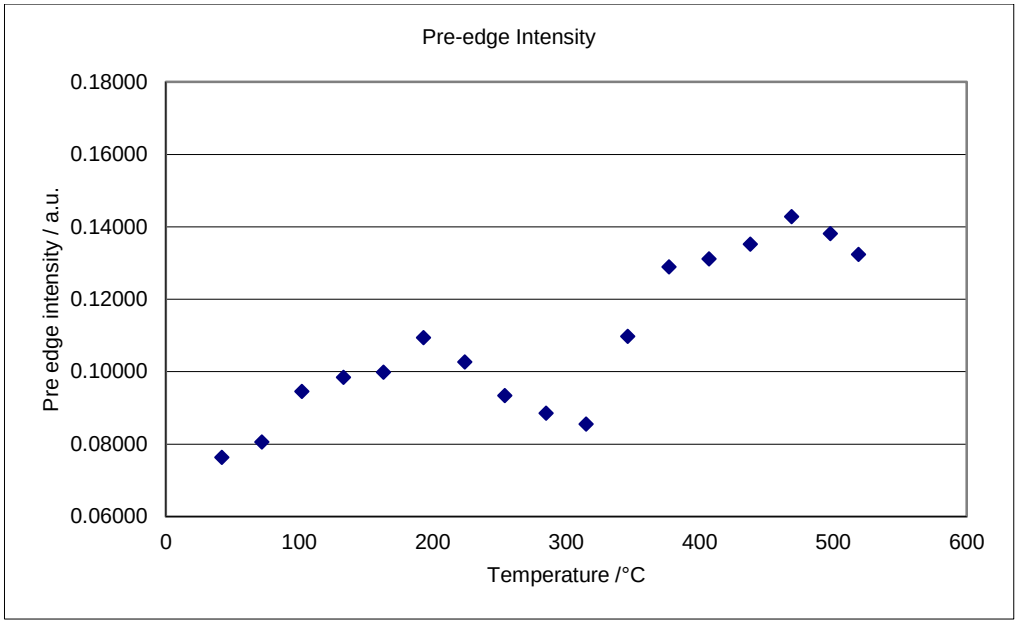

Figure 4.9 *Variation of the maximum pre-edge intensity for the normalised Fe K-edge XANES data collected for FeAlPO-5 during activation in air from 30-550°C. Errors for the pre-edge intensity ± 5%.*

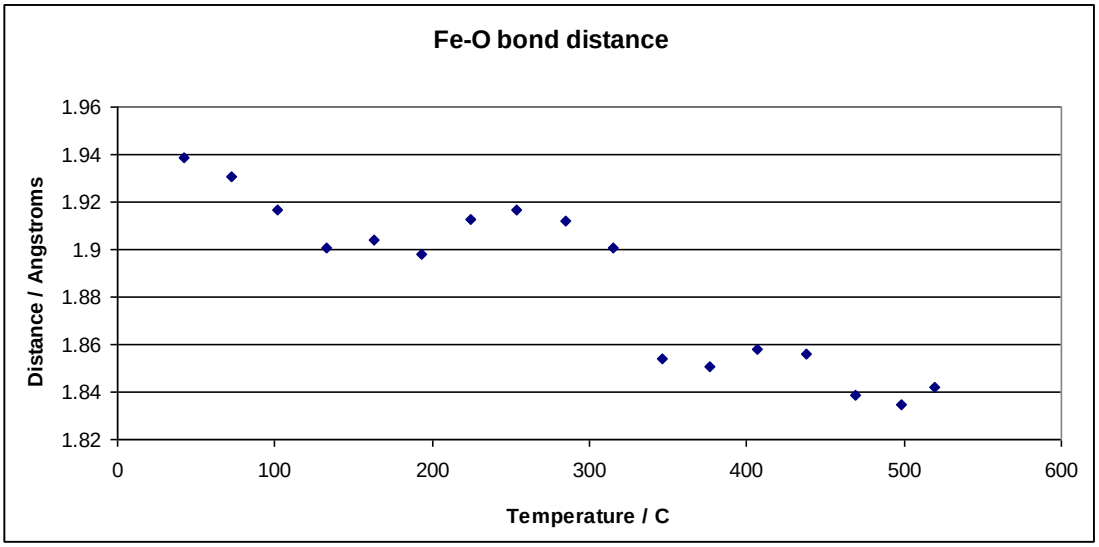

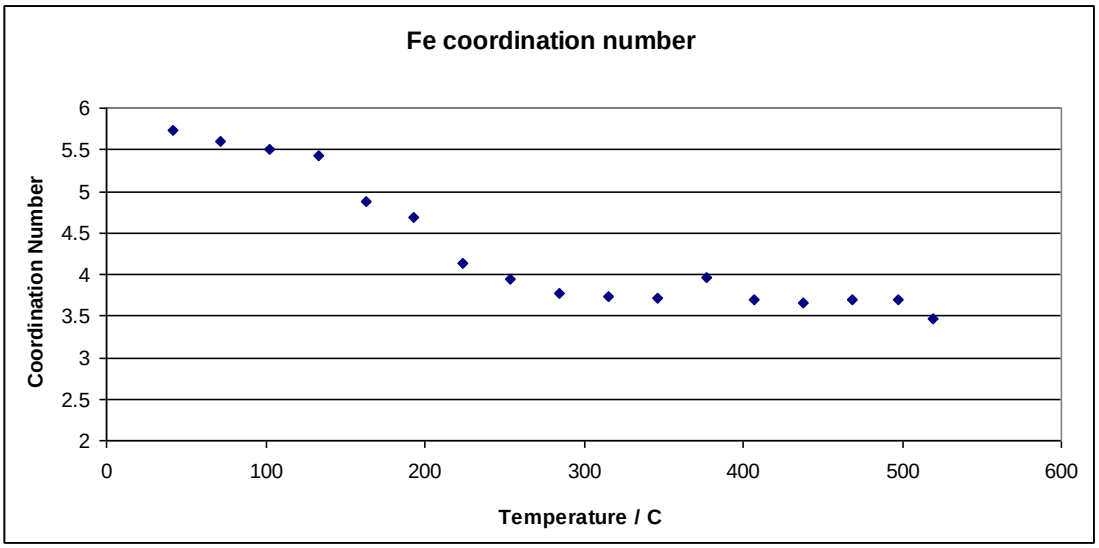

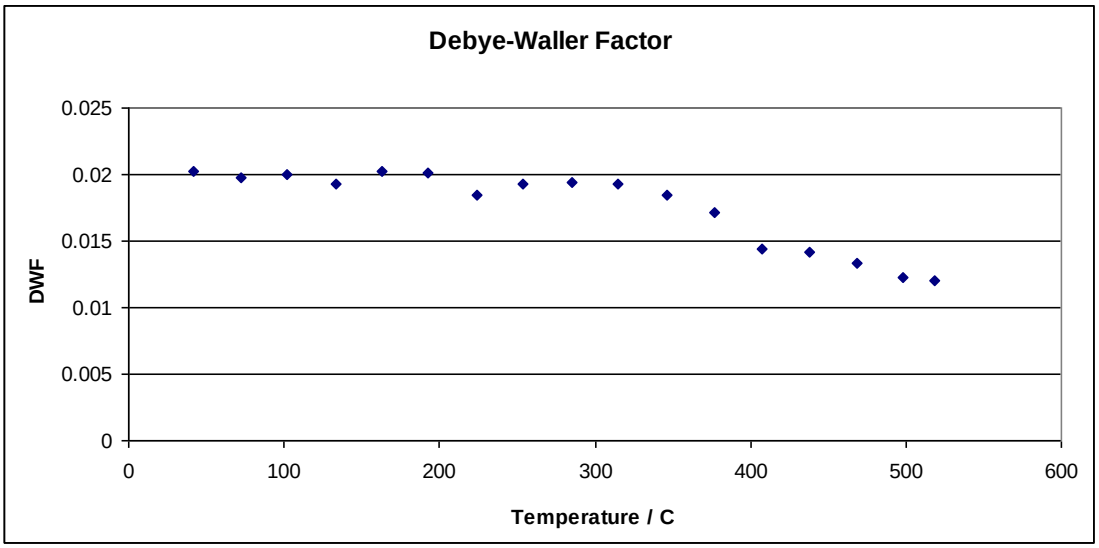

Figure 4.10 *Variation of parameters from Fe K-edge EXAFS fits during activation in flowing air up to 550°C for FeAlPO-5; (a) Fe-O bond length, (b) Fe-O coordination*

number, (c) Debye-Waller factor. Errors for bond lengths are ± 0.01 Å. Errors in coordination number N, and $2\sigma^2$ are ~10%.

Detailed analysis of the EXAFS data revealed that in the as-prepared form, the majority of Fe ions are found in an octahedral coordination environment, with a refined value for the average Fe-O bond distance calculated to be 1.94 Å. The coordination number and Debye-Waller factors were also refined. Figure 4.10 shows the variation in the Fe-O bond distance, Debye-Waller factor (σ^2), and O coordination number, as well as the relative intensity of the pre-edge feature, plotted as a function of temperature.

Upon heating, up to about 150°C the Fe-O bond distance appears to decrease from 1.94 to a value of 1.90 Å. This occurs concurrently with a decrease in coordination number averaging the loss of one coordinated oxygen atom, along with a spike in pre-edge intensity. This process can be interpreted as being due to the loss of the water molecules coordinated to Fe in the framework. A small increase of about 0.02 Å is then observed at 250°C, after which it then contracts gradually as the temperature is increased, reaching a minimum value of 1.84 Å at about 500°C.

This temperature window where the Fe-O bond shrinks most prominently above 250°C interestingly corresponds to the same temperature range in the earlier in-situ HR-XRD experiments in Chapter 3, where the *c* axis of the unit cell in FeAlPO-5 is seen to expand dramatically.

During the heating ramp the calculated average coordination number of the Fe in FeAlPO-5 is seen to drop from an initial refined value of 5.7 at room temperature, to ~ 3.7 by 300°C, whereby it remains at this value even at higher temperatures. This change in coordination number is supported by the pre-edge plot, that shows an increase in pre-edge intensity at around 300°C (Figure 4.10) corresponding to the symmetry breaking caused by this change increasing the probability of the formally "forbidden" pre-edge transition. It should be noted that not only is there at least 10% error in the determination of coordination number, but it is also highly correlated with the Debye-Waller factor which is observed to decrease above 280°C. This drop in value of the

Debye-Waller factor (which is affected by both static and thermal disorder) occurs at a similar temperature range where the sudden decrease in Fe-O bond distance also seen, indicating the final static disorder of the FeO_x species in the system is now lower than the initial, following an autoreductive transition. The correlation of the pre-edge intensity change over temperature from the XANES part of the spectrum, and the calculated EXAFS parameters is an important one, in that it helps to confirm that the refined values are sound.

Based on this data and the changes observed in the pre-edge intensity from a low value of 0.08, to that of 0.13 by around 400°C, we can confirm the case of FeAlPO-5 the octahedral Fe^{3+} centres gradually desorb water molecules at around 150-300^{o}C, to yield a fraction of tetrahedrally coordinated Fe^{3+}in the catalyst – a species much more alike to the iron found in quartz-phase $FePO_4$.

Further reduction in Fe coordination and the extraction of some Fe from the framework is also evident at higher temperatures especially once the organic template molecules have been lost in calcination. A slight change in the value of E_0 values shifting from 7124.3 eV (similar to that of octahedrally coordinated Fe in $FePO_4.2H_2O$ at 7124.5 eV) to 7122.9 (identical to as that of Fe_2O_3) confirms that the iron remains as Fe(III) but changes coordination geometry, possibly forming a fraction of extra-framework FeO_x type clusters.

4.5.2 FeSAPO-34 XAS

A first shell fit analysis was performed for the data collected during the activation treatment for FeSAPO-34 (XRD shown in Figure 4.11), with oxygen as the nearest neighbouring atom to the absorbing central Fe atom using a k range = 3.5-10 $Å^{-1}$. Errors for all parameters were less than 10%; R factors were again very good and in the range of R ~ 27-35% for all scans. Figure 4.12 shows FeSAPO-34 background subtracted, normalised EXAFS data analysed in k-space (k^3 weighting) and corresponding Fourier transform plots at 30°C and 550°C.

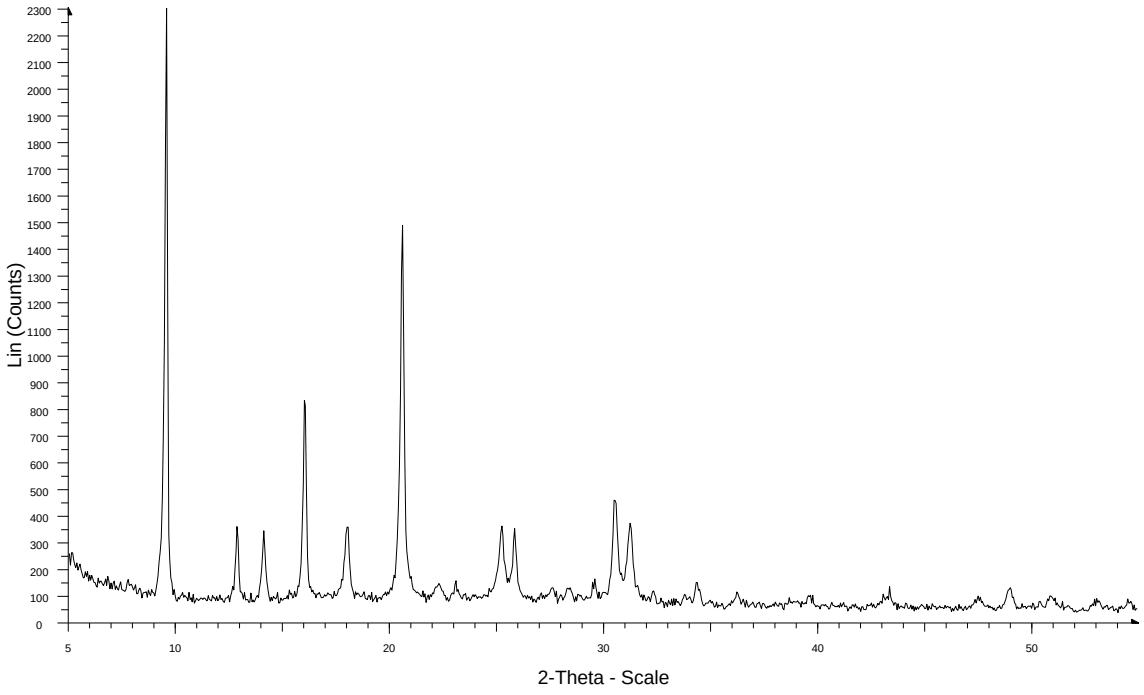

Figure 4.11 *XRD plot for Fe-SAPO-34 collected on lab diffractometer.*

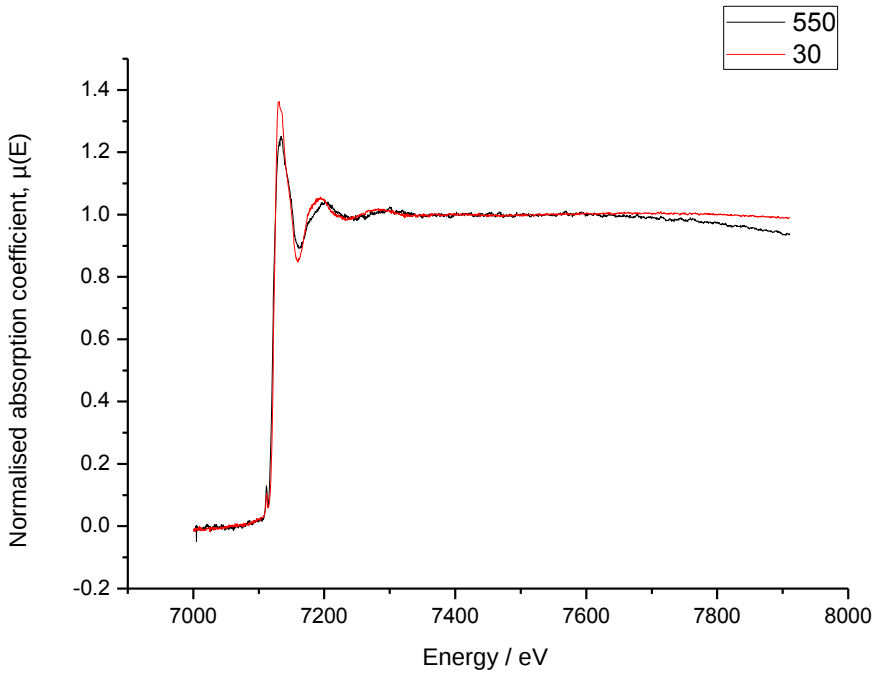

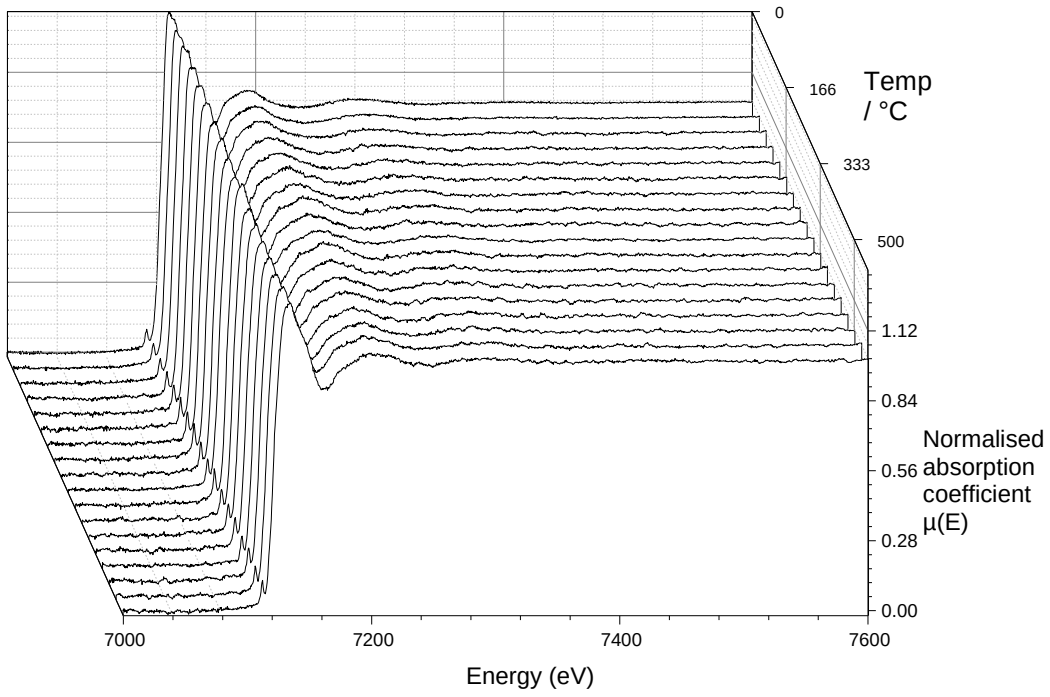

Figure 4.12 Fe K-edge ~ X-ray absorption spectra recorded during calcination of *FeSAPO-34* from *30°C* to 530°*C*, in air.

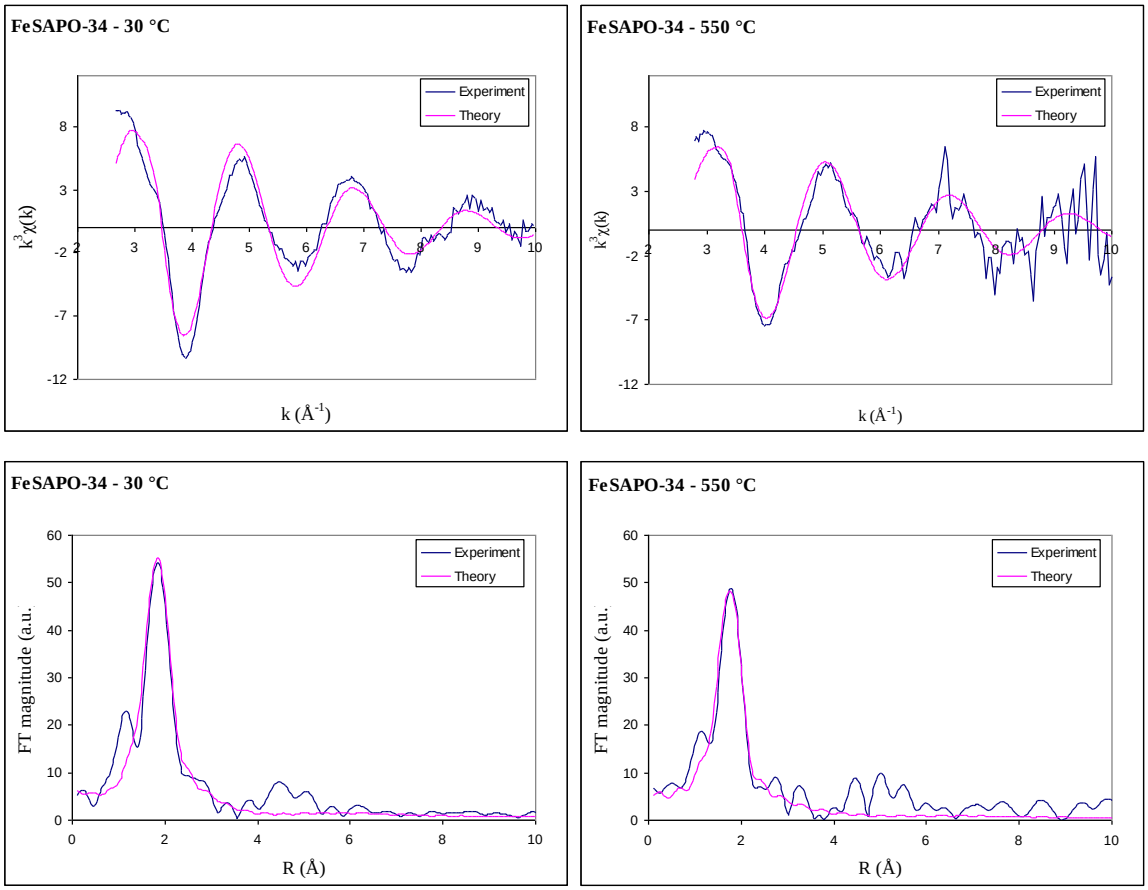

Figure 4.13 *EXAFS and Fourier transform plots from EXCURVE analysis for FeSAPO-34*

Figure 4.15 shows the calculated Fe-O bond distance, Debye-Waller factor ($2\sigma^2$), and coordination number for FeSAPO-34 plotted against increasing temperature. In the as-synthesised FeSAPO-34 before calcination the Fe-O bond distance was found to be 1.93 Å, very similar to that found in FeAlPO-5, and within error, essentially the same. Upon heating in air up to 350°C the Fe-O bond distance appears to contract in an almost linear manner, reaching a value of 1.86 Å by 350°C. The Fe-O bond distance remains around this value, even upon further heating to 550°C. Interestingly there is evidence for a small transient increase in the Fe-O distance, which peaks at 250°C, which was also seen in the results for FeAlPO-5. This may indicate two overlapping reduction processes being observed in more than one Fe species each system, however this canot be confirmed using these methods and is small and may be treated as insignificant. The average Fe coordination number begins to drop from 5.5 at around 160°C, to 3.6 at

350°C. The coordination number does not change significantly at temperatures higher than this, which corroborates with the temperature range of greatest change in the calculated Fe-O bond distance. The Debye-Waller factor for FeSAPO-34 is observed to decrease in the temperature range where the Fe-O bond distance decreases, however the change is less dramatic than that of FeAlPO-5, and may not be statistically significant. At high temperatures $2\sigma^2$ reaches a minimum value of 0.020 $Å^2$ for SAPO-34, whereas this value was much lower at 0.012 $Å^2$ for FeAlPO-5, indicating a higher degree of disorder in the oxygen atoms coordinated to the iron atoms, which can be both due to the presence of Si in the sample, as well as the differing framework structure and density.

The measured normalised pre-edge maximum intensity (Figure 4.14) also increases from 250°C onwards, reaching a peak at 460°C, which roughly correlates with the temperature range showing the decrease in coordination number, and concurrent formation of a system containing Fe in a mainly tetrahedral environment.

It is not surprising to see a decrease in Debye-Waller factor for both compounds with increasing temperatures, since this occurs when the average Fe-O bond distance changes from *ca* 1.94 Å to 1.85 Å suggesting that although thermal disorder must increase slightly with temperature, less static disorder is clearly present in the tetrahedral coordination, compared to that of octahedral, leading to an overall decrease in total system disorder even though thermal disorder through increased vibrational modes and time-average displacements must be increasing with temperature.

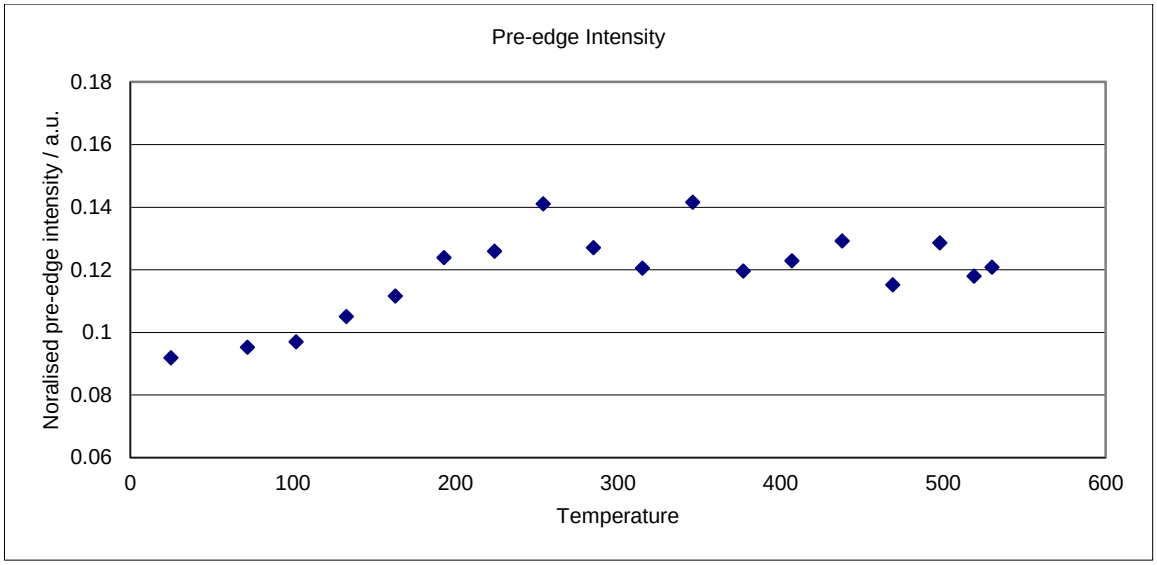

Figure 4.14 *Variation of the maximum pre-edge intensity for the normalised Fe K-edge XANES data collected for FeSAPO-34 during activation in He from 30-550°C. Errors for the pre-edge intensity ± 5%.Fe-SAPO-34*

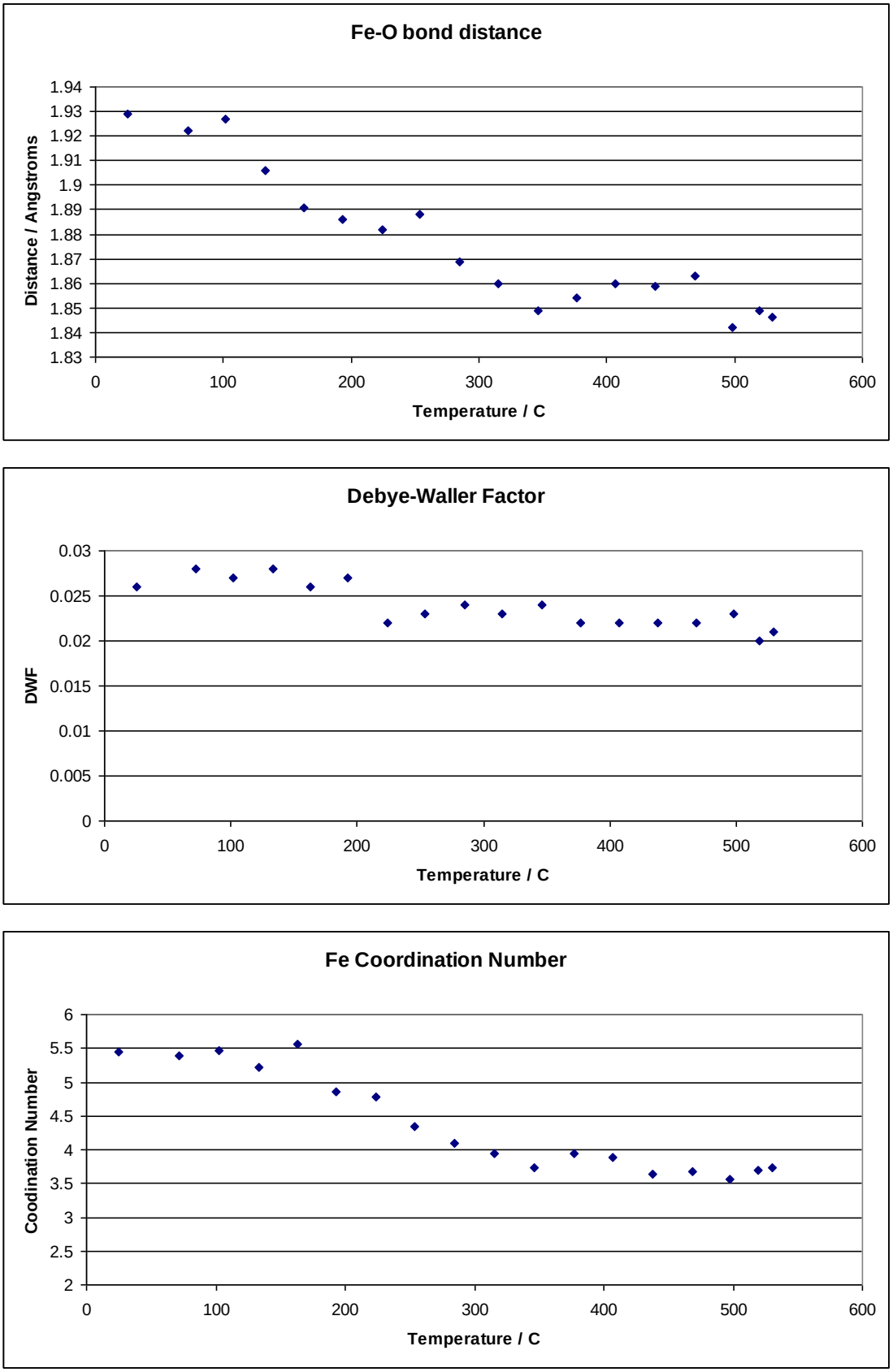

Figure 4.15 *Variation of parameters from Fe K-edge EXAFS fits during activation in He up to 880°C for FeSAPO-34; (a) Fe-O bond length, (b) Fe-O coordination number*

(c) Debye-Waller factor. Errors for bond lengths are ± 0.01 Å. Errors in coordination number N, and $2\sigma^2$ are ~10%.

Table 4.1. *White line energy E_0, pre-edge intensity and pre-edge energy position of selected samples and references. The data was collected is in air.*
Variation of the maximum pre-edge intensity for the normalised Fe K-edge XANES data collected for FeAlPO-5 during activation in He from 30-550°C. Errors for the pre-edge intensity ± 5%.

Sample	***White line energy, E0 /eV***	***Pre-edge energy /eV***	***Pre-edge intensity /a.u.***
Fe metal 30°C	7112.0	-	-
Fe (II) oxide 30°C	7119.9	7112.8	0.07
Fe (III) oxide 30°C	7122.9	7113.0	0.05
$FePO_4$-quartz 30°C	7122.1	7113.0	0.12
$FePO_4.2H_2O$ 30°C	7124.5	7113.0	0.07
FeMFI as synthesised	7121.3	7113.0	0.09
FeMFI calcined 30°C	7122.2	7113.0	0.08
FeAlPO-5 as synthesised 30°C	7124.4	7112.9	0.05
FeAlPO-5 calcined 530°C	7122.9	7112.9	0.08
FeSAPO-34 as synthesised 30°C	7124.5	7112.9	0.04
FeSAPO-34 calcined 530°C	7123.5	7112.9	0.08

The Fe in FeSAPO-34 begins mainly in a tetrahedral Fe^{3+} framework position. This iron undergoes a transformation between 250-300°C where it becomes dislodged from framework positions to extra-framework and sudden congruent reduction to Fe^{2+}. By 350°C it re-oxidises to Fe^{3+} in extra-framework positions. Similar behaviour was also observed by Sankar et al. in SAPO-18 systems[33]. In the case of FeAlPO-18, in its uncalcined as-synthesised state begins with a mixture of tetrahedral Fe^{2+} ions and

octahedral Fe^{3+}, both of species of iron seem to fully convert to purely tetrahedrally coordinated Fe^{3+} after prolonged high temperature treatment in air.

4.6 Conclusions

In both catalysts studied there was an appreciable amount of loss of octahedral Fe and increase in tetrahedral Fe forming coordinatively unsaturated active sites. These sites possess distorted tetrahedral symmetry and have shorter Fe-O bond distances than their respective starting materials. Both AlPO-5 and SAPO-34 show similar behaviour during calcination and show substantial formation of extra framework iron that stabilised above 350°C, although via different pathways. Loss of water was observed at low temperatures between 30-200°C. This process can be summarised by a comparative plot of the pre-edge intensity for both samples as the activation treatment proceeds, showing changes in the symmetry of the Fe atoms (Figure 4.16).

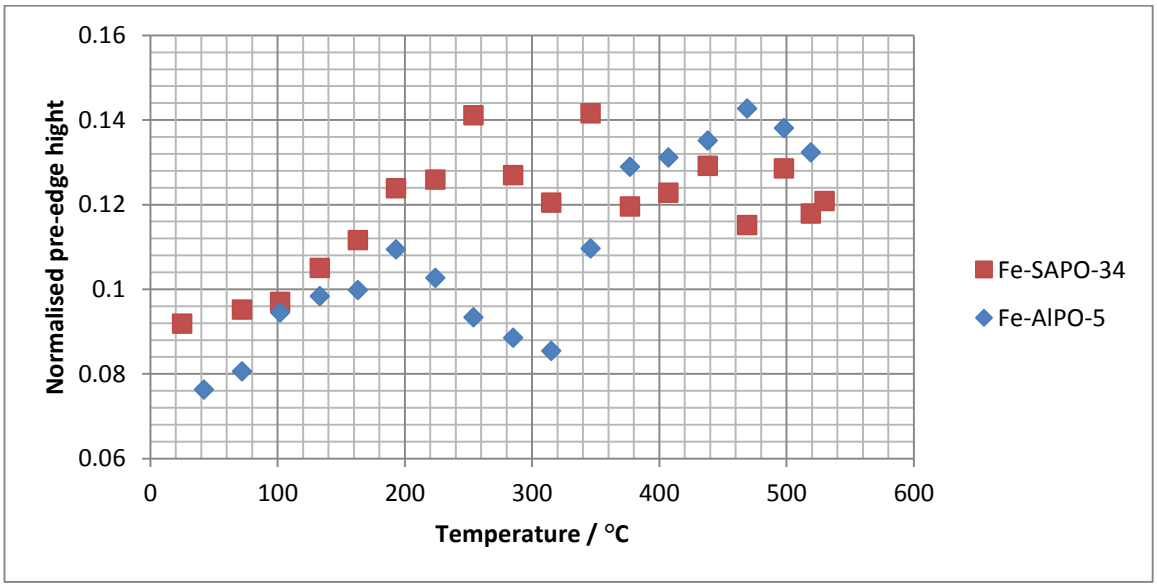

Figure 4.16. *Comparative plot of normalised maximum pre-edge intensity vs temperature for FeAlPO-5 and FeSAPO-34 during activation in He from 30-550°C. Errors for the pre-edge intensity ± 5%.*

References

1 S. T. Wilson , B. M. Lok , C. A. Messina , T. R. Cannan , E. M. Flanigen *Journal of the American Chemical Society.*, (1982), 104 (4), pp 1146–1147

2 http://www.iza-structure.org/databases/books/Atlas_6ed.pdf - accessed 22/05/14

3 E.G. Derouane, F. Lemos, C. Naccache F. R. Ribeiro *Zeolite Microporous Solids: Synthesis, Structure, and Reactivity*; (2012) Springer Science & Business Media.

4 H.G. Karge J. Weitkamp, *Zeolites as Catalysts, Sorbents and Detergent Builders: Applications and Innovations,* (1989) Elsevier

5 N. N. Greenwood, A. Earnshaw, (1997). *Chemistry of the Elements* (2nd ed.). Butterworth-Heinemann.

6 P. Meriaudeau,, V. A. Tuan, , V. T. Nghiem, , S. Y. Lai, , L. N. Hung, C. Naccache,, (1997), *Journal of Catalysis*, 169(1), pp.55-66.

7 B. M. Lok, C. A. Messina, R. L. Patton, R. T. Gajek, T. R. Cannan, E. M. Flanigen *Journal of the American Chemical Society*, (1984), 106 (20), pp 6092–6093

8 J. Liang, , H. Li,, S. Zhao,, W. Guo,, R. Wang, M. Ying, *Applied Catalysis*, (1990), 64, pp.31-40.

9 K. Leistner, L. Olsson, *Applied Catalysis B: Environmental*, (2015), 165, pp.192-199.

10 P. Forzatti, *Applied Catalysis A: General*, (2001), 222(1), pp.221-236.

11 I. Nova, E. Tronconi (Eds.), *Urea-SCR Technology for deNOx After Treatment of Diesel Exhausts,* (2014) Springer, New York,

12 P.G. Blakeman, E.M. Burkholder, H.-Y. Chen, J.E. Collier, J.M. Fedeyko, H. Jobson,R.R. Rajaram, Catalysis Today, 231 (2014) 56–63

13 T. Ishihara, M. Kagawa, F. Hadama, Y. Takita, *Journal of Catalysis*, 169 (1997) 93–102

14 J.H. Kwak, D. Tran, S.D. Burton, J. Szanyi, J.H. Lee, C.H.F. Peden, *Journal of Catalysis*, 287 (2012) 203–209

15 R. Martínez-Franco, M. Moliner, C. Franch, A. Kustov, A. Corma, *Applied Catalysis B*, 127 (2012) 273–280

16 P.G. Blakeman, E.M. Burkholder, H.-Y. Chen, J.E. Collier, J.M. Fedeyko, H. Jobson,R.R. Rajaram, *Catalysis Today* 231 (2014) 56–63

17 .W. Fickel, E. D'Addio, J.A. Lauterbach, R.F. Lobo, *Applied Catalysis B* 102 (2011) 441–448

18 F. Gao, J. Kwak, J. Szanyi, C.F. Peden, Top. Catal. 56 (2013) 1441–1459

19 M. Briend, R. Vomscheid, M.J. Peltre, P.P. Man, D. Barthomeuf, *Journal of Physical Chemistry* 99 (1995) 8270–8276.

20 J.C. Poshusta, R.D. Noble, J.L. Falconer, *Journal of Membrane Science*, 186 (2001) 25–40

21 Andonova, S., Tamm, S., Montreuil, C., Lambert, C. and Olsson, L., *Applied Catalysis B: Environmental*, *180*, (2016) pp.775-787.

22 Lee, H.T. and Rhee, H.K., *Korean Journal of Chemical Engineering*, 19(4), (2002) pp.574-579.

23 Hereijgers, J., Desmet, G., Breugelmans, T. and De Malsche, W., *Microelectronic Engineering*, (2015) 132, pp.1-13.

24 Y. Wang, K. Otsuka, Journal of Molecular Catalysis A: Chem. 111 (1996) 341

25 Raja, R., Sankar, G. and Thomas, J.M., *Journal of the American Chemical Society*, 121(50), (1999), pp.11926-11927.

26 Chen, F., Do, M.H., Zheng, W., Cheng, D.G. and Zhan, X., *Catalysis Communications*, *9*(15), (2008) pp.2481-2484.

27 G. Sankar, N. R. Shiju, I. D. Watts, S. Nikitenko and W. Bras, *Reserches in Chemical Intermediates* 34, (2008), 5-7, 649-658,

28 http://www.iza-structure.org/databases/ModelBuilding/Introduction.pdf

29 M.A. Zanjanchi,A. Ghanadzadeh, F. Khadem-Nahvi, *Journal of inclusion phenomena and macrocyclic chemistry*, (2002) *42*(3-4), pp.295-299.

30 L. Čapek, V. Kreibich,J. Dědeček, T. Grygar, B. Wichterlova, Z. Sobalik, J. A. Martens, R. Brosius, V. Tokarova, (2005) *Microporous and Mesoporous Materials*, 80(1), pp.279-289.

31 http://cars9.uchicago.edu/ifeffit/BruceRavel/Horae

32 http://xafs.org/Software/excurve

33 J. Chen, P. A. Wright, J. M. Thomas, S. Natarajan,L. Marchese, S. M. Bradley, G. Sankar, C. R. A. Catlow, P. L. Gai-Boyes, *The Journal of Physical Chemistry*, (1994), 98(40), pp.10216-10224.

Chapter 5

In situ XAS investigation of Fe and Fe/Ru substituted microporous catalysts under operating conditions

Summary

As well as iron, ruthenium is also active for catalytic selective oxidation reactions when introduced to zeolite materials. In order to examine the possible synergistic effect between metals, Ru was introduced into Fe-substituted nanoporous catalysts via wet impregnation. FeMFI, FeSAPO-5, RuFeMFI and RuFeSAPO-5 then were studied using *in situ* Fe and Ru K-edge EXAFS during calcination in air, activation in He, and pulsed experiments with N_2O/benzene. Results show reduction of Fe upon the introduction of benzene to the system, indicating that the catalytic mechanism for the reaction may require this step for the generation of the active Fe species.

5.1 Introduction

Iron-containing solids, in particular, FeZSM-5 and FeAlPOs have higher catalytic activity in the selective oxidations of hydrocarbons such as benzene using nitrous oxide under relatively mild conditions in comparison with other transition metals such as Co and Mn[1,2]. Later studies on related catalysts then showed that bimetallic catalysts prepared by doping Fe substituted zeolites such as Fe-Ferrierite with noble metals such as Pt, Rh and Ru leads to an activation effect for the catalytic decomposition of nitrous oxide to N_2 and surface oxygen species[3].

This reaction is also the first step of the catalytic mechanism for the oxidation of hydrocarbons with N_2O, generating the active iron coordinated α-oxygen species within the catalyst that can then go on to oxidise the hydrocarbon[4]. More specifically a comparative study[5] between and Rh-ZSM-5 (prepared by incipient wetness impregnation) and Fe-ZSM-5 (prepared by liquid-ion exchange) were shown to have displayed low (< 550 K) and high (> 650 K) temperature catalytic activity, respectively for the decomposition of N_2O. This has been proposed to be due to significantly stronger reversible N_2O adsorption and faster desorption of O-species on the Rh catalyst. Catalytic studies on FeRu-Ferrierite (FER) zeolites highlight a synergic effect of between Ru and Fe species as a conversion of this reaction is much higher than the sum of the individual monometallic analogues Fe-FER and Ru-FER if some NO is present[6]. This effect also manifests itself in the presence of O_2 and H_2O, which traditionally have been found to deactivate the catalysts, leading to the possibility of such novel bi-metallic catalysts to be useful in real-world exhaust stream applications.

The enhanced activity of these bimetallic catalysts is thought to be the result of a synergistic interaction between Fe and Ru found in close proximity to each other, with the Ru lowering the activation barrier required to reduce the active Fe sites[7]. It has been demonstrated that this synergistic effect gives superior N_2O decomposition activity under realistic working conditions in nitric acid production plants, i.e. in the presence of water and NO, at temperatures as low as 350°C.[8] It was found that in the presence of NO, the total conversion of N_2O over the bimetallic zeolite catalysts was found to

exceed the sum of conversions over the equivalent monometallic analogues of the individual components. A synergistic effect between the metals is proposed to be responsible for this phenomenon, and such synergies are often down to interesting phenomena such as redox coupling. It was also found that the bimetallic catalysts were much more resistant to inhibition by both O_2 and H_2O than their monometallic analogues[8].

Due to the remarkable change in activity induced by Ru in the nitrous oxide decomposition (NOD) reaction, we were very interested in studying related bimetallic Fe-Ru systems, in order to investigate whether the catalytic oxidation of benzene to phenol reaction (OBP) is also enhanced by the presence of Ru in FeMFI and FeSAPO-5. FeSAPO-5 is particularly interesting to study as the Si in the framework, unlike FeAlPO-5 studied earlier, confers different bonding sites and acidic properties, which may change the catalytic activity and thermodynamic stability of the catalyst[5,9,10]. Ru was incorporated into the nanoporous zeolite samples via wet impregnation using a ruthenium nitrosyl nitrate. The surface coverage of a surface metal oxide species is generally an important parameter in modulating the selectivity since it can suppress side reactions and affect reactions that require two adjacent sites[11]. Similarly, secondary surface metal oxide additives, such as Ru in this study, can also modulate the reaction selectivity by influencing side reactions or enhancing the desired reaction (especially if the reaction requires two adjacent surface sites). XAS studies on RuFe-ZSM-5 and RuFe-SAPO-5 have not been reported in the literature; however an XAS study of Fe-Ru/SiO_2 has shown that the presence of Ru helps to facilitate the reduction of Fe on SiO_2[12].

In order to examine the synergistic effect between iron and ruthenium and the resultant catalytic activity, *in-situ* studies during both the activation of the catalysts and the catalytic decomposition of nitrous oxide (NOD) and oxidation of benzene to phenol (OBP) reaction was carried out at beamline B18 at the Diamond Light Source.

The aims of the experiment were:

(i) To study the structure of Ru-impregnated Ru-Fe and pure Fe-based microporous catalysts and the changes occurring to the metal atoms during autoreductive activation by heating in He.

(ii) To investigate the effect of Ru on the state of Fe in substituted microporous catalysts.

(iii) To obtain insights as to the catalytic mechanism and reactant interactions with the Fe and Ru active sites.

The low Fe and Ru doping in these materials and the non-uniform distribution of metal ions make XAS a most valuable tool for the detailed understanding of these systems, especially when combined with XRD data. *In situ* Fe and Ru K-edge EXAFS measurements were carried out to monitor the effects of calcination in air up to 500°C, pre-treatment in He up to 800°C, and the introduction of benzene and N_2O at 350°C as a sequence of pulses in order to ascertain more detail on the role of the reactants on the Fe and Ru in the system. Throughout the course of the experiments it became clear that the amount of sample used in the EXAFS measurements was too small for the acceptable flow rates and gas volumes used in the experiment to detect the production of any oxidised benzene products with any confidence. The MS was still used during the experiment for monitoring gas purity, leaks and successful switching between gas streams.

5.2 Experimental

5.2.1 Catalyst Preparation

All nanoporous Fe catalysts were prepared via a traditional hydrothermal synthesis route from inorganic precursor salt solutions and structure-directing organic templates.

FeMFI with an Si/Fe ratio of 1:33 and 2wt% Fe was prepared via an isomorphous substitution method using hydrothermal synthesis. In typical synthesis for FeMFI, water was first acidified with H_2SO_4 until reaching a pH between 0-1. To this solution the appropriate amount of iron sulphate heptahydrate ($FeSO_4.7H_2O$) was added and stirred until fully dissolved (~1 hour) leaving a deep red solution. Tetraethyl orthosilicate ($Si(OC_2H_5)_4$) was then very slowly added drop wise, to the acidified iron solution with vigorous stirring. The organic structure directing template TPAOH (tetrapropylammonium hydroxide) was then added and the solution and stirred at 200rpm for 2 hours forming a homogenous cloudy gel, the composition being $3SiO_2$:25TPAOH:$230H_2O$. The resulting gel was then placed in a Teflon lined stainless steel autoclave and heated to 165°C under autogenous pressure for 4 hours. Following this the crystallised product was then filtered, washed several times with deionized water until a neutral pH was obtained from the washing solution, and then dried at 120°C overnight, The powder was then subsequently calcined in air for 5 hours at 550 °C resulting in a fine tan coloured powder.

FeAlPO-5 and FeSAPO-34 were synthesised with an Fe and Si content of 4 wt%. Aluminium hydroxide hydrate ($Al(OH)_3.xH_2O$) was first dissolved in a solution of phosphoric acid (H_3PO_4, 85%) with deionised water in a polypropylene beaker. An aqueous solution of iron acetate ($Fe(CH_3COO)_2.4H_2O$) was then dissolved in a minimum amount of water and added drop wise to the solution mixture under stirring. In the FeSAPO-34 synthesis, an appropriate amount of colloidal silica sol (SiO_2) was also added to the solution mixture at this point of the preparation. This mixture was then stirred until homogeneous for 4 hours. After rigorous stirring, the organic template TEAOH (tetraethyl ammonium hydroxide) was then added slowly to the solution. The final gel composition was $0.94.Al_2O_3$:$0.8P_2O_5$:$0.04Fe_2O_3$:0.75TEAOH:30.8;H_2O for FeAlPO-5 and 0. $04SiO_2$:$1.0Al_2O_3$:$1.0P_2O_5$:$0.04Fe_2O_3$:0.75TEAOH:30.8;H_2O for

FeSAPO-34. The final viscous orange gels are then stirred vigorously for 20 hours at 300 rpm. A Teflon liner was filled with the gel to 50% of the total volume and was placed in a stainless steel autoclave and heated under autogenous pressure at 165°C, for 4.5 hours and 2 days for FeAlPO-5 and FeSAPO-34 respectively. After cooling, the product was recovered by filtration and washed several times with deionized water until a neutral pH was obtained from the washing solution. This was then dried at 120°C for 12 hours, followed by subsequent calcination in air for 5 hours at 550 °C resulting in fine white powders.

All of the Ru impregnated derivatives were synthesised by incipient wetness-impregnation of the calcined Fe-zeolite powders, using an appropriate amount of 16% Ru ruthenium nitrosyl nitrate solution ($Ru(NO)(NO_3)_x(OH)_y$). This was then dried at 120°C for 12 hours, followed by subsequent calcination in air for 5 hours at 550 °C giving fine dark red-brown coloured powders. The amount of Ru in the final calcined catalyst was calculated to be 4wt%.

5.2.2 *In situ* XAS Measurements

The EXAFS spectra were processed, refined and fit to simulated model data in order to examine a range of information, including studying the effects of redox behaviour. Information from *in situ* XAS measurements was then analysed. This focused predominantly on the changes to the oxidation state and local coordination geometry of Fe and Ru species in the sample, particularly the effect of pre-treatment with autoreduction in He, and the behaviour under operating conditions with some samples also being examined under in-situ measurements performed whilst switching between a benzene or N_2O enriched atmosphere as a sequence of pulses using a specially designed microreactor setup[13]. This sample environment consisted of a generic sample cell with temperature control and gas mixing switching capabilities which covers a wide range of catalytic processes. The set up allows one to mimic operating conditions and at the same time, offers the flexibility to be able to study the catalyst's structural properties by a wide range of techniques. The reactor used was compatible with combinations of X-ray absorption spectroscopy, mass spectrometry and X-ray diffraction measurements under time-resolved, in situ conditions.

I*n-situ*, time and temperature-resolved Fe and Ru K-edge EXAFS measurements were performed at the main XAS beamline, B18 at the Diamond Light Source in Oxfordshire. The samples of Fe/Ru-containing microporous catalysts FeMFI, FeSAPO-5, and their Ru doped counterparts Ru/FeMFI and Ru/FeSAPO-5 were studied in order to examine the effect of the introduction of Ru to the system, as well attempt to as any synergy between bimetallic species formed such as the presence of possible Fe-O-Ru type bonding arrangements or Fe-Ru alloy formation.

The *in-situ* experiments performed during both the activation of the catalysts, the catalytic decomposition of nitrous oxide (NOD) and oxidation of benzene to phenol (OBP) reaction were carried out using a custom built furnace connected to a mass spectrometer for product analysis. The aim was to establish a detailed understanding of the active species in the sample, the effect of Fe-Ru interactions, the evolution of Fe and Ru species throughout activation in He, and details on catalytic mechanism of the NOD and OBP reaction via analysis of the composition outflowing products gas stream. The low Fe and Rh concentrations (3% and 1% respectively) and the random or non-

uniform locations of the substituted metal atoms and clusters, and the likely existence of amorphous phases of interest in these materials, make XAS a most valuable tool for the detailed understanding of these types of systems.

During this beamtime, three Fe-based microporous catalysts Fe-ZSM-5, FeSAPO-5 as well as their Ru-doped bimetallic counterparts, Ru/Fe-ZSM-5 and Ru/FeSAPO-5 were investigated by *in-situ* Fe K-edge X-ray absorption spectroscopy (XAS) during the following activation and reaction conditions:

1. Fe K-edge XAS measurements on the activation of FeMFI, Ru/FeMFI, FeSAPO-5 and Ru/FeSAPO-5 catalysts by heating in He gas from room temperature up to 850^{o}C.

2. Ru K-edge XAS measurements on the activation of RuFe-MFI and RuFe-SAPO-5 by heating in He gas from room temperature up to 550^{o}C.

3. Following both of the above activation treatment experiments, *in-situ* catalysis experiments of the above samples were attempted. The samples were to be cooled down from the activation temperature to 350°C in flow of He. Once the catalyst sample was at this temperature, pulsed reactant gas switching experiments were performed. This involved introducing a flow of N_2O and benzene, to the sample via a gas switching microreactor system in sequential 15 minute pulses. He gas was used as a carrier medium for the benzene vapour, which was introduced to the gas stream by bubbling through the liquid benzene at room temperature. The i*n-situ* Fe and Ru K-edge XAS measurements performed during this experiment were designed to help elucidate the effect the reactants have on the catalytically active Fe and Ru species in the samples. By separating the two reactant gases into sequential pulses the changes in properties such as oxidation state, coordination, and geometry of the region surrounding the absorbing atoms could be deduced from the XAS data. The series of experiments was unfortunately not able to be carried out exactly as planned due to technical problems, but some of the experiments on RuFeSAPO-5 samples provided good data and were analysed showing interesting changes to the Fe and Ru in the system.

EXAFS measurements of the Fe and Fe/Ru catalytic materials were performed in an appropriate *in situ* high-pressure capillary cell (Figure 5.1). Samples were placed

within a 0.5 mm diameter sapphire capillary and held in place via stopping the ends with glass wool. At one end is the gas inlet port, and on the other the outlet flow to a quadrupole mass spectrometer to monitor gas purity and composition.

The gas micro-reactor system that was commissioned at Diamond and built by Anna Kroner with assistance from myself was used for this experiment.

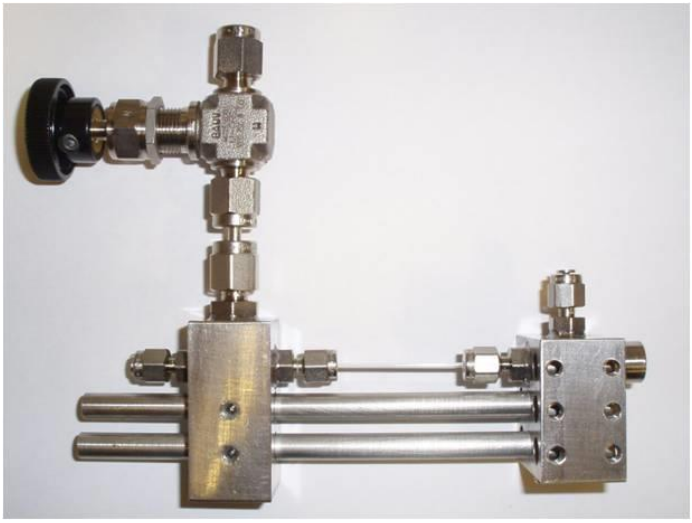

Figure 5.1. *Image of the high-pressure capillary sample cell used for the in-situ studies*

The gas-switching micro-reactor system developed in-house at the Diamond Light Source was used to switch and deliver the gases throughout the experiment. Gas phase composition was monitored simultaneously with EXAFS scans using a quadrupole mass spectrometer. The microreactor was equipped with a gas supply system combining controlled flow-rate and fast switching valves, an integrated heating system (air gun) and a quadrupole mass spectrometer to monitor gas composition online under various conditions. This set up allowed one to carry out investigations of the sample under changing temperature composition and flow conditions using a variety of gases.

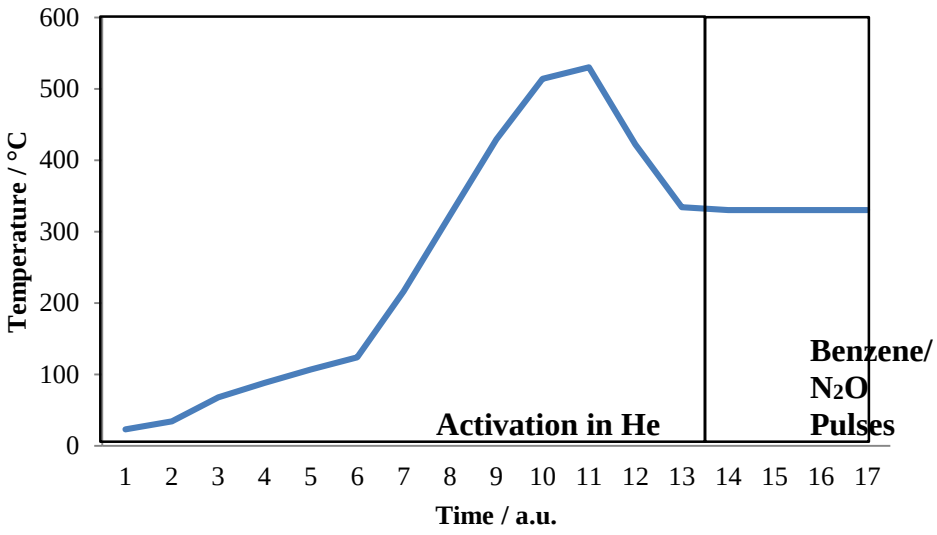

Figure 5.2. *Temperature profile of the high temperature activation of the catalysts in He to 550°C, followed by the pulsed benzene/N_2O experiment at 350°C.*

Following activation of the catalyst samples in flow of He gas at high temperature (550 or 850°C) the sample was then cooled down at a rate of 10°C/min back to 350°C, which is the reported active temperature for the OBP reaction using these types of nanoporous catalysts.[14,15] All this was conducted under a continuous flow of He at a flow rate of 15 ml/min. Once at 350°C the pulsed experiments were begun, whereby first benzene vapour diluted in He was passed through the sample for 15 minutes. Then the gas was switched to N_2O gas in He for a further 15 minutes. The procedure was repeated twice more yielding data 3 pulses of each alternate gas mix.

Unfortunately various technical problems were encountered, most often during the start of the pulse test that did not allow most of the experiments to be completed according to the original experimental plan. This included back-pressure causing the failure of the tubing connections, causing ambient air and into the system, unexpected detector re-fills, beam down-time due to failure of the RF boosters in the synchrotron storage ring, and at one point the quadrupole MS filament and gasket needing replacing during a gas switching experiment. Notwithstanding these issues however, good quality data was

collected for all samples, and the results have afforded a valuable insight into the changes occurring to both Fe and Ru in such bimetallic nanoporous materials.

Out of the 4 samples studied in 6 attempted experiments (4 Fe K-edge and 2 Ru K-edge), only one experiment could be completed for the Fe K edge including the pulsed N_2O/benzene tests - that of RuFeSAPO-5). Data from partial or fully completed activation procedures in He was collected for all samples and will be discussed thoroughly, as well as the results from the successful pulsed experiment, its analysis and implications of the data interpretation.

5.3 Results and Discussion

The data were processed to obtain the oscillatory $\chi(k)$ function by removing the background and normalizing the data above the rising edge and using the program ATHENA with the standard procedure used in EXAFS analysis. The program EXCURVE was used to fit the Fe K-edge data and the program ARTEMIS was used to process the Ru K-edge data. The use of two different programs was decided due to the different natures of the Fe vs. Ru species. Firstly ARTEMIS, whilst being a newer program, was found not suitable for analysing the Fe K-edge data, whereas EXCURVE provided good results that concurred with the expected states, gave a good fit of model and theory spectra with low statistical error (*R*-values). This is because EXCURVE can perform single-scattering calculations from the inputted parameters (absorbing atom -Fe surrounding atoms – O, Si/Al/P etc., initial values of N, σ^2, $R_{\text{Fe-O}}$) and create a suitable physical model to fit the EXAFS results. ARTEMIS however, although based on the same physical principles, uses a different algorithm for generating the atomic potentials and scattering paths from different atoms, which requires the provision of a crystal structure (*.cif* file) to be input before any potentials and scattering paths can be calculated for the fitting model. The small concentration and random distribution of the Fe atoms in the materials does not allow this use of a crystal structure in the calculation, as none exist that provide any justifiable model for the iron sites in this type of material. Indeed qualitative comparison of the Fe K-edge EXAFS data obtained in FeMFI and FeSAPO-5 is distinctly different from that of all iron oxide references used for comparison. XRD results also fail to show any bulk FeO, Fe_2O_3 or Fe_3O_4 phases, indicating the presence of either highly dispersed mononuclear or oligonuclear Fe species. Any bulk oxide particles that may be present are too small for detection via XRD. The data for the Fe K-edge XAS measurements was also quite noisy and high k-components were hard to resolve, but adequate fits were achievable by merging the Fe data scans in groups of three. This reduced the time (and temperature) resolution from 6 minutes scan time to 18 minutes (ΔT ~ 20°C) between points. The EXCURVE algorithm however can fit both amorphous and average environments very well and was found to provide the most logical, consistent and reliable results.

Alternatively the Ru-Kedge results show the starting material to have an EXAFS $|\chi|2$ component which is qualitatively (and as it turns out, quantitatively) similar to the signal obtained from the reference RuO_2 compound whose XAS data was also collected at room temperature in air.

Fits obtained using the program ARTEMIS based on initial scattering paths computed from model crystal data for RuO_2[16] were found to generate good fits for the Ru-K-edge data at low temperature, when considering a single first oxygen shell fit. Ru K-edge EXAFS data was of much better quality than the corresponding Fe K-edge data, particularly considering the signal to noise ratio. Based on this, an attempt was made to fit the Ru data to a more complex model involving 3 different O shells and one Ru shell over a larger R-range. However when comparing these model results to the single O shell fitted data, no statistical improvement in reliability of the fit was found, and thus this avenue was abandoned after various attempts using both ARTEMIS and EXCURVE programs in single and multiple scattering procedures.

The program ATHENA was used to remove the background effects and normalise the data. The absorption spectrum EXAFS oscillation was converted to k-space over the region from 1-10 $Å^{-1}$ for Fe K edge data, and between 2-13 $Å^{-1}$ for Ru K-edge data. A sound analysis requires reliable values of the parameter known as the amplitude reduction factor, S_0 . S_0 is a correction to the EXAFS theory which accommodates the relaxation of the outer shell electrons in the presence of the absorption induced core-hole. It is well approximated by a single number and is typically between 0.7 and 1.0, but it is not usually known *a priori* for any element.[17,18]

The amplitude reduction factor is usually treated as an empirical parameter in EXAFS data analysis, although a few values have been calculated theoretically [19]. In the majority of past studies, as in this one, it is assumed that the value of S_0 is constant for each specific element regardless of the environment or compounds it is incorporated into. This is an assumption that the author would like to question based on the apparent importance and dependence of other parameters such atomic potentials and phase shifts which are perturbed by the surrounding atoms. The practice of assuming an unchanging value of S_0 for each element regardless of the surrounding ligand field has recently been questioned and investigated by Reher et al[20]. They compared the

experimentally measured amplitudes of the EXAFS spectrum which were are smaller, typically by a factor of ½ than results calculated from one-electron theories. This has led to suggestions that the discrepancies in the reduction factor may be largely accounted for by a theory based on the relaxation of passive electron orbitals accompanying the photoemission process - which allowed a straightforward approximate calculation in terms of a many-body overlap integral. Using ab initio Hartree-Fock-Roothaan calculations and estimates for correlation effects, they managed to calculate the reduction factors of 0.60, 0.64, and 0.64 (±0.04) for F_2, Cl_2, and Br_2, respectively, which was in approximate agreement with experiment. These numbers were 7%-14% smaller than those for free halogen atoms, and indicated that chemical effects (particularly molecular charge transfer) are important in determining the EXAFS reduction factor. The possible contributions to the EXAFS spectrum from these channels was estimated to be about 10% of the total amplitude – correlating to errors in coordination number which is directly dependant on the S^0 term and highly correlated to the Debye-Waller factor. Such refinements to the theoretical values of S^0 are beyond the scope of this work but important for the future development of XAS interpretation and modelling. However by being consistent in methodology, processing and data fitting one can help minimise any variation between data sets for a particular element and obtain good quality fit results where the calculated values of the coordination number are reliable, particularly as a relative comparison.

However as is the standard procedure, using spectra collected for the known structures of $FePO_4$–quartz and RuO_2 as reference compounds, the amplitude reduction factors used in the calculations were computed and then set to 0.7414 and 0.8567 for the individual elements Fe and Ru respectively.

The data were then k^3 –weighted to enhance the high-k signal and then Fourier-transformed to produce a partial radial distribution (p-RDF) function around absorbing atom. The fits were carried out in the region 1.0 Å < r < 3.5 Å using a Kaiser-Bessel window spanning this data range in R-space. The now processed and normalised data from samples were then analysed using EXCURVE (for Fe) or the FEFF code (ARTEMIS – for Ru) to obtain average bond distance (*R*), coordination number (*N*) and the Debye-Waller factor ($2\sigma^2$) for the nearest Fe-O, Ru-O and Ru-Ru neighbours. Continuous refinement of the model and the inclusion/exclusion of parameters is then

carried out until an adequate model that both describes the plausible physical configuration of the system and results in a statistically sound fit between the calculated and measured spectra is generated. This also involves ensuring that the number of refined parameters, N_{ind} is a low as possible for a given k-space and R-space window used in order to give reliable parameter values.

5.3.1. FeMFI

The activation of FeMFI via heating in helium gas was successfully monitored using XAS during the activation procedure. The background-subtracted and normalized stacked X-ray absorption data, as well as the variation of the normalized pre-edge intensity recorded during the activation of FeMFI as at various temperatures from 30-850°C are presented in Figure 5.3.

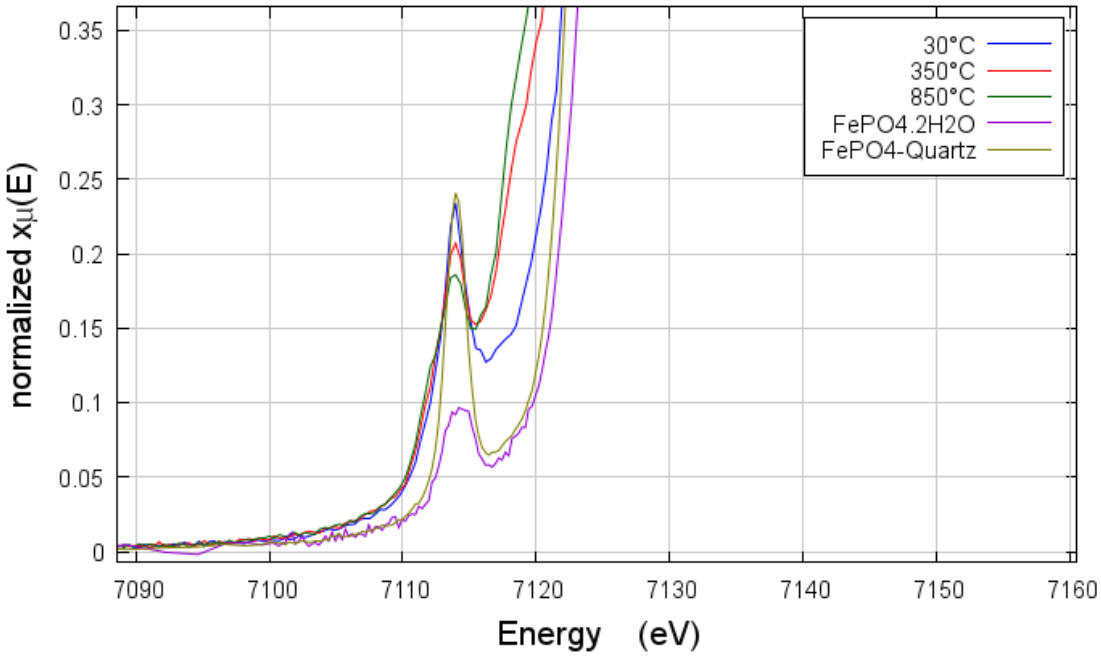

Figure 5.3. *Variation of the position of the rising edge absorption energy E_0 and maximum pre-edge intensity values for the normalised Fe K-edge XANES data collected for FeMFI during activation in He at 30°C (blue), 350°C (red) and 850°C (green). The reference compounds $FePO_4$-quartz (brown - T_d geometry) and $FePO_4.2H_2O$ (purple - O_h geometry) are also plotted for comparison. As the temperature is increased the E_0 moves to lower values as the Fe ions in the catalyst are reduced. The pre-edge feature also drops as the temperature is raised, indicating a reduction of symmetry from a near totally octahedral state to one with the majority of ions in a tetrahedral coordination state.*

As explained earlier in Chapter 2.4.1, the intensity of the pre-edge transition feature in the XAS spectrum depends on the geometry around the absorbing metal and can be correlated to structural symmetry[21]. Atomic bonding arrangements with high centrosymmetry are found to have a relatively low pre-edge intensity, whereas the intensity increases as the symmetry of the system is reduced. This change is due to the higher mixing of the *4p* with the *3d* orbitals, allowing the particular excitation to occur more readily in the system.

It is clear from the XANES spectrum shown in Figure 5.3 that the pre-edge feature for the canonically forbidden Fe *1s* → *3d* transition undergoes an appreciable change in intensity. The energy position, shape and intensity distribution, of the pre-edge feature were found to vary systematically with spin state, oxidation state, geometry, and bridging ligation. The most sensitive property to affect the pre-edge feature however is the coordination geometry of the absorbing atom. The pre-edge feature rises slightly in intensity as the temperature is ramped from 30°C to 850°C. This is attributed to the change in symmetry and corresponding increased transition state probability for the forbidden *1s* → *3d* transition to occur decreasing, due to the reduction in symmetry from an octahedral to a tetrahedral geometry. This is similar to but less pronounced than the effect observed earlier where calcination causes an increase in the pre-edge feature as the octahedrally coordinated Fe loses two coordinated Fe-O bonds as water and template molecules are removed, leaving behind mainly tetrahedrally coordinated Fe ions. For comparison, Figure 5.3 also shows the pre-edge feature collected for the standard Fe^{3+} references, dehydrated quartz-phase $FePO_4$ (tetrahedral geometry), and the dihydrate, $FePO_4.2H_2O$ (octahedral geometry – the Fe centre is octahedral with two mutually *cis*- water ligands).

Although the breaking of some Fe-O bonds seems to be occurring the majority of the Fe is still in the tetrahedral state as evidenced from the still quite large pre-edge feature. This increase in pre-edge can be assigned to the creation of extra-lattice Fe ions produced during autoreduction in He and further loss of any adsorbed water. The slight rise in pre edge seen here is likely due to the homogenisation and formation of Fe^{2+} principally in a tetrahedral configuration. This coincides with the change in the rising edge position in the XANES, as it is shifted from 7121.45 eV at room temperature to 7120.80 eV by 850°C, a total of 0.65 eV as some of the Fe^{3+} is reduced to Fe^{2+}.

Unfortunately the energy resolution at the relevant region was not adequate enough to observe the expected small corresponding change in the centroid position of the pre-edge feature as well as the change rising edge.

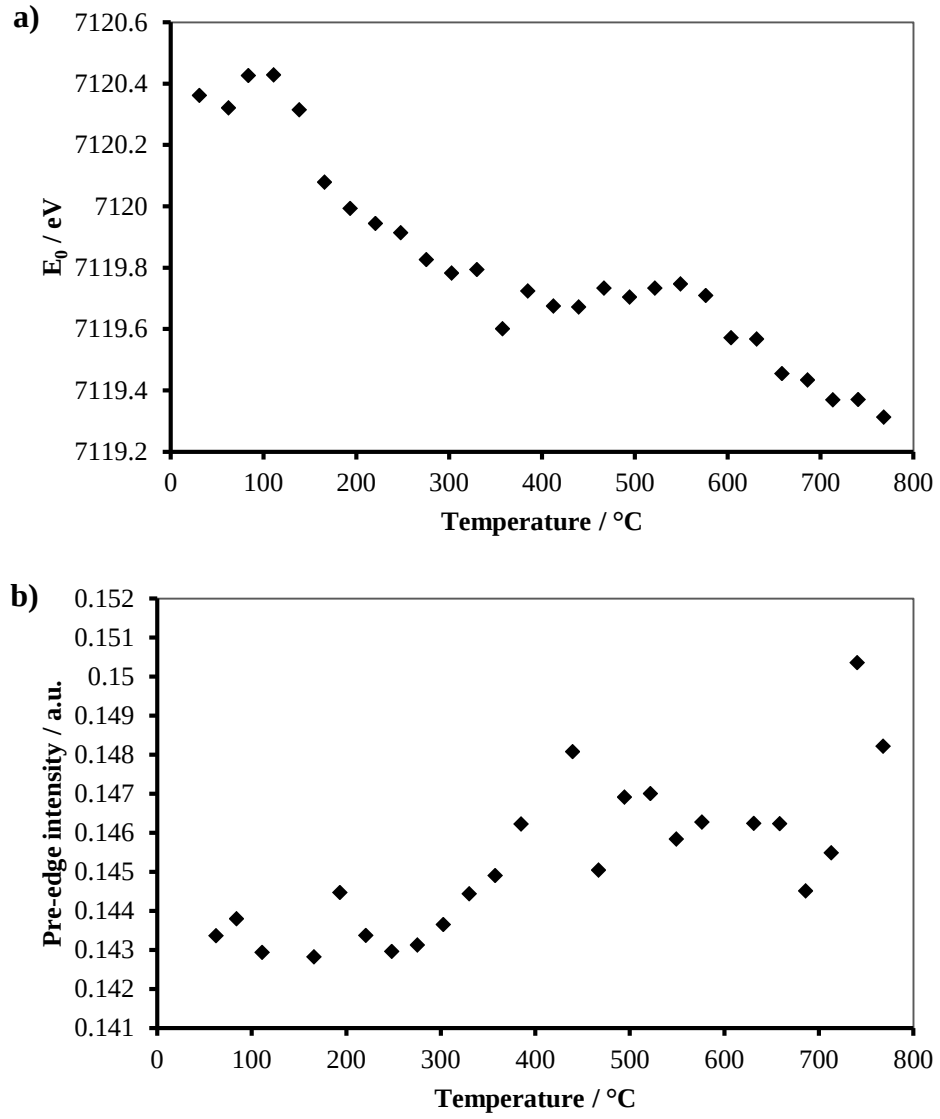

Figure 5.4. *Variation of rising edge absorption energy E_0,(a) and maximum pre-edge intensity (b) values for the normalised Fe K-edge XANES data collected for FeMFI during activation in He up to 800°C. Errors of the white line positions are ± 0.1 eV, and for pre-edge intensity ± 5%.*

Table 5.1. *White line energy E_0, pre-edge intensity and pre-edge energy position of selected samples and references. Errors in the white line positions are ± 0.1 eV, and for pre-edge intensity ± 5%.*

Sample	***White line energy, E0 /eV***	***Pre-edge intensity /a.u.***
Fe metal 30°C	7112.0	-
FeMFI in He at 850°C	7119.3	0.15
FeSAPO-5 in He at 570°C	7119.2	0.11
Fe (II) oxide 30°C	7119.9	0.07
FeMFI in He at 30°C	7120.3	0.14
FeSAPO-5 in He at 30°C	7120.9	0.10
FeMFI as synthesised	7121.3	0.09
FeMFI calcined 30°C	7122.2	0.08
$FePO_4$-quartz 30°C	7122.1	0.12
Fe (III) oxide 30°C	7122.9	0.05
$FePO_4.2H_2O$ 30°C	7124.5	0.07
FeAlPO-5 as synthesised 30°C	7124.4	0.05
FeAlPO-5 calcined 530°C	7122.9	0.08
FeSAPO-34 as synthesised 30°C	7124.5	0.04
FeSAPO-34 calcined 530°C	7123.5	0.08

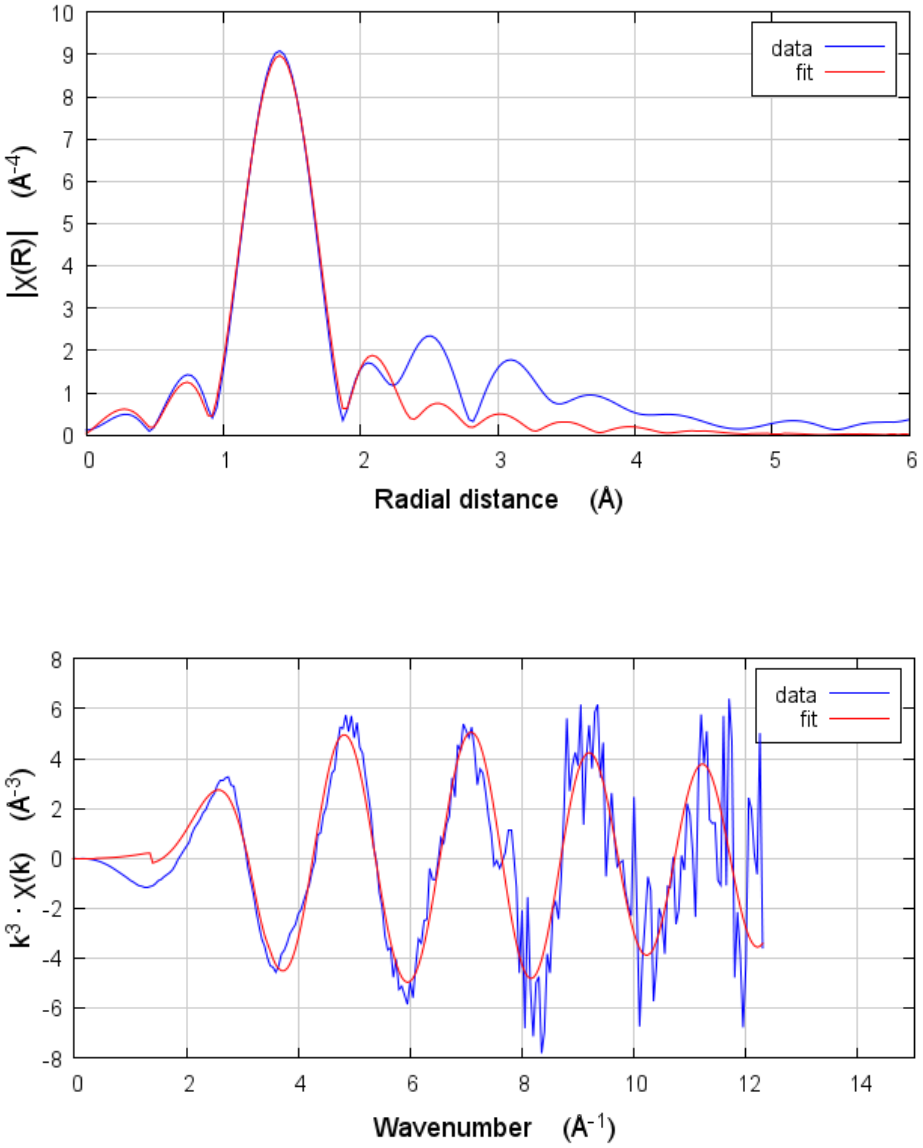

Figure 5.6. *Fits tot the Fe-Kedge EXAFS data analysed in k-space.(k^3-weighted) with associated Fourier transforms for FeMFI in helium at 30°C.*

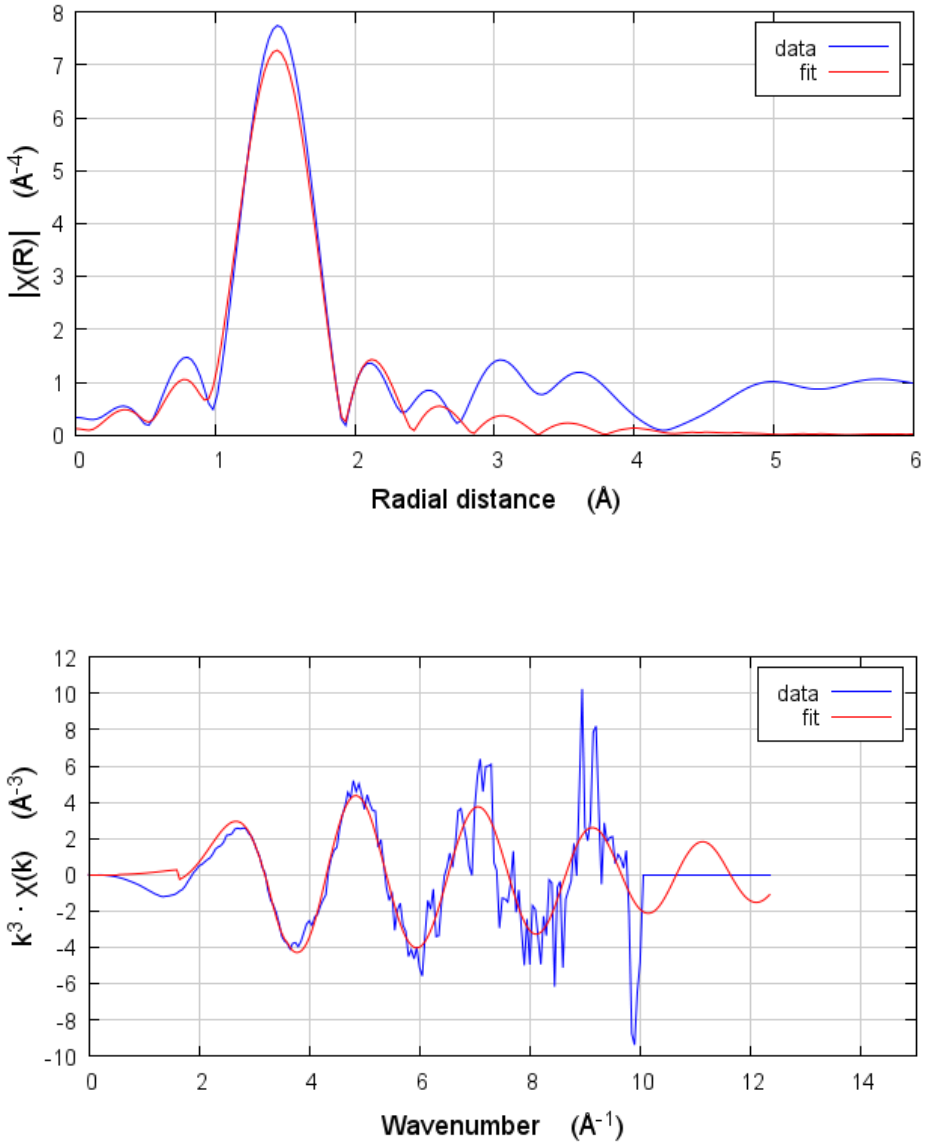

Figure 5.7. *Fits tot the Fe-Kedge EXAFS data analysed in k-space.(k^3-weighted) with associated Fourier transforms for FeMFI in helium at 850°C.*

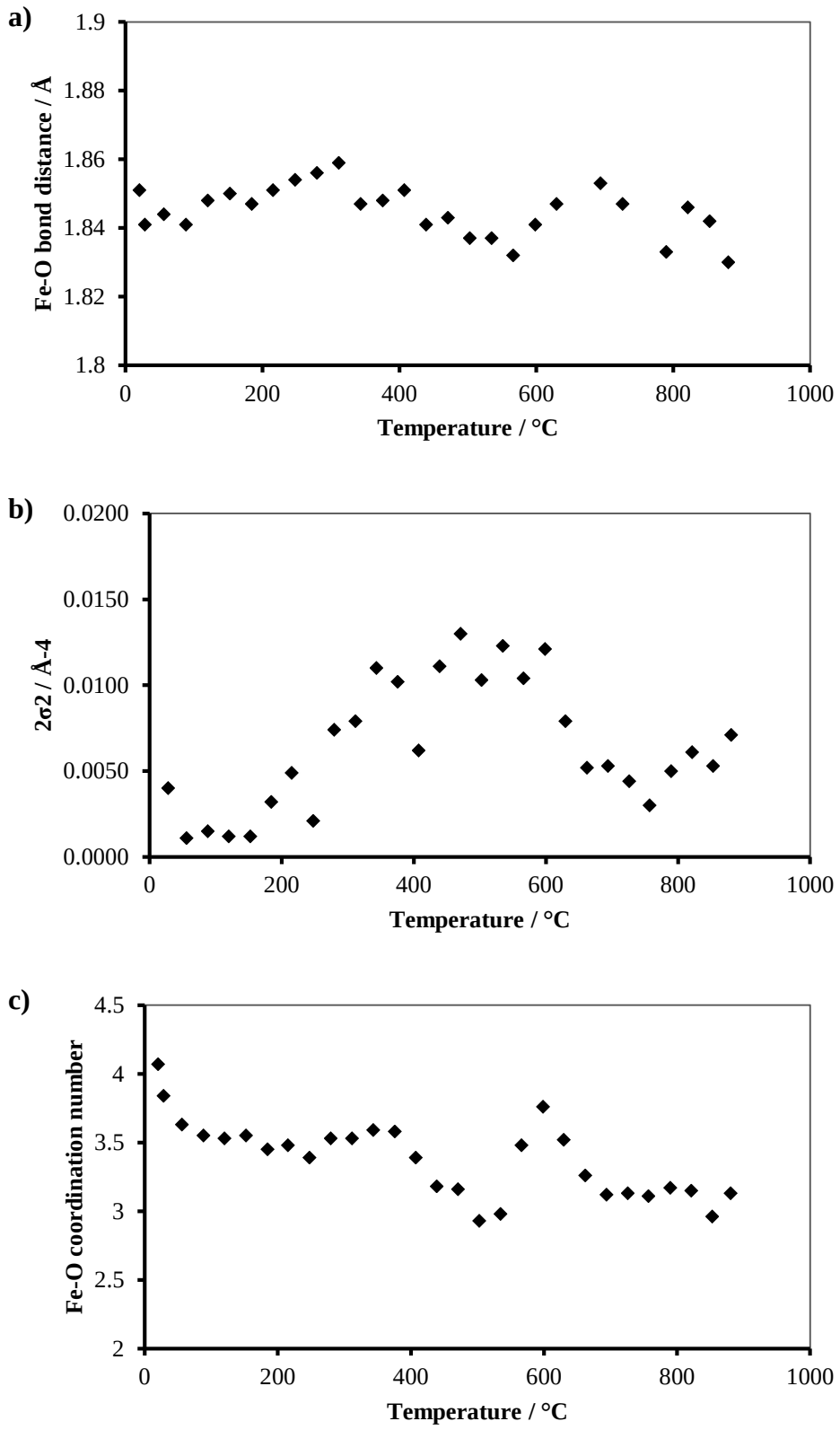

Figure 5.8. *Variation of parameters from Fe K-edge EXAFS fits during activation in He up to 880°C for FeMFI; (a) Fe-O bond length, (b) Debye-Waller factor, (c) coordination number. Errors for bond lengths are ± 0.01 Å. Errors in coordination number N, and* $2\sigma^2$ *are ~10%.*

The Fe K-edge Extended X-ray Absorption Fine Structure (EXAFS) spectrum, together with the associated Fourier transforms (FT) of the experimental and calculated data, are presented in Figure 5.7. The calculated data is based on the best fit to the first shell (Fe-O), in R space, since the primary aim of the study is to understand the oxidation state and local environment around the central iron atom, and how this evolves over temperature range as it is heated in He in a typical activation procedure for an FeZSM-5-type catalyst.

The largest band in the Fourier transform plot found between 1-2 Å for the EXAFS data collected for FeMFI is easily assigned to the first shell O atoms. A small set of peaks can be found at larger distances between 2-4 Å. These are the result of higher shell contributions, and although attempts were made to fit these higher shells they proved difficult and no unambiguous assignment of 2^{nd} or 3^{rd} shell neighbouring atoms could be made using Fe, Si or O atoms. The possible elucidation of Fe-Fe neighbours or Fe-O-Fe type bonding arrangements particularly in the activated state was anticipated; however they could not be fit satisfactorily in a manner that restrained the number of independent parameters used in the fit in the given R-range, as defined by the Nernst criterion as defined in Chapter 2. The possibility of a large scale disorder at large R-values is a possibility due to the multiple heterogeneous environments the Fe could be potentially in could also contribute to the complexity of the data.

The EXAFS data analysis showed that at 30°C calculated average Fe-O bond distance is 1.85 Å. From the outset of the heating ramp, the Fe-O coordination number drops from 4 to 3.5 up till 100°C. This can be assigned to the loss of coordinated water molecules from Fe ions[22]. This remains much the same until 400°C where a fluctuation occurs. The bond length seems to steadily increase up to about 310°C, where it then begins to drop until about 600°C, where it reaches a minimum value around ~1.83 Å concurrent with a fall in the coordination number from 4 to 3. This corresponds to the same temperature where we observe an increasing Debye-Waller factor, which reaches a maximum of 0.0140 $Å^{-2}$ in which the system is highly disordered. This is likely due to steric disorder caused by the transitioning of various oxide species as the Fe in the sample is auto-reduced in He, as the total Debye-Waller factor then drops to lower

values at higher temperatures once the temperature rises above 600°C. This transition is substantiated by the fact that the calculated coordination number briefly rises to a higher value of 3.8 at this temperature region as well and the Fe-O bond distance also shrinks to 1.83Å. This can be explained by the removal of Fe ions from the framework during autoreduction, forming mononuclear tetrahedral Fe species dispersed in the zeolite cavities. At the transition occurring around 600°C the total $2\sigma^2$ value then drops dramatically by half, from 0.0120 $Å^{-2}$, until stabilising around 0.060 $Å^{-2}$ indicating that the earlier peak increase in entropy was dependent on static contributions from varying Fe coordination geometries. This drop in $2\sigma^2$ to a stable low value at at temperatures above 600°C to 800°C shows the Fe system has reached a thermodynamically stable phase.

The observed rise in the pre-edge intensity and calculated fits of EXAFS results show that further Fe is extracted from the framework and more lower symmetry tetrahedral species are created during He treatment along with the concurrent reduction of Fe^{3+} to Fe^{2+}. In the autoreductive He treatment a transition is observed to occur at around 600°C, leading to less static disorder and more coordinatively unsaturated Fe.

During the activation procedure between 30 and 100°C H_2O is lost from the coordination shell of the Fe ions in the system. After this two main redox phase transitions can be said to be occurring between 100 – 400°C and another above 600°C as evidenced from the E_0 position and calculated EXAFS parameters. Whether the observed changes in average environment of the Fe in the sample are due to two successive transformations of the same Fe species or two or more different species undergoing reduction separately at two different temperatures cannot be concluded definitively from these experiments, but more characterisation can help shed light on this, such as the use of XPS or Mossbauer spectroscopy. Following reduction in He up to 800°C the system contains more Fe^{2+} versus Fe^{3+} ions in extra-framework positions. These are likely to be highly coordinatively unsaturated monodispersed Fe atoms in a distorted tetrahedral environment or possibly Fe-O-Fe dimers grafted to the framework as evidenced by the E_0 values, Fe-O bond lengths and low coordination numbers as well as other calculated parameters. However an Fe-O-Fe shell for the iron at the expected distance of around 3Å could not be fit for any of the data. This may be due to the

absence of binuclear clusters or if they are present the large disorder at these R-values based on the inhomogeneous nature of Fe in the samples. Many authors[23,24,25] purport to a bimetallic oxygen bridged Fe-O-Fe type active sites as being responsible for benzene hydroxylation in FeMFI. However the work herein was unable to find any contributions from any Fe scattering paths at the expected distance from the central absorbing Fe atom, beyond the first shell oxygen atoms. Other studies[26,27] have also since indicated that the earlier assumption that binuclear Fe-O-Fe bridged species were the most active species for NOD and OBP into question. Although good quality EXAFS data was obtained, the work in this thesis which does not find any evidence for a nearby Fe-O-Fe type scattering path sheds doubt on the purported wide occurrence of such species in all the microporous samples studied herein, both in the as synthesised, calcined, and He activated samples . That there could be such species present is not in doubt, but they must form a very small fraction of the total Fe species in the samples, the majority of them being more like isolated FeO_4 type tetrahedra grafted onto the framework, or very small FeOx nano-clusters.

The active sites formed in the FeMFI sample investigated in this thesis are in good agreement with earlier EXAFS studies[28,29] which report the distances for the Fe–O bonds at the low iron concentration in the range of 1.80–2.25Å. The EXAFS results also corroborate with recent computations based on monometallic Fe model active sites by Sirijaraensre and Limtrakul[30]. In the study different forms of iron-oxo species were considered for the active center of Fe-ZSM-5, including $[FeO]^+$, $[FeO_2]^+$ and $Fe(OH)_2]^+$. A comparison of the energetic profiles suggested that a dehydration process would take place through the oxidative dehydration mechanism in which an $[FeO]^+$ type species is both common and also the most reactive form of mononuclear Fe in Fe-ZSM-5.They computed the Fe–O to all lie in the range of 1.82–2.16Å. For the $[FeO]^+$ cation active site the iron center was computed to be trigonally coordinated with an a-oxygen and the two atoms of bridging-oxygen with the Fe–O bond distances of 1.64, 1.99, and 2.07 A. This corresponds to the pre-edge increase we observe during activation, and the coordination number, *N* change from 4.1 at room temperature to 3.1 following activation. The one-step oxidation of benzene with N_2O to phenol was also studied over the iron zeolite catalysts FeMFI by Pillai *et al.*[27] A plot of the activity as a function of the loading with accessible Fe, showed that mono-nuclear sites were much more active for the reaction than binuclear sites. Steam activation at 923 K of the catalysts was found to be instrumental in the formation of extra-framework Fe sites, required for the

reaction. Their work also implicated that H_2O plays an important role in the reaction mechanism by displacing the phenol from the sites.

It is likely that mononuclear, binuclear and oligonuclear Fe can all be present at different concentrations in active catalyst samples, depending on synthesis procedure, composition and activation history and all types may be active sites for the reaction, albeit at different rates.[31,32] An attempt at the pulsed experiments was then tried but at the first instance of introducing gas into the system it was found that there was a leak in the system causing the sample to be re-oxidised, thus ending the experiment prematurely.

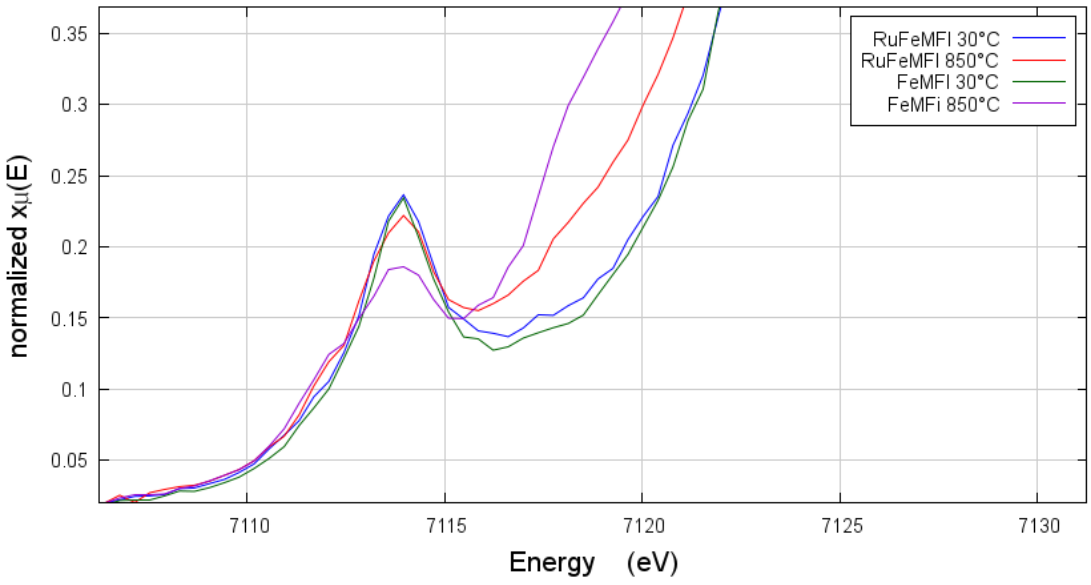

Figure 5.9. *Comparison of the variation of position of the rising edge absorption energy E_0 and maximum pre-edge intensity, for the normalised Fe K-edge XANES data collected for FeMFI and RuFeMFI during activation in He. From the movement of the rising edge to lower energy values and the drop in pre-edge peak intensity it is clear that the sample is both being reduced, and undergoing a change to lower symmetry from an original tetrahedral-like geometry. The Fe in both samples starts in a very similar state, but the evolution of Fe reduction and uncoordination during the pre-tereatment seems to be affected to a large extent by the presence of Ru in the samples. The Fe in RuFeMFI does not reach as high a level of reduction as the FeMFI at 850°C.*

5.3.2 RuFeMFI

RuFeMFI was synthesised by the incipient wetness impregnation and calcination of FeMFI using an aqueous solution of $Ru(NO_3)_3NO$. Based on the calculated Fe-O bond distances and Debye-Waller factors, obtained from fits to the EXAFS data, it is clear that the local environment of Fe does not seem to change very significantly over the whole temperature range studied, especially when compared to the results seen earlier in the activation of the un-doped FeMFI The most dramatic change to occur is in the temperature range between 30 and 200°C. This is especially true in terms of the coordination number for RuFeMFI which begins at ~3.5 throughout the experiment. This is seen to drop to a value of 3 by the time the temperature reaches 250°C. An obvious corresponding change in Debye-Waller factor and Fe-O bond length is not as easy to pick out from the EXAFS data, but this drop in coordination number is accompanied by a simultaneous dramatic reduction in the edge jump energy E_0 which changes from 7121.5 eV at 30°C to 7120.8 eV by 250°C. On the other hand the pre-edge intensity remains largely statistically the same considering the spread of values, with only a slight increase over the whole pre-treatment apparent indicating the loss of symmetry for the Fe ions as they change their geometry and coordination during autoreduction.

From the calculated EXAFS data it can be seen that RuFeMFI begins with a coordination number of 3.5 which is lower than that of the un-doped FeMFI which began at 4, whose pre-edge and N value indicating Fe in a tetrahedral geometric configuration. This could be explained that this sample has undergone a second calcination that followed the impregnation step with $Ru(NO)(NO_3)_3$ to remove the nitrogenous ligands and form Ru-zeolite support interactions. This would have led to the dehydration of the Fe and creation of extra-framework species as well as sintering the Ru in the sample and creating ruthenium oxide species. The RuO_x in the system may prevent the Fe ions from becoming re-hydrated following subsequent cooling of the sample in air. There is also the possibility of forming Fe-Ru alloyed metallic nanoparticles in He at high temperatures and low oxygen partial pressures.

The values obtained for the Fe-O bond distance show some fluctuation, but this is all within error (10 % or roughly ~0.20 Å) of a value that is the same as that for the distance measured at the start of the experiment with FeMFI. The R_{Fe-O} value remains around this value until above 600°C where a small drop occurs to 1.84Å.

More obvious is the change in Debye-Waller factor which gradually increases from an initial value of 0.002 to 0.014. This corresponds to the increased disorder of the system which can be attributed both to the thermal effects caused by increased bond and lattice vibrations, and the generation of a higher number of different Fe species in the sample, such as Fe^{2+} moieties formed by the autoreduction of extra-framework Fe^{3+} formed during calcination, as well as the formation of possible Ru/Fe alloy, although during the data analysis, the results could not be fit to any Fe-Ru scattering contributions and no evidence could be deduced of their vicinal interaction via the EXAFS analysis.

The increase in Debye Waller factor is also the opposite behaviour to that seen during the calcinations carried out in Chapter 4, where the Debye-Waller factors were seen to decrease as the static disorder for the system was reduced.

Compared to the data from FeMFI it is surprising to see that there is less change in the coordination number and also a dramatically lower Debye-Waller factor, that gradually increases throughout the activation procedure. This shows a gradual evolution of the Fe species whose transformations that occurred at 500 °C, are possibly suppressed by the presence of Ru in the system. This could be related to RuO_2 type species in the microporous voids or coating the surface of the zeolite microcrystals may prevent the migration and reduction of Fe, especially considering how much more facile Ru is to reduction by He. The reduction of Fe in this compound is also apparent but to lesser degree compared to FeMFI (Figure 5.10). Overall further reduction and extraction of Fe^{3+} moieties in RuFeMFI to extra-framework positions seems to be partly inhibited bu RuO_2 nanoparticles, but grafted Fe atoms in the framework are likely able to undergo some dehydration and distortion during NTE and high temp treatment, explaining the reduction of the pre-edge feature and drop in coordination number.

Interestingly when to its Fe only counterpart, the Fe K-edge white line position E_0 is consistently higher for RuFeMFI during the activation procedure, by about 1 eV (Figure

5.10) This is indicating that the Fe is stabilised at a higher oxidation state (i.e. more Fe^{3+} compared to Fe^{2+}). At room temperature the E_0 value for FeMFI is at 2121.4 eV which remains constant up to about 200°C. At By 250°C (the same temperature corresponding to a drop in Fe-O coordination number) the value drops suddenly to ~7120.5 eV, just above the room temperature E_0 value for FeMFI at 7120.4 eV. C and thereafter gently rises to stabilise at a slightly higher value of around 7120.8 eV by 400°C. Throughout the activation the Fe in RuFeMFI is consistently more oxidised, and the lowest average oxidation state achieved is in fact comparable to the starting oxidation state of FeMFI. This shows that when Ru is in the system the Fe cannot be reduced to the same extent as in the traditional types of catalyst. The fact that RuFeMFI starts at higher oxidation state was to be expected due to the wet-impregnation and subsequently required second calcination step, meaning that effectively the Fe in RuFeMFI has undergone two such harsh oxidative procedures.

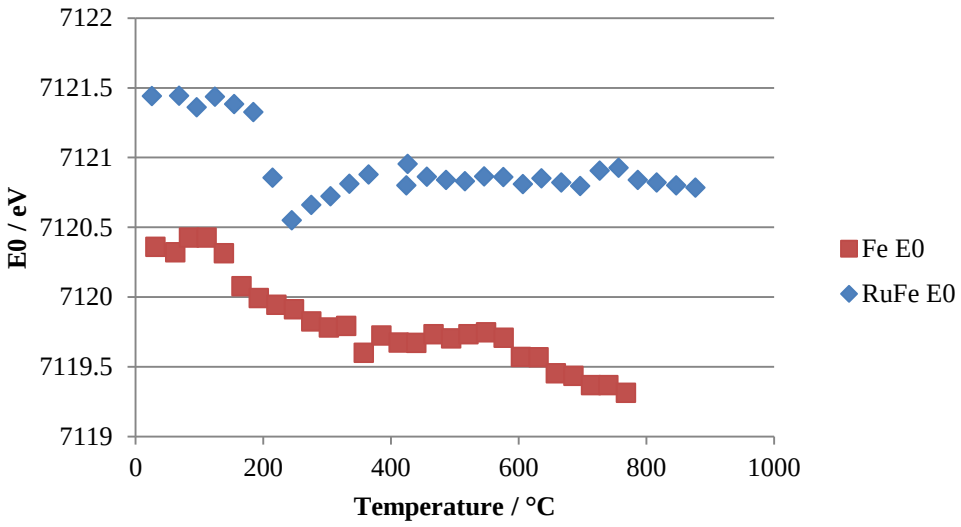

Figure 5.10. *Comparison of E_0 value for FeMFI and RuFeMFI between 30-850°C in helium. Errors of the white line positions are ± 0.1 eV.*

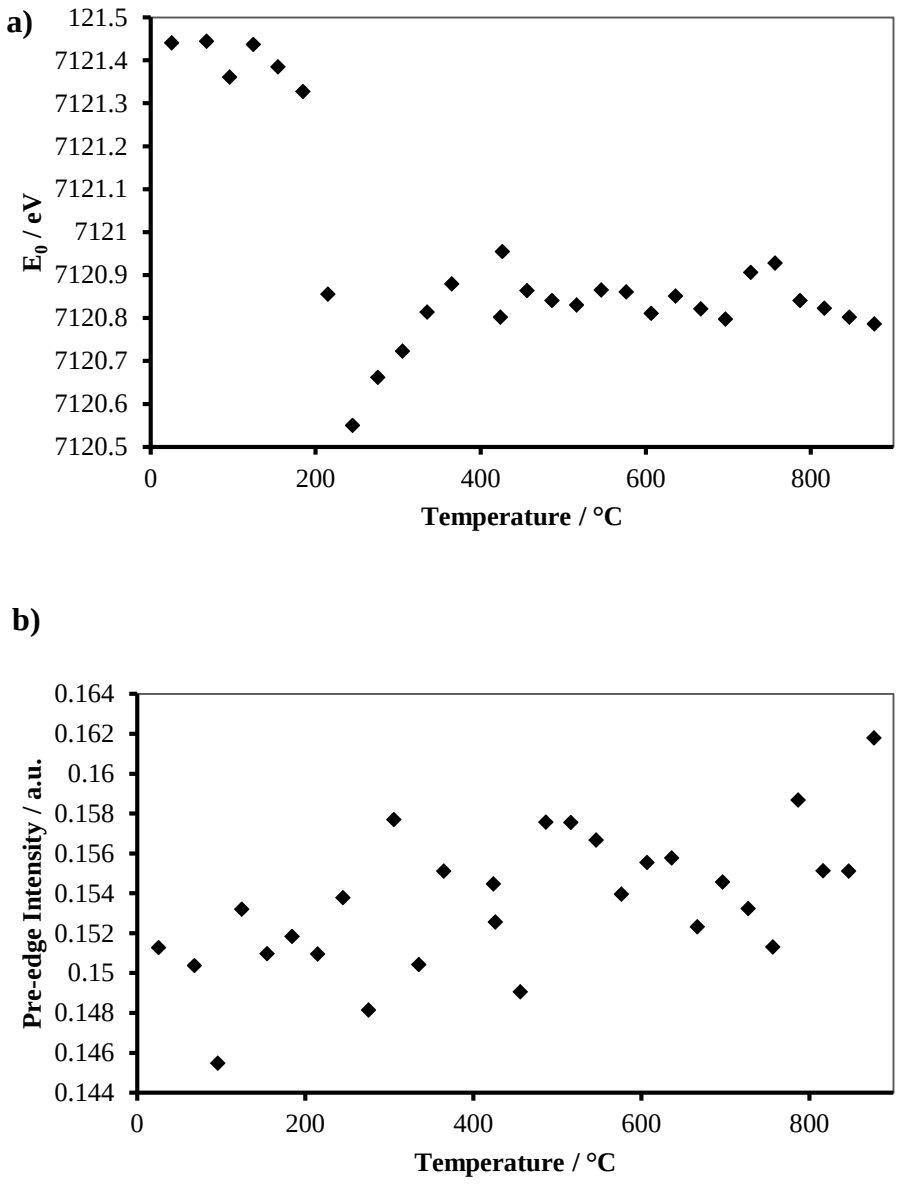

Figure 5.11. *Variation of the Fe K-edge absorption energy E_0 (a), and maximum pre-edge intensity (b) values for the normalised XANES data collected for Ru/FeMFI during activation in He up to 850°C. The general trend is observable showing a general increase in pre-edge feature form an average value of 0.151 at 30°C intensity as the temperature is increased, to 1.62 at 800°C. Errors of the white line positions are ± 0.1 eV, and for pre-edge intensity ± 5%.*

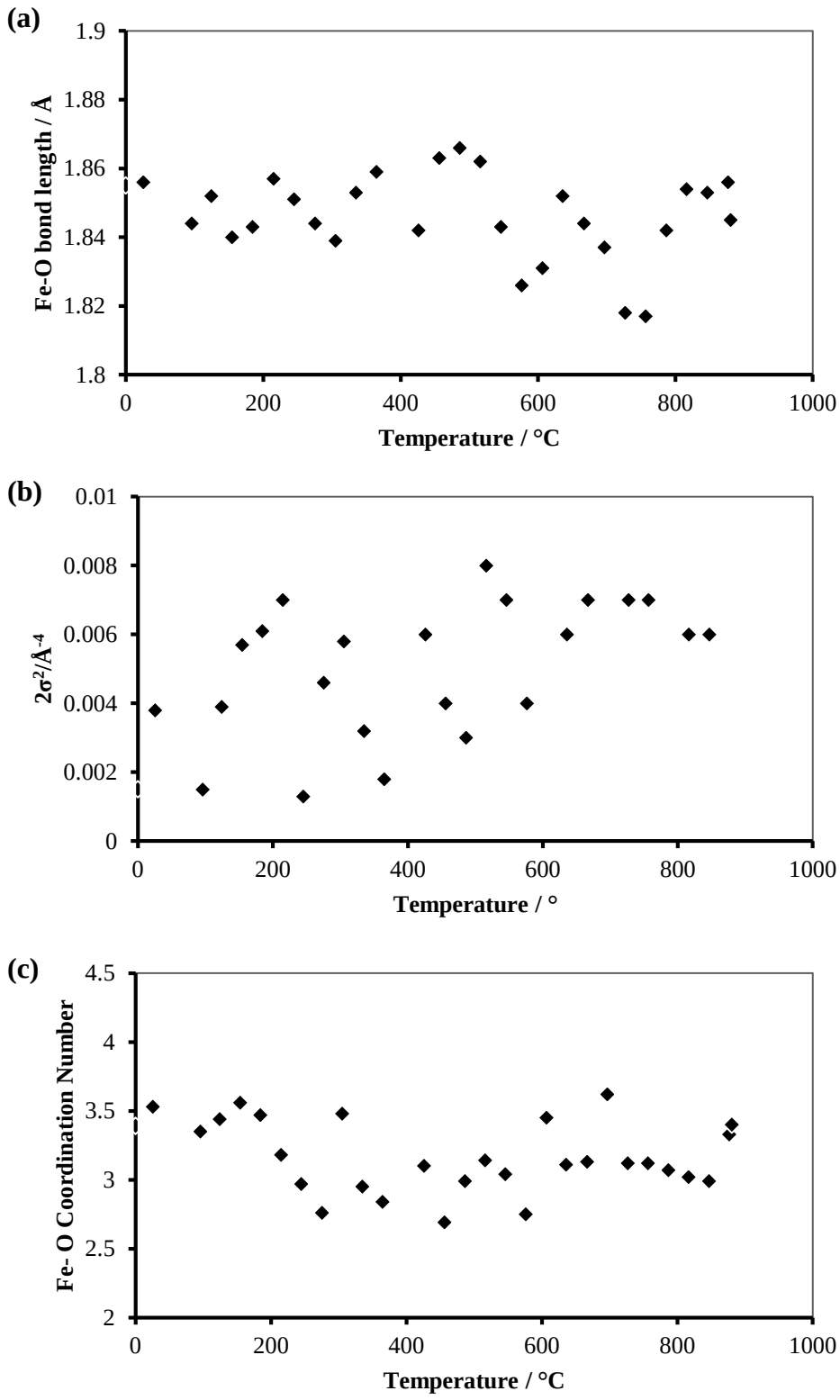

Figure 5.12. *Variation of parameters from EXAFS fits during activation in He up to 880°C for Ru/FeMFI; (a) Fe-O bond length, (b) Debye-Waller factor, (c) coordination*

number. Errors for bond lengths are ± 0.01 Å. Errors in coordination number N, and $2\sigma^2$ *are ~10%.*

Ru K edge Data of Ru/FeMFI

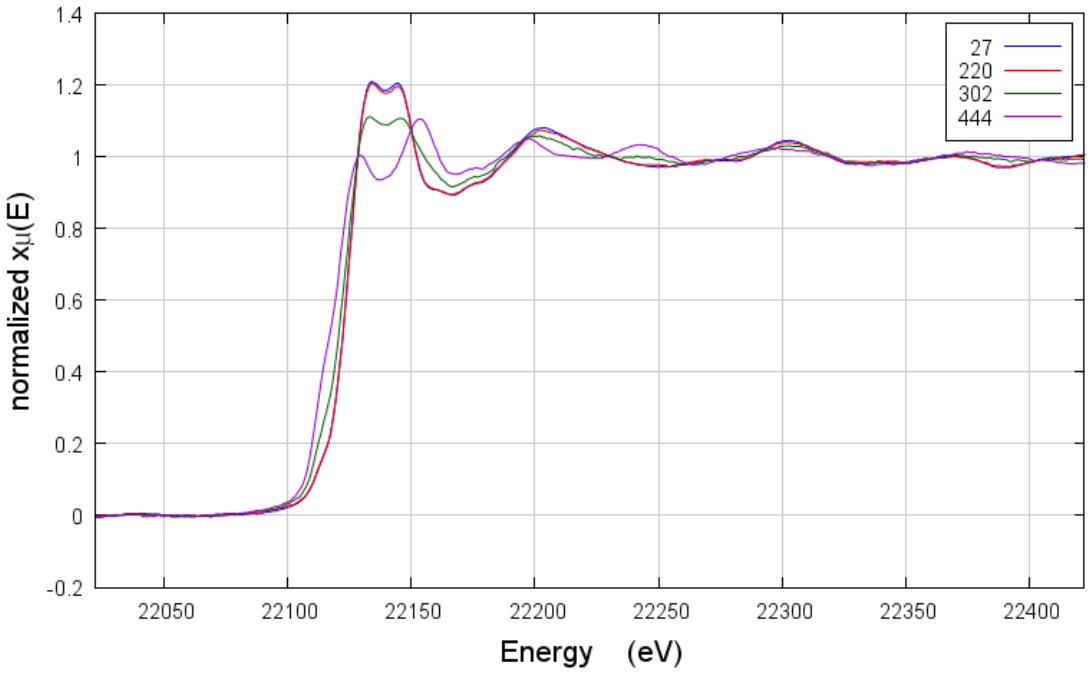

Figure 5.13. *Ru K-edge EXAFS spectra measured during activation in He up to 450°C for Ru/FeMFI.*

The Ru K-edge EXAFS spectra measured during activation in He up to 450°C for Ru/FeMFI are represented in Figure 5.13. The EXAFS spectrum for Ru/FeMFI was seen to remain stable as it was heated from room temperature to close to 300°C. At this temperature the spectrum is observed to change dramatically from a profile representative of RuO_2 clusters to a more disordered reduced phase. A drop in the rising edge height from 1.2 to 1.0 is seen to occur between 220 and 444°C, with the spectrum measured at 302°C having an edge maximum in between those values. This change is also accompanied by a shift in the edge position E_0 to lower energy values as plotted in Figure 5.13. Here we see the E_0 value hover at around 22121.8 eV between 27-200 °C, after which it falls almost linearly at a rate of 0.004 eV K^{-1} reaching

22120.6 eV. This lower transition energy is indicative of a reductive process as a fraction of the Ru^{4+} (RuO_2) in the zeolite is reduced. This reduced value of 22120.6 eV is close to that of Ru^{3+} in $RuCl_3$ whose E_0 is 22120 eV. [33]

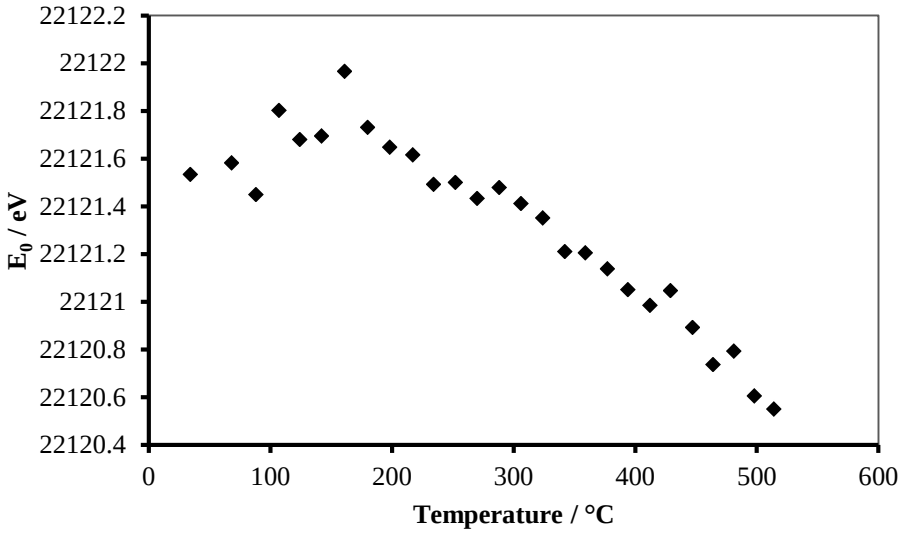

Figure 5.14. *Variation of rising edge absorption energy E_0 for the normalised Ru K-edge XANES data collected for RuFeMFI during activation in He up to 570°C. Errors of the white line positions are ± 0.1 eV.*

The Ru K-edge rising-edge position, E_0 for RuFeMFI is shown in Figure 5.14. At room temperature the E_0 value is at 22121.5 eV. This then rises on average to max value of 22121.7 eV by 180°C. Following this the value then gradually drops in an almost linear fashion achieving a value of 22120.4 eV by 530 °C. An inflexion point at or near 300°C is not observed as would be expected from the changes observed in the EXAFS fits where the oxygen coordination number drops from approximately 6 to 2, accompanied by a large increase in disorder (Figure 5.15). This indicates that the ruthenium oxide species are reduced rather gradually, and by 300°C a coordination state change occurs as the sample is auto-reduced by loss of a coordinated oxygen atom as is corroborated in the refined parameters outlined in Figure 5.15. This could indicate a mixture of at least two separate ruthenium species, one of which is reduced gradually, possibly bulk particles RuO_2, and another that undergoes a single rapid reduction step at

around 300°C, which indicates the possible presence of isolated Ru species coordinated to framework oxygen atoms or perhaps small oligonuclear RuO_x clusters.

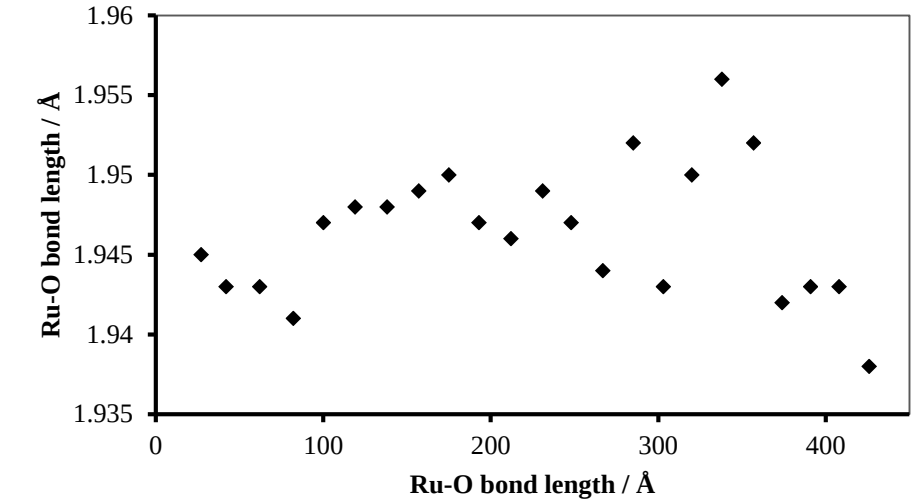

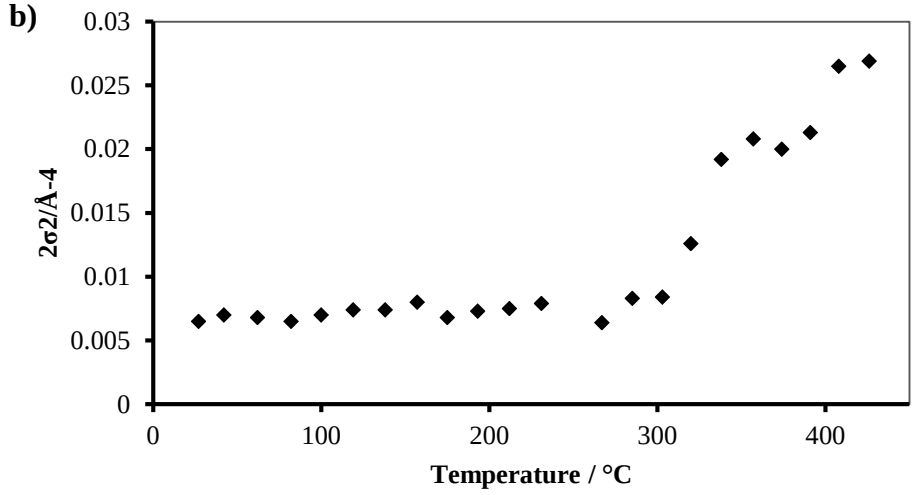

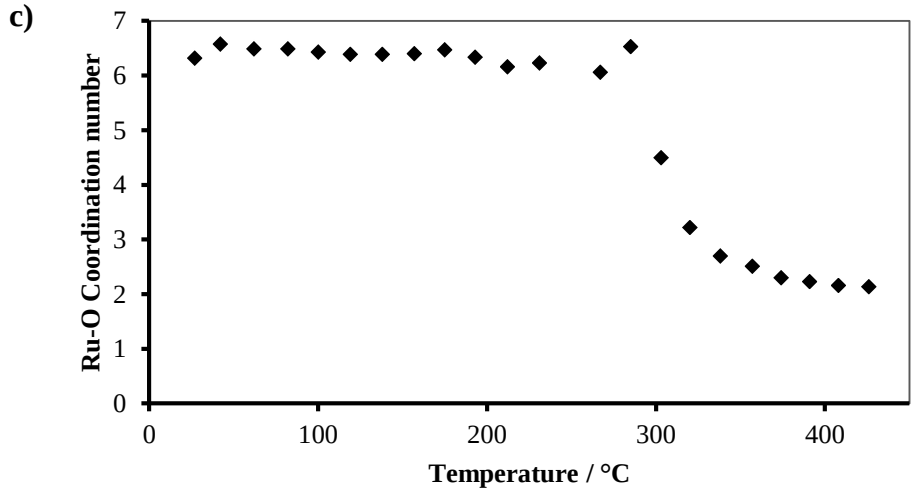

Figure 5.15. *Variation of parameters from Ru K-edge EXAFS fits during activation in He up to 450°C for Ru/FeMFI; (a) Ru-O bond length, (b) Debye-Waller factor, (c)*

coordination number. Errors for bond lengths are ± 0.01 Å. Errors in coordination number N, and $2\sigma^2$ are ~10%.

The gradual nature of the changes occurring during the reduction of RuO_2 when heated in He inferred from the drop in E_0 value, is however not reflected in the temperatures corresponding to the changes observed in the refined EXAFS parameters fitted to the data (Figure 5.15). The parameters corroborate with the changes in the EXAFS profile shown in Figure 5.13 which showed relative stability in the ruthenium oxide species up to 300°C in He at which a definite change in the material occurs. Examination of the EXAFS data and the parameters resultant from fits to the first Ru-O shell provide much more detail on the phase transformation that occurs above 300°C as seen in Figure 5.15. At 300°C the coordination number initially at ~ 6 falls dramatically at first with a gradually decreasing gradient until it reaches a value of 2.2 by 400°C by which it seems to plateau. Within the same 100°C temperature window a concurrent change in the Debye Waller factors for the Ru-Ru shell increased to much higher values from around 0.008 at 300°C to 0.027 by the end of the heating ramp indicating a much more inhomogeneous Ru environment in the reduced state, which is expected following the autoreductive decrease in oxygen coordination, especially if multiple Ru species are present, as was evidenced from the XANES analysis. These results clearly indicate the decomposition of the RuO_2 species to a highly coordinatively unsaturated, lower oxidation state species. Thus the ruthenium ions in RuFeMFI can be said to be extremely facile to auto-reduction in He.

It is worth noting at this point that the RuO_x species in RuFeMFI is more easily reduced than that seen in RuFeSAPO-5. RuFeSAPO-5 did not show a large metallic fraction until adding benzene at 350°C but under He at 550°C no metallic Ru was present, whereas in RuFeMFI Ru was reduced in He at around 300°C.

5.3.4 FeSAPO-5

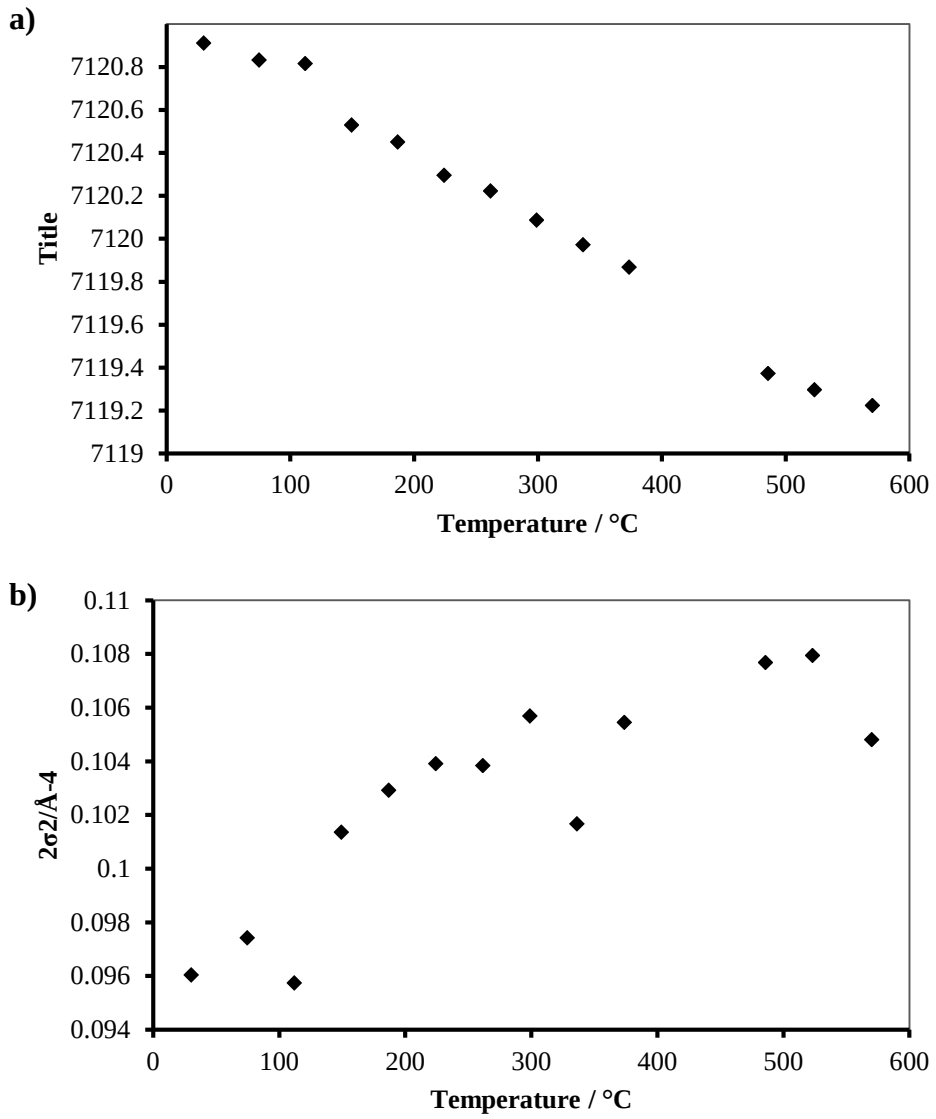

Figure 5.16. *Variation of rising edge absorption energy E_0,(a) and maximum pre-edge intensity (b) values for the normalised Fe K-edge XANES data collected for FeSAPO-5 during activation in He up to 570°C. Errors of the white line positions are ± 0.1 eV, and for pre-edge intensity ± 5%.*

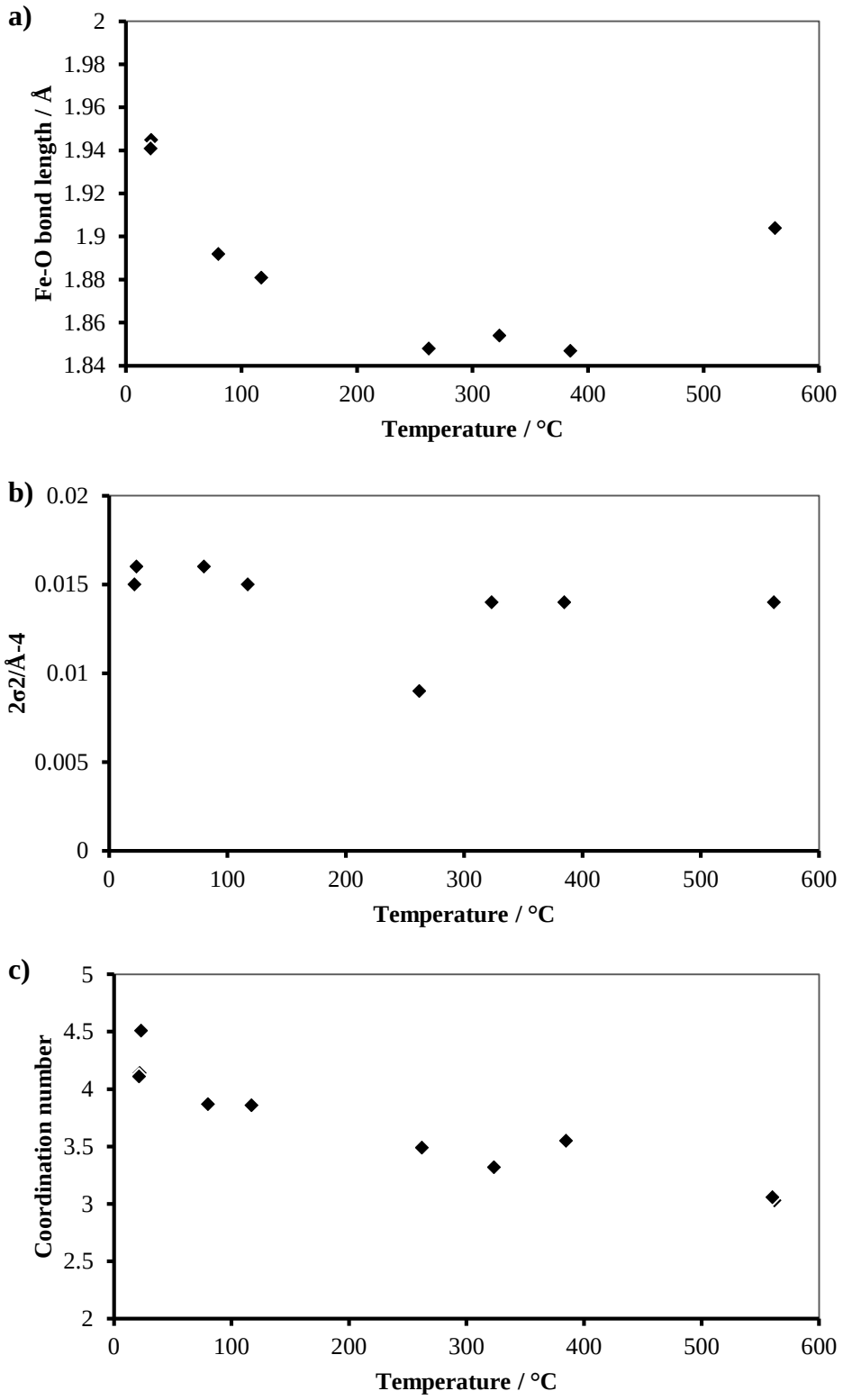

Figure 5.17. *Variation of parameters from Fe K-edge EXAFS fits during activation in He up to 600 °C for FeSAPO-5; (a) Fe-O bond length, (b) Debye-Waller factor, (c)*

coordination number. Errors for bond lengths are ± 0.01 Å. Errors in coordination number N, and $2\sigma^2$ are ~10%.

Figure 5.16 shows E_0 values for the spectra of FeSAPO-5 collected during activation by heating in He to 560 °C. There are gaps in the data caused by a periodic re-filling of gas in the ionisation chambers that took place during the experiment. This occurred during heating between 120-250°C and 390-540°C. Even though these issues lead to poorer quality spectra than expected and gaps in the data, the EXAFS results could be fitted using a single scattering calculation for the first Fe-O coordination shell for the data between 30-120°C, 262-348°C and at the end of the heating ramp at 560°C where 6 scans were taken and merged for achieving better quality data for robust parameter fitting of the data.

As expected following prior calcination the majority of the iron in FeSAPO-5 begins with an average tetrahedral coordination, computed as an average coordination number of 4.5, slightly higher than the starting coordination for Fe in FeMFI which was 4. The FeSAPO-5 coordination number his then drops during heating in He steadily throughout the reduction treatment, finally reaching an average value of 3 by 550°C (Figure 5.17c). This is a slightly lower value than the one expected, but was the most consistent result with the best R-value obtainable using the single shell model employed. It should be remembered here that the coordination number, N and the Debye-Waller factor, $2\sigma^2$ are highly correlated and a more accurate refinement of one parameter, will necessarily require loss of confidence in the other. Increasing the number of computed parameters or fixing the highly correlated $2\sigma^2$ parameter during the calcination would have increased the error of the other values or skewed the model being fit in ways that would misrepresent the system. In any case one would find difficulty in finding and selecting fixed σ values that could be treated with any confidence from secondary sources. It is worth remembering here that the error in the coordination number is the highest of all the computed parameters at a base value of approximately 15%, although many publications frequently neglect this consideration or play it down.

The Fe-O bond distance $R_{Fe\text{-}O}$, begins with an initial value of 1.96 Å which shrinks dramatically up until 120°C to a smaller distance of 1.84 Å after which it shows little variation at higher temperatures in the points plotted. The Debye-Waller factors are not

observed to change very much staying around ~ 0.015Å^{-2} throughout the activation procedure. This suggests that there is little change in the total disorder of the system, although Fe-O bond distance changes are occurring up until 120°C, this is not evidenced by the Debye Waller factor. This could be due to the increased thermal disorder from the heating process and lattice vibrations may be cancelled out by the gain in static disorder from increased homogeneity and the loss of H_2O molecules during this early part of the heating ramp[14,]. This temperature, where the Fe-O bond distance was seen to shrink the most, also corroborates with the temperature range where the c-axis of the FeAlPO-5 lattice parameter undergoes its massive contraction due to water loss as seen in the calcination discussed in Chapter 3. The fact that such geometry changes are seen at the same temperatures, even though the sample atmosphere is dramatically different in its composition and redox properties in both the XRD calcination results and these Fe K-edge analyses, points towards the crucial role of Fe on the framework expansion properties. It has been reported [34] that the isomorphous substitution of T atoms in AlPOs by transition metals often confers changes in the size of the crystal unit cell as well as thermal expansion properties.

Fe K-edge XAS results reveal that iron is present in the calcined catalysts as tetrahedral and octahedral Fe^{3+} in the RuFeSAPO-5 structure. This is then reduced to Fe $^{2+}$, with the generation of a fraction of Fe in a tetrahedral coordination environment. There was no evidence of any Fe-Fe interactions and the data could not be fit using an iron shell as well as an oxygen one. This was in fact the case for all catalysts studied. It is proposed that there are a number of possible forms for Fe in calcined FeAlPO-5 and FeSAPO-5, as evidenced by electron spin resonance measurements (ESR) identifying tetrahedral coordination Fe^{3+} in the framework, amorphous Fe_2O_3, and distorted octahedral Fe^{3+} species.[35] This agrees with our results, however during our pre-treatment a majority of the iron if found in extra-framework positions in a reduced Fe^{2+} oxidation state. This contrasts with the results of pulsed experiments were attempted but the sample moved due to gas pressure during the switch and so we aborted that section of the investigation for this sample.

5.3.5 Ru/FeSAPO-5

Fe K-edge Data

This experiment was completed according to the original plan and involved running EXAFS measurements whilst ramping the temperature sample to 550°C under a helium atmosphere to study activation. The sample was kept at this temperature for 30 minutes and then ramped down to 350°C still under He. The pulsed experiments which introduced nitrous oxide and benzene sequentially in 15 minute intervals were then carried out successfully. The gas composition throughout was checked in real time using the quadrupole mass spectrometer. It was hoped that the MS would also be able to identify molecular fragments from the products of the reaction (i.e. ionic fragments of partially oxidised benzene), but unfortunately the sample amount used was too low compared to the total volume and flow rate of the reactant gases to register unambiguously on the instrument.

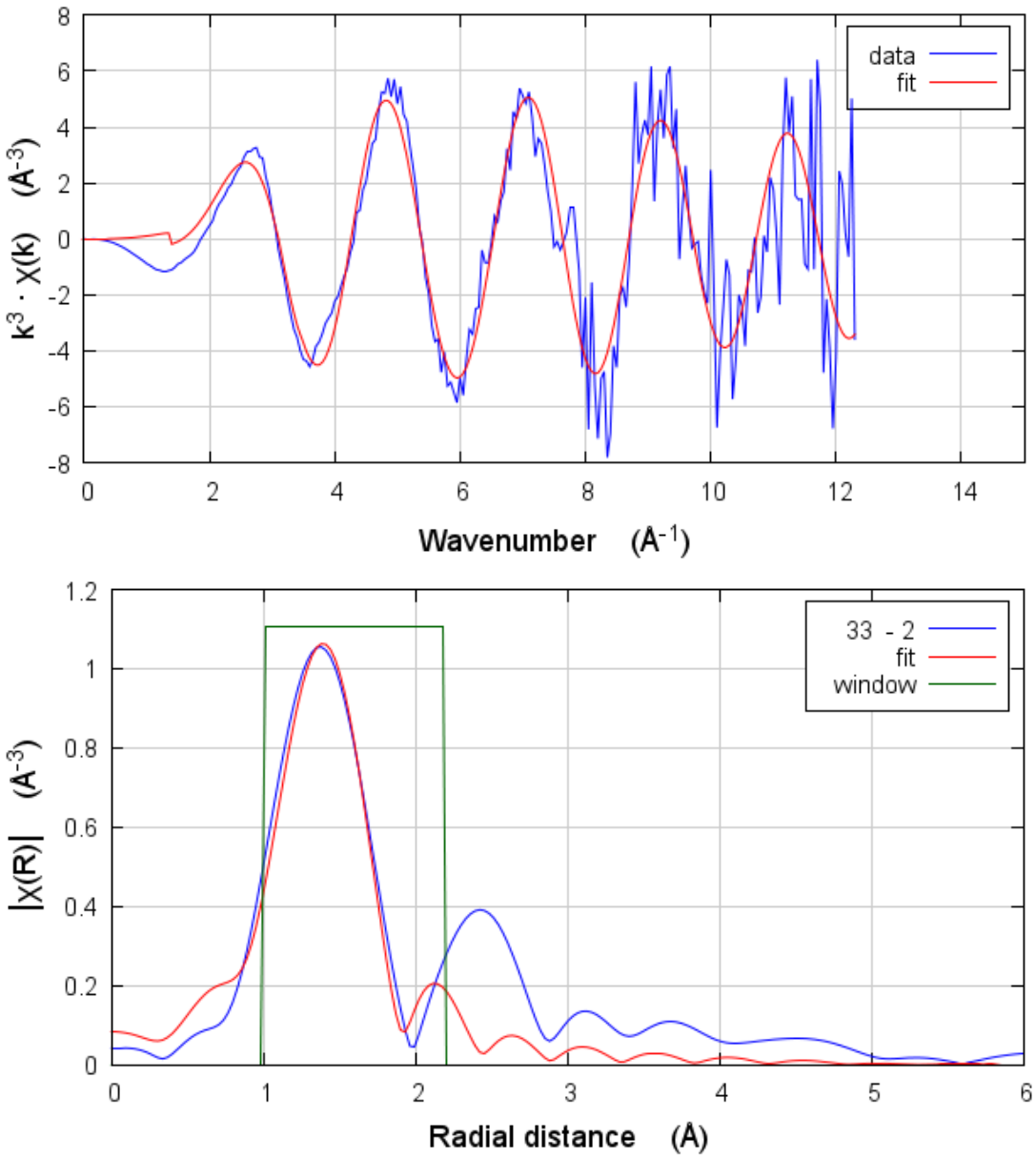

Figure 5.18. *Fits to the Fe-K edge EXAFS data analysed in k-space (k^3-weighted) with associated Fourier transforms for RuFeSAPO-5 in helium at 30 °C.*

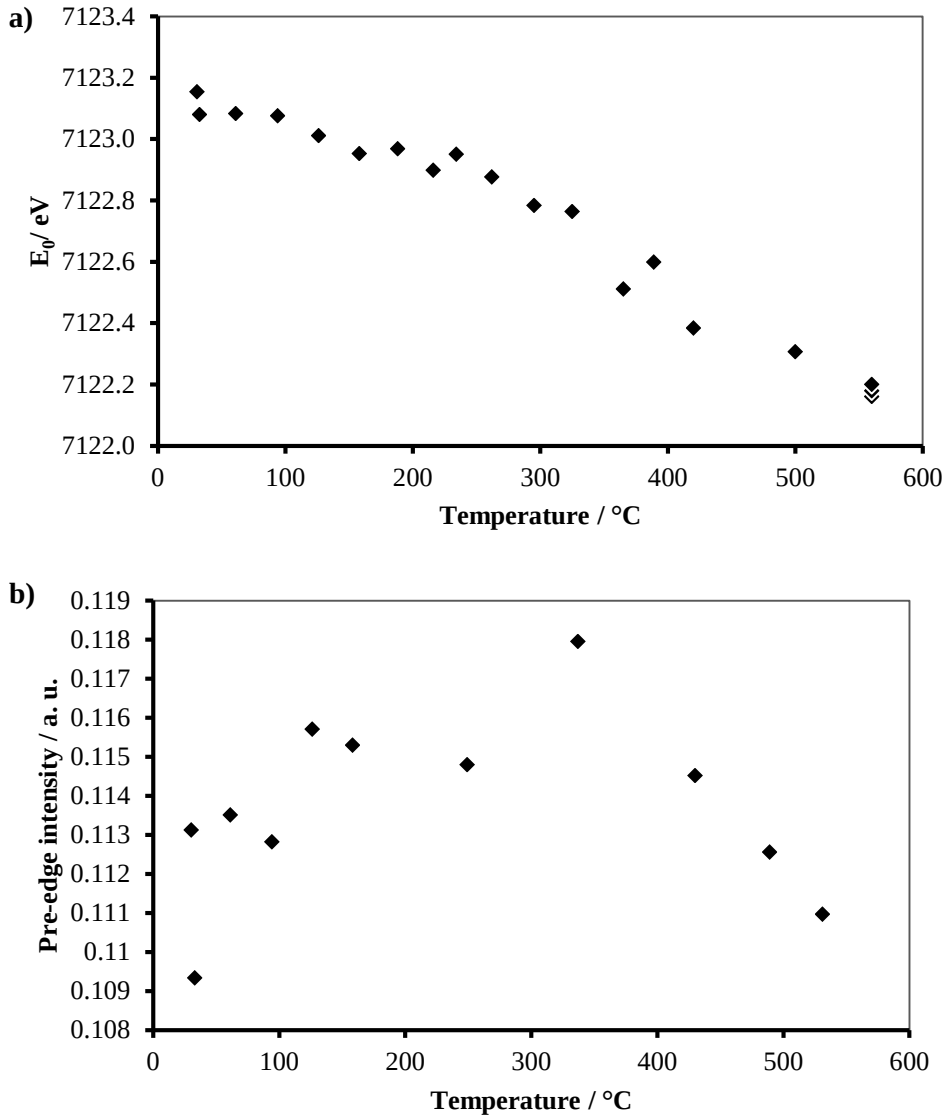

Figure 5.19. *Variation of rising edge absorption energy E_0,(a) and maximum pre-edge intensity (b) values for the normalised Fe K-edge XANES data collected for Ru/FeSAPO-5 during activation in He up to 530 °C. Errors of the white line positions are ± 0.1 eV, and for pre-edge intensity ± 5%.*

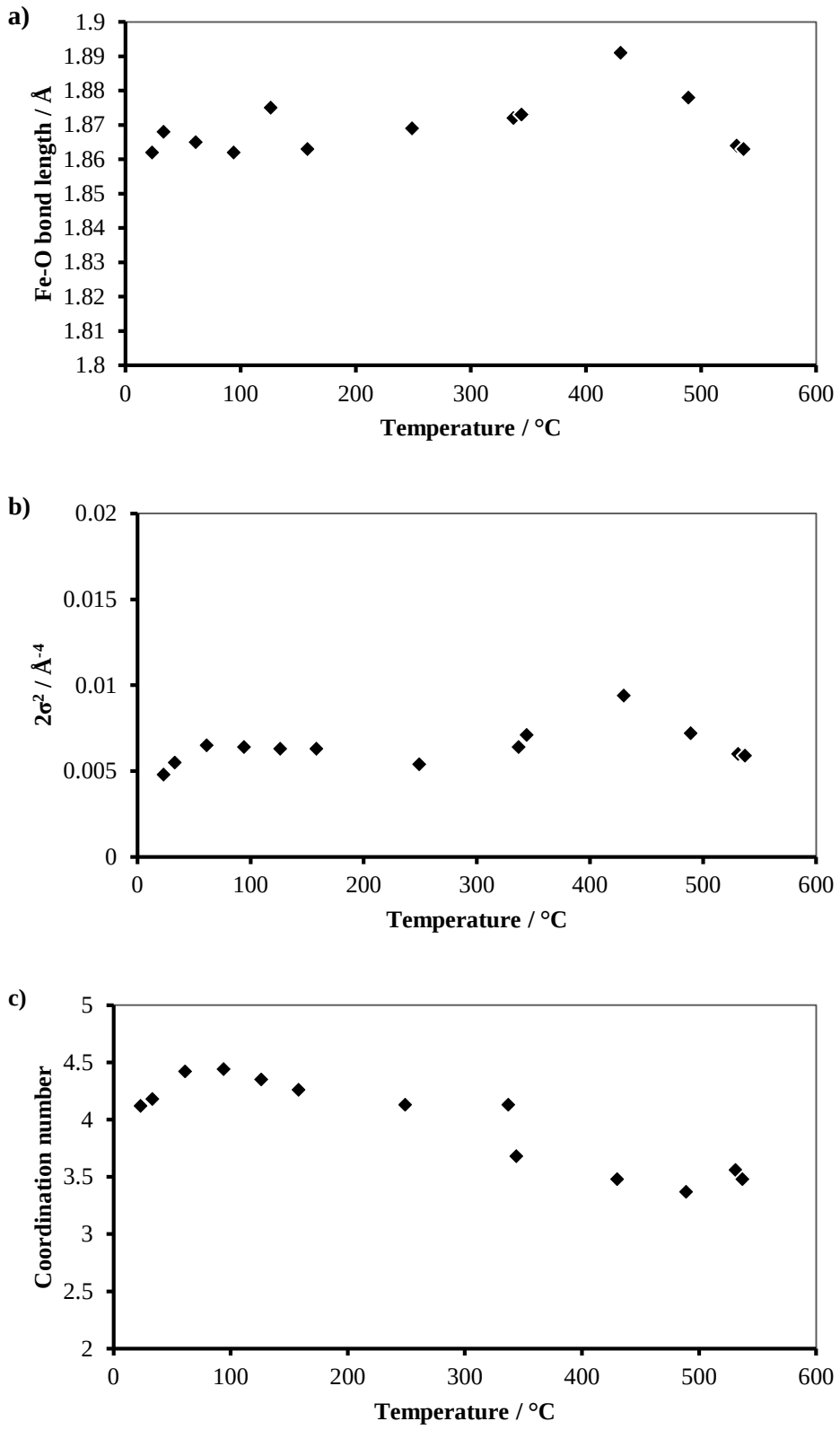

Figure 5.20. *Variation of parameters from Fe K-edge EXAFS fits during activation in He up to 530 °C for RuFeSAPO-5; (a) Fe-O bond length, (b) Debye-Waller factor, (c) coordination number. Errors for bond lengths are ± 0.01 Å. Errors in coordination number N, and* $2\sigma^2$ *are ~10%.*

Figure 5.19 shows the value of E_0 and the pre-edge intensity for RuFeSAPO-5 throughout its reduction in He. Initially at room temperature the spectrum exhibits a rising edge at 7123.2 eV. Throughout the activation process the Fe E_0 value decreases in energy as expected during the autoreduction process to a steady plateau at 7122.2 eV by 560°C. Also shown in the Figure 5.19b is the intensity of the pre-edge feature, which rises to a maximum at 337 °C and then falls steadily throughout the rest of the heat ramp. Again as seen earlier then pre-edge feature provides information on coordination changes occurring at specific temperatures, in this case the formation of more tetrahedrally coordinated Fe in the first half of the heating ramp (i.e. through loss of O from an initial octahedral or 5-coordinate Fe complex) followed by the loss of this symmetry at higher temperatures. This can be attributed to the autoreduction of framework Fe, leading to the loss of coordinated oxygen and then subsequent migration of the Fe from framework to isolated extra-framework positions.

Evidence of such a process is also corroborated by the refined EXAFS parameters shown in Figure 5.20. As seen, the Fe-O bond distance, coordination number and Debye-Waller factor are all relatively stable with small fluctuations about their starting values. It is between 337 and 344 °C that the phase change can be said to occur. Here the average coordination number drops suddenly from 4.1 to 3.7. This is followed by an expansion Fe-O bond length from 1.87 to 1.89 by 430°C, and congruent fluctuation in the Debye-Waller factor.

5.4 RuFeSAPO-5 - Fe K-edge Pulsed Experiments

Figure 5.21 shows the E_0 value throughout the whole experiment including the heat ramp, and pulsed experiments.

a)

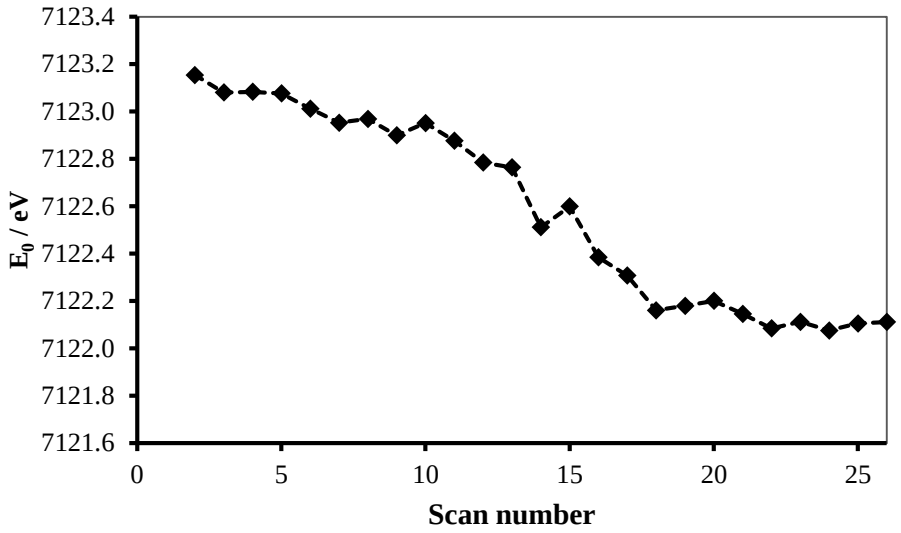

b)

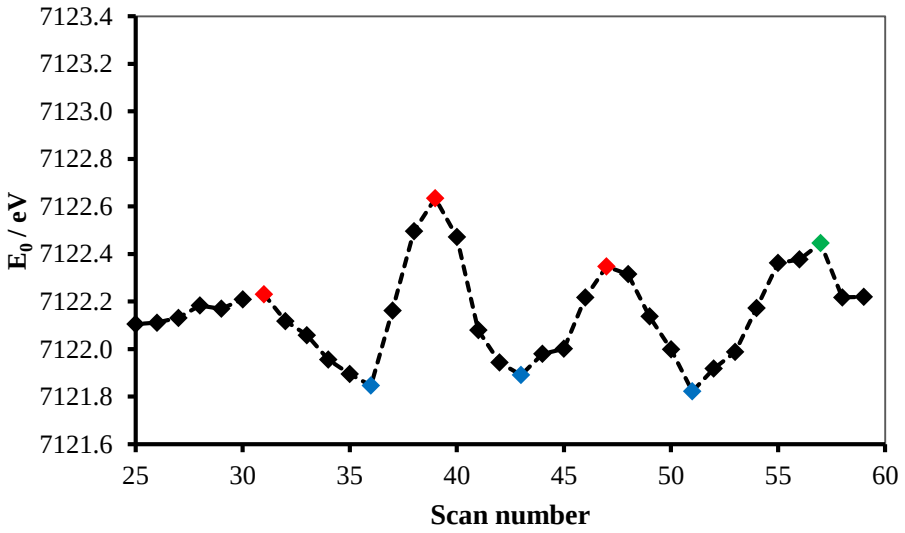

Figure 5.21. *Variation of rising edge absorption energy E_0 values for the normalised Fe K-edge XANES data (from each individual measurement – not merged like EXAFS data) collected for Ru/FeSAPO-5 during the pulsed experiment. (a) During activation ramp to 550°C. (b) Pulsed gas experiment. Red marks indicate the introduction of benzene and blue marks a switch to N_2O. Green at the end denotes a return to He*

atmosphere to purge the system of reactant gas. Errors of the white line positions are ± 0.1 eV. Each scan took around 6 minutes.

Table 5.2. *Variation of calculated parameters E_0, R_{Fe-O}, $2\sigma^2$, and coordination number N, for the normalised Fe K-edge XANES data collected for Ru/FeSAPO-5 during pulsed experiment. Each value is calculated from the merged XAS spectra of the last three scans taken after 15 minutes under each respective gas flow.*

Switchover	***Gas***	***E_0 / eV***	***R_{Fe-O} / Å***	***$2\sigma^2$ / Å $^{-4}$***	***N_{Fe-O}***
0	He	7122.2	1.87	0.0036	3.7
1	C_6H_6	7121.8	1.91	0.0079	3.1
2	N_2O	7122.6	1.95	0.0071	4.4
3	C_6H_6	7121.9	1.94	0.0086	3.5
4	N_2O	7122.3	1.91	0.0062	4.2
5	C_6H_6	7121.8	1.92	0.0067	3.4
6	N_2O	7122.4	1.90	0.0062	3.9
7	He	7122.2	1.86	0.0048	3.6

As seen in Figure 5.21 and Table 5.2, in the pulsed experiments on RuFeSAPO-5 the Fe active sites are observed to be facile to reversible reduction and oxidation by benzene and N_2O respectively. The introduction of benzene reduces the initial Fe active site as shown by the reduction in E_0. Fe-O coordination numbers are also larger for the N_2O pulses which oxidises the Fe, showing the generation of oxygen species coordinated to the iron sites, which are lost on the re-addition of benzene. The changes appear fully reversible for the three cycles carried out at 550°C.

Upon switching from He to benzene at 350°C a change in E_0 occurs of around 0.4 eV indicating partial reduction of the Fe ions in the sample. A reversible change of 0.4-0.5 eV is also seen to occur when switching gases between N_2O and benzene. These observations along with the changes observed in calculated Fe-O coordination number indicate likely coordination of O onto Fe active sites from N_2O decomposition. The

subsequent introduction of benzene leads to reduction of Fe-O coordination number, indicating the coordinated oxygen created by the decomposition of N_2O is lost, likely due to its incorporation into the benzene as it is hydroxylated to phenol.

An interesting observation is that although there is reduction of the Fe during the activation ramp as indicated by the changes in E0 value, there is a further initial reduction step once benzene is introduced. This suggests that benzene reduces the Fe more than He. Following the redox cycles during the pulsed experiment, returning to He atmosphere returns the Fe to the same initial oxidation state as before. Benzene is a stronger reducing agent than He in the case of RuFe-SAPO-5. This is also most likely similar as that of FeSAPO-5, and may come some way explain the differences seen in the different catalytic properties of FeZSM-5 and FeALPO-5, with steam activation and reduction of Fe^{3+} to Fe^{2+} being necessary for FeMFI, but not for FeAlPO-5. The most likely active Fe sites in the sample are sterically available coordinatively unsaturated Fe^{3+} grafted to framework by Fe-O-P groups where Fe has replaced Al. Multiple possibilities of Fe substitution site make this deduction difficult and the addition of Si in the framework in the case of this FeSAPO framework means that Fe may be bonded to Si or electrostatically trapped in Si "nests". However reduction in He leads to partial reduction of the Fe species. However at 550°C, the introduction of benzene into the system leads to further reduction of Fe than in He alone, to a mainly 2+ oxidation state. This corresponds to the Fe active site species in FeMFI generated by the autoreduction in He. Interestingly FeAlPO-5 has been shown to be active for the OBP reaction, even though it does not need any pre-treatment and its Fe ions are almost entirely in the 3+ state. As evidenced from our pulsed experiments the introduction of benzene reduces the Fe in RuFeSAPO-5. We can also assume that a comparable effect occurs for the non-Ru doped counterpart although as seen earlier of FeMFI and RuFeMFI the ruthenium does indeed affect the redox behaviour of the Fe in the materials, but if anything it is likely to repress reduction. It can be postulated that this reduction effect would be greater in FeSAPO-5.

5.5 RuFeSAPO-5 - Ru K edge – Activation and Interactions with Benzene

Unlike the RuFeMFI sample, the data for RuFeSAPO-5 could not be fixed to a RuO_2 type model, nor was it found to be metallic in nature. A good fit to the data at room temperature however could be obtained using a combination of two models, one based on RuO_2, and the other on metallic Ru^0, weighted using two parameters x_O and x_{Ru} respectively. In these fits the Ru-O and Ru-Ru coordination number had to be fixed (although this is most definitely not the case in reality) to obtain reliable fits and rationalise the changes occurring in the data. Instead the variation of the mass fraction of the phases contributing to the EXAFS signal were used, and the other parameters such as Ru-Ru and Ru-O bond distance, and Debye-Waller factor were refined.

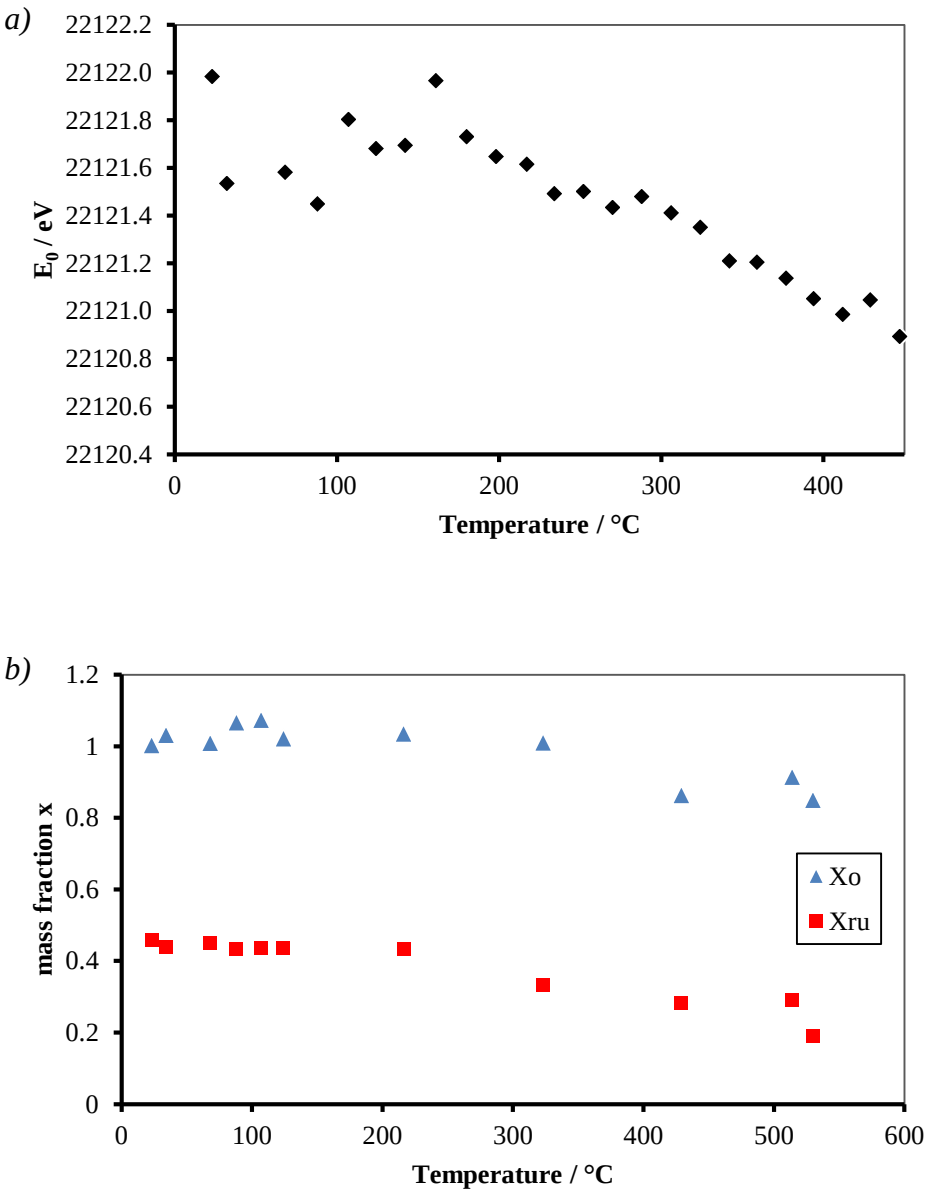

Figure 5.22 *Variation of rising edge absorption energy E_0,(a) and Ru/RuO_2 mass fraction (b), values for the normalised Ru K-edge XAS data collected for Ru/FeSAPO-5 during activation in He up to 530 °C. Errors of the white line positions are ± 0.1 eV, and for mass fraction ± 10%.*

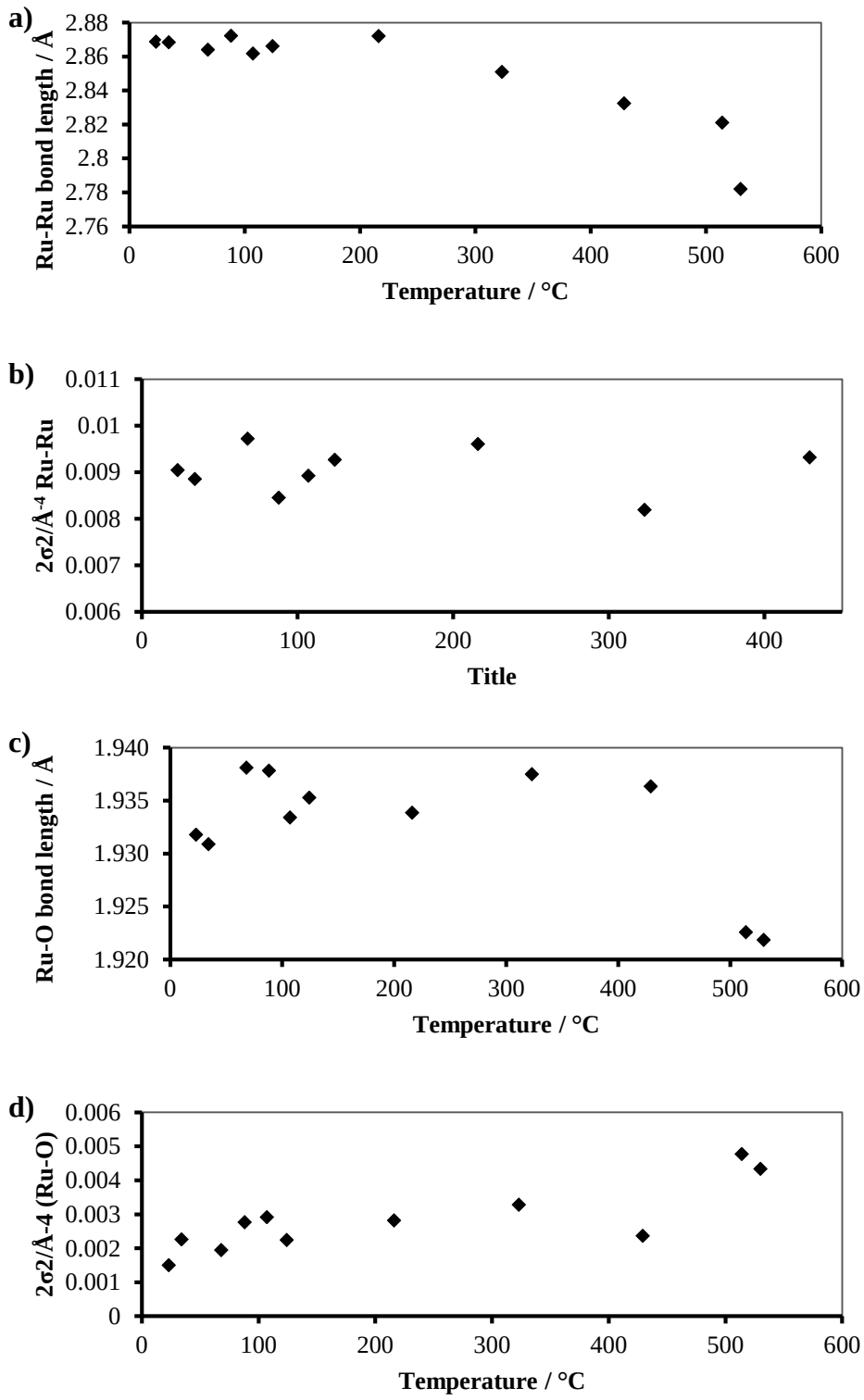

Figure 5.23. *Variation of parameters from Ru K-edge EXAFS fits during activation in He up to 530 °C for RuFeSAPO-5; (a) Ru-Ru bond length, (b) Ru-Ru Debye-Waller factor, (c) Ru-O bond length coordination number (d) Ru-Ru Debye-Waller factor. Errors for bond lengths are ± 0.01 Å. Errors in* $2\sigma^2$ *are ~10%.*

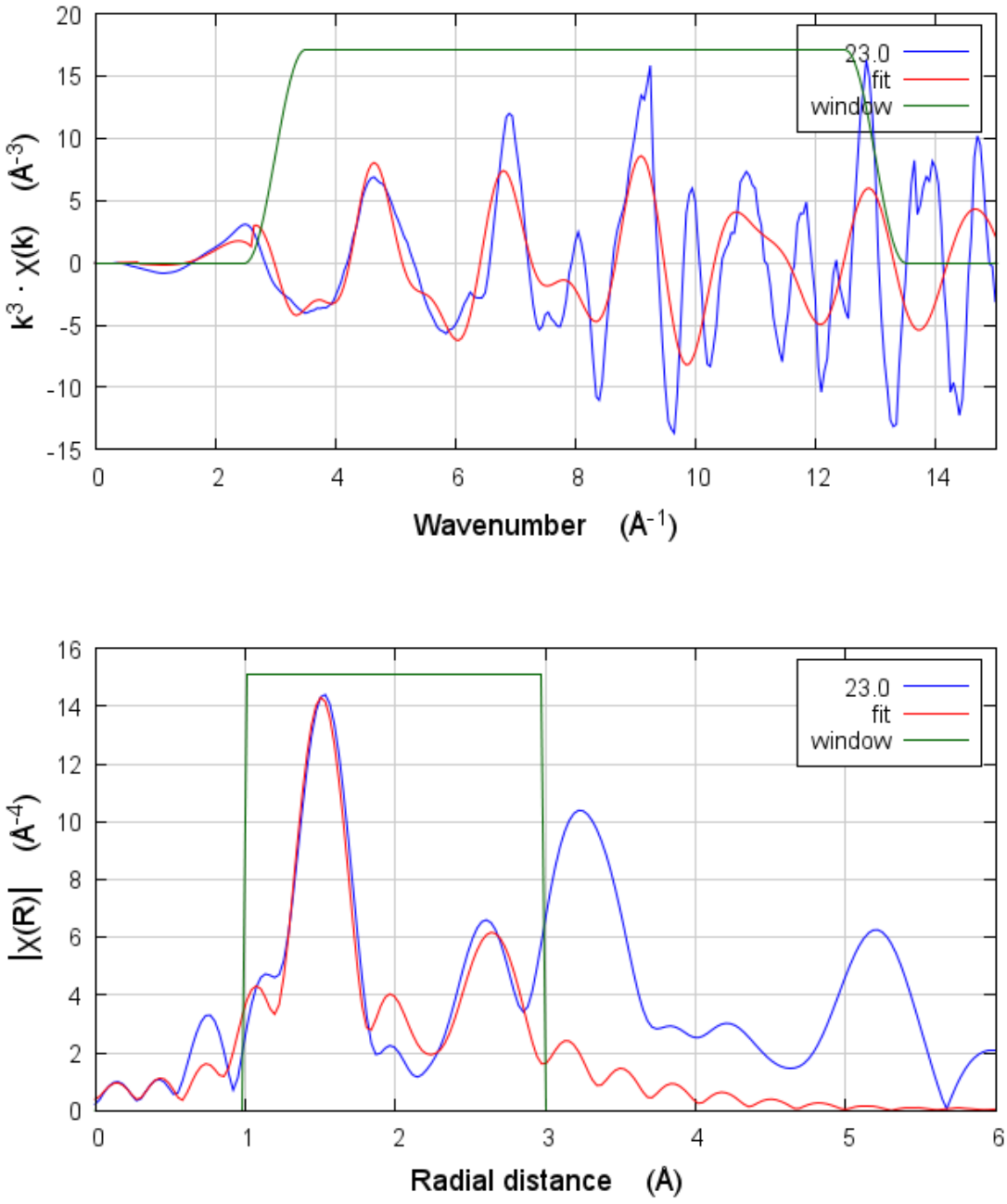

Figure 5.24. *EXAFS and resulting fourier transform plot for Ru K edge data of RuFeSAPO-5 at 23°C*

At the start of the experiment the sample was heated at 5°C/min up to 100°C. Then this heating ramp was increased to 10°C/min and the temperature increased until a max of 530°C was reached. The sample was then held here for one hour. This was the

activation portion of the experiment. The sample was then cooled down at a rate of 10°C/min back to 350°C, the active temperature for the OBP reaction using these types of zeolytic catalysts. All this was conducted under a continuous flow of He at a flow rate of 15 ml/min. Once at 350°C the pulsed experiments were begun, whereby first benzene diluted in He was passed through the sample for 15 minutes. Despite various attempts using different background data normalisation procedures, various starting values for the parameters and a number of fitting windows, this sample could not be fit to a simple one shell Ru-O model such as the earlier Ru K-edge data fitted for RuFeMFI. The incorporation of a neighbouring Ru shell and 2nd O shell also did not yield improved results. The ruthenium species in RuFeSAPO-5 are likely more disordered and inhomogeneous compared to than simple RuO_2 whose initial parameters were used to model RuFeMFI, and amorphous phases may dominate.

Data was fit to the contribution of two phases – each phase had fixed coordination number, the oxide fraction represented by IFFIT derived scattering paths calculated for RuO_2 with 6 Ru-O bonds at an initial distance of 1.96Å, and a metallic fraction with the central Ru coordinated to 12 other Ru atoms at a distance of 2.68Å. Although the coordination numbers were fixed for the two models based on the model reference data, the Debye-Waller factors, bond distances, and relative contribution of each phase was refined for the data (x_{Ru} and x_{RuO}) from the sample. The two phases can be thought to represent the two extremes between fully oxidised octahedral Ru^{4+}, and reduced metallic Ru^0. This use of an appropriate oxide and metallic reference as models for the EXAFS analysis gave good results in agreement with a disordered RuO_2 phase which gradually loses oxygen and transforms to one more metallic in nature.

a)

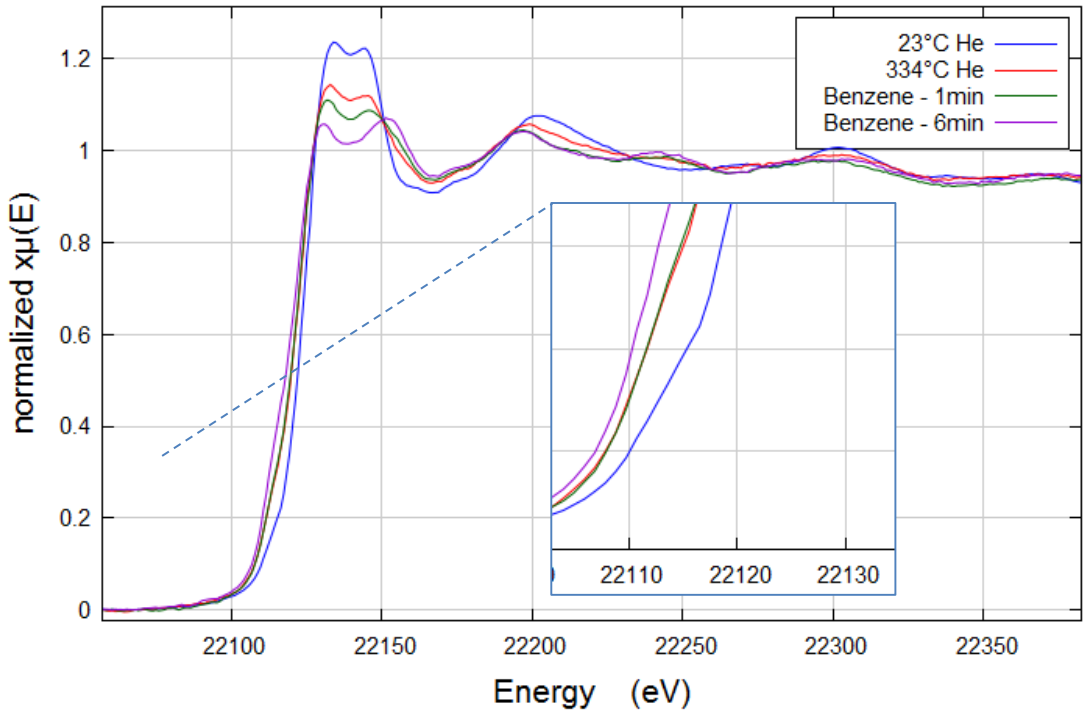

b)

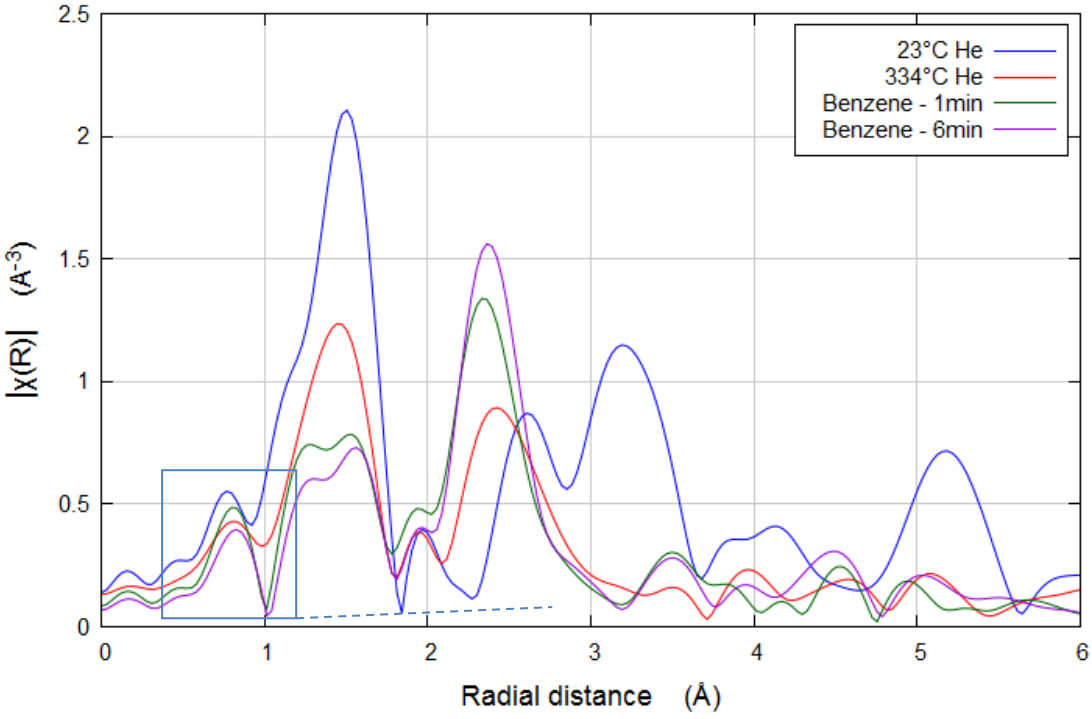

Figure 5.25 *a) Change in rising-edge position and intensity of Ru K-edge XANES spectrum for RuFeSAPO-5 in He and benzene. b) FT EXAFS plot showing clear differences in environment around Ru under different atmospheres.*

During the activation treatment in He as the temperature is raised from room temperature to about 200°C we see that the calculated parameters remain relatively unchanged. Above this temperature a contraction in both the Ru-O and Ru-Ru bond lengths is observed as well as an increase in the corresponding Debye-Waller factor for Ru-O. A drop in the Debye-Waller factor for Ru-Ru however occurs at the highest temperature, where the calculated mass fraction of ruthenium oxide relative to metallic ruthenium in the sample (X_{RuO}) is also seen to reach a lower value as more metallic Ru^0 begins to be formed. This does not go to completion but is only partially reduced unlike the results for RuFeMFI where the transformation is more obvious above 300°C and is completely reduced to metallic Ru by the end of the pre-treatment in helium. In this sample following treatment of RuFeSAPO-5 in He the oxide is only partially reduced by 530°C and stays reduced to the same extent during cooling to 350°C. However upon introduction of benzene to the system the oxide is reduced and the metallic fraction dominates the spectrum and fits the results best. A fully reduced non-oxide Ru phase only occurs in the RuFeSAPO-5 sample once benzene is introduced to the system (Figures 5.25 and 5.26).

Others have found similar states and behaviour for Ru in active catalysts. Detailed studies of Ru on activated carbon catalysts for the production of 2,5-dimethylfuran (DMF) by catalytic transfer hydrogenation with 2-propanol have observed similar coexistence of Ru^0 and RuO_2.[36] They investigated the active phase of the Ru/C catalyst by using extended X-ray absorption fine structure, X-ray photoelectron spectroscopy, and high-resolution TEM analyses. The results revealed that RuO_2 was the dominant phase in the active catalyst and is reduced to metallic Ru during the reaction with the hydrogen produced in situ from 2-propanol. They suggest that both metallic Ru and RuO_2 are active phases necessary for the selective production of DMF.

Reduction of thin RuO_2 films by H_2 was studied by Ugur *et al.*[37] They found the reduction kinetics is dominated by the creation of oxygen vacancies and their annihilation upon transformation of RuO_2 into metallic Ru. The temperature-dependent reduction rate increases linearly with H_2 pressure. In the temperature range of 100-200 °C hydrogenation of the RuO_2 (110) surface was found to occur. Then oxygen vacancies are created due to desorption of water vapour, which accelerates the reduction. Apparently, the annihilation of oxygen vacancies during reduction is more

prominent with increasing temperature. This may be the case for the Ru in our samples, although autoreduction is occurring in a less reducing atmosphere – namely He not H_2. This suggests an autoreduction process is occurring, with a concerted loss of $2O^{2-}$ as O_2 and the formation of oxygen vacancies.

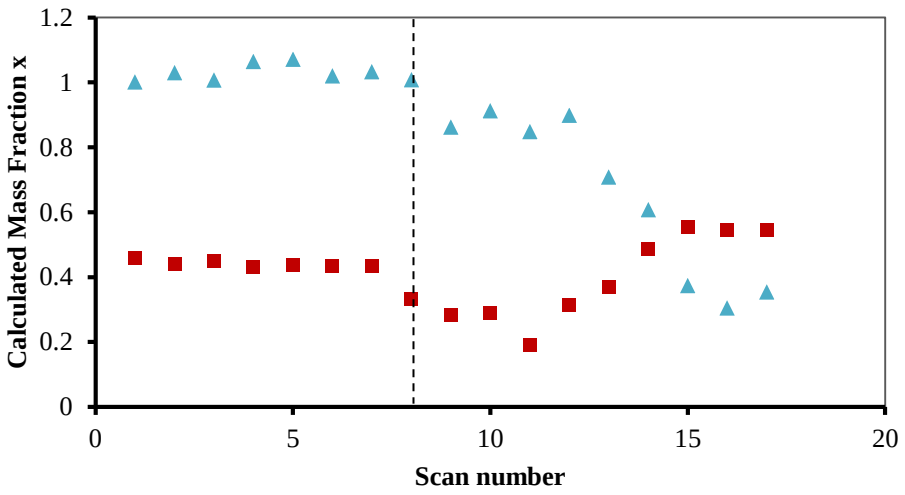

Fig 5.26. *Comparison of evolution of RuO_2-like fraction (blue triangles) and metallic Ru^0 fraction (red squares) over the course of the experiment at 350°C. Benzene vapour was introduced at the point indicated by the dotted line in helium at 350°C. Time between scans is 3 minutes. Errors in the calculated mass fraction are approximately ±10%.*

5.6 UV-Vis Spectroscopy

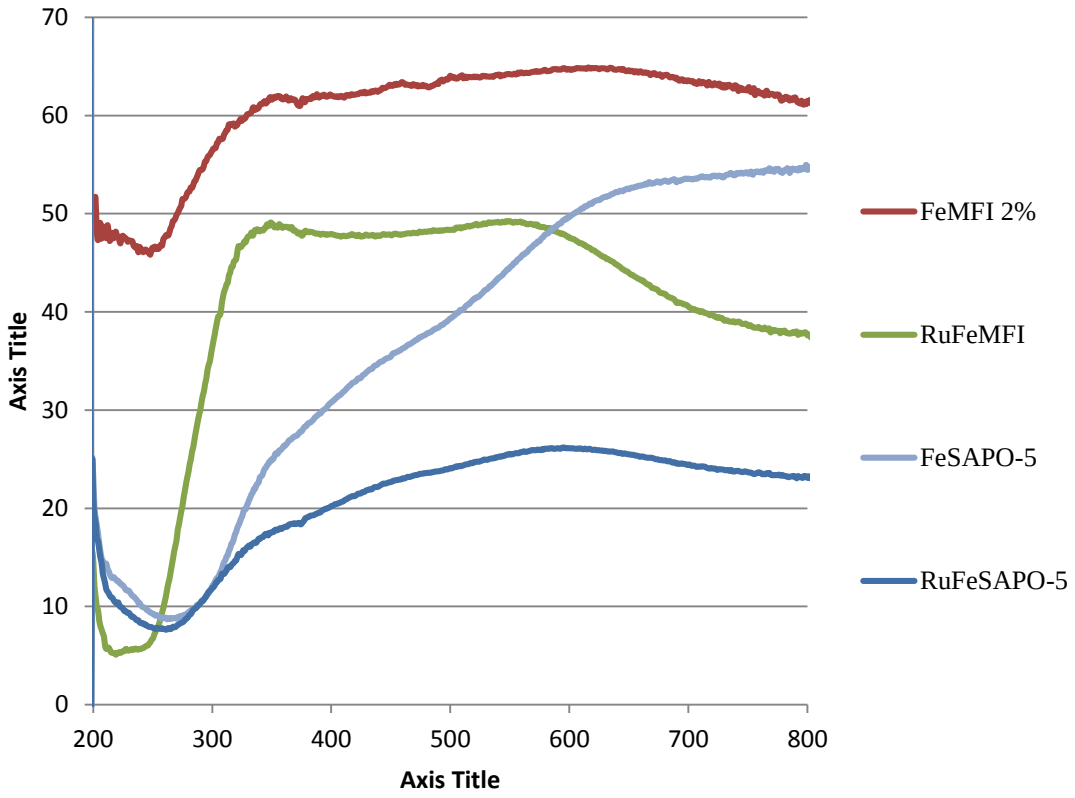

Fig 5.27. *UV-Vis Diffuse Reflectance spectra of selected catalysts.*

Fig. 5.27 shows the DR-UV-Vis spectra of as-synthesized, calcined and steamed nanoporous iron aluminophosphate catalysts recorded under ambient conditions. For all as-synthesized samples, a strong peak centred at 260 nm is apparent, which is ascribed to the ligand to metal charge transfer band of Fe^{3+} in tetrahedral positions.

FeSAPO-5 and RuFeSAPO-5 also seems to exhibit a broad band between 400 and 500 nm indicating some possible clustering of iron species. That the peak is shifted to 210-230nm for the Ru FeMFI sample could be due to isolated Ru species. Furthermore a broad band appears in the region between 500 and 800 nm, which is proposed to be related to the presence of a mixed Fe-Ru phase following impregnation, and corroborates to the synergy in reduction behaviour exhibited by this sample in the pulsed experiments. Since steamed samples are likely to be extensively hydrated, the

participation of hydrated complexes to the UV-Vis absorption spectra can not to be excluded.

5.7 SEM Images of Catalyst Samples

In Figure 5.28-5.31 are collections of SEM images taken for the samples used in the study in this chapter and described in the captions. The EDX measurement resolution on the SEM used was insufficient to determine any differences in composition between the large particles and smaller clusters, but all samples showed the expected traces for elements used in the synthesis.

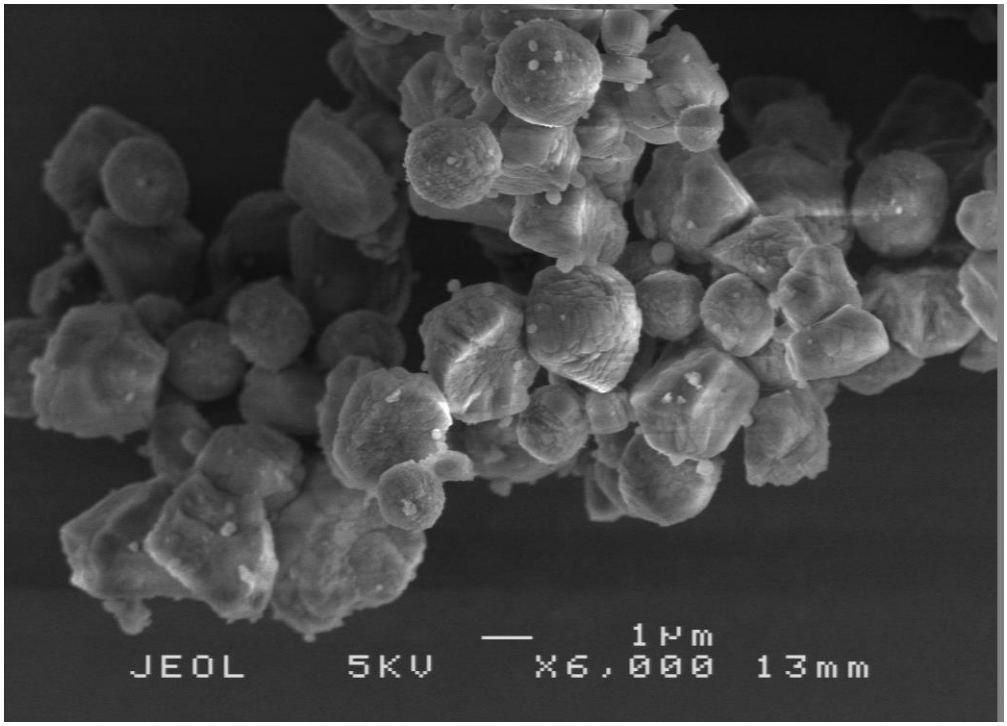

Fig 5.28. *SEM image of FeMFI.*

The sample is shown to consist of small prismatic crystal agglomerates of around 2-5μm.

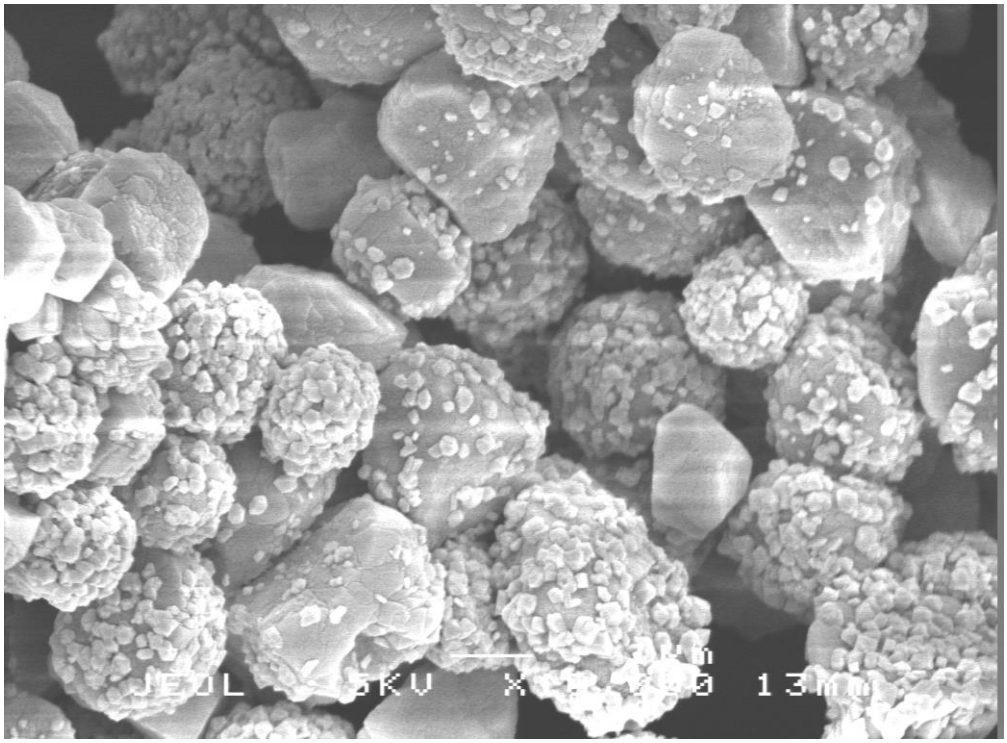

Fig 5.29. *SEM image of RuFeMFI.*

The sample is also shown to consist of small prismatic crystal agglomerates of around 2-5μm. Other small clusters seem to be imbedded onto the surface of the large zeolite crystal agglomerates, possibly Ru species. The EDX instrument on the SEM was unable to determine if there was any difference in composition between the small and large crystals, but the difference in image contrast does also point to a contrast in electron density.

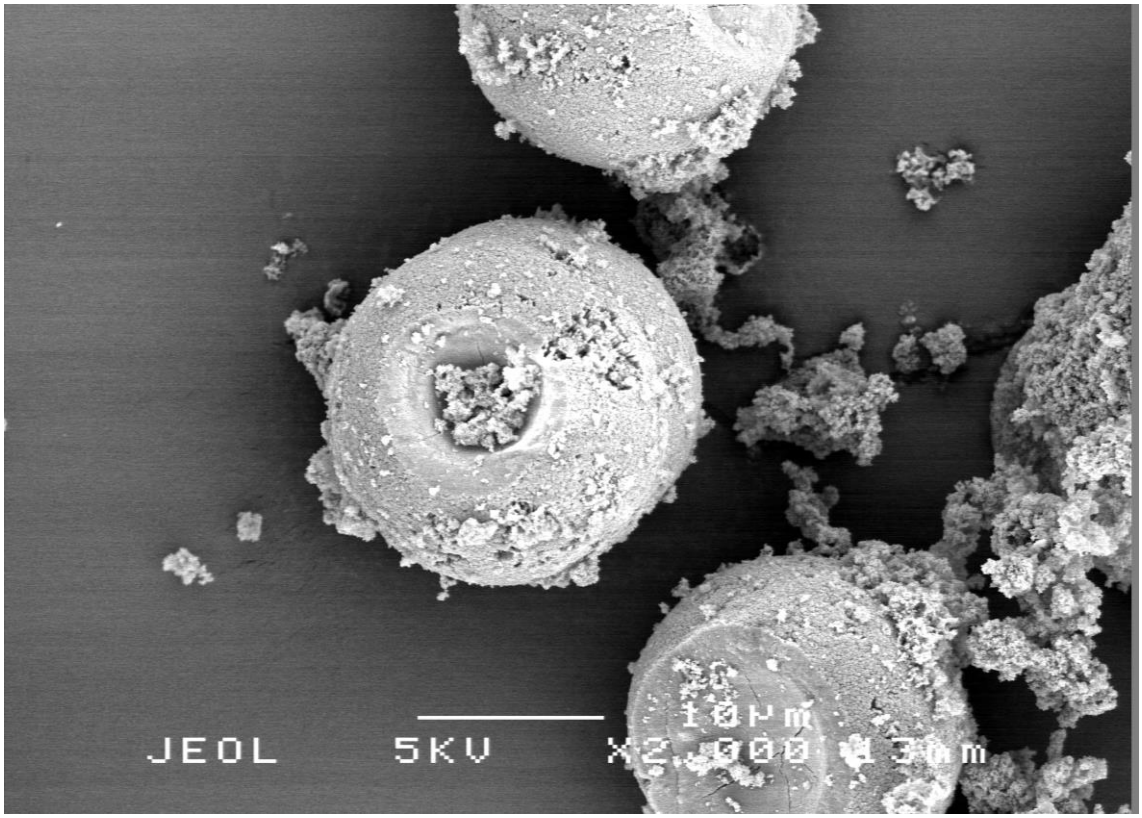

Fig 5.30. *SEM of FeSAPO-5*

From scanning electron microscopy (SEM) analysis, the crystals of the FeSAPO-5 samples were found to have a rod/needle like shape that agglomerated into large spheres of around 20nm in diameter. Smaller microcrystals are also visible, forming irregular agglomerates of around 1-2nm.

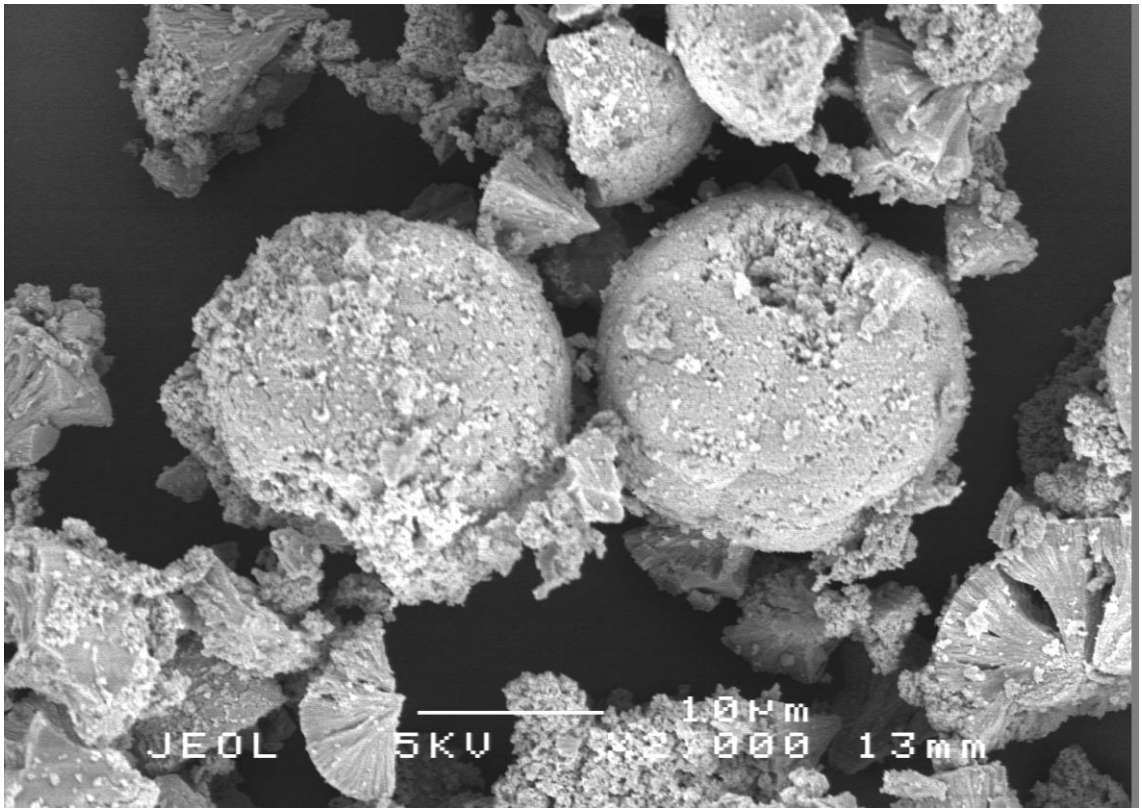

Fig 5.31. *SEM of RuFeSAPO-5*

RuFeSAPO-5 samples were also found to have a rod/needle like shape that agglomerated into large spheres of around 20nm in diameter. The majority of the spheres seem to be fractured and smaller microcrystals are also visible.

5.8 Conclusion

Removal of the extra-lattice O atoms during high-temperature pre-treatments can result in autoreduction. Oxidation of reduced Fe sites often results in the formation of highly reactive oxygen species coordinated to iron active sites. These Fe sites are either in the 2+ oxidation state or a 3+ state that can easily be reduced by benzene to yield the active Fe^{2+}. Overall, He activation depends on the interplay of structural factors such as the type of zeolite and sizes of the channels and cages and chemical factors such as the Si/Al ratio and the nature, charge, and distribution of the charge-balancing cations. Fundamental knowledge of the geometric and electronic structures of the reactive active site can help in the design of novel selective oxidation catalysts.

Analysis of the data has shown highly reversible changes in oxidation changes upon in both Fe and Ru K-edge data during the pulsed experiments. Benzene appears to act as a strong reducing agent, has a greater reducing effect on the Fe sites than that of treatment in He alone. This illuminates the possible role it may play in the catalytic mechanism. Calcination in inert gas at high temperature was seen to evidence to de-hydroxylation and auto-reduction of a significant fraction iron centres in all samples, although with the events occurring and different stages in the heating ramp, likely related to both their composition and different framework structures. Iron ions of the isomorphously synthesized zeolites investigated seem to migrate during calcination from the crystalline lattice into zeolite micropores or extra-framework iron ions are rearranged to create active sites. Very little evidence of the formation of bulk iron oxide is observed. EXAFS measurements by others performed on a isomorphously substituted Fe-ZSM-5 also indicate that before activation iron is located in tetrahedral positions in the MFI framework, but that after activation, the iron migrates and is presented as isolated Fe^{3+} cations in FeMFI.[38,39,40] Analysis of the data has shown highly reversible changes in oxidation changes upon in both Fe and Ru K-edge data during the pulsed experiments. Benzene appears to act as a strong reducing agent, has a greater reducing effect on the Fe sites than that of treatment in He alone. This illustrates the possible role it may play in the catalytic reaction mechanism. Overall, high temperature helium activation depends on the interplay of structural factors such as the type of zeolite and sizes of the

channels and cages and chemical factors such as the Si/Al ratio and the nature, charge, and distribution of the charge-balancing cations.

Experiments under changing atmospheric composition on RuFeSAPO-5 afforded interesting information as to the potential effects of reactants with the active metal atoms. Redox and coordination number changes to the Fe were seen to occur reversibly with the introduction of N_2O and benzene and Ru was substantially reduced in benzene more than in He alone. A group studying the adsorption and desorption of 1,2-dichloroethane (DCE) confined within ZSM-5 found ZSM-5-regeneration was effective when thermally treating at ~300 °C[41]. Once regenerated and reloaded Rietveld refinement of HRXRD data indicated that both DCE location and content remain substantially unchanged thus confirming ZSM-5 is able to re-adsorb DCE in amounts comparable to that adsorbed in the first cycle. This was only 50°C above the temperature used in the gas switching experiments carried out by ourselves, and although there are obvious differences preventing a direct analogy, this mirrors the reversible changes seen in the *in-situ* XAS experiment under He, N_2O and benzene.

The presence of several different Fe (and Ru) sites hinders the full direct study of the spectroscopic features of the active site. However XAS techniques are very capable of selectively probing these sites, even if they only constitute a minor fraction of the total amount of the total material and are thus very valuable. Fundamental knowledge of the changing state of Fe and Ru in this study is of relevance to the understanding of the geometric and electronic structures of the reactive active sites in nanoporous solids and can help in the design of novel selective oxidation catalysts.

References

1 L. Zhou, J. Xu, C. Chen, F. Wang, X. Li, *J. Porous Mater.*, 15, (2008), 7-12

2 N. R. Shiju, S. Fiddy, O. Sonntag, M. Stockenhuber, G. Sankar, *Chemical Communications*, (2006) 4955-4957

3 Z. Sobalík, K. Jíša, D. Kaucký, A. Vondrová, Z. Tvarůžková, J. Nováková, (2007). *Catalysis Letters*, 113 (3-4), 124-129.

4 I. Yuranov, D. A. Bulushev, A. Renken, L. Kiwi-Minsker, *Journal of Catalysis*, 227, (2004) 138-147

5 E. V. Kondratenko, V. A. Kondratenko, M. Santiago, J. Pérez-Ramírez, *Journal of Catalysis*, (2008) 256(2), pp.248-258.

6 J.A.Z. Pieterse, S. Booneveld, G. Mul, R.W. van den Brink, *Studies in Surface Science and Catalysis*, 158, Part B, (2005) 1915-1920

7 Z. Sobalík, K. Jíša, D. Kaucký, A. Vondrová, Z. Tvarůžková, J. Nováková, *Catalysis letters*, (2007) 113(3-4), pp.124-129.

8 J. A. Z. Pieterse, G. Mul, I. Melian-Cabrera and R. W. Brink, *Catalysis Letters*, 99, Nos. 1-2, (2004) 41-44,

9 S. Hedge, P. Ratnasamy, L. Kustov, V. Kazansky, *Zeolites*, 8(2), (1988) pp.137-141.

10 L. Marchese, A. Frache, E. Gianotti, G. Martra, M. Causà, S. Coluccia, *Microporous and Mesoporous Materials*, 30(1), (1999) pp.145-153.

11 I. E. Wachs, G. Deo, J-M. Jehng1, D. S. Kim, and H. Hue,*Preprints – American Chemical Society Devision of Petroleum Chemistry* 41 (1996): 64-67.

12 Martens, J. *Journal of Catalysis*, 108(1), (1987) pp.259-262.

13 http://www.diamond.ac.uk/industry/Case-Studies/Case-Study-Microreactor-Sasol-XAS.html accessed on 02/05/2016

14 N. Al-Hazmi, *Proceedings of the 19th International Congress of Chemical and Process Engineering CHISA* (2010) Prague, Czech Republic, 28 August - 1 September, pp. 27 - 36

15 P. Kubánek, B. Wichterlová, and Z. Sobalí. *Journal of Catalysis* 211.1 (2002): 109-118

16 W. H. Baur, A. A. Khan, *Acta Crystallographica, Section B* (1971), 27, 2133-2139

17 J. J. Rehr, and R. C. Albers, *Reviews in Modern Physics* . 73, 621–654 (2000)

18 http://www.slac.stanford.edu/econf/C060709/papers/037_WEPO103.PDF

19 M. Roy, S. Gurman, G. van Dorssen, *Journal Physique IV France*, 7(C2), (1997) pp.C2-151-C2-152.

20 J. J. Rehr, E. A. Stern, R. L. Martin, E. R. Davidson, *Physical Review B*, 17(2), (1978) p.560.

21 T. E. Westre, P. Kennepohl, J. DeWitt, B. Hedman, B.K. Hodgson, K. O.; Solomon, E. I. *Journal of the American Chamical Society*, (1997), 119, 6297-6314.

22 M. Martis, A. Smith, C. Tang, J. Parker, T. Hyde, M. Watson, X. Baucherel, S. Kohara, T. Wakihara, G. Sankar, *Physical Chemistry Chemical Physics*, (2013) 15(28), p.11766.

23 G. I. Panov, A. K. Uriarte, M. A. Rodkin, V. I. Sobolev, *Catalysis Today*, 41, (1998) 365-385

24 G. Yang, J. Guan, L. Zhou, X. Han, X. Bao, *Catalysis Survey. Asia 14*, (2010) 85–94

25 S. Keqiang, *Journal of Catalysis* 254.2 (2008): 383-396

26 K.S. Pillai, J.F. Jia, W.M.H. Sachtler, *Applied Catalysis A: General* 264 (2004) 133–139

27 W. M. Heijboer, D.C. Koningsberger, B. M. Weckhuysen, F. M. F. De Groot, *Catalysis today*, *110*(3), (2005) pp.228-238.

28 S. H. Choi, B. R. Wood, A. T. Bell,M. T. Janicke, K. C. Ott, *Journal of Physical Chemistry B*, (2004) 108(26):8970–8975

29 A. Zecchina M. Rivallan G. Berlier C. Lamberti G. Ricchiardi, *Physical Chemistry Chemical Physics*, (2007) 9(27):3483–3499

30 S. Jakkapan, J. Limtrakul. " *Structural Chemistry* 24.4 (2013): 1307-1318

31 S. Keqiang, H. Xia, Z. Feng , R. van Santen, E. Hensen , C. Li *Journal of Catalysis* 254.2 (2008): 383-396

32 A. Yakovlev, G. M. Zhidomirov, R. A. van Santen. *Journal of Physical Chemistry B*, 105.49 (2001): 12297-12302.

33 Z. Opre, J.-D. Grunwaldt, M. Casapu, T. Mallat and A. Baiker , *Hasylab 2005 Annual Report*, (2005) 639-640

34 K. Simmance, G. Sankar, R. G. Bell, C. Prestipino, W. Van Beek, *Physical Chemistry Chemical Physics* (2010), 12, 559-562.

35 B. Shulin Z. Fangliang X. Qinhu, *Chinese Journal of Inorganic Chemistry,* (1989) 03, en.cnki.com.cn

36 J, Jungho, *ChemCatChem* 6.3 (2014): 848-856.].

37 D. Ugur, *The Journal of Physical Chemistry C*, 116.51, (2012): 26822-26828

38 S. H. Choi, B. R. Wood, A. T. Bell, M. T. Janicke, K. C. Ott, *Journal of Physical Chemistry B* (2004), 108, (26), 8970-8975.

39 V. Valtchev, S. Mintova, M. Tsapatsis, *Ordered Porous Solids – recent advances and prospects*, (2009) Elsevier

40 G. I. Panov, A. S. Kharitonov, V. I. Sobolev, *Applied Catalysis A-General*, (1993) 98, 1-20.

41 A. Martucci, E. Rodeghero, L. Pasti, V. Bosi, G. Cruciani, *Microporous and Mesoporous Materials*, 215, (2015) pp.175-182.

Chapter 6

Conclusions

Microporous aluminosilicates and aluminophosphates have been studied variety of applications. Introducing transition metal ions and other main group elements into their framework structure allows them to be modified into functional redox catalysts for a wide range of industrially important processes. In particular, FeZSM-5 has shown remarkable catalytic activity under mild conditions for the oxidation of benzene to phenol (OBP) using N_2O. Recent work by Sankar et al. has shown that the aluminophosphate FeAlPO-5 is also equally active as a catalyst for this reaction. In this work investigate the changes occurring during the calcination activation and operation of various Fe-substituted nanoporous catalysts using synchrotron based X-ray diffraction and spectroscopy.

The low concentration and random distribution of the iron sites has made the characterisation of the active sites in Fe-substituted nanoporous materials difficult. Synchrotron based X-ray measurement techniques can however afford valuable information which is not possible using standard laboratory techniques. The complex structure, low active site concentration and the seemingly random distribution of metal ions, as well as the presence of the incorporated metal in a number of coordination environments and oxidation states, has greatly complicated the successful characterisation of microporous catalyst systems. In particular the exact identity of the active iron species in FeZSM-5 is still hotly debated. Conventional spectroscopic techniques are often not powerful enough to provide detailed information on the local structure of such sites. However techniques harnessing the intense, coherent light from synchrotron sources are well suited for these types of studies.

FeSAPO-34 and FeAlPO-5 were studied by *in situ* combined XAS/XRD experiments were performed at beamline B18 at the Diamond Light Source in order to determine the types of chemical changes occurring to the iron species during the catalyst activation procedures, as well as changes occurring in the overall framework structure. The samples were formed into pellets and inserted into a custom made *in situ* cell. In situ

XAS and XRD measurements were then performed in alternation as the temperature was increased from 30°C to 550°C with a ramp rate of 5°C min^{-1} under flow of air.

In this study, the aim was to investigate the chemical and geometric structure of the active sites in the iron-substitutes aluminophosphate FeAlPO-5 and silico-aluminophosphate FeSAPO-34. To do so we have used X-ray absorption spectroscopy at the Fe K-edge and examined the catalysts under operating conditions. In both catalysts studied there was an appreciable amount of loss of octahedral Fe and increase in tetrahedral Fe forming coordinatively unsaturated active sites. These sites possess distorted tetrahedral symmetry and have shorter Fe-O bond distances than their respective starting materials. Both AlPO-5 and SAPO-34 show similar behaviour during calcination and show substantial formation of extra framework iron that stabilised after the template molecules have been removed above 350°C. Loss of water was observed at low temperatures between 30-200°C.

The local structure and oxidation state changes of Fe located in FeAlPO-5 and FeSAPO-34 was studied using XAS during calcination in air. Ruthenium is also active for catalytic selective oxidation reactions when introduced to zeolytic materials. In order to examine the possible synergistic effect between metals, Ru was introduced into Fe-substituted nanoporous catalysts via wet impregnation. FeMFI, FeSAPO-5, RuFeMFI and RuFeSAPO-5 then were studied using *in situ* Fe and Ru K-edge EXAFS during calcination in air, activation in He, and pulsed experiments with N_2O/benzene. Results show reduction of Fe upon the introduction of benzene to the system, indicating that the catalytic mechanism for the (OBP) reaction may require this step for the generation of the active Fe species.

The synchrotron beam line is equipped with detectors able to achieve a very high sampling rate and this combined with the high brilliance and coherence of the electromagnetic radiation, also allows one to follow phase changes, thermal expansion, sintering and other physic-chemical events as close to real time as possible, down to microsecond resolution, if the experiment is designed in such a way. A detailed methodical study is ultimately needed using complementary techniques to study such complex systems in-situ to gain a full understanding of how active sites form in nanoporous materials. In the light of evidence important dynamic synergy between

steric effects caused by framework structures and the redox activity of transition metal ions has been revealed that is crucial to understanding these systems.

Understanding the incorporation of catalytically relevant heteroatoms such as Fe into the framework of nanoporous materials has been an important topic as the heteroatom imparts functional properties. The results presented in this thesis may have some significance that may lead to future practical applications in the rational synthesis of new nanoporous materials. However much future work would be required to follow up preliminary studies and further results for a number of different structure and composition types would be valuable in further rationalising the findings. The advanced X-ray based characterisation methods of XAS and XRD have been successfully employed to study a range of Fe and Fe-Ru based industrially relevant and academically interesting nanoporous materials, resulting in an improvement in the understanding of factors contributing to the activation and catalytic function of these materials. In particular the specific changes occurring to Fe and Ru atoms, as well as the large scale changes in the framework structures themselves during industrially relevant conditions of activation and under flow of reactant gases.

While XAS has been successfully employed, use of this technique cannot provide unambiguous information of the substitution of the metal ions in the framework since it is a technique that provides bulk-averaged information about the whole of the sample combined information about both framework and any extra framework species. Therefore complementary characterisation techniques such as XRD have been and must be incorporated to provide a better route into determining the extent of framework substitution where an expansion of the unit cell parameters maybe observed. Other supplementary spectroscopic techniques such as PDF or XPS as well as more standard methods such as EPR or Mossbauer spectroscopy may also be able to shed valuable complementary information. Ultimately work utilising in-situ measurements that couple together multiple techniques would be a rational direction for the future of this research topic.